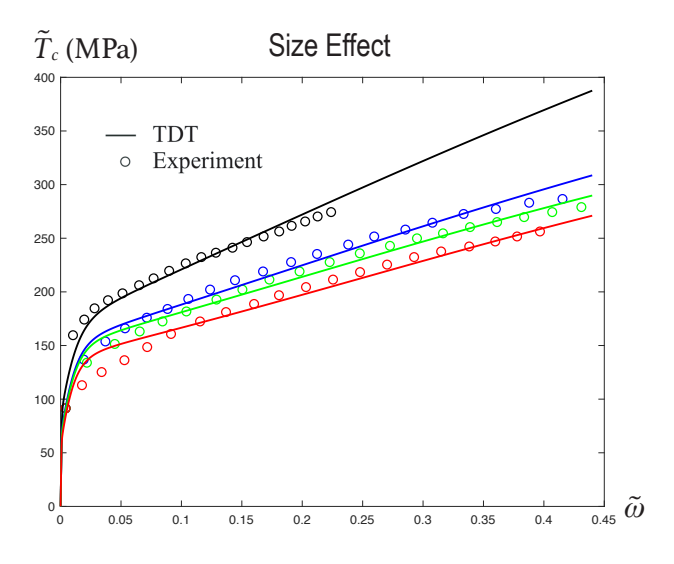
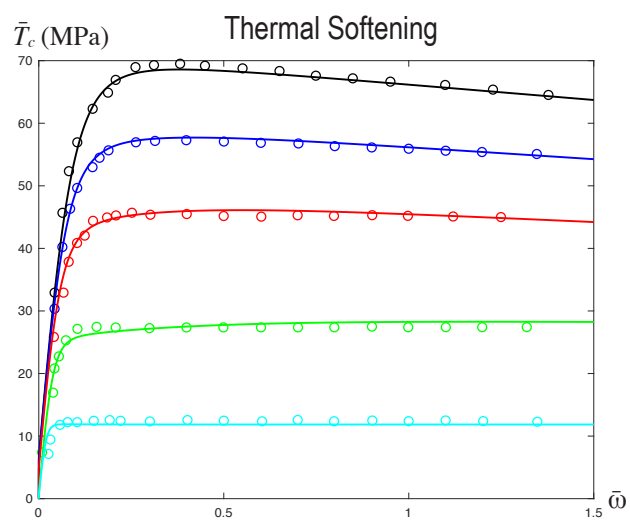


# Thermodynamic Dislocation Theory and its Applications

Yinguang Piao





## RUHR-UNIVERSITÄT BOCHUM Institut für Mechanik

## Thermodynamic Dislocation Theory and its Applications

Dissertation zur Erlangung des Grades

Doktor-Ingenieur

der

Fakultät für Bau- und Umweltingenieurwissenschaften der Ruhr-Universität Bochum

von

**Yinguang Piao** 

20.04.1989 aus Yanji, Jilin China

Bochum 2019

Herausgeber (Publisher):
Institut für Mechanik
— Schriftenreihe —
Ruhr-Universität Bochum
D-44780 Bochum

ISBN 978-3-935892-61-2

This material is presented to ensure timely dissemination of scholarly and technical work. Copyright and all rights therein are retained by the copyright holders. All persons copying this information are expected to adhere to the terms and constraints invoked by the author's copyright. These works or parts of it may not be used to repost reprint/republish or for creating new collective works for resale or redistribution to servers or lists without the explicit permission of the copyright holder.

Dieses Werk ist urheberrechtlich geschützt. Die dadurch begründeten Rechte, insbesondere die der Übersetzung, des Nachdrucks, des Vortrags, der Entnahme von Abbildungen und Tabellen, der Funksendung, der Mikroverfilmung oder der Vervielfältigung auf anderen Wegen und der Speicherung in Datenverarbeitungsanlagen, bleiben, auch bei nur auszugsweiser Verwertung, vorbehalten. Eine Vervielfältigung dieses Werkes oder von Teilen dieses Werkes ist zulässig. Sie ist grundsätzlich vergütungspflichtig. Zuwiderhandlungen unterliegen den Strafbestimmungen des Urheberrechtsgesetzes.

©2019 Yinguang Piao, Institut für Mechanik, Ruhr-Universität Bochum Printed in Germany

Einreichung der Dissertation (Thesis submission): 15.08.2019 Tag der mündlichen Prüfung (Thesis defense): 03.12.2019

Erster Referent (First referee):

Zweiter Referent (Second referee):

Dritter Referent (Third referee):

Vorsitzender (Committee chair):

Prof. Dr. rer. nat. Klaus Hackl
Prof. Dr.-Ing. Bob Svendsen
Prof. Dr.-Ing. Justin Geistefeldt

For my mentor:

Martin Groß

#### Abstract

This doctoral dissertation examines the thermodynamically consistent dislocation plasticity available on the macro- and mesoscopic scale and its applications in several benchmark problems.

In the first part of this thesis, the recently developed thermodynamic dislocation theory of Langer et al. (2010) is revisited and extended. One feature that distinguishes the latter theory from others is that it uses an effective disorder temperature (or its dual, configurational entropy) to describe non-equilibrium behavior. Therefore, it is assumed that the thermodynamic system of crystal containing dislocations consists of two weakly interacting subsystems characterized by a kinetic-vibrational temperature and an effective disorder (configurational) temperature. A system of coupled differential equations resulting from the first and second laws of thermodynamics and dislocation dynamics is derived for the analysis of strain hardening. An extension of the theory involving excess dislocations, developed by Le (2018), is also studied. It enables the investigation of nonuniform plastic deformations of crystals on the mesoscale and the investigation of dislocation-related microstructures and associated mechanical responses.

The second part of the thesis deals with applications of thermodynamic dislocation theory to crystal plasticity. Isotropic hardening by redundant dislocations as well as kinematic hardening by excess dislocations for the crystal undergoing anti-plane constraint shear are investigated. The asymptotically accurate energy density of screw dislocations in the extremely small and large range of dislocation density is calculated and extrapolated. In the twisted wire on the microscale, the size effect due to excess dislocations is investigated and the numerical simulation of the torque-twist curves is compared with the corresponding experiment. The equation for the equilibrium of microforces allows the contributions of yield stress and back stress to torque to be calculated. In the macroscale torsion problem, the hardening behaviour of single crystal copper bars and the thermal softening of polycrystalline aluminium bars are investigated. Numerical results include the evolution of dislocation density and stress state in the specimen. The temperature rise within samples during the thermal softening process is shown. Finally, the distribution of dislocations in the twisted bar is investigated by the continuum dislocation theory with the defect energy. The development of the plastic distortion and dislocation density and the distribution of dislocations are compared with those of other models.

#### Acknowledgments

This work was developed during my Ph.D. study in the years 2015-2019 at the Lehrstuhl für Mechanik - Materialtheorie at Ruhr-Universität Bochum. I appreciate unforgettable and meaningful experiences during the time staying in Germany.

Foremost, I would like to express my sincere gratitude to my advisor Prof. Khanh Chau Le, who gave me an opportunity for the study of Ph.D. and brought me to the field of dislocation mediated plasticity theory. I thank him not only for the excellent advices, unreserved teaching, and patience to discuss my work but also for the enthusiasm and attitude to the research and knowledge that motivate and encourage me. Just as important, my sincere thanks go to Prof. Klaus Hackl for providing me a comfortable environment to do the research and giving me a chance to work at the chair. Besides, I appreciate for some essential ideas came from his timely suggestion and talks in the weekly seminar.

I want to thank all of my colleagues at the chair. They are (in the order of alphabets) Barbara Fromme, Golnaz Hoormazdi, Ulrich Hoppe, Ghina Jezdan, Dustin Jantos, Philipp Junker, Asim Ullah Khan, Christopher Riedel, Stephan Schwarz, and many former colleagues. Especially I thank one of former colleagues, Tuan Minh Tran, for his cooperation and help on the numerical simulation and technical details.

Thanks to my beloved wife, Dongmei Yu, for her companion, supports, and encouragement. This journey would not have been possible without her.

I would like to acknowledge the financial support from China Scholarship Council and the chair.

### Contents

1.	Mot	ivation and State of Arts	1
	1.1.	Motivation	1
	1.2.	State of Arts	2
	1.3.	Scope of the Thesis	4
2.	Fun	damentals	7
	2.1.	Crystal Plasticity and Dislocations	7
		2.1.1. Plastic deformation	7
		2.1.2. Concept of dislocations	10
		2.1.3. Stress and strain of dislocation	13
		2.1.4. Excess and redundant dislocations and the corresponding hard-	
		ening	15
		2.1.5. Size effect	18
	2.2.	Variational Methods of Continuum Mechanics	20
		2.2.1. Calculus of variation	20
		2.2.2. Variational principles in the small displacement elasticity	21
		2.2.3. Direct methods	23
		2.2.4. Thermodynamical principles	26
	2.3.	Thermodynamic Dislocation Theory	29
		2.3.1. Introduction to the theory	29
		2.3.2. The variational approach in thermodynamic dislocation theory .	30
		2.3.3. Equations of Motion	38
3.	Non	-uniform Plastic Deformations Undergoing Anti-plane Constrained	
	She		47
	3.1.	Introduction	47
	3.2.	0,0	48
		3.2.1. A pair of screw dislocations:	48
		3.2.2. A large number of screw dislocations:	55
		3.2.3. Extrapolation of the energy density of excess dislocations:	57
	3.3.	Anti-plane Constrained Shear Deformation and Numerical Simulations	59
	3.4.	Conclusion	69
4.	The	rmodynamic Dislocation Theory: Size Effect in Torsion	71
	4.1.	Introduction	71
	4.2.	Theory of Torsion	71
		4.2.1. Torsion of prismatic bar:	71
		4.2.2. Configuration of screw dislocations in torsion:	73
	4.3.	Thermodynamic Dislocation Theory in Torsion:	75
	4.4.	Parameter Identification and Numerical Simulations	83
	4.5.	Conclusion	92

viii Contents

5.	The	rmodynamic Dislocation Theory in Macro-scale	93		
	5.1.	Introduction	93		
	5.2.	Equations of Motion	93		
	5.3.	Hardening of Copper Bars in Torsion	96		
		5.3.1. Discretization and parameter identification	96		
		5.3.2. Numerical simulations:	100		
	5.4.	Thermal Softening during High-temperature Torsion of Aluminum Bars	102		
		5.4.1. Discretization and parameter identification	102		
		5.4.2. Numerical simulations	106		
	5.5.	Conclusion	109		
•	D:	The Control of Control of the Control of Con			
6.		ribution of Dislocations in Twisted Bar	111		
		Introduction			
	6.2.	Asymptotically Exact Energy of the Bar			
	6.3.	Dislocation Distribution at Zero Dissipation			
		Dislocation Distribution at Non-zero Dissipation			
	0.5.	Conclusion	100		
7.	Sum	mary and Outlook	135		
ΑF	PEN	IDICES	138		
A. Green's function					
Lis	t of	Figures	141		
Lis	t of	Tables	145		
Nomenclature					
Bil	bliogr	raphy	153		
Cu	rricu	lum Vitae	165		

#### 1. Motivation and State of Arts

#### 1.1. Motivation

The processed metals have been used by human beings for more than 5000 years since the bronze age. It was found that plastically deformed metals have a lot of beneficial properties, such as higher strength, as tools and weapons to be used. Despite the long history of the processing technology in metals, it remained at the empirical procedures until the discover of dislocations in the early 20th century, which are the primary carriers of plastic deformation in crystallographic materials. With the development of the microscopy techniques, people nowadays can gain knowledge of dislocations from different perspectives through different length scales from macroscopic to atomic scales and accumulated relatively deep understanding. However, we still lack fundamental theories of dislocation substructure development.

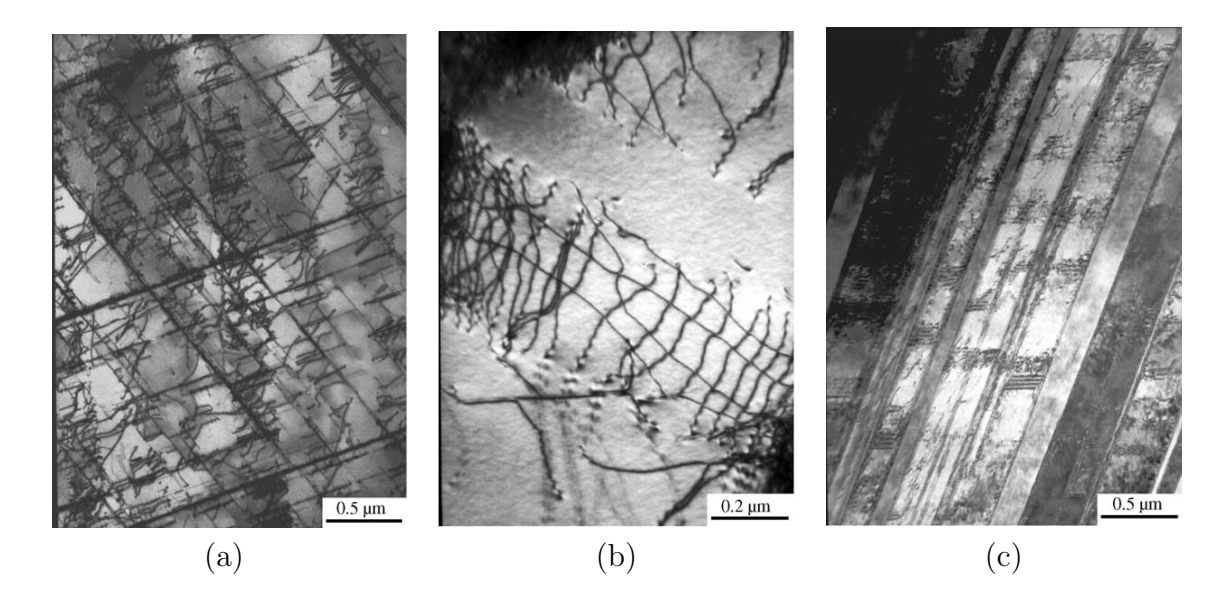


Figure 1.1.: TEM of cryogenic deformation microstructures of austenitic steels:(a) Dislocation networks, (b) Planar dislocation array, (c) Interaction between dislocation slip band and stacking fault (Fu et al., 2005). Images reprinted by permission

Three dislocation-related microstructures, as examples, observed from the impact test of austenitic steels by the transmission electron microscope (TEM) are shown in Fig. 1.1 (Fu et al., 2005), which are dislocation networks, planar dislocation array, and the interaction with other objects. Besides, there are countless rich microstructures, such as dislocation pile-ups, dislocation entanglements, dislocation pattern, polygonization, jogs, loops, and others. The complex structures and networks of dislocations

give rise to abundant macroscopic phenomenologies and mechanical properties. Understanding the mechanism and evolution of dislocations is one of the keys to study crystal plasticity.

#### 1.2. State of Arts

There are various approaches to study the dislocation-mediated plasticity of crystalline materials, such as molecular dynamics simulations on the atomistic scale, discrete dislocation dynamics on the microscopic scale, several continuum theories on the mesoscopic scale presented below, and conventional plasticity theory on the macroscopic scale. Different approaches are specialized in investigating different aspects of materials. Molecular dynamics is a useful tool for the simulation of dislocation interactions as it depends on the details of the dislocation cores. However, since the smallest cell distance in molecular dynamics simulation is smaller than the mean free dislocation path, yield stress and strain hardening are not characterized by dislocation interactions. In addition, the atomistic methods are computationally intensive so that they are limited to smaller regions and shorter time periods. Discrete dislocation dynamics, which models dislocations by line segments as discontinuities in an elastic continuum and solves their dynamics, generation, and interactions, provides detailed information on dislocation distributions. The computational costs required to track dislocation segments remain a disadvantage of this approach. Conventional plasticity theory considers the microstructure in relation to the average variables like the plastic strain or back-stress tensor that are scale-invariant so that it facilitates numerical implementation and allows the treatment of complex boundary conditions. However, as it does not take into account the intrinsic length scale like the length of the Burgers vector, various phenomena that occurred with small sample sizes could not be predicted and described.

As far as the continuum theories of plasticity on a mesoscopic scale are concerned, the first attempts to construct the continuous approach were made independently by Nye (1953); Bilby (1955); Kröner (1955). They established the relationship between plastic deformation and dislocation microstructure by introducing a second-rank dislocation density tensor called Nye's tensor. It acts as a link between the microscopic discontinuous dislocation distribution and a continuous deformation state. Berdichevsky & Sedov (1967) proposed a dynamic theory of continuously distributed dislocations based on Nye's dislocation density tensors. However, due to the absence of physically based constitutive equations, no further work was developed until various experiments (torsion of wires, bending of beams Fleck et al. (1994); Ma & Clarke (1995); Stölken & Evans (1998)) were performed on small samples, and a new phenomenon "size effect" was observed. It inspired many types of continuum theories. One of them is the strain gradient plasticity, which has many branches, such as the phenomenological strain gradient plasticity (Aifantis, 1999; Fleck & Hutchinson, 2001; Gurtin & Anand, 2005), the strain gradient plasticity based on physical dislocation mechanisms (Gao et al., 1999; Nix & Gao, 1997), the physically based gradient plasticity theory (Al-Rub & Voyiadjis, 2006) and the dislocation density based strain gradient model (Brinckmann et al., 2006), and the extensions of higher-order strain gradient plasticity (Gurtin, 2002; Kuroda & Tvergaard, 2008; Svendsen & Bargmann, 2010).

1.2. State of Arts

Another approach that takes into account the excess dislocations, the Continuum Dislocation Theory (CDT), was taken up again by Berdichevsky (2006a), which continued the work initiated in (Berdichevsky & Sedov, 1967). This approach was guided by the Low Energy Dislocation Structure (LEDS) principle first proposed by Hansen & Kuhlmann-Wilsdorf (1986) and supported by various experimental evidences (Hughes & Hansen, 1997; Laird et al., 1986). The LEDS hypothesis states that the true dislocation structure in the final state of deformation minimizes the energy of the crystal under all admissible dislocation configurations, which is the result of the Gibbs variation principle applied to crystals with dislocations (Berdichevsky, 2009). Continuum dislocation theory became successful thanks to advances in statistical mechanics for a large number of dislocations (Groma et al., 2003; Berdichevsky, 2006b, 2016, 2017; Zaiser, 2015). Berdichevsky & Le (2007) applied continuum dislocation theory to model an anti-plane constrained shear and found the analytical solution for the accumulation of dislocations in a single crystal. Afterwards, the theory was applied to many other problems, e.g., plane-strain constrained shear of single crystals having single or double slip systems (Le & Sembiring, 2008a,b), pile-ups in bicrystals (Kochmann & Le, 2008), development of the deformation twinning (Kochmann & Le, 2009a), polygonization (Le & Nguyen, 2012), bending of the beam (Le & Nguyen, 2013), nonlinear continuum dislocation theory (Le & Günther, 2014), martensitic phase transition (Le & Günther, 2015), formation of grains (Koster et al., 2015), indentation (Baitsch et al., 2015), torsion of the bar (Kaluza & Le, 2011; Le & Piao, 2016) and three-dimensional continuum dislocation theory. However, since redundant dislocations and effective disorder temperature are completely ignored, the above CDT cannot properly describe the dissipative process, isotropic hardening and sensitivity of hardening curves to temperature and strain rate.

Continuum dislocation dynamics (CDD), a direct generalization of the continuum theory by Kröner (1958), was initiated by Hochrainer et al. (2007). This theory was applied further by Sandfeld et al. (2011); Hochrainer et al. (2014); Wulfinghoff & Böhlke (2015) for several problems, including dislocation patterning and the size effect. Since CDD describes the kinematic evolution of dislocation system, it has a potential of predicting the time evolution of the dislocation network to equilibrium. Apart from the continuum theory, worth mentioning is the critical thickness theory (CTT) proposed by Matthews & Blakeslee (1974) and developed further by Dunstan et al. (2004, 2009); Dunstan (2012); Motz & Dunstan (2012). It has not only the ability to analyze the phenomenon in microstructures but also the possibility to predict the material length scale in the strain gradient plasticity that is regarded as a phenomenological fitting parameter based on the physical quantities (Dunstan, 2016; Liu & Dunstan, 2017).

In ideal gas or some liquids, elimination of parameters of the time scale of atomic motion gives rise to the macroscopic parameters, such as the pressure, temperature, and density, while it is not the case for solids. So configurational entropy and effective temperature should be taken into account, for they are key thermodynamic parameters in the modeling of the behavior of random structures (Berdichevsky, 2008, 2019). He is not the first to argue that those parameters should be involved. Mehta & Edwards (1989) were perhaps the first to point out the idea by defining the effective temperature as the derivative of the volume (analogous to the energy) with respect to the configurational entropy in the granular materials, and the studies were further done by Edwards (1990, 1994). Using this idea, successful applications and encouraging results have been made in glassy materials and amorphous plasticity (Cugliandolo,

1997; Ono et al., 2002; Haxton & Liu., 2007; Langer, 2008; Bouchbinder & Langer, 2009b; Sollich & Cates, 2012; Kamrin & Bouchbinder, 2014), and in recent year, it was applied to crystal plasticity (Langer et al., 2010; Langer, 2015, 2017a,b,c; Chowdhury et al., 2016; Le & Tran, 2018; Le et al., 2017, 2018). Le (2018, 2019) extended the theory by Langer et al. (2010) into non-uniform deformation in crystals and applied to a number of benchmark problems (Le & Piao, 2018; Le et al., 2018; Le & Tran, 2018; Le & Piao, 2019a,b).

#### 1.3. Scope of the Thesis

Following this introduction, Chapter 2 is dedicated to the overview of the physical, mathematical fundamentals of this dissertation and the introduction to the thermodynamic dislocation theory. In the first part for physical background, it includes a short explanation of plastic deformation, the nature of dislocations, and their properties as well as their types. Mathematical fundamentals comprise the calculus of variation, variational methods, and some useful techniques used in this dissertation. Moreover, the thermodynamical principles are briefly reviewed. In the last part of this chapter, we introduce the thermodynamic dislocation theory to readers in detail. The governing system of the coupled partial differential equations is derived by a variational approach, and comprehensive explanation for each equation of motion is clarified. Four applications of the thermodynamic dislocation theory are studied in the following four chapters.

In Chapter 3, we outline a method to compute the energy for a pair of screw dislocations in the crystal bar with a rectangular cross-section. We then compute the asymptotically exact energy density of a large number of screw dislocations. It is based on the conjecture that the distribution of a moderately large number of excess screw dislocations must be locally double-periodic. A modification of the formula for the defect energy that extrapolated in the extremely small and large range of dislocation density is treated. With the mentioned defect energy, the thermodynamic dislocation theory is applied to solve anti-plane constrained shear deformation. We decoupled an equation for the microforce equilibrium from the governing system of equations, and its analytical solution is found. The evolution of the plastic slip and dislocation density is illustrated, and the kinematic and isotropic hardening are studied. At last, the influence of different boundaries to hardening, as well as the Bauschinger effect, are investigated.

Chapter 4 starts with a brief introduction to the elastic theory of torsion and the configuration of screw dislocations in a twisted crystal bar. Then, another type of non-uniform plastic deformation, torsion of a wire, is investigated. The derivation of the governing equations of thermodynamic dislocation theory for the twisted wire in the cylindrical coordinate system is systematically discussed. The modified Read-Shockley surface energy is involved in the free energy. The simulated torque-twist curves are compared with the data from experiments where the samples of wire are on microscopic scales. The results comprise the size effect of crystals, the distribution of the plastic distortion, and the contribution of back stress to the torque.

In Chapter 5, we still deal with the problem of torsion, but on the macroscopic scale. On this scale, equation of motion for the microforce equilibrium is neglected, and a simple extension of the thermodynamic dislocation theory is applied. The hardening behavior of copper bars is well described by the theory, and in order to capture the thermal softening during high-temperature torsion of aluminum bars, an additional equation of motion for the ordinary temperature is introduced. It turns out that this theory is capable to address the dependency of twist rate and temperature to the hardening. The simulations are compared with the data from the corresponding experiments, and a satisfactory result is obtained.

Chapter 6 treats a specific case that a rank-one defect energy, instead of the one aforementioned, is used in the continuum dislocation theory to study the distribution of dislocations. Non-dissipated process of the twisted bar is investigated, and the results comprise the onset of plastic deformation, stress distribution in the cross-section, and the torque-twist curve in terms of the twist. Moreover, the distribution of excess screw dislocations in a nanowire is studied by the proposed continuum theory and compared with the numerical simulations by Weinberger (2011), showing an excellent agreement. Furthermore, the evolution of plastic distortion by the proposed theory is compared with the results by Kaluza & Le (2011) and Liu et al. (2018), which exhibit several common features.

Chapter 7 summarizes and discusses the results studied in the preceding chapters and shows some outlooks.

#### 2.1. Crystal Plasticity and Dislocations

#### 2.1.1. Plastic deformation

Almost all crystalline solids have a certain elasticity. Elastic deformation is defined as the deformation that disappears as soon as the external forces vanish. The deformation is proportional to the applied force, and the corresponding stress is reversible, insensitive to the strain rate. The elastic deformation only persists at strains of about  $10^{-5}$  up to  $10^{-3}$ . When the strain exceeds this limit, it no longer follows the elastic rule, and the permanent, irreversible plastic deformation occurs. When the applied force is removed after plastic deformation, the solid material does not return to its original shape. In contrast to elasticity, the plastic reaction of crystalline solids depends on temperature and strain rate. Another significant difference between the elastic and plastic deformations can be seen in Fig. 2.1 on an atomic scale. In the elastic deformation by shear stress, all atoms participate in the process, whereas in plastic deformation only a few atoms are involved.

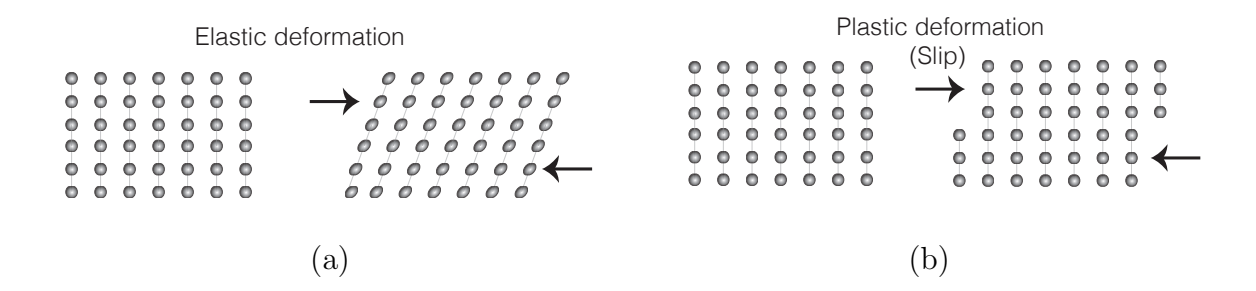


Figure 2.1.: (a) Elastic and (b) Plastic deformation on atomic scale

Plastic deformation in crystalline solids is mainly achieved by slips on individual crystal planes under shear stress, and in addition to slips, it can also be achieved by forming material twins. The slip planes are those of the densest atomic packing, and the slip process also tends to take place in the preferred direction, which has proved to be almost exclusively the densely packed direction, i.e., the slip direction. The combination of a slip plane and a slip direction is called a slip system. The crystal structures of the most common metals can be of the following types: face-centered cubic (FCC), body-centered cubic (BCC) and hexagonal close-packed (HCP). Each crystal structure has different slip systems, and even in the same crystal structures, there can be different slip planes and a different number of slip systems with different materials. Considering, for example, the FCC structure where the {111} family is tightly packed, there are four sliding planes, and in each plane, there are three sliding

Table 2.1.: Slip systems in face-centered cubic crystal with S.P denotes slip plane and S.D indicates slip direction. In each slip system there are three slip directions.

S.P-1	S.D	S.P-2	S.D	S.P-3	S.D	S.P-4	S.D
$\boxed{(111)}$	$[0\bar{1}1]$	$(11\bar{1})$	[011]	$(\bar{1}11)$	$[0\bar{1}1]$	$(1\bar{1}1)$	[011]
<b>\</b>	$[\bar{1}01]$	<b>\</b>	$[1\bar{1}0]$	<b>\</b>	[101]	<b>\$</b>	$[\bar{1}01]$
						$(\bar{1}1\bar{1})$	

directions, such that twelve slip systems in total, as shown in table 2.1. Note that  $(1\,1\,1)$  and  $(\bar{1}\,\bar{1}\,\bar{1})$  indicate the same slip plane. Analogously, the remaining 6 slip planes are classified by 3 different ones. For the description of the crystal structure, we use Miller indices, where the brackets [] and () imply specific directions and planes, and {} } refers to planes of the same type. Fig. 2.2 schematically illustrates slip systems within the FCC unit cell and correspondingly within the cylindrical sample bar in which bar axis is oriented toward [1 1 0].

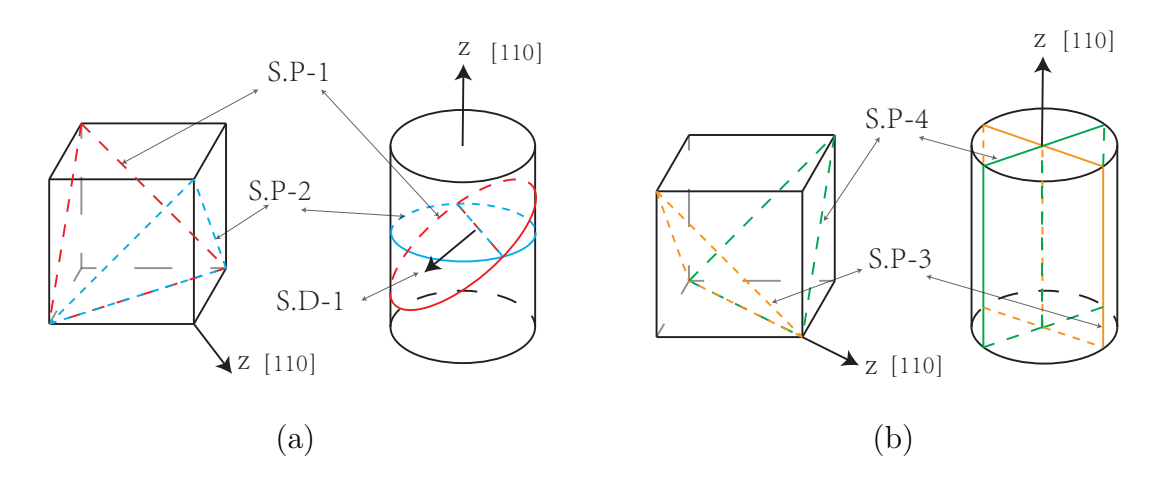


Figure 2.2.: Four slip systems in unit cell of lattice and in the corresponding cylindrical sample: S.P-1 (red lines); S.P-2 (blue lines); S.P-3 (orange lines); S.P-4 (green lines).

In order to investigate the condition under which slip occurs, the tensile or compressive stress applied need to be resolved into the shear stress acting on the slip plane and in the slip direction. This stress is called resolved shear stress, whose magnitude depends not only on the applied stress but also on  $\phi_1$  and  $\phi_2$ , where  $\phi_1$  represents the angle between the normal vector to the slip plane and the direction of the applied stress, and  $\phi_2$  represents the angle between the slip direction and the applied stress. Consequently, the resolved shear stress  $\tau_R$  can be written as follows,

$$\tau_R = \tau \cos \phi_1 \cos \phi_2. \tag{2.1}$$

If the applied stress  $\tau$  is perpendicular to the slip plane as S.P. 2 in Fig. 2.2(a), the angle  $\phi_2$  is 90°, and the resolved shear stress is zero. Likewise, if the applied stress is parallel to the slip planes, as S.P 3 and S.P 4 in Fig. 2.2(b), the angle  $\phi_1$  is 90° so that  $\tau_R$  is zero. In principle, the maximum resolved shear stress can be reached up to half the applied stress, if both angles  $\phi_1$  and  $\phi_2$  are 45°. All other combinations of angles result in a resolved shear stress less than that.

In single crystals, when the resolved shear stress reaches a particular critical value, the slip commences on the corresponding slip system, and this particular critical value is called critical resolved shear stress  $\tau_{cr}$ . If the critical resolved shear stress of the material is known, by (2.1), the magnitude of the yield stress  $\tau_Y$  required to deform plastically can be obtained,

$$\tau_Y = m_s \tau_{cr}, \quad \text{where} \quad m_s = \frac{1}{\cos \phi_1 \cos \phi_2}.$$
(2.2)

The factor  $\cos \phi_1 \cos \phi_2$  is known as Schmid factor. Polycrystals also possess yield stress that must be overpassed to produce plastic deformation. A polycrystalline material consists of many grains which shapes and sizes may vary one to another. Each grain is a single crystal, but due to the fact that slip direction of each grain is not consistently oriented, it makes the plastic deformation more complex. For polycrystals, a similar equation is used to evaluate the yield stress

$$\tau_Y = m_t \tau_{cr}, \tag{2.3}$$

where  $m_t$  is known as the Taylor factor. As a reference,  $m_t \approx 3$  for FCC and BCC materials.

For a single crystal specimen with slip plane inclined to bar axis and the slip direction as shown in Fig. 2.3(a) being the activated slip system in tension test, the slip results in the formation of steps on the surface of the crystal sample as schematically indicated in Fig. 2.3(a). This behavior is experimentally observed that the slips in a Zn single

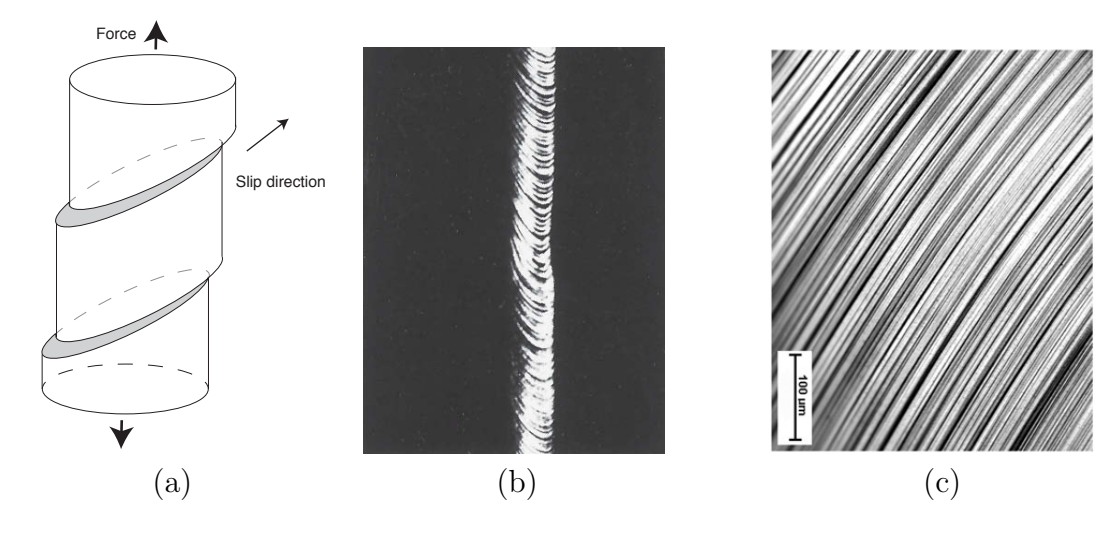


Figure 2.3.: Slips in tension: (a) Schematics of slips in a single crystal under tension, (b) Slips in a Zn single crystal (Callister & Rethwisch, 2012), (c) Slip line pattern on the surface of cylindrical Zn single crystal (Diameter 6mm) in tension (Wrobel & Piela, 2010). Images reprinted by permission

crystal under tension occur at many points along the equivalent slip planes and slip directions through the specimen length (Fig. 2.3(b)). A noticeable detailed image of the slip line pattern produced during the tension of Zn single crystal with  $\phi_1 = \phi_2 = 45^{\circ}$  is shown in Fig. 2.3(c). As it does in tension, the slip mechanism takes place in the same manner in compression test, even on the samples of much smaller size scales. In the Fig. 2.4(a), the material samples choose the favorably oriented planes and directions to slip, forming small steps on the surface. Fig. 2.4(b) and (c) are the

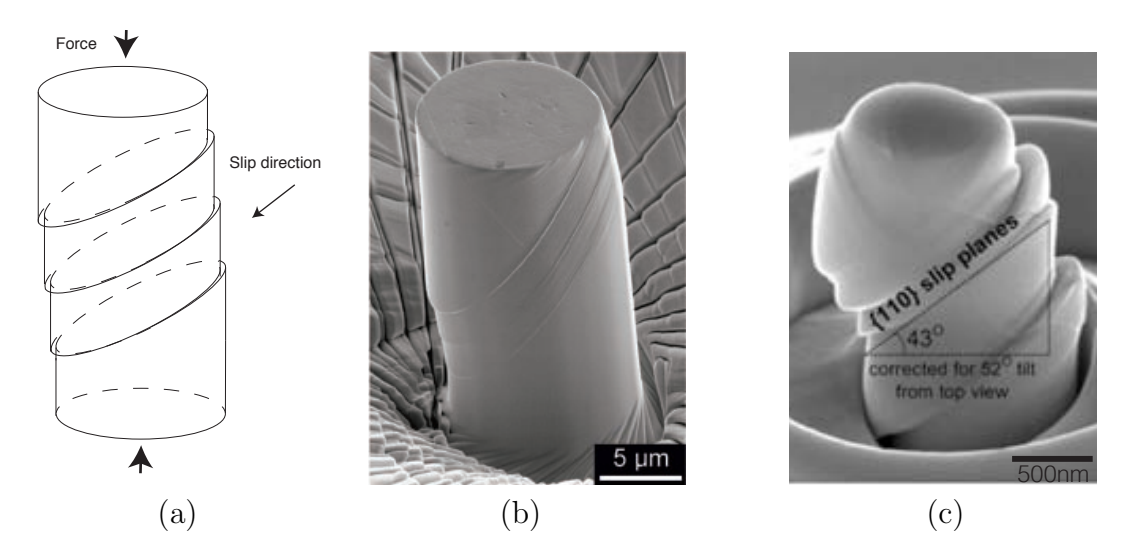


Figure 2.4.: Slips in compression: (a) Schematics of slips in a single crystal under compression, (b) Compressed cylindrical microsample of Ni with 10-μm diameter (Uchic *et al.*, 2004), (c) Severely compressed nanopillar of the single-crystal Nb (Kim *et al.*, 2009). All images reprinted by permission

experimental evidences of slips in compression test performed with different material samples of the diameter  $10\mu$ m and 500nm showing parallel slip lines at the surface. Note that when the sample size decreases to the microscale or lower, it exhibits an important phenomenon, named size effect. The experimental results in two figures illustrate the slip mechanism in various crystal structures (FCC in nickel, BCC in niobium and HCP in zinc) and a wide range from macroscale to nanoscale. The slip process of the crystal plastic deformation is produced by the motion of dislocations, where the forming step on the sample surface is a result of the release of dislocations along the same slip plane from the body. The dislocation plays a crucial role in the plasticity of a crystalline material, and it is the next topic to discuss.

#### 2.1.2. Concept of dislocations

The discrepancy between the theory and experiments: The theoretical estimation for the stress to shear the crystal one atomic distance through the slip plane is much high in comparison with the shear stress in experiment. This discrepancy between the theoretical and experimental results inspired scientists an idea, at the beginning of the 20th century, that crystals contain defects that reduce the strength of the crystal. In 1934, this problem was explained by Taylor, Orowan, and Polanyi simultaneously using the concept of dislocations.

Observation of dislocations: Early in the 1950s, the presence of dislocations are revealed by growth spirals and etch pit techniques, but limited only at the surface. Observation of dislocation may be first done with the aid of transmission electron microscopy (TEM) in 1956, and the dislocation structure detected is consistent with the physical concept that Taylor proposed. In the last half-century, there are many experimental direct observations of dislocations. One example of dislocation observation is shown in Fig. 2.5. The rectangle and cube in Fig. 2.5(a) indicate two views of a metal foil, where a slip plane (orange plane) is inclined inside the body. The green lines

in the slip plane indicate dislocations. Since the thickness of the foil is small, when one sees from the top, dislocations appear as line segments. Fig. 2.5(b) is dark-field TEM image of the initial low-angle tilt grain boundary in strontium titanate bicrystal, and the periodic array of edge dislocations forming a grain boundary are shown. The thickness of the foil is estimated to be about 300 nm, and the interval of the edge dislocations is estimated to be about 19 nm.

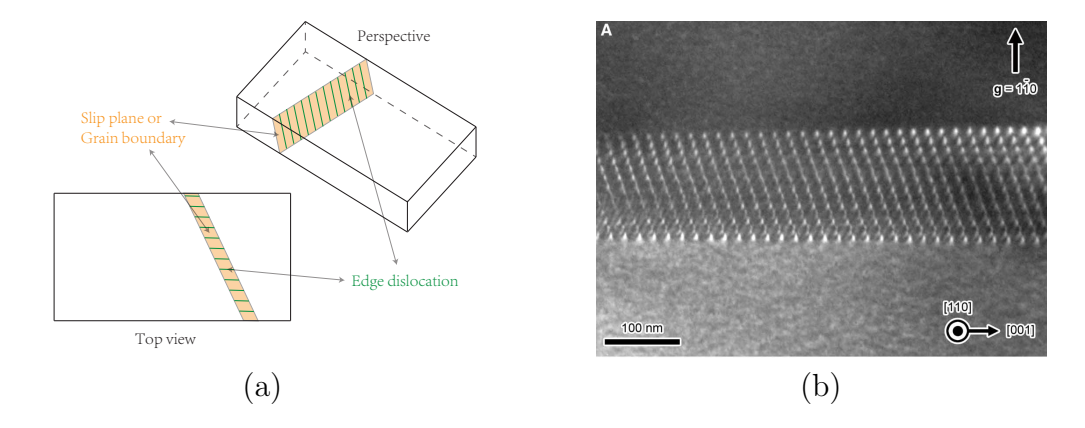


Figure 2.5.: Dislocation observation: (a) Two schematic illustrations of perspective and top view showing the arrangement of grain boundary and the edge dislocations, (b) Dark-field TEM image of the initial low-angle tilt grain boundary consisting of an array of edge dislocations (Kondo *et al.*, 2016). Image reprinted by permission

Lattice defects: In crystals, it is hard to have the atoms perfectly arranged, which leads to the imperfection of crystals that comprises various kind of defects. Unmatched with its name, the defects give many advantages in crystal. Proper treatments enhance desired properties of crystalline solids and enable the materials to have numerous features in engineering usages. According to the dimensions, the defects can be grouped into the point, line, planar, and volume defects. Point defects may include vacancies, self-interstitial atoms, substitutional impurity atom, and interstitial impurity atoms. The line defects are dislocations which are one of the main ingredients in the study of crystal plasticity. One well known planar defect is grain boundary, and the examples of volume defects may include precipitates and voids. The dislocations interact with other sorts of defects, for example, vacancies help the edge dislocations in the climb mechanism, and the grain boundary impedes the movement of dislocations leading to dislocation pile-ups.

Edge and screw dislocations: There are two primary types of dislocations, namely edge dislocation and screw dislocation, characterized by the direction of Burgers vector to the dislocation line. Two types of dislocations are shown in Fig. 2.6(a) and Fig. 2.7(a). Basic ideas on edge dislocation can be obtained from Fig. 2.6(a). Suppose that the gray-colored plane is slip plane dividing the regularly arranged crystal into upper and lower parts. The edge dislocation is indicated by inserting an extra half-plane given by cyan color into the upper part, and the green line, the intersection of two planes, is dislocation line. Normally, the symbol  $\bot$  represents the edge dislocation, where the horizontal line denotes the slip plane and the vertical line indicates the extra half-plane. Neither the extra plane nor the intersected line is the dislocation, but it is a group of atoms around the dislocation line, where those atoms are extruded

from the original position leading the lattice distorted. Therefore, the motion of the dislocation involves the collective motion of many atoms associated. As mentioned, to characterize the dislocation more precisely, a Burgers vector  $\mathbf{b}$  has to be used. The Burgers vector is defined by introducing a Burgers circuit in a crystal containing the dislocation inside the loop, an atom-to-atom path. If one applies a sequence that closes the circuit in a perfect crystal to a dislocation embedded crystal, then the circuit in the latter crystal does not close. Provide that the sequence of the step-by-step circuit in a perfect crystal is  $4\times3$  shown in Fig. 2.6(b) by red line, applying the same sequence in the crystal containing edge dislocation, the starting point does not coincide with the endpoint (Fig. 2.6(a)). A vector required to complete the circuit is the Burgers vector, and this vector is perpendicular to the edge dislocation line. As a result, the slip planes in which the dislocation line and Burgers vector lie is well and uniquely defined. Note that the closure failures of Burgers circuit are not driven by other crystal defects, such as vacancies and interstitials.

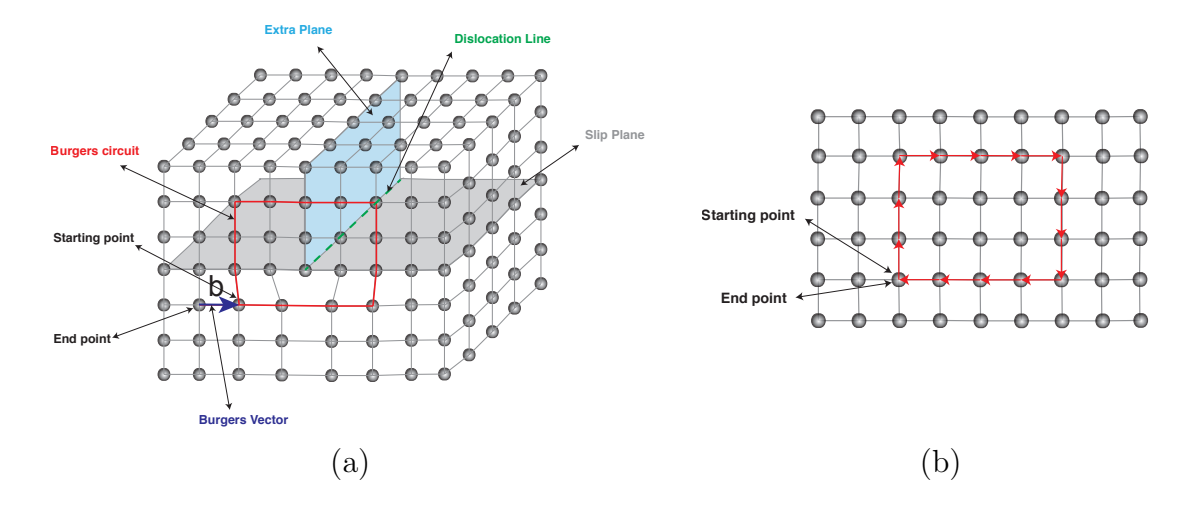


Figure 2.6.: (a) Edge dislocation, (b) Closed circuit drawn in perfect crystal.

Again suppose there is a slip plane divides the crystal upper and lower as shown in Fig. 2.7. Instead of inserting an extra half-plane, we pull the point A front and push the point B back by one atomic spacing, then the following screw dislocation structure is obtained (Fig. 2.7(a)). The green line in the figure is screw dislocation line. By applying the same method of Burgers circuit and connecting the end and starting point, we find a Burgers vector parallel to the screw dislocation line. For that reason, the slip plane is not uniquely defined. Hence, a screw dislocation may move any direction perpendicular to its line and can cross on any plane out of the original slip plane, while the cross slip of edge dislocation is rather constrained by the slip plane. Cross slip of edge dislocation is generally achieved with the aid of the diffusion of vacancies at elevated temperature by climb mechanism. It is necessary to note that, instead of pure edge and pure screw dislocations, dislocations appear in the crystal, generally, in the form of mixed type. The mixed dislocation can be decomposed into the edge and screw components by resolving its Burgers vector into two mutually orthogonal components.

So far, we can summarize essential rules based on geometry of dislocations. Edge dislocation lies perpendicular to its Burgers vector but moves parallel to it. On the other hand, screw dislocation lies parallel to the Burgers vector but moves perpendicular to

the vector.

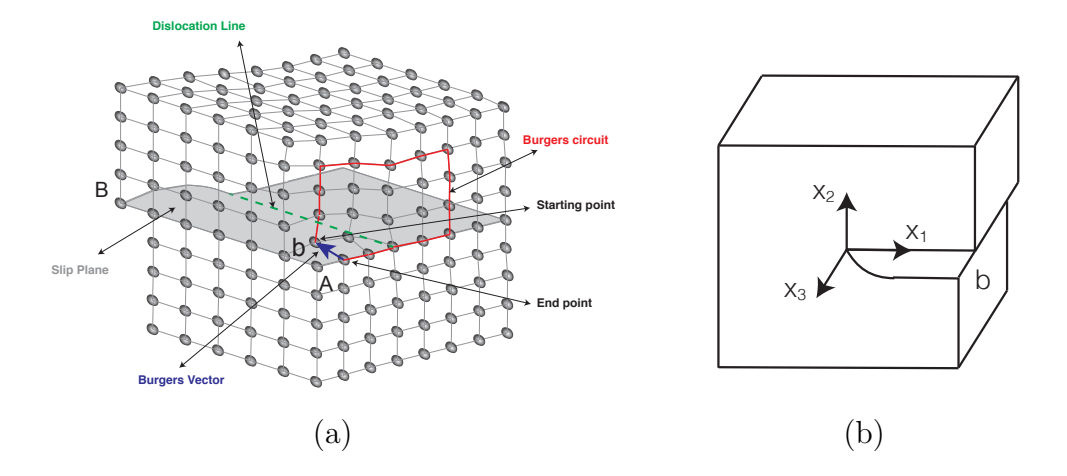


Figure 2.7.: (a) Screw Dislocation, (b) Crystal with screw dislocation located at the origin with the dislocation line oriented towards  $x_3$ -axis.

Dislocation motion and plastic deformation: With the concept of dislocations, the plastic deformation can be explained by the motion of the dislocation under applied shear stress, as an intermediate process from non-slipped to slipped states of the crystal shown in Fig. 2.8. An edge dislocation enters the crystal from the left surface, and moves along the slip direction, then leaves the body and reaches the final state being plastically deformed. In each step of the dislocation motion, only a few atoms are required to rearrange in order to move the extra half-plane (array of hollow balls) toward the right. Consequently, the corresponding stress is much less than that of breaking all bonds of atoms in slip plane at one time, and the crystal performs plastic deformation in much more efficient way as many behaviors that nature does.

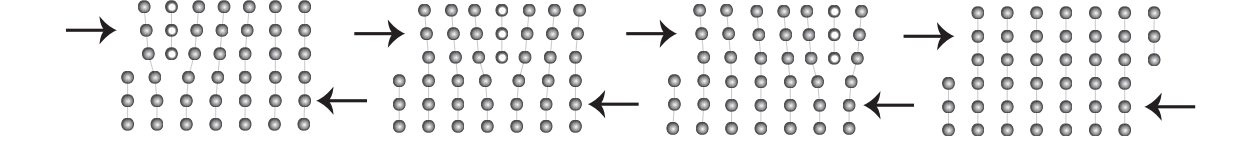


Figure 2.8.: Dislocation Motion leading to plastic slip.

#### 2.1.3. Stress and strain of dislocation

Strain and stress around a dislocation can be sought by finding the displacement field caused by dislocation and inserting it into the kinematics and Hooke's law (Hull, 2011). Here, we introduce an alternative way using the stress function (Le, 2010).

**Screw dislocation:** Consider a screw dislocation lying on the  $(x_1, x_3)$  plane with the dislocation line parallel to  $x_3$ -axis as shown in Fig. 2.7(b). The plastic distortion tensor field,  $-\beta$  (see Sec. 2.3.2), has only one non-zero component given by

$$-\beta_{32} = bH(x_1)\delta(x_2),$$

where  $\delta(x)$  is Dirac delta function, defined as

$$\delta(x) = \begin{cases} \infty, & x = 0, \\ 0, & x \neq 0, \end{cases}$$

and it is constrained to satisfy

$$\int_{-\infty}^{\infty} \delta(x) \mathrm{d}x = 1.$$

As a consequence,  $\delta(x)$  can be regarded as H'(x), which represents the derivative of H(x) with respect to x with H(x) being the Heaviside step function, where H(x) = 0 for x < 0 and H(x) = 1 otherwise. Therefore,

$$-\beta_{32,1} = b\delta(x_1)\delta(x_2) = b\delta(\mathbf{x}),\tag{2.4}$$

where  $\mathbf{x}$  denotes the position of screw dislocation on  $(x_1, x_2)$  plane, and the comma in index denotes the partial derivative with respect to the corresponding coordinate. Suppose that  $\mathcal{A}$  is an area surrounded by a closed circuit containing one screw dislocation, and da is the area element, according to Green's formula, we obtain

$$-\int_{\mathcal{A}} \beta_{32,1} da = -\int_{\partial \mathcal{A}} \beta_{32} dx_2 = b.$$

Since the stress tensor for screw dislocation contains no tensile or compressive components but only two independent non-zero components,  $\sigma_{31}$  and  $\sigma_{32}$ , the equilibrium equation,  $\sigma \cdot \nabla = 0$ , implies the existence of a stress function,  $\Phi$ , satisfying

$$\sigma_{31} = \Phi_{.2}, \quad \sigma_{32} = -\Phi_{.1}.$$
 (2.5)

Recalling the kinematics from Sec. 2.3.2 and with Hooke's law, in isotropic material we have

$$\sigma_{31} = 2\mu\varepsilon_{31}^e = \mu u_{3,1}, \quad \sigma_{32} = 2\mu\varepsilon_{32}^e = \mu(u_{3,2} - \beta_{32}),$$
 (2.6)

where  $\mu$  is shear modulus, and  $\varepsilon_{31}^e$  and  $\varepsilon_{32}^e$  are non-zero components in the elastic strain. Inserting (2.4) and (2.5) into (2.6), we obtain a Poisson's equation

$$\frac{1}{\mu}\nabla^2\Phi = -b\delta(\mathbf{x}),$$

where  $\nabla^2$  is the Laplace operator. In the full plane, this equation has been easily solved in terms of the distance to the position of screw dislocation,  $r = \sqrt{x_1^2 + x_2^2}$ , and the solution is

$$\Phi = -\frac{\mu b}{2\pi} \ln r.$$

Note that, the stress function of the screw dislocation in a particular plane, such as the half-plane or rectangular plane, can be found using Green's function of Laplace operator. Differentiating the stress function according to (2.5), we obtain the non-zero stresses

$$\sigma_{31} = -\frac{\mu b}{2\pi} \frac{x_2}{r^2}, \quad \sigma_{32} = \frac{\mu b}{2\pi} \frac{x_1}{r^2},$$

and the corresponding elastic strains are

$$\varepsilon_{31}^e = -\frac{b}{4\pi} \frac{x_2}{r^2}, \quad \varepsilon_{32}^e = \frac{b}{4\pi} \frac{x_1}{r^2}.$$

The variable r in the denominator of the stresses and strains leads the two components to infinity as  $r \to 0$ . Since no material can undergo infinite stress, the elasticity theory is no longer valid near the origin. In other words, when r is smaller than a specific value  $r_0$ , it comes to a region within which the linear-elastic solution breaks down. This region is called the core of the dislocation, and  $r_0$  is the radius of dislocation core. In most cases, it is thought that  $r_0 \leq 1$ nm.

Edge dislocation: Since this thesis deals mainly with screw dislocations for crystal plasticity and the microstructures, we omit the derivation of stresses and strains of an edge dislocation and show only the results. The details and further information can be found in Le (2010). The stress function of an edge dislocation is found to be the solution of following equation

$$\frac{1 - \nu_p}{2\mu} \nabla^2 \nabla^2 \Phi = -b\delta_{,2}(\mathbf{x})$$

with  $\nu_p$  being Poisson's ratio. Its particular solution is

$$\Phi = \frac{\mu b}{2\pi (1 - \nu_p)} x_2 \ln r,$$

and the non-zero components of the stress tensor are

$$\sigma_{11} = -\frac{\mu b}{2\pi (1 - \nu_p)} \frac{x_2 (3x_1^2 + x_2^2)}{(x_1^2 + x_2^2)^2}, \quad \sigma_{22} = -\frac{\mu b}{2\pi (1 - \nu_p)} \frac{x_2 (x_1^2 - x_2^2)}{(x_1^2 + x_2^2)^2},$$

$$\sigma_{12} = -\frac{\mu b}{2\pi (1 - \nu_p)} \frac{x_1 (x_1^2 - x_2^2)}{(x_1^2 + x_2^2)^2}, \quad \sigma_{33} = -\frac{\mu b \nu_p}{\pi (1 - \nu_p)} \frac{x_2}{x_1^2 + x_2^2}.$$

The corresponding elastic strains are then

$$\varepsilon_{11}^{e} = -\frac{b}{4\pi(1-\nu_{p})} \frac{x_{2}[(3-2\nu_{p})x_{1}^{2} + (1-2\nu_{p})x_{2}^{2}]}{(x_{1}^{2}+x_{2}^{2})^{2}},$$

$$\varepsilon_{22}^{e} = \frac{b}{4\pi(1-\nu_{p})} \frac{x_{2}[(1+2\nu_{p})x_{1}^{2} - (1-2\nu_{p})x_{2}^{2}]}{(x_{1}^{2}+x_{2}^{2})^{2}},$$

$$\varepsilon_{12}^{e} = \frac{b}{4\pi(1-\nu_{p})} \frac{x_{1}(x_{1}^{2}-x_{2}^{2})}{(x_{1}^{2}+x_{2}^{2})^{2}}.$$

We see that the crystal containing an edge dislocation is in a state of plane strain.

#### 2.1.4. Excess and redundant dislocations and the corresponding hardening

Besides the type in accordance to the Burgers vector relative to dislocation's line (edge and screw dislocation), another one can be made through the geometric consequence in which dislocations are decomposed into excess and redundant dislocation. In literature, they have another name, so-called the Geometrically Necessary Dislocation (GND) and the Statistically Stored Dislocation (SSD), respectively.

Excess dislocations exist in order to fulfill the compatibility condition of the strain tensor, simultaneously to accommodate the curvature of crystal lattices. In other words, this lattice curvature emerged from gradients of plastic deformation requires excess dislocations to be stored to maintain the lattice continued. When a crystal sample subjects to non-uniform deformation or a gradient of stress, for instance, torsion of bar, bending of thin beam and indentation in small object, a group of dislocations possessing one sign will be separated from those of opposite sign and accumulate in different regions. The density of accumulated signed dislocations is called excess dislocation density. It is first introduced by Nye (1953) and further studied by Bilby (1960), Kröner (1962) and Ashby (1970). In recent years, the study on excess dislocation is widely investigated since the development of high-end engineering applications requires knowledge about the properties of materials in micro or sub-micron sizes. On such small scales, the excess dislocations play an essential role in microstructure, plastic flow, and hardening of crystals, for they inherently contain an intrinsic material length-scale, while classical continuum mechanics doesn't, such that it fails to predict size effect behavior. One intrinsic length-scale in crystal plasticity is the length of Burgers vector because it characterizes the excess dislocation, and it is highly related to the density of excess dislocations which is a state variable in the free energy of the crystal. The other intrinsic length-scale could be grain size in polycrystals. However, it is beyond the scope of this study, and we will use either single crystal or the polycrystals with same grain size in order to make the influence of Hall-Petch effect as little as possible.

The remainder out of total dislocation density is that of redundant dislocation. Each redundant dislocation may also possess a sign. However, each dislocation is paired with the other of the opposite sign with the same slip system. Thus, two dislocations form a dislocation dipole. In continuum level, the sign of redundant dislocations is canceled out and is not taken into consideration. As a result, the Burgers vector of redundant dislocations vanishes. Redundant dislocations are comprised of dislocation dipoles and (or) planar dislocation loops, which are examples of dislocation structure of zero Burgers vector (Arsenlis, 1999). With high enough resolution, the redundant dislocation probably can be observed. However, it is not possible to identify it as being redundant or excess dislocation. Since redundant dislocations as dipoles do not accommodate plastic strain gradient, it does not lead to lattice curvature. Under uniform deformation, such as uniaxial tension, redundant dislocations are evolved from mutual trapping processes. It is believed that as long as a crystal is strained plastically, redundant dislocations become stored. The plastic deformation in metals enhances the dislocation formation and dislocation storage. Dislocation storage leads to material hardening because it impedes the motion of other dislocations, and more strength is needed to overcome the barrier. This process is regarded as short-range interaction and is the primary mechanism of hardening by redundant dislocations—the evolution of redundant dislocation results in the isotropic hardening.

On the other hand, excess dislocations cause additional storage of defects by acting as individual obstacles to the slip of redundant dislocations, and it increases the deformation resistance so that the material is hardened (Gao et al., 1999). Besides, excess dislocations contribute to hardening by producing back stress that influences the equilibrium of microforces for the crystallographic slip. It is possible because excess dislocations possess a non-zero Burgers vector within the material body, and these dislocations induce long-range stresses resulting in back stress. This will be shown

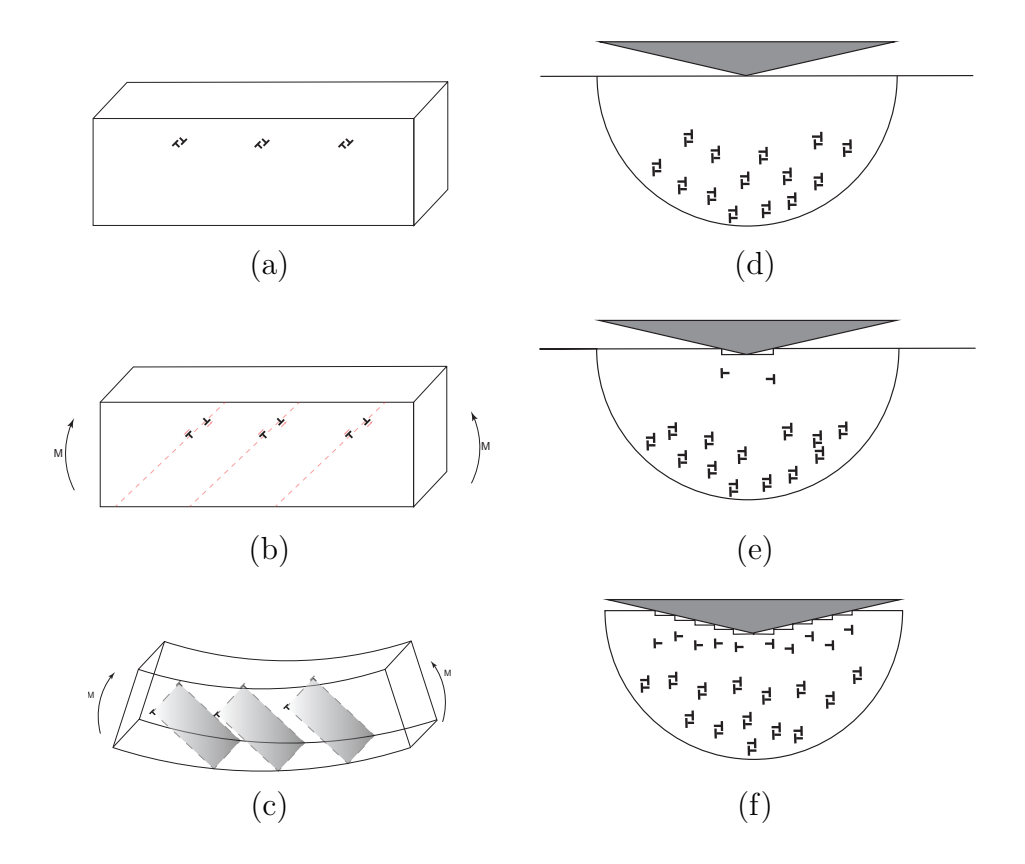


Figure 2.9.: Schematic illustration of the mechanism of the bending and indentation:

(a) A crystal containing dislocations, (b) Dissolved dislocations from edge dislocation dipoles under applied moment, (c) Bent beam by having additional half planes, (d) A crystal before indentation, (e) One atomic plastic deformation formed by storing a pair of edge dislocations, (f) The crystal indented further.

in the subsequent chapters that excess dislocations are responsible for the kinematic hardening.

The concept that how the beam under bending requires excess dislocations for geometrical needs to accommodate the lattice curvature has been specified by the mechanism of the expansion of dislocation loops (Arsenlis (1999)). Here we introduce the dissolution of dipoles, which may also explain the bending mechanism as depicted in Fig. 2.9. Assume that a crystal contains edge dislocation dipoles, Fig. 2.9(a). When a moment is applied to the beam and exceeds the particular critical value, the dislocation dipoles are decomposed into positive and negative edge dislocations, and they start to slip along with its slip system. Red dashed lines in Fig. 2.9(b) are the slip planes perpendicular to the paper plane. Under the applied shear, the negative edge dislocations move toward the neutral line of beam, while the positives move to bottom and top of the beam and leave the free surface. As a result, negative dislocations remain in the crystal body. Since edge dislocations lead the crystal to have additional half-planes as shown in Fig. 2.9(c) (shaped plane), they accommodate the curvature of lattices. Gao & Huang (2003) has illustrated another example of geometrical needs of excess dislocation in the indentation process. Fig. 2.9(d) shows the original shape of the material surface under the indenter. Suppose the indenter produces one atomic plastic deformation to the material, it has to store an excess dislocation to permit the

plastic deformation as shown in Fig. 2.9(e) and more excess dislocations are generated when the indenter deforms plastically further, Fig. 2.9(f). In this case, the positive dislocations dissolved from dislocation dipoles congregate around the indenter to accommodate the plastic deformation, while the negatives move apart from it.

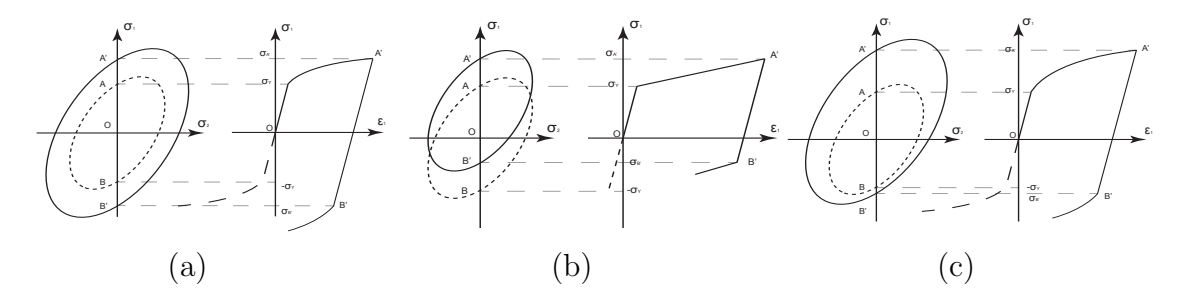


Figure 2.10.: Three types of work hardening: (a) Isotropic hardening, (b) Kinematic hardening, (c) The combination of isotropic and kinematic hardening

Let us here briefly overview hardening behaviors caused by excess dislocations and by redundant dislocations, namely, kinematic hardening and isotropic hardening, respectively. Suppose a material has an elliptical initial yield surface, the isotropic hardening is understood that the yield surface inflates uniformly remaining its shape unchanged, while the center of geometry does not move as illustrated in the left of Fig. 2.10(a), where  $\sigma_1$  and  $\sigma_2$  are the principal stresses. The right figure is the corresponding response in the stress-strain curve including loading process OA' and reversal process A'B'. Its main characteristic is that the magnitude at yielding point A' and B' are equal. In pure kinematic hardening, the yield surface is shifted in the absence of expansion and rotation. Fig. 2.10(b) exemplifies a linear kinematic hardening of a material. In the presenting case, since AB = A'B', the sum of elastic range in tension and compression is not changed by plastic strain so that  $|\sigma_{A'}| + |\sigma_{B'}| = 2\sigma_Y$ . Kinematic hardening gives rise to the Bauschinger effect, a phenomenon that a specimen in the reloading process begins to flow at reduced stress, when the specimen is plastically deformed in one direction and then immediately reloaded in the opposite direction.

#### 2.1.5. Size effect

Metals on small scales exhibit inconsistent physical behaviors as they do on the macroscales. The strengthening of crystalline materials is one of the issues, and it is called the size effect that characterizes the phenomenon that "the smaller, the stronger."

One can distinguish three main types of size effects. The first type, the intrinsic size effect, is in general caused by restricting dislocation motion, such as boundary strengthening and particle hardening. One typical example is the Hall-Peach effect (the effect of grain size) in metals. Hall (1951) and Petch (1953) concluded that the flow stress increases inversely with the square root of the grain size d that can be expressed as  $\sigma_Y \propto d^{-1/2}$ . It is widely accepted that the grain boundaries act as obstacles hindering the dislocation movement and the pile-ups of dislocations induced by grain boundaries require the stronger stress to yield the materials. However, this effect is not valid for all material sizes. Note that an inverse Hall-Petch effect appears below a specific grain size with the scale of the nanometer (Chokshi et al., 1989). Besides the grain

boundaries, the reinforcement of particles can also restrict the dislocation movement to lead the intrinsic size effect. Another type of size effect is generally attributed to the excess dislocations due to non-uniform deformation. Fleck et~al.~(1994) performed experiments on the polycrystalline copper wires with several different wire diameters ranging from 12 to 170  $\mu$ m, which exhibited strong size dependence of strength in torsion, while a minor influence of wire diameter on tensile behavior. The experiment in torsion is recently further confirmed with different circumstances (Liu et~al., 2012; Gan et~al., 2014). Note that since the conventional theories of plasticity are lack of the intrinsic material length scale, such as the Burgers vector, they can not capture this phenomenon. On the contrary, there is a type of size effect in the absence of gradients of the plastic strain, which is shown by the experiments performed on gold at sub-micron scale (Uchic et~al., 2004). This size effect is ascribed to the mechanism of dislocation starvation (Greer et~al., 2005), causing the nucleation of dislocations rather than the motion of the existing ones to dominate the plasticity.

The main interest of this study is the investigation of the size effect attributed to the excess dislocation. Aside from torsion, there are some other examples of non-uniform plastic deformation in material science and engineering corresponding to this phenomena, such as the bent beams (Stölken & Evans, 1998; Wang et al., 2003; Motz et al., 2005; Demir et al., 2010; Hayashi et al., 2011), and indentation test (Ma & Clarke, 1995; Nix & Gao, 1997; Kysar et al., 2010). Those advanced experiments spurred the interest in the concept of excess dislocation densities (Nye, 1953; Bilby, 1955; Kröner, 1955) and further inspired to the development of various theories, for example strain gradient plasticity theory (Fleck et al., 1994; Fleck & Hutchinson, 2001; Gurtin & Anand, 2005; Huang et al., 2004; Al-Rub & Voyiadjis, 2004; Kuroda & Tvergaard, 2008; Bardella & Panteghini, 2015). Mention that, earlier than the works aforementioned, Berdichevsky & Sedov (1967) proposed a dynamic theory of continuously distributed dislocations introducing the higher-order displacement gradients (plastic strain gradients) into the internal energy and dissipation potential. However, as criticized by Aifantis (2009b), due to its formal complexity and weak transparency, no further work was directly motivated. Continuum dislocation theory (CDT) accounting for excess dislocations, proposed for instance in (Le & Stumpf, 1996; Berdichevsky, 2006a; Kaluza & Le, 2011; Le & Nguyen, 2013; Le & Günther, 2014; Baitsch et al., 2015; Le & Piao, 2016; Liu & Dunstan, 2017; Liu et al., 2018), is more predictive as kinematic hardening, and size effect are captured by the first principle calculation of energy of dislocated crystals. Also worth mentioning are the continuum dislocation dynamics (CDD) and the critical thickness theory (CTT) (Dunstan et al., 2004, 2009; Dunstan, 2012; Motz & Dunstan, 2012) that have the potential to describe the size effect.

#### 2.2. Variational Methods of Continuum Mechanics

#### 2.2.1. Calculus of variation

Let  $L(x, u, u_{,i})$  be a continuously differentiable function with respect to its arguments. Suppose  $x = \{x_1, x_2, x_3\}$  is a point in 3-dimensional space, and u(x) is a function of x. Our interest is to find the functions for which the functional

$$I(u) = \int_{\mathcal{V}} L(x_i, u, u_{,i}) d\mathcal{V}, \quad \text{with} \quad u_{,i} = \frac{\partial u}{\partial x_i},$$
 (2.7)

has an extremum on the piecewise smooth region  $\mathcal{V}$  in 3-dimensional space, where function L is called Lagrangian. Note that the Lagrangian can contain n unknown functions for the set  $\{u^1(x), ..., u^n(x)\}$ . On  $\partial \mathcal{V}_u$ , one part of the boundary  $\partial \mathcal{V}$  of region  $\mathcal{V}$ , the function u(x) may subject to a constraint,

$$u(x) = \bar{u}(x)$$
 at  $\partial \mathcal{V}_u$  (2.8)

where the bar notation indicates that function u(x) is prescribed with a given boundary value. A necessary condition for the differentiable functional I(u) to have an extremum is that its variation vanishes for all admissible variations  $\delta u$ , namely

$$\delta I = \int_{\mathcal{V}} \left( \frac{\partial L}{\partial u} \delta u + \frac{\partial L}{\partial u_{,i}} (\delta u_{,i}) \right) d\mathcal{V} = 0.$$

Since function  $\delta(u_{,i})$  is dependent on  $\delta u$ , the second term in the integrand can be expanded by integration by parts, and the variation of the functional (2.7) becomes

$$\delta I = \int_{\mathcal{V}} \left[ \left( \frac{\partial L}{\partial u} - \frac{\partial}{\partial x_i} \frac{\partial L}{\partial u_{,i}} \right) \delta u + \left( \frac{\partial L}{\partial u_{,i}} \delta u \right)_{,i} \right] dx$$
$$= \int_{\mathcal{V}} \left( \frac{\partial L}{\partial u} - \frac{\partial}{\partial x_i} \frac{\partial L}{\partial u_{,i}} \right) \delta u dx + \int_{\partial \mathcal{V}} \frac{\partial L}{\partial u_{,i}} n_i \delta u da,$$

where  $n_i$  denotes the unit normal vector to the area element da. The value  $\delta u$  changes independently inside  $\mathcal{V}$  and on the boundary  $\partial \mathcal{V}$ , which implies that

$$\frac{\partial L}{\partial u} - \frac{\partial}{\partial x_i} \frac{\partial L}{\partial u_{,i}} = 0, \quad \text{in} \quad \mathcal{V}.$$
(2.9)

Eq.(2.9) is known as Euler equation of the functional (2.7). Since (2.8) implies that

$$\delta u = 0, \quad \text{on} \quad \partial \mathcal{V}_u,$$
 (2.10)

on the boundary out of  $\partial \mathcal{V}_u$ , the following relation is satisfied

$$\frac{\partial L}{\partial u_{,i}} n_i = 0.$$

Laws of variations: The following relations are useful when dealing with the variational operator  $\delta$ . Suppose that  $L_1$  and  $L_2$  are functions of dependent variable u(x) with x being the independent variable,

$$\delta(L_1 + L_2) = \delta L_1 + \delta L_2, 
\delta(L_1 L_2) = \delta L_1 L_2 + L_1 \delta L_2, 
\delta(L_1)^n = n(L_1)^{n-1} \delta L_1.$$

If L is a function of several dependent variables as L(u, v, w), then

$$\delta L = \delta_u L + \delta_v L + \delta_w L,$$

where  $\delta_u$ ,  $\delta_v$  and  $\delta_w$  denote the partial variation with respect to u, v, w, respectively. The relations for variation of differential and integral of the variable are

$$\delta(\nabla u) = \nabla(\delta u),$$

$$\delta\left(\int_{\mathcal{V}} u \, d\mathcal{V}\right) = \int_{\mathcal{V}} \delta u d\mathcal{V}.$$
(2.11)

#### 2.2.2. Variational principles in the small displacement elasticity

Governing equations: The governing equations in the small displacement elasticity theory may consist of the strain-displacement relations, equilibrium equations and constitutive equations that are summarized as follows.

Strain-displacement equations: The attention is focused on the geometry of motion and deformation without consideration of forces. The displacement vector  $\mathbf{u}$  is the change of the particle position from the reference configuration to the current configuration. The strain tensor is connected to displacement vector by taking the symmetric part of deformation gradient,

$$\boldsymbol{\varepsilon} = \frac{1}{2}(\nabla \mathbf{u} + \mathbf{u}\nabla).$$

Equations of equilibrium: The stress acting on the material body is denoted by  $\sigma$ , while the external force  $\mathbf{f}_B$  indicates the body force. Besides, there is one more sort of external force acting on the boundary of the body, namely surface force  $\mathbf{f}$ . The equation of equilibrium shown below is the consequence of the principle of conservation of linear momentum for the static problem,

$$\operatorname{div}\boldsymbol{\sigma} + \mathbf{f}_B = 0.$$

Constitutive equation: The study of mechanical behavior is described by the constitutive equation, which relates the strain to the stress. They do not follow directly from the physical law but are rather a result of experimental observation. In elasticity theory of solids, the constitutive law is in the form of Hooke's law. The 81 (=  $3^4$ ) components in the fourth-order tensor  $\mathbb C$  can be reduced to 2 independent coefficients, Lamé parameters  $\mu$  and  $\lambda$ , by virtue of the assumption of hyperelastic materials, isotropic material behavior, and the symmetry of stress and strain tensor,

$$\sigma = \mathbb{C} : \varepsilon = 2\mu\varepsilon + \lambda(\mathbf{tr}(\varepsilon))\mathbf{I}.$$

In addition, from the principle of conservation of angular momentum, we have  $\boldsymbol{\sigma} = \boldsymbol{\sigma}^T$  and due to the uniqueness of displacement field from a given strain field, the compatibility equations  $\nabla \times \boldsymbol{\varepsilon} \times \nabla = 0$  must be fulfilled. Furthermore, the variables  $\boldsymbol{\sigma}$  and  $\mathbf{u}$  satisfy the boundary conditions

$$\boldsymbol{\sigma} \cdot \mathbf{n} = \mathbf{f}, \quad \text{on} \quad \partial \mathcal{V}_t,$$
  
 $\mathbf{u} = \bar{\mathbf{u}}, \quad \text{on} \quad \partial \mathcal{V}_u.$  (2.12)

where  $\partial \mathcal{V} = \partial \mathcal{V}_t \cup \partial \mathcal{V}_u$  and  $\partial \mathcal{V}_t \cap \partial \mathcal{V}_u = 0$ .

**Principle of virtual work**: We assume that the body executes an arbitrary set of infinitesimal virtual displacement  $\delta u$ , then the integral of the multiplication of equilibrium equation and the virtual displacement over the body gives us

$$-\int_{\mathcal{V}} \left[ (\operatorname{div} \boldsymbol{\sigma} + \mathbf{f}_B) \cdot \delta \mathbf{u} \right] d\mathcal{V} = 0.$$

Concerning the symmetry of the stress and using (2.11) and divergence theorem, we have

$$\int_{\mathcal{V}} [\boldsymbol{\sigma} : \delta \boldsymbol{\varepsilon} - \mathbf{f}_B \cdot \delta \mathbf{u}] d\mathcal{V} - \int_{\partial \mathcal{V}_t} (\boldsymbol{\sigma} \cdot \mathbf{n}) \cdot \delta \mathbf{u} da - \int_{\partial \mathcal{V}_u} (\boldsymbol{\sigma} \cdot \mathbf{n}) \cdot \delta \mathbf{u} da = 0.$$

Applying the boundary conditions (2.10) and  $(2.12)_1$ , we arrive at the principle of virtual work, Eq. (2.13),

$$\int_{\mathcal{V}} (\boldsymbol{\sigma} : \delta \boldsymbol{\varepsilon} - \mathbf{f}_B \cdot \delta \mathbf{u}) d\mathcal{V} - \int_{\partial \mathcal{V}_t} \mathbf{f} \cdot \delta \mathbf{u} da = 0.$$
 (2.13)

The work done by the actual forces through a virtual displacement of the actual configuration is called virtual work. According to the forces, it can be divided into two functions,

$$\delta W_{int} = \int_{\mathcal{V}} \boldsymbol{\sigma} : \delta \boldsymbol{\varepsilon} d\mathcal{V},$$
  
$$\delta W_{ext} = \int_{\mathcal{V}} \mathbf{f}_{B} \cdot \delta \mathbf{u} d\mathcal{V} + \int_{\partial \mathcal{V}_{t}} \mathbf{f} \cdot \delta \mathbf{u} da$$

where  $\delta W_{int}$  is internal virtual work stored in the body, and  $\delta W_{ext}$  is external virtual work. With  $\delta W_{int} = \delta W_{ext}$ , the principle of virtual work states that a continuous body is in equilibrium if and only if the virtual work of all forces acting on the body is zero in a virtual displacement.

**Principle of minimum total potential energy**: The principle of virtual work (2.13) can be expressed as

$$\int_{\mathcal{V}} (\boldsymbol{\sigma} : \delta \boldsymbol{\varepsilon} - \mathbf{f}_B \cdot \delta \mathbf{u}) d\mathcal{V} - \int_{\partial \mathcal{V}_1} \mathbf{f} \cdot \delta \mathbf{u} da = \int_{\mathcal{V}} \delta \psi(\boldsymbol{\varepsilon}) d\mathcal{V} + \int_{\mathcal{V}} \delta \varphi_1(\mathbf{u}) d\mathcal{V} + \int_{\partial \mathcal{V}_2} \delta \varphi_2(\mathbf{u}) da = 0,$$

if there exist the potential functions  $\varphi_1$  and  $\varphi_2$  and a strain-energy function  $\psi$ , such that

$$\sigma = \frac{\partial \psi(\varepsilon)}{\partial \varepsilon}, \quad \varphi_1(\mathbf{u}) = -\mathbf{f}_B \cdot \mathbf{u}, \quad \varphi_2(\mathbf{u}) = -\mathbf{f} \cdot \mathbf{u},$$

accordingly,

$$\delta \int_{\mathcal{V}} \psi(\boldsymbol{\varepsilon}) d\mathcal{V} = \int_{\mathcal{V}} \boldsymbol{\sigma} : \delta \boldsymbol{\varepsilon} d\mathcal{V}, \quad -\delta \varphi_1(\mathbf{u}) = \mathbf{f}_B \cdot \delta \mathbf{u}, \quad -\delta \varphi_2(\mathbf{u}) = \mathbf{f} \cdot \delta \mathbf{u}.$$

Note that when the Helmholtz free energy is solely a function of  $\varepsilon$ , it is same as the strain-energy function. Then we arrive at the principle of minimum total potential energy (2.14), which states that if a body is in equilibrium, among all admissible fields

satisfying (2.12), the one that makes  $\Pi$  a minimum corresponds to the equilibrium solution,

$$\delta\Pi = 0. \tag{2.14}$$

where  $\Pi$  is called the total potential energy,

$$\Pi(\mathbf{u}) = \int_{\mathcal{V}} (\psi(\boldsymbol{\varepsilon}) + \varphi_1(\mathbf{u})) d\mathcal{V} + \int_{\partial \mathcal{V}_t} \varphi_2(\mathbf{u}) da.$$

#### 2.2.3. Direct methods

**Dual variational principle**: It is known that an Euler equation can be derived from different functionals. This means that the solution of a problem can be sought by different variational principles, such as the principle of minimum total potential energy and the principle of minimum complementary energy in elasticity theory. All of which implies the idea of duality that the variational problem might be transformed into the one dual to the initial problem.

Suppose that we are interested in the minimization problem of a functional I(u)

$$\check{I} = \min_{u} I(u), \tag{2.15}$$

where u is an unknown function, and the minimizing element of (2.15) is denoted by  $\check{u}$ ,  $\check{I} = I(\check{u})$ . In order to find the corresponding dual problem, we introduce a functional F(u, v) with u and v being its variables, such that the functional I(u) is expressed as

$$I(u) = \max_{v} F(u, v). \tag{2.16}$$

Inserting (2.16) into (2.15), the initial minimization problem becomes a mini-max problem of functional F(u, v), that is

$$\check{I} = \min_{u} \max_{v} F(u, v).$$

Provide that the order of maximization and minimization can be changed, the problem becomes

$$\check{I} = \max_{v} \min_{u} F(u, v).$$

Note that in mini-mini problem, the change of orders always holds that

$$\min_{u} \min_{v} F(u, v) = \min_{v} \min_{u} F(u, v),$$

but converting the mini-maxi to the maxi-mini problem does not hold always true. Therefore, in constructing the dual variational problems, one must choose the functional F(u, v) so that

$$\min_{u} \max_{v} F(u, v) = \max_{v} \min_{u} F(u, v). \tag{2.17}$$

If the minimization of F(u, v) with respect to u can be easily and explicitly found, denoting it by J(v)

$$J(v) = \min_{u} F(v, u),$$

then the maximization problem equivalent to minimization problem is constructed, as shown in (2.18)

$$\check{I} = \max_{v} J(v). \tag{2.18}$$

To check the validity of (2.17), one needs to compare  $J(\check{v})$  to  $I(\check{u})$ , where  $\check{v}$  is the element leading  $F(\check{u},v)$  to take its maximum. If  $J(\check{v})=I(\check{u})$ , then (2.17) holds. We call (2.18) is the dual variational problem of (2.15). The dual variational principle is meaningful because it is sometimes easier to find the stationary point of the functional with respect to its dual variable. In constructing the functional F(u,v), Legendre transformation, as well as Legendre-Fenchel transformation, is a useful tool.

**Legendre transformation**: As stated before, the Legendre transformation can be used in constructing the dual variational principle and finding the dual variables. Suppose that we have a twice continuously differentiable function f(x), then we can define the dual variables  $x_i^*$  to  $x_i$  as

$$x_i^* = \frac{\partial f(x)}{\partial x_i},$$

where  $x = \{x_1, x_2, ...\}$ , and  $x_i^* = x_i^*(x_i)$  is function of  $x_i$ . Provide that there is an inverse function (matrix) of  $x^*$ , we have

$$x_i = x_i(x_k^*).$$

Then Legendre transformation  $f^{\times}(x^*)$  of the function f(x) is defined in (2.19) as

$$f^{\times}(x^*) = x_k^* x_k - f(x(x^*)). \tag{2.19}$$

For some functions, such as the absolute functions, the Legendre transformation is meaningless. In this case, a generalization of the Legendre transformation can be applied,

$$f^*(x^*) = \max_{x} [x_i^* x_i - f(x(x^*))],$$

where  $f^*(x^*)$  is known as the Legendre-Fenchel transformation of function f(x), and it has a property that for any functions the corresponding Legendre-Fenchel transformation is convex. Note that the Legendre-Fenchel transformation is identical to the Legendre transformation if the function f(x) is a strictly convex function.

An application of Legendre transformation is the derivation of the Hamiltonian equation of the mechanical system from Lagrange equation, where the Lagrange equation is the difference between the kinetic and the potential energy, while the Hamiltonian equation is interpreted as the sum of these two energies. Besides, the Legendre transformation can be used in thermodynamic potentials. Let  $\mathcal{U}(V,S)$  be internal energy of an ideal gas and be a convex function, where V and S are volume and entropy of the system, respectively. We find that the negative of the Legendre transformation of  $\mathcal{U}(V,S)$ , denoted as  $-\mathcal{U}^{\times}$ , with respect to the entropy gives rise to the Helmholtz free energy  $\mathcal{F}(V,T)$ ,

$$\mathcal{F}(V,T) = -\mathcal{U}^{\times}(V,S^*) = \mathcal{U}(V,S(T)) - TS(T), \text{ where } S^* = \frac{\partial \mathcal{U}}{\partial S} = T,$$

note that the dual variable of S, denoted as  $S^*$ , is turned out to be the temperature T. In the same manner, the enthalpy can be obtained by Legendre transformation

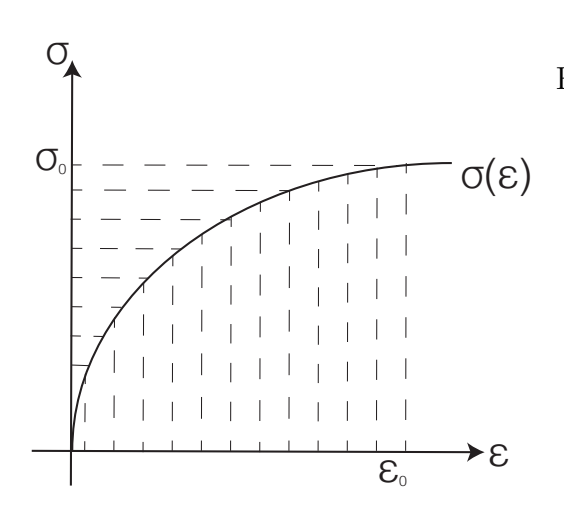


Figure 2.11.: Vertically shaded area: the strain energy  $\mathcal{F}(\varepsilon_0)$ , and the horizontally shaded area: the complementary energy  $\mathcal{F}^c(\sigma_0)$  in one dimensional elasticity theory..

of internal energy  $\mathcal{U}(V, S)$  with respect to the volume and the Gibbs free energy is obtained, likewise, by that with respect to volume and entropy.

In the elasticity theory, the Helmholtz free energy  $\mathcal{F}(\varepsilon,T)$  is a function of the strain  $\varepsilon$  and the temperature T, and by the Legendre transformation with respect to the strain, we obtain the complementary energy  $\mathcal{F}^c$  as

$$\mathcal{F}^c(\boldsymbol{\sigma},T) = \mathcal{F}^{\times}(\boldsymbol{\varepsilon}^*,T) = \int_{\mathcal{V}} \boldsymbol{\sigma} : \boldsymbol{\varepsilon} d\mathcal{V} - \mathcal{F}(\boldsymbol{\varepsilon},T), \quad \text{where} \quad \boldsymbol{\varepsilon}^* = \frac{\partial \mathcal{F}(\boldsymbol{\varepsilon},T)}{\partial \boldsymbol{\varepsilon}} = \boldsymbol{\sigma},$$

here  $\sigma$  is a symmetric tensor. Fig. 2.11 schematically indicates the strain energy and the complementary energy in one-dimensional elasticity. Let the temperature be constant, then the strain energy  $\mathcal{F}(\varepsilon)$  and the complementary energy  $\mathcal{F}^c(\sigma)$  are expressed as

$$\mathcal{F}(\varepsilon_0) = \int_0^{\varepsilon_0} \sigma(\varepsilon) \mathrm{d}\varepsilon, \quad \mathcal{F}^c(\sigma_0) = \int_0^{\sigma_0} \varepsilon(\sigma) \mathrm{d}\sigma = \sigma_0 \varepsilon_0 - \mathcal{F}(\varepsilon_0).$$

The strain energy is illustrated by the shaded area by vertical dashed lines, and the complementary energy is equal to the area shaded by horizontal lines.

**Clapeyron's Theorem**: If a functional I(u) consists of two parts, the quadratic and linear functionals, as the case in many linear problems of continuum mechanics, the Clapeyron's theorem can be applied. We denote the quadratic functional by E(u) and the linear functional by I(u),

$$I(u) = E(u) - l(u),$$

$$E(u) = \int_{\mathcal{V}} \alpha_1 u^2 \, d\mathcal{V}, \quad l(u) = \int_{\mathcal{V}} \alpha_2 u \, d\mathcal{V},$$
(2.20)

where  $\alpha_1$  and  $\alpha_2$  are coefficients that are given. The Clapeyron's theorem states that the minimizer element  $\check{u}$  of I(u) fulfills the relation

$$2E(\check{u}) = l(\check{u}). \tag{2.21}$$

Plugging (2.21) in  $(2.20)_1$ , one obtains two useful forms as the consequences of Clapeyron's theorem, which express the extremum of the functional in terms of the quadratic functional and the linear functional, respectively,

$$I(\check{u}) = -E(\check{u}) = -\frac{1}{2}l(\check{u}).$$

In the elasticity theory of static problem, the Clapeyron's theorem adequately represents that the half of the work done by the externally applied forces is stored in the body in the form of strain energy, while the rest half is dissipated.

In the subsequent chapter, we use the above introduced dual variational principle, the Legendre transformation, and Clapeyron's theorem to find the defect energy of screw dislocations.

#### 2.2.4. Thermodynamical principles

The first law of thermodynamics: Total energy  $\mathcal{E}$  is the sum of the kinetic energy  $\mathcal{K}$  and the internal energy  $\mathcal{U}$ . The first law of thermodynamics states that the rate of the total energy equals the sum of the rate of external work done and the rate of heat supply. It can be expressed as

$$\dot{\mathcal{E}} = \dot{\mathcal{K}} + \dot{\mathcal{U}} = \mathcal{P} + \mathcal{R},\tag{2.22}$$

where  $\mathcal{P}$  is the input power, and  $\mathcal{R}$  denotes the the rate of heat supply. The rate of kinetic and internal energy are given in the form

$$\dot{\mathcal{K}} = \frac{\mathrm{d}}{\mathrm{d}t} \int_{\mathcal{V}} \frac{1}{2} \rho_0 \mathbf{v}^2 d\mathcal{V} = \int_{\mathcal{V}} \rho_0 \dot{\mathbf{v}} \cdot \mathbf{v} d\mathcal{V},$$
$$\mathcal{U} = \int_{\mathcal{V}} U d\mathcal{V},$$

where a dot () represents the time derivative,  $\mathbf{v}$  the velocity vector,  $\rho_0$  the material's density, and U the internal energy per unit volume. The mechanical power consists of the rate of work done by body force  $\mathbf{f}_B$  and surface force  $\mathbf{f}$ , as shown

$$\mathcal{P} = \int_{\mathcal{V}} \mathbf{f}_B \cdot \mathbf{v} d\mathcal{V} + \int_{\partial \mathcal{V}} \mathbf{f} \cdot \mathbf{v} da.$$
 (2.23)

Applying Cauchy's relation (2.12) and the divergence theorem, the second term of right-hand side in (2.23) can be transformed as

$$\int_{\partial \mathcal{V}} \mathbf{f} \cdot \mathbf{v} da = \int_{\partial \mathcal{V}} (\boldsymbol{\sigma} \cdot \mathbf{n}) \cdot \mathbf{v} da = \int_{\mathcal{V}} (\boldsymbol{\sigma} \cdot \mathbf{v}) \cdot \nabla d\mathcal{V} = \int_{\mathcal{V}} (\operatorname{div} \boldsymbol{\sigma} \cdot \mathbf{v} + \boldsymbol{\sigma} : \nabla \mathbf{v}) d\mathcal{V}. \quad (2.24)$$

Plugging (2.24) in (2.23) and by the principle of conservation of linear momentum ( $\operatorname{div} \boldsymbol{\sigma} + \mathbf{f}_B = \rho_0 \dot{\mathbf{v}}$ ), the mechanical power can be rewritten as

$$\mathcal{P} = \int_{\mathcal{V}} (\rho_0 \dot{\mathbf{v}} \cdot \mathbf{v} + \boldsymbol{\sigma} : \dot{\boldsymbol{\varepsilon}}) \, d\mathcal{V}.$$

The rate of heat supply can also be divided into two parts, where one is the heat flux  $\mathbf{q}$  through the surface, and the other one is the internal heat source h

$$\mathcal{R} = \int_{\mathcal{V}} h d\mathcal{V} - \int_{\partial \mathcal{V}} \mathbf{q} \cdot \mathbf{n} da = \int_{\mathcal{V}} (h - \nabla \cdot \mathbf{q}) d\mathcal{V},$$

with **n** being the normal vector on the surface. Substituting expressions for  $\mathcal{K}$ ,  $\mathcal{U}$ ,  $\mathcal{P}$ , and  $\mathcal{R}$  into (2.22), we obtain the local form of the thermodynamics first law

$$\dot{U} = \boldsymbol{\sigma} : \dot{\boldsymbol{\varepsilon}} + h - \text{div}\mathbf{q}. \tag{2.25}$$

The second law of thermodynamics: The second law of thermodynamics states that the rate of entropy  $\dot{S}$  possessed by a continuum body must be greater than the rate of external entropy  $\dot{S}^{\text{ext}}$  (entropy input rate),

$$\dot{S} \geqslant \dot{S}^{\text{ext}} = \frac{\mathcal{R}}{T}$$
, with  $\dot{S} = \frac{\mathrm{d}}{\mathrm{d}t} \int_{\mathcal{V}} s \, \mathrm{d}\mathcal{V}$ , and  $\dot{S}^{\text{ext}} = \int_{\mathcal{V}} \frac{h}{T} \mathrm{d}\mathcal{V} - \int_{\partial \mathcal{V}} \frac{\mathbf{q} \cdot \mathbf{n}}{T} \mathrm{d}a$ . (2.26)

It has an alternative expression that the rate of total entropy production  $\dot{\Sigma}$  must be greater than zero, where  $\Sigma = S - S^{\rm ext}$ . Substituting  $\dot{S}$  and  $\dot{S}^{\rm ext}$  into the inequality (2.26) and applying the divergence theorem, we arrive at the second law of thermodynamics in local form,

$$\dot{s} \geqslant \frac{h}{T} - \operatorname{div}\frac{\mathbf{q}}{T} \quad \text{or} \quad \dot{s}^{p} = \dot{s} - \dot{s}^{\text{ext}} = \dot{s} - \frac{h}{T} + \operatorname{div}\frac{\mathbf{q}}{T} \geqslant 0,$$
 (2.27)

where  $\dot{s}$  is the specific entropy rate, and  $\dot{s}^{\rm ext}$  denotes the specific external entropy input rate,  $\dot{s}^p$  the entropy production rate. Eq. (2.27) is known as Clausius-Duhem inequality. Eliminating the internal heat source h from (2.27) by means of (2.25), one obtains a new form of the second law of thermodynamics

$$T\dot{s}^p = \boldsymbol{\sigma} : \dot{\boldsymbol{\varepsilon}} - \dot{U} + T\dot{s} - \frac{1}{T}\mathbf{q} \cdot \nabla T \geqslant 0.$$
 (2.28)

Introducing the specific Helmholtz free energy  $\psi$  by  $\psi = U - Ts$  and substituting U into (2.28), one obtains the relation

$$T\dot{s}^p = \boldsymbol{\sigma} : \dot{\boldsymbol{\varepsilon}} - \dot{\psi} - s\dot{T} - \frac{1}{T}\mathbf{q} \cdot \nabla T \geqslant 0.$$
 (2.29)

Since the heat spontaneously flows from the warmer to the colder region of a body, the last term in the left-hand side of (2.28) must be non-negative and it leads the rest part to fulfill the relation as shown

$$-\frac{1}{T}\mathbf{q}\cdot\nabla T\geqslant 0,\quad \boldsymbol{\sigma}:\dot{\boldsymbol{\varepsilon}}-\dot{\psi}-s\dot{T}\geqslant 0,$$

where they are referred to as heat conduction inequality and Clausius-Planck inequality, respectively. The quantity  $T\dot{s}^p$  in (2.28) has been defined as dissipation, and it is utilized in the principle of maximum dissipation to derive evolution equations for internal variables (Hackl & Fischer, 2008; Hackl *et al.*, 2011). While in this study, we derive the equations of motion using the dissipation potential, which is often supposed to exist as a function D. With a given dissipation potential, the following variational equation can describe the dissipative process,

$$\delta I + \int_{\mathcal{V}} \frac{\partial D}{\partial \dot{\mathbf{z}}_i} \delta \mathbf{z}_i d\mathcal{V} = 0, \quad i = 1, 2, ...,$$
(2.30)

for which in our study, the functional I is given by

$$I = \int_{\mathcal{V}} \psi(\mathbf{u}, \mathbf{z}_i) \, d\mathcal{V} - l(\mathbf{u}), \quad \text{where} \quad l(\mathbf{u}) = \int_{\mathcal{V}} \mathbf{f}_B \cdot \mathbf{u} \, d\mathcal{V} + \int_{\partial \mathcal{V}_t} \mathbf{f} \cdot \mathbf{u} \, da,$$

with  $\psi$  being the specific Helmholtz free energy and the linear term  $l(\mathbf{u})$  being the external work done to the system.  $\mathbf{u}$  is the displacement field, and  $\mathbf{z}_i$  are the state variables. Eq. (2.30) follows the spirit of d'Alembert principle that focuses on the

equilibrium of forces, where  $\partial \psi/\partial \mathbf{z}_i$  emerged from the variation of the functional I give rise to the driving forces and the differential of D with respect to the rate of state variables,  $\partial D/\partial \dot{\mathbf{z}}_i$ , refer to the dissipative force, such that

$$\frac{\partial \psi}{\partial \mathbf{z}_i} + \frac{\partial D}{\partial \dot{\mathbf{z}}_i} = 0. \tag{2.31}$$

A similar form has appeared in the minimum principle for the dissipation potential (Hackl & Fischer, 2008), where the evolution equations are found by minimizing a potential  $\mathcal{L}^* = \dot{\psi} + D$  with respect to the state variables.

### 2.3. Thermodynamic Dislocation Theory

### 2.3.1. Introduction to the theory

In crystalline solids, the plastic deformation is mainly carried by dislocations which are line defect. By interacting and entangling each other, dislocations form complex structures. Their networks give rise to rich macroscopic performances so that in continuum plasticity modeling it is common to involve the energy of dislocations into the stored energy as a function of dislocation density, mostly in the form of scalar, averaged tensor or its combination. On the other hand, we also know that the entropy of dislocation is extremely small in comparison with the total entropy of the crystal so that in abundant literature the entropy of dislocations has been ignored from the thermodynamic principle since last century. However, Berdichevsky (2008); Bouchbinder & Langer (2009b) asserted that the evolution of dislocations, as well as the microstructure, must be associated with the entropy of its own, which is a big deviation from the conventional approaches in solid mechanics.

Langer et al. (2010) proposed that, even though dislocation has small entropy, it is an essential ingredient in crystal plasticity of dislocation-mediated theory. He introduced two thermodynamically well-defined temperatures, namely ordinary temperature T and effective temperature  $\chi$ , which characterize two weakly interacted subsystems, kinetic-vibrational subsystem and configurational subsystem, respectively. The ordinary temperature depicts the ordinary thermal fluctuations, while the effective temperature describes the atomically slow configurational degrees of freedom of deforming solids. Regarding the thermodynamic system as two separated subsystems is based on the fact that the thermal vibration is on atomic timescale, while the timescale characterizing structural relaxation and defect motion is at a much lower level. Such timescale separation leads to the decomposition of subsystems. The effective temperature, defined as the derivative of configurational energy with respect to the configurational entropy, measures the disordered state of the subsystem, and its evolution represents how the mechanical work raises the energy of the subsystem based on the first law of thermodynamics.

Note that the basic idea of two temperature thermodynamics framework might appeared first in the statistical physics community (Cugliandolo, 1997; Berthier, 2000) and many applications are investigated in amorphous plasticity, e.g., Shear Transformation Zone model (Bouchbinder & Langer, 2009a,b,c), soft glassy rheology(Sollich & Cates, 2012), and cavitation near crack tips(Rycroft & Bouchbinder, 2012). In crystal plasticity, Le et al. (2017) simulated 12 stress-strain curves in plane strain compression tests for aluminum and steel over a wide range of temperatures and strain rates with only a set of physics-based parameters and obtained satisfactory agreements with the experiments. Langer (2018) showed the TDT and the Livermore molecular dynamics simulations of dislocation-mediated solid plasticity are in substantial agreement in describing the strain-rate-dependent steady plastic flow and the transient stress peaks associated with initially small dislocation densities. Other applications include material hardening(Langer et al., 2010), softening(Langer, 2016; Le & Piao, 2019b), effects of grain size(Langer, 2015), yielding transitions(Langer, 2017b), adiabatic shear banding(Le et al., 2018), non-uniform plastic deformations(Le, 2018), size effect(Le &

Piao, 2019a), Bauschinger effect(Le & Tran, 2018).

### 2.3.2. The variational approach in thermodynamic dislocation theory

The aim of this section is to discuss the underlying variational principle in thermodynamic dislocation theory(TDT) and to derive the governing equations. TDT starts with identifying the energy functional, which is given by

$$I = \int_{\mathcal{V}} \psi(\boldsymbol{\varepsilon}^e, \rho^g, \rho^r, T, \chi) d\mathcal{V} - \int_{\partial \mathcal{V}_t} \mathbf{f} \cdot \mathbf{u} da, \qquad (2.32)$$

with  $d\mathcal{V}$  denoting the volume element, da the area element, and  $\psi$  the free energy density per unit volume.  $\mathcal{V}$  is the domain in space occupied by the material body, and its boundary  $\partial \mathcal{V}$  consists of two non-intersecting surfaces,  $\partial \mathcal{V}_u$  and  $\partial \mathcal{V}_t$ . The displacement vector  $\mathbf{u}(\mathbf{x})$  is a given function of coordinates on  $\partial \mathcal{V}_u$ ,

$$\mathbf{u}(\mathbf{x}) = \bar{\mathbf{u}}(\mathbf{x}), \quad \text{for } \mathbf{x} \in \partial \mathcal{V}_u,$$

while on the boundary  $\partial \mathcal{V}_t$ , the traction force  $\mathbf{f}$  is specified. Provide that there is no body force acting on the crystal. The second term in the right-hand side of (2.32) represents the potential of external forces.

The state variables of free energy density in thermodynamic dislocation theory comprise the elastic strain  $\varepsilon^e$ , excess dislocation density  $\rho^g$ , redundant dislocation density  $\rho^r$ , kinetic-vibrational temperature T, and the effective temperature  $\chi$ . All of them characterize the current state of the crystal material. The excess dislocation density  $\rho^r$  possesses an internal length scale that is the magnitude of Burgers vector. The failure of classical continuum mechanics in small-scale devices is due to the lack of the internal length scale into the modeling. Both excess and redundant dislocation density  $\rho^r$  depend only on the characteristics of dislocations so that they are proper choices as state variables, while the plastic distortion is excluded from the choice because it depends on the whole history of creating dislocations (Le et al., 2016). Besides, Langer (2017c) has also argued about the qualification of plastic deformation as the state variable due to the reason that the irreversible processes forget their histories of past deformation. We set the kinetic-vibrational temperature T constant so that it can be dropped from the lists of arguments of the free energy density. Following Le (2018), free energy density has the following form,

$$\psi = \psi_e + \psi_r + \psi_m + \psi_\gamma,\tag{2.33}$$

The first term of (2.33) is the elastic strain energy, given by

$$\psi_e = \frac{1}{2} \boldsymbol{\varepsilon}^e : \mathbb{C} : \boldsymbol{\varepsilon}^e,$$

where  $\mathbb{C}$  denotes the fourth rank elastic stiffness tensor. For an isotropic material, the stress is given as

$$\sigma = \mathbb{C} : \varepsilon^e = \lambda \mathbf{tr}(\varepsilon^e)\mathbf{I} + 2\mu \varepsilon^e,$$

with  $\lambda$  and  $\mu$  being Lamé parameters. The second term  $\psi_r$  is the self-energy of redundant dislocations, and the isotropic hardening is dominantly accounted for by  $\psi_r$ .

The third term  $\psi_m$  is the defect energy density caused by excess dislocations, which models kinematic hardening as well as some phenomena of microstructure, such as the size effect. The last term (2.33) is the energy due to the effective temperature  $\chi$  introduced by Langer *et al.* (2010).

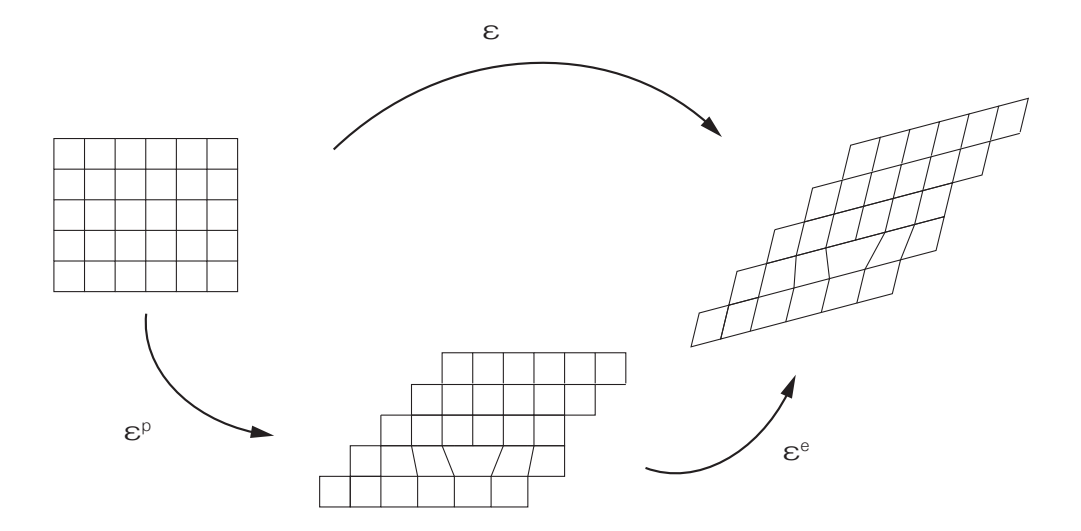


Figure 2.12.: Additive decomposition of the total strain

### **Kinematics:**

Before going into deep, let us first describe the kinematics. In small deformation, we can ignore the differences between the Lagrangian and Eulerian coordinates and further assume that the displacement gradient (total distortions) is additively decomposed into elastic and plastic distortions,  $\beta^e$  and  $\beta$ , respectively

$$\boldsymbol{\beta}^t = \nabla \mathbf{u} = \boldsymbol{\beta}^e + \boldsymbol{\beta},\tag{2.34}$$

where  $\mathbf{u}(\mathbf{x})$  is displacement field, and  $\mathbf{x}$  is a position vector of a material point in the body  $\mathcal{V}$ . The plastic distortion of crystal with one slip system activated can be described as follows

$$\boldsymbol{\beta}(\mathbf{x}) = \beta(\mathbf{x})\mathbf{s} \otimes \mathbf{m},$$

with **s** denoting unit vector of slip direction, and **m** is the unit vector normal to the slip plane ( $|\mathbf{s}| = 1$ ,  $|\mathbf{m}| = 1$ ,  $\mathbf{s} \cdot \mathbf{m} = 0$ ). The plastic slip function is denoted by  $\beta(\mathbf{x})$  and assumed to be continuously differentiable. When n slip systems are activated, the plastic distortion is given by

$$\beta(\mathbf{x}) = \sum_{\alpha=1}^{n} \beta^{\alpha}(\mathbf{x}) \mathbf{s}^{\alpha} \otimes \mathbf{m}^{\alpha},$$

where  $\mathbf{s}^{\alpha}$  and  $\mathbf{m}^{\alpha}$  indicate, analogously, the unit vectors of slip direction and vectors normal to the slip planes of the corresponding  $\alpha$ -th slip system. By definition, since  $\mathbf{s}^{\alpha}$  and  $\mathbf{m}^{\alpha}$  are mutually orthogonal, the diagonal elements of plastic distortion take the value of zero so that  $\mathbf{tr}(\boldsymbol{\beta}) = 0$ , which implies volume-preserving. The total strain  $\boldsymbol{\varepsilon}$  and the plastic strain  $\boldsymbol{\varepsilon}^{p}$  are the symmetric part of displacement gradient and plastic distortion, respectively, such that

$$\boldsymbol{\varepsilon} = \frac{1}{2}(\nabla \mathbf{u} + \mathbf{u}\nabla), \quad \boldsymbol{\varepsilon}^p = \frac{1}{2}(\boldsymbol{\beta} + \boldsymbol{\beta}^T).$$

Accordingly, the elastic strain is equal to the subtraction of plastic term from the total strain,

$$\boldsymbol{\varepsilon}^e = \boldsymbol{\varepsilon} - \boldsymbol{\varepsilon}^p. \tag{2.35}$$

Fig.2.12 illustrates the relationship between the total and elastic, plastic deformation. As shown, plastic deformation can be regarded as irreversible shifts of the crystal at the boundary along with specific slip system. It is accomplished by the glide of excess dislocations through and leaving the material volume element. These dislocations do not distort nor rotate the lattice, while the lattice distortion is associated with those excess dislocations created by plastic distortion  $\beta$  inside the body, which can change their positions in the crystal without deforming the material. On the other hand, the elastic deformation leads to the subsequent rotation and stretching of the coherent structure having frozen dislocations. Note that an important feature of (2.35) is that the total strain is compatible, while the elastic and plastic strain tensors are incompatible. Physically the incompatibility of plastic strain tensor ensures the necessity of excess dislocations, and the Nye's tensor measures the excess dislocation density. However, this tensor does not account for the accumulation of redundant dislocations because the resultant Burgers vector vanishes in the representative volume element. Hence, they do not change the lattice shape in continuum limits.

The displacement gradient can be additively decomposed into a symmetric tensor and an antisymmetric tensor,

$$\mathbf{u}\nabla = \frac{1}{2}(\nabla \mathbf{u} + \mathbf{u}\nabla) + \frac{1}{2}(\nabla \mathbf{u} - \mathbf{u}\nabla) = \boldsymbol{\varepsilon} + \boldsymbol{\Omega},$$

obviously the symmetric part is the total strain tensor, and the antisymmetric part is the total rotation tensor,

$$\Omega = \frac{1}{2}(\nabla \mathbf{u} - \mathbf{u}\nabla), \text{ where } \Omega = -\Omega^T.$$

Analogically, the plastic rotation tensor is the antisymmetric part of the plastic distortion,

$$\mathbf{\Omega}^p = \frac{1}{2}(\boldsymbol{\beta} - \boldsymbol{\beta}^T).$$

Accordingly, the elastic rotation tensor is

$$\Omega^e = \Omega - \Omega^p$$
.

Since the crystal misorientation can be mapped by Laue microdiffraction (Ziemann et al., 2015), and the lattice rotation can be measured by the electron backscatter technique (Kysar et al., 2010), the rotation tensor may be used in the comparison of numerical simulation with the experiment.

Although not the scope of this work, we briefly mention the deformation gradient normally used in finite deformation. Suppose that an intermediate imaginary configuration, denoted by  $d\mathbf{p}$ , is obtained from the reference configuration by plastically deforming infinitesimal line segment  $d\mathbf{X}$  with the plastic deformation gradient  $\mathbf{F}^p$  as their transformation, and further,  $d\mathbf{p}$  is mapped to the current configuration vector  $d\mathbf{x}$ 

by elastic deformation with  $\mathbf{F}^e$  being the elastic deformation gradient. It is expressed mathematically

$$d\mathbf{p} = \mathbf{F}^p d\mathbf{X}, \quad \text{and} \quad d\mathbf{x} = \mathbf{F}^e d\mathbf{p}.$$
 (2.36)

Then, we obtain the multiplicative decomposition of the deformation gradient

$$\mathbf{F} = \frac{\partial \mathbf{x}}{\partial \mathbf{X}} = \frac{\partial \mathbf{x}}{\partial \mathbf{p}} \cdot \frac{\partial \mathbf{p}}{\partial \mathbf{X}} = \mathbf{F}^e \cdot \mathbf{F}^p. \tag{2.37}$$

With the aid of the relation,  $\mathbf{F} = \partial \mathbf{x}/\partial \mathbf{X} = \mathbf{I} + \partial \mathbf{u}/\partial \mathbf{X} = \mathbf{I} + \boldsymbol{\beta}^t$ , we can express the deformation gradient in terms of elastic and plastic distortions as follow

$$\mathbf{F} = \mathbf{F}^e \cdot \mathbf{F}^p = (\mathbf{I} + \boldsymbol{\beta}^e) \cdot (\mathbf{I} + \boldsymbol{\beta}) = \mathbf{I} + \boldsymbol{\beta}^e + \boldsymbol{\beta} + \boldsymbol{\beta}^e \cdot \boldsymbol{\beta}. \tag{2.38}$$

When the deformation is small, the term  $\beta^e \cdot \beta$  is negligible, and thus the displacement gradient,  $\nabla \mathbf{u} = \mathbf{F} - \mathbf{I}$ , for small strains in geometrical linear theory comes to (2.34).

### Nye's dislocation tensor:

Since the resultant Burgers vector  $\mathbf{B}$  resulting from crystallographic slip complete the Burgers circuit c, we have

$$\mathbf{B} = \oint_c \mathbf{d}\mathbf{u}^p = \oint_c \boldsymbol{\beta} \mathbf{d}x,$$

where  $\boldsymbol{\beta} = \nabla \mathbf{u}^p$ , and  $\mathbf{u}^p$  is the relative displacement caused by slip. Using Stokes' theorem,

$$B_i = \int_S \alpha_{ij} n_j \mathrm{d}S$$

where S denotes the surface bounded by Burgers circuit with  $\mathbf{n}$  being the plane normal vector,  $\boldsymbol{\alpha}$  denotes Nye's dislocation tensor that is the curl of plastic distortion,

$$\alpha_{ij} = \operatorname{curl}(\boldsymbol{\beta})_{ij}.$$

This tensor is introduced by Nye (1953), Bilby (1955) and Kröner (1955), and further studied by Ashby (1970). Fleck *et al.* (1994) expressed this tensor in the form of index notation as

$$\alpha_{ij} = \epsilon_{jkl} \beta_{il,k}.$$

Concerning the curl computation of second-order tensor, there are different approaches, as discussed by Das *et al.* (2018). The pre-curl of second-order tensor  $\mathbf{V}$ , denoted by  $(\nabla \times \mathbf{V})_{ij}$ , is used in Ma *et al.* (2006); Sun *et al.* (1998), while Le *et al.* (2016); Le (2016a) used the post-curl,  $(\mathbf{V} \times \nabla)_{ij}$  to compute the Nye's dislocation tensor. Note that pre-curl and post-curl of the same second-order tensor may lead to different outcomes; however, with correct tensor chose and consistent application, both curl definitions lead to the same result. Since two curl operators fulfill the following relation

$$post-curl(\mathbf{V}) = -(pre-curl(\mathbf{V})^T)^T,$$

the Nye's tensor  $\alpha$  in different computations are,

post-curl : 
$$\alpha = -\beta \times \nabla$$
  
pre-curl :  $\alpha = (\nabla \times \beta^T)^T$ 

The continuity condition demands the line integral of the displacement to vanish around any area in the material,

$$\oint_{\mathcal{C}} \mathbf{d}\mathbf{u} = \oint_{\mathcal{C}} \boldsymbol{\beta}^t \mathbf{d}x = 0.$$

It implies the relationship between plastic and elastic distortion,

$$\operatorname{curl}(\boldsymbol{\beta})_{ij} = -\operatorname{curl}(\boldsymbol{\beta}^e)_{ij}.$$

So the Nye's dislocation tensor using the elastic distortion as a measure of incompatibility is

$$\alpha_{ij} = -\epsilon_{jkl}\beta_{il,k}^e$$
.

Since Nye's dislocation tensor is not necessarily symmetrical, it has nine independent components. However, those elements are not enough to determine the densities of excess dislocation unambiguously because typical crystals have more than nine slip systems. In such a case, the minimization is needed to estimate the excess dislocation density(Arsenlis, 1999; Kysar *et al.*, 2010; Das *et al.*, 2018). On the other hand, in the case that only limited slip systems are activated, the dislocation density can be well estimated (Le, 2016a) with given the formula for screw dislocation density  $\rho_{\parallel}^{\alpha}$  and edge dislocation density  $\rho_{\parallel}^{\alpha}$  for particular slip system

$$\rho_{\parallel}^{\alpha} = \frac{1}{h} |\mathbf{s}^{\alpha} \cdot \mathbf{t}^{\alpha}| |\partial_{\nu}\beta^{\alpha}|, \quad \rho_{\perp}^{\alpha} = \frac{1}{h} |\mathbf{s}^{\alpha} \cdot \mathbf{v}^{\alpha}| |\partial_{\nu}\beta^{\alpha}|, \tag{2.39}$$

with  $\mathbf{t}^{\alpha}$  being the unit normal vector to dS,  $\mathbf{v}^{\alpha} = \mathbf{m}^{\alpha} \times \mathbf{t}^{\alpha}$  the vector lying on the slip plane and perpendicular to  $\mathbf{t}^{\alpha}$  and  $\partial_{v}\beta^{\alpha} = \nabla\beta^{\alpha} \times \mathbf{v}^{\alpha}$ .

### Variational formulation:

Back to the free energy density, Le (2018) has proposed for each term of (2.33) as follow,

$$\psi_e = \frac{1}{2}\lambda(\varepsilon_{kk}^e)^2 + \mu\varepsilon_{ij}^e\varepsilon_{ij}^e, \qquad \psi_r = \gamma_D\rho^r,$$
  
$$\psi_\chi = -\chi(-\rho\ln(a^2\rho) + \rho)/L,$$

where the energy  $\psi_{\chi} \mathcal{V}$  is the product of effective temperature  $\chi$  and the configurational entropy of dislocations,  $S_C = \mathcal{A}(\rho \ln(a^2 \rho) + \rho)$ . We assume that the total dislocation density is additively decomposed into excess dislocation density  $\rho^g$  and redundant dislocation density  $\rho^r$ ,

$$\rho = \rho^g + \rho^r. \tag{2.40}$$

 $\gamma_D = e_D/L$  is the dislocation energy per unit length, where  $e_D$  is the energy per dislocation. Parameter a is a length scale of the order of atomic spacings that indicates the minimum spacing between noninteracting dislocations. As a result,

$$\psi = \frac{1}{2}\lambda(\varepsilon_{kk}^e)^2 + \mu\varepsilon_{ij}^e\varepsilon_{ij}^e + \gamma_D\rho^r + \psi_m - \chi(-\rho\ln(a^2\rho) + \rho)/L,$$

where each term is in a unit of energy per volume. Provided that the area of the cross-section is  $\mathcal{A}$  and its boundary satisfies  $\partial \mathcal{A} = \partial_s \cup \partial_k$  and  $\partial_s \cap \partial_k = 0$ , then with the free energy density, one can write down the energy functional. The surface force  $\mathbf{f}$  is applied on the boundary  $\partial_s$ , and we assume the crystal is free from the body force, the displacement  $\mathbf{u}(\mathbf{x})$  and plastic slip  $\beta(\mathbf{x})$  are subjected to the boundary condition on  $\partial_k$ 

$$\mathbf{u}(\mathbf{x}) = \bar{\mathbf{u}}(\mathbf{x}) \quad \text{and} \quad \beta(\mathbf{x}) = 0.$$
 (2.41)

The energy function of the crystal bar per unit depth is defined as

$$I[\mathbf{u}(\mathbf{x}), \beta(\mathbf{x}), \rho^r(\mathbf{x}), \chi(\mathbf{x})] = \int_A \psi(\boldsymbol{\varepsilon}^e, \rho^r, \rho^g, \chi) \, da - \int_{\partial_{\boldsymbol{\varepsilon}}} \mathbf{f} \cdot \mathbf{u} \, ds.$$

Note that  $\boldsymbol{\varepsilon}^e$  and  $\rho^g$  are dependent variables with respect to  $\mathbf{u}$  and  $\beta$ , while  $\rho^r$  and  $\chi$  are independent variables. The applied work to the crystal may lead to nucleation, multiplication, and motion of dislocations, which give rise to the plastic deformations in crystal. In this process, dislocations always suffer the resistance causing the energy dissipation. In addition to the term for rate-independent plasticity, thermodynamic dislocation theory proposes that the increase of dislocation density and the increase of configurational temperature contribute to energy dissipation. The dissipation potential proposed has the form

$$D(\dot{\beta}, \dot{\rho}, \dot{\chi}) = \tau_Y |\dot{\beta}| + \frac{1}{2} d_{\rho} \dot{\rho}^2 + \frac{1}{2} d_{\chi} \dot{\chi}^2, \tag{2.42}$$

where  $\tau_Y$  is the flow stress during plastic yielding,  $d_{\rho}$ , and  $d_{\chi}$  are certain functions that to be discussed later. In such an irreversible process that dissipation potential is involved, the governing equations can be derived from the following variational principle: the true displacement field  $\check{\mathbf{u}}$ , the true plastic slips  $\check{\beta}(\mathbf{x})$ , the true density of redundant dislocations  $\check{\rho}(\mathbf{x})$ , and the true configurational temperature  $\check{\chi}(\mathbf{x})$  obey the variational equation

$$\delta I + \int_{A} \left( \frac{\partial D}{\partial \dot{\beta}} \delta \beta + \frac{\partial D}{\partial \dot{\rho}} \delta \rho + \frac{\partial D}{\partial \dot{\chi}} \delta \chi \right) da = 0, \tag{2.43}$$

for all variations of admissible fields  $\mathbf{u}(\mathbf{x})$ ,  $\beta(\mathbf{x})$ ,  $\rho(\mathbf{x})$  and  $\chi(\mathbf{x})$  satisfying the constrains (2.41). Derivation of (2.43) allows one to find out the necessary conditions which must be satisfied at the final state of deformation in equilibrium. Expanding the first term of (2.43), we have

$$\delta I = \int_{\mathcal{A}} \left[ \sigma_{ij} (\delta \varepsilon_{ij} - \delta \varepsilon_{ij}^{p}) + \gamma_{D} \delta \rho^{r} + \frac{\partial \psi_{m}}{\partial \rho^{g}} \delta \rho^{g} + \frac{\chi \ln(a^{2} \rho)}{L} (\delta \rho^{r} + \delta \rho^{g}) + \frac{\rho \ln(a^{2} \rho) - \rho}{L} \delta \chi \right] da - \int_{\partial_{s}} f_{i} \delta u_{i} ds,$$

where

$$oldsymbol{\sigma} = rac{\partial \psi}{\partial oldsymbol{arepsilon}^e}, \qquad oldsymbol{\sigma} = oldsymbol{\sigma}^T.$$

While plugging (2.42) into the variational equation, we have the second term of (2.43)

$$\int_{\mathcal{A}} \left( \frac{\partial D}{\partial \dot{\beta}} \delta \beta + \frac{\partial D}{\partial \dot{\rho}} \delta \rho + \frac{\partial D}{\partial \dot{\chi}} \delta \chi \right) da = \int_{\mathcal{A}} \left[ \tau_Y \delta \beta + d_\rho \dot{\rho} (\delta \rho^r + \delta \rho^g) + d_\chi \dot{\chi} \delta \chi \right] da.$$

Since  $\rho^r$  and  $\chi$  are independent variables, we can directly obtain two governing equations in the material body. Variation with respect to  $\rho^r$  and  $\chi$  yields that

$$\gamma_D + \chi \ln(a^2 \rho) / L + d_\rho \dot{\rho} = 0,$$
  
 $(\rho \ln(a^2 \rho) - \rho) / L + d_\chi \dot{\chi} = 0.$ 
(2.44)

Excluding the variation term with respect to  $\rho^r$  and  $\chi$  from (2.43) and using (2.44), we have the remaining part

$$\int_{\mathcal{A}} \left[ \sigma_{ij} (\delta \varepsilon_{ij} - \delta \varepsilon_{ij}^{p}) + \left( \frac{\partial \psi_{m}}{\partial \rho^{g}} - \gamma_{D} \right) \delta \rho^{g} + \tau_{Y} \delta \beta \right] da - \int_{\partial_{s}} f_{i} \delta u_{i} ds.$$

With the aid of the kinematic relations, formula for excess dislocation density and integration by parts, we obtain

$$\int_{\mathcal{A}} \left[ -\sigma_{ij,j} \delta u_{i} - s_{i} \sigma_{ij} m_{j} \delta \beta - \frac{\partial^{2} \psi_{m}}{\partial (\rho^{g})^{2}} \frac{\partial \rho^{g}}{\partial \bar{x}} \delta \tilde{\beta} + \tau_{Y} \delta \beta \right] da 
+ \int_{\partial_{z}} \left[ (\sigma_{ij} n_{j} - f_{i}) \delta u_{i} + \left( \frac{\partial \psi_{m}}{\partial \rho^{g}} - \gamma_{D} \right) \delta \tilde{\beta} \right] ds, \quad (2.45)$$

where the tilde accent  $\tilde{\ }$  denotes the rescaled variable towards the slip direction, divided by the magnitude of Burgers vector. Summing up the terms with respect to the variations of deformation  $\mathbf{u}(\mathbf{x})$  and plastic slip  $\beta(\mathbf{x})$  in the material body we have,

$$\sigma_{ij,j} = 0, \tag{2.46}$$

$$\tau - \tau_B - \tau_Y = 0, \tag{2.47}$$

where  $\tau = s_i \sigma_{ij} m_i$  is the resolved shear stress acting on the slip system, and

$$\tau_B = -\frac{\partial^2 \psi_m}{\partial (\rho^g)^2} \beta_{,\tilde{x}\tilde{x}} \tag{2.48}$$

is the back stress. As we can see from this formula, the back stress emerges from the defect energy which may describe the sum of self and interaction energy of excess dislocations. The flow stress  $\tau_Y$  is perceived to be attributed to total dislocation density as proposed by Langer *et al.* (2010). Physically, (2.46) can be interpreted as the balance of linear momentum for static problems in the absence of body force, and (2.47) as the balance of microforces acting on dislocations. From the second term of (2.45), we obtain information about boundary conditions acting on  $\partial_s$ 

$$\sigma_{ij}n_j = f_i \quad \text{and} \quad \frac{\partial \psi_m}{\partial \rho^g} = \gamma_D,$$
 (2.49)

and as we mentioned before on the boundary  $\partial_k$ , the deformation **u** subjects to Dirichlet boundary condition, and plastic slip to homogeneous Dirichlet boundary condition. System of governing equations from the variational principle becomes

$$\tau - \tau_B - \tau_Y = 0, 
\gamma_D + \chi \ln(a^2 \rho) / L + d_\rho \dot{\rho} = 0, 
(\rho \ln(a^2 \rho) - \rho) / L + d_\chi \dot{\chi} = 0.$$
(2.50)

In the variational approach of thermodynamic dislocation theory, there is no direct principle to construct the exact expression of dissipation function conjugate to each state variable. However, one can notice that if we choose

$$d_{\chi} = \frac{\rho - \rho \ln(a^{2}\rho)}{k_{\chi} \frac{\tau_{Y} q(\tau_{Y}, \rho)}{\mu t_{0}} [1 - \frac{\chi}{\chi_{0}}] L},$$

$$d_{\rho} = \frac{-e_{D} - \chi \ln(a^{2}\rho)}{k_{\rho} \frac{\tau_{Y}}{\gamma_{D}} \frac{q(\tau_{Y}, \rho)}{t_{0}} [1 - \frac{\rho}{\rho^{ss}(\chi)}] L}.$$

$$(2.51)$$

Eqs.  $(2.50)_{2,3}$  become consistent with those equations for  $\rho$  and  $\chi$  described in Langer et al. (2010) as

$$\dot{\chi} = k_{\chi} \frac{\tau_Y q(\tau_Y, \rho)}{\mu t_0} \left[1 - \frac{\chi}{\chi_0}\right],\tag{2.52}$$

$$\dot{\rho} = k_{\rho} \frac{\tau_Y}{\gamma_D} \frac{q(\tau_Y, \rho)}{t_0} \left[1 - \frac{\rho}{\rho^{ss}(\chi)}\right]. \tag{2.53}$$

Since we assume the system is driven by the constant shear rate, the total strain rate and plastic strain rate can be expressed by dimensionless form  $q_0$  and  $q(\tau_Y, \rho)$ , respectively, where  $t_0$  is the characteristic microscopic time scale,  $e_D = \gamma_D L$  is assumed to be the single-dislocation energy.  $\chi_0$  is the steady-state configurational temperature, and  $\rho^{ss}(\chi)$  is the steady-state dislocation density, which has a form

$$\rho^{ss}(\chi) = \frac{1}{a^2} e^{-e_D/\chi}.$$

We further adopt the flow stress  $\tau_Y$  based on Hooke's law, Orowan's equation and the dislocation depinning mechanism proposed by Langer *et al.* (2010),

$$\dot{\tau}_Y = \mu \left[ \frac{q_0}{t_0} - \frac{q(\tau_Y, \rho)}{t_0} \right]. \tag{2.54}$$

The coefficient factor  $k_{\rho}$  and  $k_{\chi}$ , as well as the function  $\nu(\Theta, \rho, q_0)$  and detailed explanation on each equation of motion, will be discussed in the next section. Eq. (2.47) together with (2.54), (2.53) and (2.52) yield a system of coupled partial differential equations as

$$\tau - \tau_{B} - \tau_{Y} = 0, 
\dot{\tau}_{Y} = \mu \left[ \frac{q_{0}}{t_{0}} - \frac{q(\tau_{Y}, \rho)}{t_{0}} \right], 
\dot{\chi} = k_{\chi} \frac{\tau_{Y} q(\tau_{Y}, \rho)}{\mu t_{0}} \left[ 1 - \frac{\chi}{\chi_{0}} \right], 
\dot{\rho} = k_{\rho} \frac{\tau_{Y}}{\gamma_{D}} \frac{q(\tau_{Y}, \rho)}{t_{0}} \left[ 1 - \frac{\rho}{\rho^{ss}(\chi)} \right],$$
(2.55)

where the first equation in (2.55) subjects to the boundary conditions (2.41) on  $\partial_k$  and (2.49) on  $\partial_s$ , and the rest equations subject to initial conditions.

### 2.3.3. Equations of Motion

In this subsection, we go through each equation of motion in detail by discussing how they are derived and the physical interpretation behind the mathematical expression.

### Equilibrium of microforces on dislocations:

$$\tau_Y = \tau - \tau_B, \tag{2.56}$$

This equation is the microforce balance on dislocations inferred from virtual displacements (see Eq.(2.45)). In strictly speaking, (2.55) is the governing equations for non-uniform plastic deformation due to the presence of back stress  $\tau_B$  in microforce balance equation. This back stress is the resolved stress conjugate to excess dislocations. Hence, the stress is probably caused by the accumulation of excess dislocations. When a crystal undergoes a non-uniform deformation, such as torsion of the wire, bending of the beam, and indentation, in order to fulfill the geometrical continuity of the sample, excess dislocations are required to accommodate the curvature of crystal lattices. As given in (2.48), the back stress is proportional to the second derivative of defect energy  $\psi_m$  with respect to the excess dislocation density  $\rho^g$ . Therefore, the correct choice of  $\psi_m$  plays a significant role in modeling microstructures of the crystals.

Note that there is a various formulation of this defect energy in the literature leading to kinematic hardening as well as the size effect. Besides the quadratic potential, the authors (Kametani et al., 2012; Wulfinghoff et al., 2014) have assumed the defect energy to be linear with respect to the excess dislocation density, and Berdichevsky (2016) has proposed another example of rank-one defect energy of screw dislocations. The latter linear potential has been adopted by Le & Piao (2016), which showed the linear defect energy leads to not only size effect but also a jump of the plastic warping across the boundary between the dislocation-occupied and dislocation-free region of twisted crystal bar. The third type is logarithmic defect energy proposed by Berdichevsky (2006b), and it has been applied to continuum dislocation theory in many applications, e.g. Dislocation pile-ups, deformation twinning, polygonization, bending, torsion, formation of grains and indentation (Kochmann & Le, 2008, 2009b; Le & Nguyen, 2012, 2013; Kaluza & Le, 2011; Koster et al., 2015; Baitsch et al., 2015). Moreover, a new type of defect energy of screw dislocations is proposed by Le & Piao (2018) based on the asymptotically exact free energy density of excess dislocation (Berdichevsky, 2017), and the applications will be shown in the subsequent chapters. On the other hand, uniform plastic deformation, like tension and compression tests, mainly requires the redundant dislocations rather than the excess so that the back stress  $\tau_B$  vanishes. Apparently, in this case, the equilibrium of microforces becomes

$$\tau = \tau_Y$$

such that the system reduces to

$$\dot{\tau} = \mu \left[ \frac{q_0}{t_0} - \frac{q(\tau, \rho)}{t_0} \right], 
\dot{\chi} = k_\chi \frac{\tau q(\tau, \rho)}{\mu t_0} \left[ 1 - \frac{\chi}{\chi_0} \right], 
\dot{\rho} = k_\rho \frac{\tau_Y}{\gamma_D} \frac{q(\tau_Y, \rho)}{t_0} \left[ 1 - \frac{\rho}{\rho^{ss}(\chi)} \right],$$
(2.57)

which has been proposed by Langer et al. (2010). Besides the case in the uniform plastic deformation, the other utilization of (2.57) is when the sample stays on a macroscopic scale. We know that in small devices of microscale or nanoscale, excess dislocations play a significant role in the size effect phenomena because the portion of excess dislocation density gets relatively high. But for samples in millimeter, the effect of  $\tau_B$  is no longer evident so that it can be ignored from the system of equations. Two applications in torsion analysis ignoring the back stress will be shown in chapter 5.

### Equation of motion for flow stress $\tau_Y$ :

Following Langer (2015), we consider a simple situation that a slab of material with the area  $\mathcal{A}$  and thickness L lies in the plane of applied shear stress. We suppress the tensor notation of stress and strain for simplicity. The dislocations driven by the stresses move through the material body and produce the flow stress, and by Hooke's law we have

$$\tau_Y = \mu(\varepsilon - \varepsilon^p). \tag{2.58}$$

The Orowan equation relates the strain rate to the movement of dislocations. Hence, in the model for the plasticity based on dislocation mechanics, this relation is a good choice to start with. One principle idea of thermodynamic dislocation theory is that the overwhelmingly dominant mechanism controlling plastic deformation is thermally activated depinning of dislocation, which relates to Orowan's relation,

$$\dot{\varepsilon}^p = \rho b v, \tag{2.59}$$

with b being the magnitude of the Burgers vector,  $\rho$  the dislocation density, and v the average velocity of dislocation. The assumption made in the theory is that during the motion of dislocations, each dislocation segment moves rapidly from one pinning point to another and be trapped there. With the aid of applied stress and thermal fluctuation, they get rid of the pinned state and move to the next pinning site. They proceed pinning and depinning process again and again until to the final state. We denote the average distance between two pinning sites by  $l = 1/\sqrt{\rho}$ , then the speed of dislocation is expressed as

$$v = \frac{l}{t_P}$$

where  $1/t_P$  is a thermally activated depinning rate given by

$$\frac{1}{t_P} = \frac{1}{t_0} e^{-U_P(\tau_Y)/k_B T}.$$

The microscopic time  $t_0$  is of the order of  $10^{-12}$ s (Langer, 2017c), and T denotes the ordinary temperature. This depinning rate emerges from the physical observation that the applied stress and temperature influence the response of plastic deformation (Haasen, 1958; Kocks & Mecking, 2003). It is assumed that there is a potential well in the pinning site given by

$$U_P(\tau_Y) = k_B T_P e^{-\tau_Y/\tau_T},$$

where  $k_B$  is the Boltzmann factor,  $T_P$  the activation temperature, and  $\tau_T$  the Taylor stress.  $T_P$  is large so that in the absence of external stress, by thermal fluctuation

itself, dislocations can not escape from the trap unless the temperature of materials reaches  $T_P$ , which is physically not possible in the solid-state, for  $T_P$  may be higher than the melting temperature. However, when the stress is applied, potential well depth is reduced by the coefficient, a exponential function of the stress. Taylor stress  $\mu_T$  is that  $\mu$  times the strain required to move a dislocation segment a small fraction of an atomic spacing away from a pinning point,

$$\tau_T = \mu b'/l = \mu \frac{b'}{b} b \sqrt{\rho} = \mu_T b \sqrt{\rho}, \tag{2.60}$$

with b'/b being a coefficient such that  $\mu_T$  is proportional to  $\mu$ . One assumption made on the speed of dislocations is that the time for depinning process takes much longer than that of dislocation moving from one to another pinning site so that we neglect this contribution to the speed in Orowan's relation. As a result, from (2.59), we have the dimensionless plastic strain rate as

$$q(\tau_Y, \rho) = \dot{\varepsilon}^p t_0 = b\sqrt{\rho} [f_P(\tau_Y) - f_P(-\tau_Y)], \tag{2.61}$$

where

$$f_P(\tau_Y) = \exp\left[-\frac{T_P}{T}e^{-\tau_Y/\tau_T(\rho)}\right].$$

The antisymmetry is required in (2.61) for dealing with the reversal process, where the reflection symmetry must be preserved and the second law,  $\tau_Y q \ge 0$  (see Eq.(2.77)), not be violated. From this formula, we observe that the plastic strain rate is relatively sensitive to the temperature change and the applied stresses. Solving (2.61) for stress as a function of  $\rho$ , q, and T, we have

$$\tau_Y = \tau_T(\rho)\nu(\rho, q, T), \tag{2.62}$$

where

$$\nu(\rho,q,T) = \ln(\frac{T_P}{T}) - \ln\left[\ln(\frac{b\sqrt{\rho}}{q})\right].$$

As shown,  $\nu(\rho, q, T)$ , a logarithmic function of inverse T and double logarithm with respect to  $\rho$  and q, is a slowly varying function of its arguments. We introduce further the dimensionless form of total strain rate,  $q_0 = \dot{\varepsilon} t_0$ , and plugging it together with (2.61) into the rate form of Hooke's law, we obtain

$$\dot{\tau}_Y = \mu \left[ \frac{q_0}{t_0} - \frac{q(\tau_Y, \rho)}{t_0} \right].$$

Since we analyze the problem driven by constant strain rate, we can replace the time derivative with strain derivative by chain rule,  $\frac{\partial}{\partial \varepsilon} = \frac{\partial}{\partial t} \frac{\partial t}{\partial \varepsilon}$ , and we have

$$\frac{\partial \tau_Y}{\partial \varepsilon} = \mu \left[ 1 - \frac{q(\tau_Y, \rho)}{q_0} \right]. \tag{2.63}$$

### Equation of motion for the effective temperature $\chi$ :

Eq.  $(2.55)_3$  is an equation of motion for the effective temperature  $\chi$ . It is a statement of the first law of thermodynamics for the configurational subsystem as reference. We assume that the thermodynamic system of the material body consists of two subsystems, namely kinematic-vibrational subsystem and configurational subsystem. The kinetic-vibrational degrees of freedom describe the vibration of atoms about its normal position in a substance, while the configurational degrees of freedom describe the atomic rearrangements, taking the configurational subsystem from one inherent structure to another, associated with irreversible plastic deformation. Although the inherent structures might be possible to include some other defects, such as vacancies, grain size or stacking faults, we restrict ourself in this study on dislocations, which work as a carrier of plastic deformation. Since dislocations possess large energies and slow time scales compared to thermal fluctuations, they are poorly coupled from kinetic-vibrational degrees of freedom and, therefore, two subsystems are considered as weakly interacted, connected with each other by poor heat conductor.

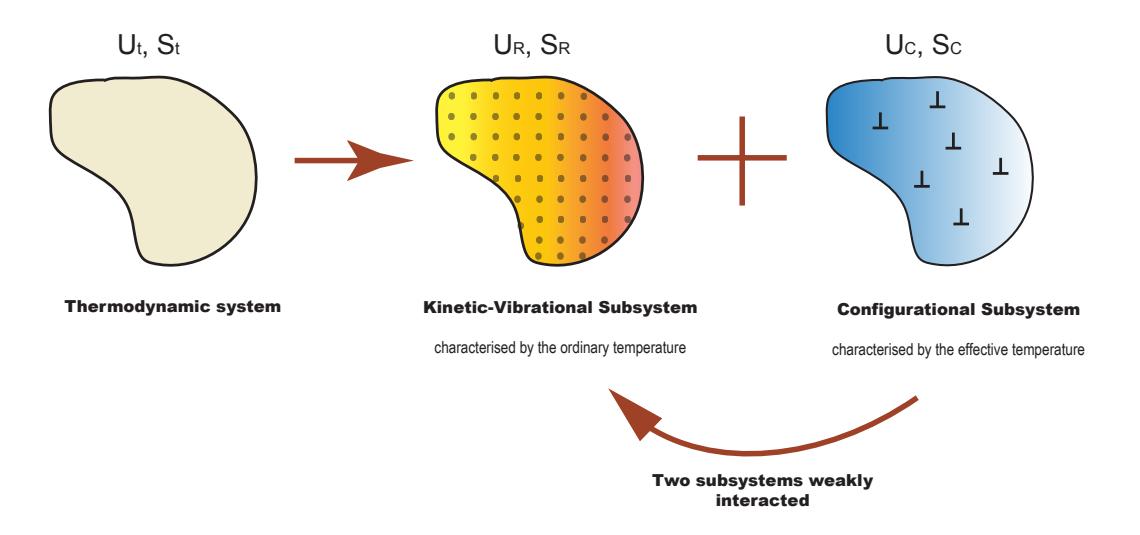


Figure 2.13.: Decomposition of thermodynamic system into kinetic-vibrational and configurational subsystems

Fig. 2.13 illustrates the decomposition of the thermodynamic system into two subsystems (Chowdhury *et al.*, 2018). The total internal energy of the thermodynamic system is the sum of that of kinematic-vibrational and configurational subsystems

$$U_t = U_R(S_R) + U_C(S_C, \rho).$$
 (2.64)

 $U_R(S_R)$  is the kinetic-vibrational energy characterized by the ordinary thermal temperature given by

$$\Theta_R = k_B T = \frac{\partial U_R}{\partial S_R},$$

where  $S_R$  is the entropy of the kinetic-vibrational subsystem. The temperature  $\Theta_R$  is linked with T in degrees Kelvin, and it has the dimension of energy by Boltzmann's

factor  $k_B$ .  $U_C(S_C, \rho)$  is the configurational energy of materials containing dislocations with  $S_C(U_C, \rho)$  being the entropy of its subsystem and  $\rho$  being the dislocation density. Then we have another thermodynamically well-defined temperature, effective temperature,

$$\chi = \left(\frac{\partial U_C}{\partial S_C}\right)_{\rho},\tag{2.65}$$

which characterizes the configurational subsystem. Assume that the configurational energy can be written as

$$U_C(S_C, \rho) = U_0(\rho) + U_1(S_1). \tag{2.66}$$

Here  $U_0$  and  $S_0$  are the configurational energy and the entropy associated with dislocations, and  $U_1$  and  $S_1$  are the energy and the entropy of all the configurational degrees of freedom other than those pertaining to the dislocations. Likewise, we have

$$S_C(U_C, \rho) = S_0(\rho) + S_1(U_1). \tag{2.67}$$

Moreover, by taking derivative of (2.66) with respect to dislocation density  $\rho$  at given  $S_C$  and by using (2.67), one obtains

$$\left(\frac{\partial U_C}{\partial \rho}\right)_{S_C} = \frac{\partial U_0}{\partial \rho} - \chi \frac{\partial S_0}{\partial \rho}.$$
(2.68)

The first law of thermodynamics for the system states that

$$\mathcal{V}\tau_Y \dot{\varepsilon}^p = \dot{U}_t = \dot{U}_R + \dot{U}_C. \tag{2.69}$$

Note that the rate of energy due to the reversible elastic strain cancels out of the equation. Supposed that the system has no external heat source inside the material body  $\mathcal{V}$ , and neither has heat flux through the surface that supplies external energy to the material body, the rate of the internal energy is balanced with the rate of external work input. Since the fast kinetic-vibrational degrees of freedom are combined with the external environment to serve as a single heat bath at a single temperature T, the loss of heat energy through the surface is included in (2.69). Plugging (2.64) and (2.65) into the first law, we get

$$\mathcal{V}\tau_{Y}\dot{\varepsilon}^{p} = \Theta_{R}\dot{S}_{R} + \chi\dot{S}_{C} + \left(\frac{\partial U_{C}}{\partial\rho}\right)_{S_{C}}\dot{\rho}.$$
(2.70)

The first term in the right-hand side of (2.70) is interpreted as the heat flux flowing from the configurational subsystem into the thermal reservoir. In other words, the subsystem of dislocations absorbs energy from external work, and it exchanges heat with its surroundings as expressed by

$$Q = \Theta_R \dot{S}_R = \mathcal{K}(\chi - \Theta_R), \tag{2.71}$$

where K is a non-negative thermal transport coefficient. While using (2.67), the second term in the right-hand side of (2.70) can be written as

$$\chi \dot{S}_C = \chi \left( \frac{\partial S_0}{\partial \rho} \dot{\rho} + \frac{\partial S_1}{\partial \chi} \dot{\chi} \right) = \chi \frac{\partial S_0}{\partial \rho} \dot{\rho} + \mathcal{V} c_{eff} \dot{\chi}$$
 (2.72)

where  $c_{eff} = \chi \frac{\partial S_1}{\partial \chi} / \mathcal{V}$  denotes the effective specific heat. Using (2.71), (2.72) and (2.68), the first law is transformed into the form of the effective temperature evolution as

$$\mathcal{V}c_{eff}\dot{\chi} = \mathcal{V}\tau_{Y}\dot{\varepsilon}^{p} - \frac{\partial U_{0}}{\partial \rho}\dot{\rho} - \mathcal{Q}.$$

Dislocation energy  $U_0$  is given by

$$U_0(\rho) = \mathcal{A} \rho e_D$$
, where  $e_D = \gamma_D L$ .

Since the effective temperature is much higher than the ordinary one, we can regard that  $Q \approx \mathcal{K}\chi$ , and moreover, in the steady-state, all work done is dissipated as heat such that  $Q = \mathcal{V}\tau_Y\dot{\varepsilon}^p$ . As stated in Langer (2015), the stead-state configurational temperature  $\chi_{ss}$  equals to a constant  $\chi_0$  for the case that the strain rate is not extremely fast, which implies that  $\mathcal{K} = \mathcal{V}\tau_Y\dot{\varepsilon}^p/\chi_0$ . As a result,

$$c_{eff}\dot{\chi} = \tau_Y \dot{\varepsilon}^p \left[ 1 - \frac{\chi}{\chi_0} \right] - \gamma_D \dot{\rho}.$$

The second term of the right-hand side is dropped due to the reason that there is no experimental situation where it is shown to play a significant role (Langer, 2017c). Introducing the dimensionless factor

$$K_{\chi} = \frac{\mu}{c_{eff} \, e_D},$$

and by chain rule, we obtain

$$\frac{\partial \chi}{\partial \varepsilon} = K_{\chi} \frac{e_D \tau_Y q}{\mu q_0} \left( 1 - \frac{\chi}{\chi_0} \right). \tag{2.73}$$

### Equation of the motion for the dislocation density $\rho$ :

The development of equation for the dislocation density is based on the second law of thermodynamics. It states that the rate of change of total entropy is never negative and it is expressed as

$$\dot{S}_t = \dot{S}_C + \dot{S}_R \geqslant 0 \tag{2.74}$$

where the total entropy  $S_t$  is the sum of entropies of two subsystems. Evaluating  $S_C$  from (2.70) and substituting it into (2.74), one obtains

$$\frac{1}{\chi} \left[ \mathcal{V} \tau_Y \dot{\varepsilon}^p - \left( \frac{\partial U_C}{\partial \rho} \right)_{S_C} \dot{\rho} \right] + \left( 1 - \frac{\Theta_R}{\chi} \right) \dot{S}_R \geqslant 0. \tag{2.75}$$

Since  $S_R$  is independent of  $\varepsilon^p$  and  $\rho$ , each term in (2.75) should satisfy the non-negativity to avoid the violation of the inequality (Coleman & Noll, 1963). The second term is automatically satisfied because  $\chi$  is always larger than  $\Theta_R$ . Concerning the first term, provided that the mechanical power is always positive, instead of  $(\partial U_C/\partial \rho)_{S_C} \dot{\rho} \leqslant \mathcal{V}\tau_Y \dot{\varepsilon}^p$ , Langer (2015) has proposed the inequality

$$\left(\frac{\partial U_C}{\partial \rho}\right)_{S_C} \dot{\rho} \leqslant 0,$$
(2.76)

which also satisfies (2.75). One of the simplest form of  $\dot{\rho}$  to fulfill the inequality (2.76) is

$$\dot{\rho} = -\mathcal{M} \left( \frac{\partial U_C}{\partial \rho} \right)_{S_C},$$

where  $\mathcal{M}$  is a non-negative rate factor. Adopting the formula proposed by Langer (2017c) for the entropy of dislocations

$$S_0(\rho) = -\mathcal{A} \rho \ln(a^2 \rho) + \mathcal{A} \rho,$$

and using (2.68), one obtains

$$\dot{\rho} = -\mathcal{M}[\mathcal{A} e_D + \mathcal{A} \chi \ln(a^2 \rho)] = -\mathcal{A} \mathcal{M} \chi \left[ -\ln(e^{-\frac{e_D}{\chi}}) + \ln(a^2 \rho) \right]$$
$$= -\mathcal{A} \mathcal{M} \chi \ln \left( \frac{\rho}{\rho^{ss}(\chi)} \right),$$

where  $\rho^{ss}(\chi) = (1/a^2)e^{-e_D/\chi}$  is dislocation density in the steady-state, which leads (2.68) to be zero. The factor  $\mathcal{A}\mathcal{M}\chi$  is thought to be proportional to the input power, hence we set  $\mathcal{A}\mathcal{M}\chi = \kappa_{\rho}\tau_{Y}\dot{\varepsilon}^{p}/\gamma_{D}$ , where  $\gamma_{D}$  is involved due to the dimensional consistency. In case that  $\rho$  is closed to  $\rho^{ss}(\chi)$ , we have

$$\ln\left(\frac{\rho}{\rho^{ss}(\chi)}\right) = \frac{\rho}{\rho^{ss}(\chi)} - 1,$$

such that

$$\dot{\rho} = \kappa_{\rho} \frac{\tau_{Y} \dot{\varepsilon}^{p}}{\gamma_{D}} \left( 1 - \frac{\rho}{\rho^{ss}(\chi)} \right). \tag{2.77}$$

This equation has a physical interpretation that some portion of input power converts into the dislocation energy with  $\kappa_{\rho}$  being a dimensionless factor. Note that the second term in the bracket includes the annihilation mechanism of dislocations. Converting it into strain derivative, it becomes

$$\frac{\partial \rho}{\partial \varepsilon} = \kappa_{\rho} \frac{\tau_{Y} q}{\gamma_{D} q_{0}} \left( 1 - \frac{\rho}{\rho^{ss}(\chi)} \right). \tag{2.78}$$

As commented by Langer (2015), this equation of motion for dislocation density, originated from the second law of thermodynamics, can recover the result (Kocks & Mecking, 2003) that the onset slope for strain hardening in copper almost does not vary with the temperature and strain rate change. It can be explained by

$$\mathcal{M}_{0} = \frac{1}{\mu} \frac{\partial \tau_{Y}}{\partial \epsilon} = \frac{1}{\mu} \frac{\partial \tau_{Y}}{\partial \rho} \frac{\partial \rho}{\partial \epsilon} = \kappa_{\rho} \frac{(b \nu \mu_{T})^{2}}{2\mu \gamma_{D}}, \tag{2.79}$$

where from (2.60) and (2.62), we have  $\partial \tau_Y/\partial \rho = b \nu \mu_T/(2 \sqrt{\rho})$  and from (2.78)  $\partial \rho/\partial \varepsilon = \kappa_\rho b \mu_T \nu \sqrt{\rho}/\gamma_D$ . Note that the term  $q/q_0$  is dropped from the derivative of  $\rho$  with respect to  $\varepsilon$  because of  $q \approx q_0$  at the onset of the hardening. The second term in the bracket of (2.78) is vanished, for we consider the initial dislocation density is much smaller than that in steady-state. One may wonder the validity of (2.78) in small  $\rho$ , but it can be explained by the factor  $\kappa_\rho$  which can correct the deviation.  $\mathcal{M}_0$  is independent with strain rate, and it is affected little by temperature, for  $\nu$  is a slow

variable on temperature and  $\gamma_D$  is proportional to  $\mu$  so that the temperature-dependent shear modulus is neutralized. If we set a new conversion factor as

$$K_{\rho} = \frac{2a^2\mu^2}{b^2\mu_T^2}\mathcal{M}_0,\tag{2.80}$$

where parameter a is applied in the coefficient in order to keep  $K_{\rho}$  dimensionless, we obtain the governing equation for the density in the form

$$\frac{\partial \rho}{\partial \varepsilon} = K_{\rho} \frac{\tau_Y \, q}{a^2 \, \mu \, \nu^2 \, q_0} \left( 1 - \frac{\rho}{\rho^{ss}(\chi)} \right).$$

At last, we end this chapter by showing the system of governing equations

$$\tau - \tau_B - \tau_Y = 0,$$

$$\frac{\partial \tau_Y}{\partial \varepsilon} = \mu \left[ 1 - \frac{q(\tau_Y, \rho)}{q_0} \right],$$

$$\frac{\partial \chi}{\partial \varepsilon} = K_\chi \frac{e_D \tau_Y q}{\mu q_0} \left( 1 - \frac{\chi}{\chi_0} \right),$$

$$\frac{\partial \rho}{\partial \varepsilon} = K_\rho \frac{\tau_Y q}{a^2 \mu \nu^2 q_0} \left( 1 - \frac{\rho}{\rho^{ss}(\chi)} \right).$$
(2.81)

# 3. Non-uniform Plastic Deformations Undergoing Anti-plane Constrained Shear

### 3.1. Introduction

The aim of this chapter is to extend Berdichevsky's formula for the free energy density of excess screw dislocations (Berdichevsky, 2017) to anti-plane shear deformation. This asymptotically exact energy density is based on the assumption that a moderate number of excess screw dislocations locally form a double-periodic structure (Weinberger, 2011). A modification, however, must be made by extrapolating this formula to a range of extremely small and large dislocation densities in order to use it in posing correct boundary-value problems. With the energy density of excess screw dislocations, we develop thermodynamic dislocation theory for non-uniform plastic deformations of crystals undergoing anti-plane constrained shear. The evolution of plastic slip, dislocation distribution, isotropic and kinematic hardening are presented. Finally, the stress-strain curves at different sample sizes are calculated, and the different types of strain hardening are discussed.

### Anti plane constrained shear:

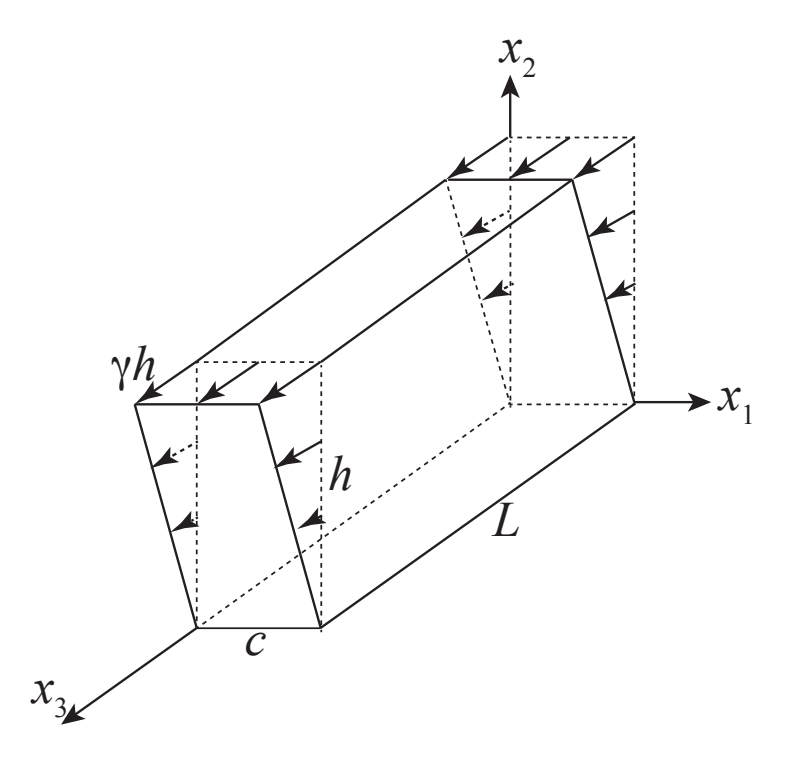


Figure 3.1.: Anti-plane constrained shear.

Consider a single crystal layer undergoing anti-plane shear deformation. The anti-

plane shear is defined as one in which

$$u_1 = u_2 = 0, \quad u_3 = w(x_1, x_2),$$

where  $\mathbf{u} = (u_1, u_2, u_3)$  denote the displacement and  $x_1, x_2, x_3$  are three axis in a Cartesian coordinate. Then the scalar components of strain tensor must have the form

$$\varepsilon_{11} = \varepsilon_{22} = \varepsilon_{33} = \varepsilon_{12} = 0$$
 and  $\varepsilon_{31} = \frac{1}{2}u_{3,1}$ ,  $\varepsilon_{32} = \frac{1}{2}u_{3,2}$ .

Let  $\mathcal{A}$  be the cross-section of the layer perpendicular to the  $x_3$ -axis. For simplicity, we take  $\mathcal{A}$  as a rectangle,  $\mathcal{A} = (0, c) \times (0, h)$ , with c and h being the width and the height of the cross-section, respectively. We place this single crystal in a "hard" device with the prescribed displacement at the boundary  $\partial \mathcal{A} \times [0, L]$ , with L being the depth of the layer (see Fig. 3.1)

$$w = \gamma(t)x_2$$
 at  $\partial \mathcal{A} \times [0, L]$ . (3.1)

Hence, it is called anti-plane constrained shear. Here  $\gamma(t)$  corresponds to the overall shear regarded as a given function of time t. We assume that  $c \ll h \ll L$ . The problem is to predict the stress-strain curve as well as the dislocation density during the plastic deformation.

## 3.2. Averaging Procedure and Energy of Screw Dislocations

### 3.2.1. A pair of screw dislocations:

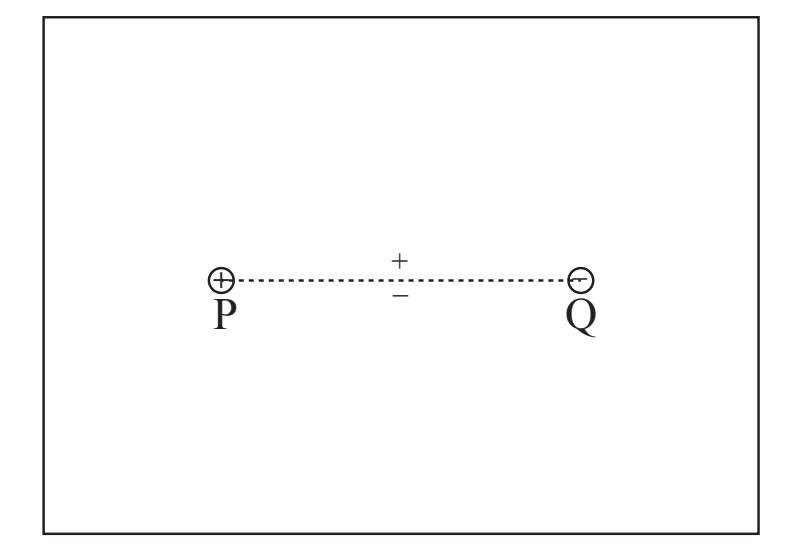


Figure 3.2.: A cut creating a pair of dislocations.

Let us first consider the equilibrium with a fixed amount of shear  $\gamma$ . If  $\gamma$  is large, then dislocations may occur in the equilibrium state of this crystal layer. Assume that a pair of screw dislocations are created by the well-known thought operations of cutting, shifting, and relaxing the crystal as shown schematically in Fig. 3.2. Here a cut  $\Lambda \times [0, L]$  is made along the straight dashed line  $\Lambda$ =PQ in the  $(x_1, x_2)$ -plane,

and the atoms on the plus side of the cut are shifted in the  $x_3$  direction through one lattice distance. Then the atoms are rejoined again, and the whole crystal is relaxed. By these operations, we have thus created a positive dislocation located at P and a negative dislocation located at Q, with the dislocation lines being parallel to the  $x_3$ -axis. Since the cut cannot reach the boundary  $\partial \mathcal{A}$  of the crystal's cross-section due to the smooth displacement specified there, dislocations must always occur in pairs. In this sense, the "hard" boundary conditions model the grain boundaries serving as obstacles and preventing dislocations from reaching them. The displacement  $w(\mathbf{x})$ , with  $\mathbf{x} = (x_1, x_2)$ , in the relaxed equilibrium state suffers a jump on the line  $\Lambda$  which is equal to the magnitude of Burgers vector b,

$$\llbracket w \rrbracket \equiv w^+ - w^- = b \quad \text{on } \Lambda, \tag{3.2}$$

where  $w^+$  and  $w^-$  are the limiting values of w on the upper and lower side of  $\Lambda$ , respectively. Gibbs variational principle states that the true displacement of the crystal in the relaxed equilibrium state minimizes the energy functional

$$I = \int_{\mathcal{A} \setminus \Lambda} \frac{\mu}{2} (w_{,1}^2 + w_{,2}^2) da$$

among all admissible displacements satisfying (3.1) and (3.2), where  $\mu$  is the shear modulus and  $da = dx_1dx_2$  denotes the area element. We get rid of the constraint (3.2) and the cut by regarding function  $w(\mathbf{x})$  as the distribution (or generalized function, Gelfand &Shilov (1964)). Then the derivatives of this generalized function are given by

$$w_{,i} = bm_i \delta(\Lambda) + w_{,i}^e,$$

where  $m_i$  is the unit normal vector to  $\Lambda$ ,  $\delta(\Lambda)$  the Dirac delta function with the support  $\Lambda$ , and  $w^e$  the multi-valued displacement defined on  $\mathcal{A}$ . In what follows the Latin indices run from 1 to 2, and over repeated indices the summation is understood. We call  $\beta_{3i} = bm_i\delta(\Lambda)$  the plastic distortion, while  $\beta_{3i}^e = w_{,i}^e$  the elastic distortion which is assumed to be regular everywhere except maybe at the dislocation line. Thus,

$$w_{,i} = \beta_{3i} + \beta_{3i}^e.$$

Since the total strain is equal to the elastic strain outside the cut, we remove the cut and reduce the above variational problem to the eigenstrain problem of minimizing the energy functional

$$I = \int_{4}^{2} \frac{\mu}{2} [(w_{,1} - \beta_{31})^{2} + (w_{,2} - \beta_{32})^{2}] da,$$

among all distributions satisfying (3.1) (Le, 2010). Changing the unknown function as  $w = \gamma x_2 + u(\mathbf{x})$ , with u = 0 at the boundary  $\partial \mathcal{A}$ , we get the minimization problem

$$I = \int_{A} \varphi_{1}(u) da = \int_{A} \frac{\mu}{2} \left[ (u_{,1} - \beta_{31})^{2} + (u_{,2} + \gamma - \beta_{32})^{2} \right] da \to \min_{u|_{\partial A} = 0}.$$

The energy (per unit depth) of the crystal containing this pair of dislocations is defined as the minimum value of this functional, I

$$\underline{I} = \min_{u|_{\partial \mathcal{A}} = 0} I. \tag{3.3}$$

It is convenient to deal with the dual variational problem. Following the standard procedure (see Berdichevsky (2009)), we transform the integral I by the Legendre-Fenchel transformation as

$$\int_{\mathcal{A}} \frac{\mu}{2} \left[ (u_{,1} - \beta_{31})^2 + (u_{,2} + \gamma - \beta_{32})^2 \right] da = \max_{\sigma_{3i}} \int_{\mathcal{A}} \left[ \sigma_{31} \beta_{31}^e + \sigma_{32} \beta_{32}^e - \frac{1}{2\mu} (\sigma_{31}^2 + \sigma_{32}^2) \right] da, \quad (3.4)$$

where the dual variables  $\sigma_{31}$  and  $\sigma_{32}$  to  $\beta_{31}^e = u_{,1} - \beta_{31}$  and  $\beta_{32}^e = u_{,2} + \gamma - \beta_{32}$  are defined as the derivative of  $\varphi_1(u)$  with respect to each variable,

$$\sigma_{31} = \frac{\partial \varphi_1(u)}{\partial \beta_{31}^e} = \mu(u_{,1} - \beta_{31}), \quad \sigma_{32} = \frac{\partial \varphi_1(u)}{\partial \beta_{32}^e} = \mu(u_{,2} + \gamma - \beta_{32}). \tag{3.5}$$

Inserting (3.4) into (3.3) and changing the order of the mini-maxi to maxi-mini problem, we obtain that

$$\underline{I} = \max_{\sigma_{3i}} \min_{u|_{\partial A} = 0} [F_1(\sigma_{3i}) + l(u)], \tag{3.6}$$

for which

$$F_1(\sigma_{3i}) = \int_{\mathcal{A}} \left[ -\sigma_{31}\beta_{31} - \sigma_{32}\beta_{32} + \sigma_{32}\gamma - \frac{1}{2\mu} (\sigma_{31}^2 + \sigma_{32}^2) \right] da,$$
$$l(u) = \int_{\mathcal{A}} (\sigma_{31}u_{,1} + \sigma_{32}u_{,2}) da.$$

With the aid of integration by parts, the functional l(u) can be decomposed into the linear functional in terms of u and the other functional that gets rid of it,

$$l(u) = l_1(u) + l_2(\sigma_{3i}), \text{ where } l_1(u) = \int_{\mathcal{A}} (\sigma_{31,1} + \sigma_{32,2}) u da,$$
  
$$l_2(\sigma_{3i}) = \int_{\partial \mathcal{A}} (\sigma_{31} n_1 + \sigma_{32} n_2) \tilde{u} ds,$$

where  $n_1$  and  $n_2$  are components of the unit normal vector **n** of the boundary  $\partial \mathcal{A}$  and  $\tilde{u}$  is a given function at the boundary. Then the minimization in (3.6) is reduced to the minimization of  $l_1(u)$ ,

$$\min_{u|_{\partial \mathcal{A}}=0} [F_1(\sigma_{3i}) + l(u)] = F_1(\sigma_{3i}) + l_2(\sigma_{3i}) + \begin{cases} 0 & \text{if } \sigma_{31,1} + \sigma_{32,2} = 0, \\ -\infty & \text{if } \sigma_{31,1} + \sigma_{32,2} \neq 0. \end{cases}$$

When  $\sigma_{31,1} + \sigma_{32,2}$  vanishes, the linear function  $l_1(u)$  has a finite minimum value that is zero. Otherwise, the minimum of  $l_1(u)$  is minus infinity, which is excluded from maximization problem. As a result,

$$\underline{I} = \max_{\sigma_{3i}} [F_1(\sigma_{3i}) + l(\sigma_{3i})] \tag{3.7}$$

with the constraint,

$$\sigma_{31.1} + \sigma_{32.2} = 0$$
, in  $\mathcal{A}$ .

Before solving the maximization problem (3.7), we must check the validity of (2.17) in this problem. Provided that  $\check{u}$  is the solution of the Euler equation of I, and the corresponding  $\check{\sigma}_{3i}$  by (3.5) satisfies the inequality

$$F_1(\check{\sigma}_{3i}) + l(\check{\sigma}_{3i}) \leqslant \max_{\sigma_{3i}} [F_1(\sigma_{3i}) + l(\sigma_{3i})] \leqslant \underline{I} = \frac{\mu}{2} [(\check{u}_{,1} - \beta_{31})^2 + (\check{u}_{,2} + \gamma - \beta_{32})^2].$$

It turns out that, by substituting  $\check{\sigma}_{3i}$  in terms of  $\check{u}_{,i}$  by (3.5),

$$F_1(\check{\sigma}_{3i}) + l(\check{\sigma}_{3i}) = \frac{\mu}{2} \left[ (\check{u}_{,1} - \beta_{31})^2 + (\check{u}_{,2} + \gamma - \beta_{32})^2 \right],$$

which implies that

$$\max_{\sigma_{3i}} [F_1(\sigma_{3i}) + l(\sigma_{3i})] = \underline{I} = \min_{u|_{\partial A} = 0} I(u).$$

Due to the boundary condition  $\tilde{u} = 0$ , the term  $l(\sigma_{3i})$  vanishes, and by using of the relation

$$\max(F_1) = -\min(-F_1),$$

the problem becomes solving

$$\min_{\sigma_{3i}} \int_{\mathcal{A}} [\sigma_{31}\beta_{31} + \sigma_{32}\beta_{32} - \sigma_{32}\gamma + \frac{1}{2\mu}(\sigma_{31}^2 + \sigma_{32}^2)] da, \tag{3.8}$$

among all shear stresses  $\sigma_{31}$  and  $\sigma_{32}$  satisfying the equilibrium equation

$$\sigma_{31.1} + \sigma_{32.2} = 0.$$

This equation is fulfilled if there exists a stress function  $\Phi(\mathbf{x})$  such that

$$\sigma_{31} = \Phi_{.2}, \quad \sigma_{32} = -\Phi_{.1}.$$

Substituting these formulas into (3.8) and integrating the first two terms by parts, we obtain the dual minimization problem in terms of the stress function  $\Phi(\mathbf{x})$ ,

$$J = \int_{\mathcal{A}} \left[ \frac{1}{2\mu} (\nabla \Phi)^2 + \alpha \Phi + \Phi_{,1} \gamma \right] da \to \min_{\Phi}, \tag{3.9}$$

where

$$\alpha = \beta_{32,1} - \beta_{31,2} = b[\delta(\mathbf{x} - \mathbf{x}^+) - \delta(\mathbf{x} - \mathbf{x}^-)].$$

Note that the energy of crystal containing these dislocations,  $\underline{I}$ , equals to the minimum of J taken with the minus sign,  $\underline{I} = -\underline{J}$ . It turns out that, if the jump of w is constant on  $\Lambda$ , the energy is infinite. Therefore this variational problem needs a regularization.

The simplest regularization of the above variational problem is to use in (3.9) the regularized dislocation density  $\alpha_r = b[\delta_{r_0}(\mathbf{x} - \mathbf{x}^+) - \delta_{r_0}(\mathbf{x} - \mathbf{x}^-)]$  instead of  $\alpha$ , where

$$\delta_{r_0}(\mathbf{x} - \boldsymbol{\xi}) = \begin{cases} \frac{1}{\pi r_0^2} & |\mathbf{x} - \boldsymbol{\xi}| < r_0, \\ 0 & \text{otherwise.} \end{cases}$$

Here,  $r_0$  is the radius of a small circle centered at  $\boldsymbol{\xi}$ , interpreted as the dislocation core.<sup>1</sup> Varying the energy functional (3.9), with  $\alpha$  being replaced by  $\alpha_r$ , we derive the following boundary value problem

$$\begin{cases}
\nabla^2 \Phi = \mu \alpha_r & \text{in } \mathcal{A}, \\
\Phi_{,1} = -\mu \gamma & \text{on } \partial \mathcal{A}_1 = (0, x_2) \text{ and } \partial \mathcal{A}_3 = (c, x_2), \\
\Phi_{,2} = 0 & \text{on } \partial \mathcal{A}_2 = (x_1, 0) \text{ and } \partial \mathcal{A}_4 = (x_1, h).
\end{cases}$$
(3.10)

The boundary conditions in (3.10) will be simplified if we change the unknown function as follows:  $\Phi = -\mu \gamma x_1 + \Psi$ . Then, in terms of  $\Psi$ , the variational problem becomes

$$J = \int_{\mathcal{A}} \left[ -\frac{1}{2}\mu \gamma^2 + \frac{1}{2\mu} \left( \nabla \Psi \right)^2 - \mu \gamma x_1 \alpha_r + \alpha_r \Psi \right] da \to \min_{\Psi}.$$
 (3.11)

This variational problem implies the Poisson equation subjected to the Neumann boundary condition for  $\Psi$ 

$$\begin{cases} \nabla^2 \Psi = \mu \alpha_r & \text{in } \mathcal{A}, \\ \Psi_{,n} = 0 & \text{on } \partial \mathcal{A}, \end{cases}$$
 (3.12)

where  $\Psi_{,n}$  is the derivative in the normal direction to the boundary of  $\mathcal{A}$ . Inserting the minimizer  $\check{\Psi}$ , the solution of (3.12), into the functional J, we get for the energy of crystal containing two dislocations

$$\underline{I} = -\underline{J} = \int_{\mathcal{A}} \left( \frac{\mu}{2} \gamma^2 + \mu \gamma x_1 \alpha_r - \frac{1}{2} \alpha_r \check{\Psi} \right) da. \tag{3.13}$$

Note that since J contains a quadratic and linear functional with respect to  $\Psi$ , a simplified form is obtained by making use of Clapeyron's theorem as shown

$$\int_{\mathcal{A}} \left( \frac{1}{2\mu} \left( \nabla \check{\Psi} \right)^2 + \alpha_r \check{\Psi} \right) da = \int_{\mathcal{A}} -\frac{1}{2} \alpha_r \check{\Psi} da.$$

As an example, let us compute this energy in the case when a positive dislocation is located at (c/2 - l/2, h/2) and a negative one at (c/2 + l/2, h/2) (see the details in Appendix). We choose h = 10 micron, c = 1 micron,  $b = r_0 = 1$  Å. The dimensionless energy of a dipole  $\underline{I}/\mu b^2$  (with the constant term  $\frac{1}{2}\mu\gamma^2 ch$  being removed) as a function of the distance l/c at three different strain are shown in Fig. 3.3(a), (b), (c). When no displacement applied, there is only the energy of dislocation dipole stored in the crystal shown in Fig. 3.3(a) (for  $\gamma = 0$ ). One can observe the graph in Fig. 3.3(a) possesses the property of rotational symmetry by an angle of 180°. The reason is that the increasing energy of the crystal near 1/c = 0 is induced by the interaction of two dislocations of opposite signs in the process of dipole dissolution, and the increasing crystal energy near 1/c = 1 is caused by the interaction of a dislocation with its image dislocation due to the boundary. Hence, the behavior at two ends are caused by the same mechanism leading to the rotational symmetry. Note that the free surface attracts the dislocation, for there is the image dislocation of the opposite sign. Conversely, the rigid surface repels the dislocation owing to the image dislocation of the same sign. Note that dissociation of edge and screw dislocations under zero stress and at 0K temperature

<sup>&</sup>lt;sup>1</sup>Other regularizations are also possible (see, e.g., Cai et al. (2006); Aifantis (2009); Po et al. (2014)).

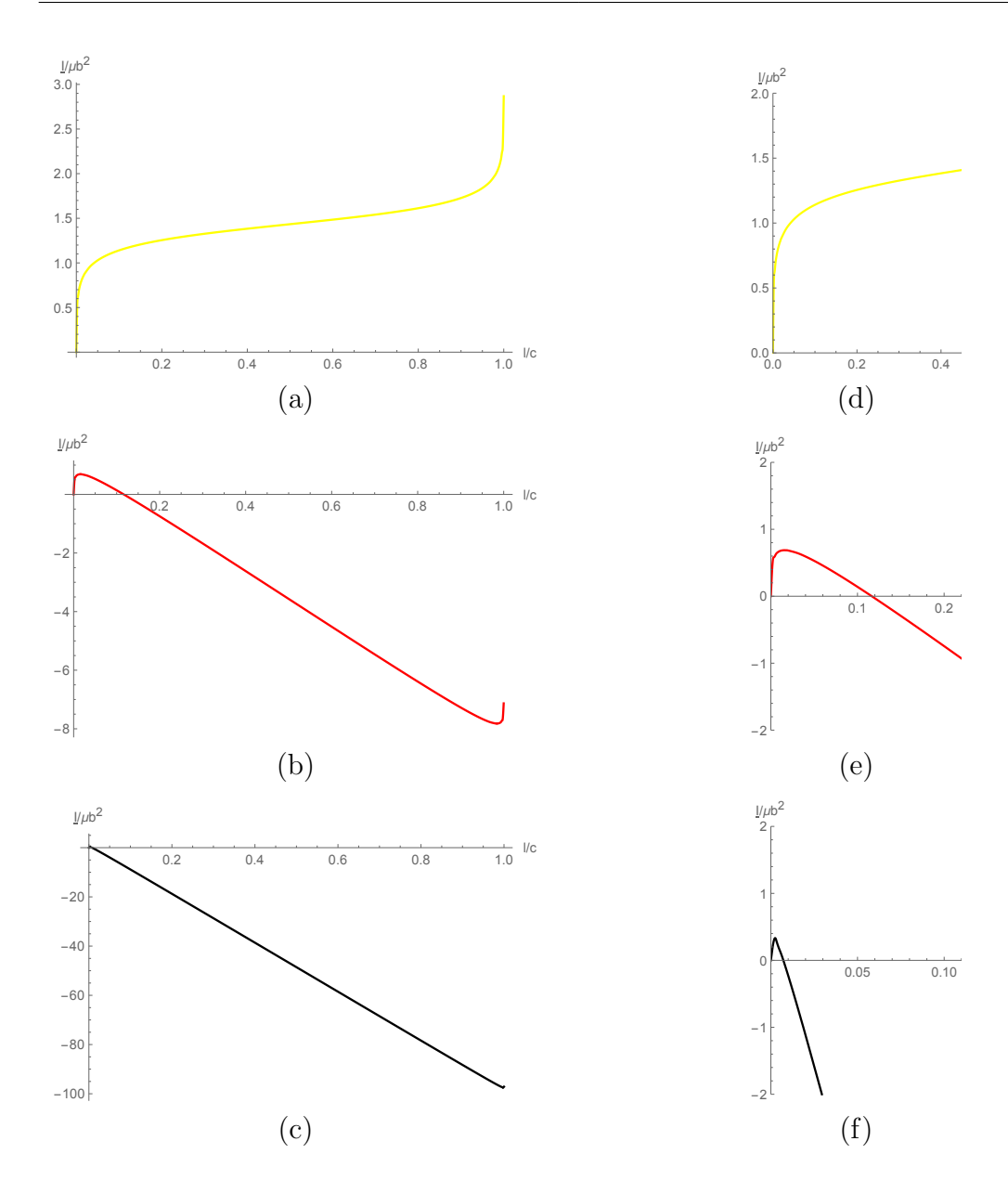


Figure 3.3.: Dimensionless energy of dislocation dipole as function of l/c: a)  $\gamma = 0$  (yellow), b)  $\gamma = 0.001$  (red), c)  $\gamma = 0.01$  (black), d) Zoom in for the case  $\gamma = 0$ , e) Zoom in for the case  $\gamma = 0.001$ , f) Zoom in for the case  $\gamma = 0.01$ .

has been studied and compared by different models on atomistic scale (Mianroodi et al., 2016).

When a nonzero  $\gamma$  is applied, it is no longer pure dipole energy stored in the crystal but also the interaction of dipoles with  $\gamma$  that is the second term in (3.13). Two cases for  $\gamma = 0.001$  and  $\gamma = 0.01$  are shown in Fig. 3.3(b) and (c). In all three cases, the energy has a local minimum at l = 0. Therefore, if no thermal fluctuation occurs, nucleation of the dislocation dipole is not energetically preferable. However, as shown in Berdichevsky & Le (2002), the presence of thermal fluctuation changes the situation. Now, for each temperature, there is a certain density of the dislocation dipoles with a fairly small mean distance between dislocations in the dipole. If the external field is applied, the dipoles can even be dissolved into freely moving dislocations if the energy barrier can be overcome. One can compare the magnitudes for three cases from Fig. 3.3(d), (e), (f) (Zoom in near the origin) and Fig. 3.4. Note that the larger

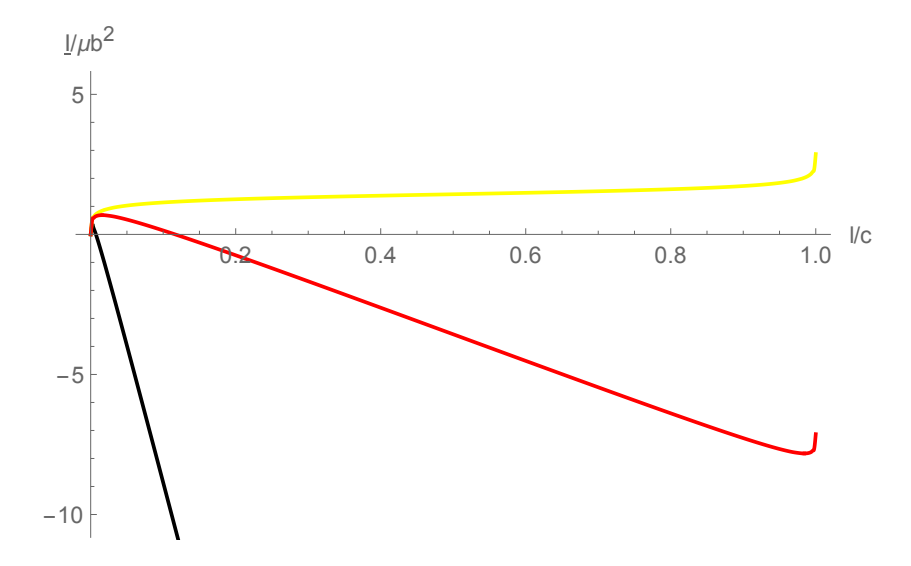


Figure 3.4.: Combination of three cases of Fig. 3.3.

the field, the smaller the energy barrier, so that the thermal fluctuation makes it easier to dissolve the dipoles if the applied shear stress is large enough.

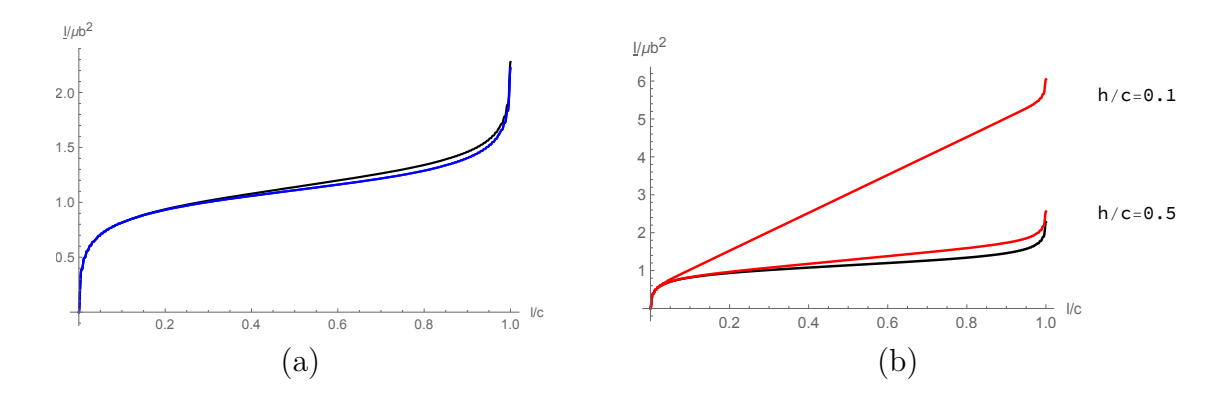


Figure 3.5.: Energy of the crystal containing a dislocation dipole for different aspect ratio h/c of the rectangular cross section: (a) h/c = 1 (black), h/c = 5 and h/c = 10 (blue, two curves overlapped), (b) h/c = 1 (black), h/c = 0.5 and h/c = 0.1 (red).

Fig. 3.5 shows the dimensionless energy of dislocation dipole for  $\gamma = 0$  with different aspect ratio h/c of the rectangular cross-section. The black curve in Fig. 3.5 is the energy with the aspect ratio h/c = 1. The blue curves in Fig. 3.5(a) indicate the cases for h/c = 5 and h/c = 10 (two curves overlapped), and the red curves in Fig. 3.5(b) represent the crystal energy with the aspect ratio h/c = 0.5 and h/c = 0.1. When the aspect ratio is beyond a certain value, roughly about 0.5, there is a tiny change in appearance of dipole energy. However, when the aspect ratio is below than that, the influence to the energy is strong. This behavior is due to the hyperbolic sine in the denominator of function  $Q_k$  in Neumann function (A.2).

One question arises whether this phenomenon relate to the report by Chen & Ngan. (2010), Keller *et al.* (2011) that the strengthening effect depends on the shape of the sample, and it is revealed as the ratio h/c (the thickness of the sample h to the grain size c) decreases from  $\sim 3$  or 4.

### 3.2.2. A large number of screw dislocations:

Now we allow an equally large number of screw dislocations of opposite signs to enter the crystal layer simultaneously. If  $h \gg c$ , we may neglect the end-effect near  $x_2 = 0$  and  $x_2 = h$ , and assume that the positive and negative dislocations are well-separated and distributed symmetrically about the straight line  $x_1 = c/2$ . In this case,  $\beta_{31} = 0$ , while

$$\beta_{32}(\mathbf{x}) \equiv \beta(\mathbf{x}) = \sum_{i=1}^{N} b\delta(\Lambda_i), \tag{3.14}$$

with  $\Lambda_i$  being the straight segments parallel to the  $x_1$ -axis with the middle points lying on the line  $x_1 = c/2$ . The regularized dislocation density is given by

$$\alpha_r(\mathbf{x}) = \sum_{i=1}^{N} b[\delta_{r_0}(\mathbf{x} - \mathbf{x}_i^+) - \delta_{r_0}(\mathbf{x} - \mathbf{x}_i^-)],$$

where  $\mathbf{x}_i^+$  and  $\mathbf{x}_i^-$  are the positions of the positive and the negative dislocations, respectively (the end-points of  $\Lambda_i$ ). Thus, the dislocation density is a piecewise constant and fast-changing function of the coordinates. We further assume that function  $\alpha_r(\mathbf{x})$  is locally double-periodic, with the characteristic period being much smaller than c. Following Berdichevsky (2017), we split the regularized dislocation density into the average dislocation density denoted by  $\check{\alpha}_r$  and the fluctuation denoted by  $\acute{\alpha}_r$ 

$$\alpha_r = \ddot{\alpha}_r + \acute{\alpha}_r. \tag{3.15}$$

Here the averaging over the cell is defined as

$$\breve{\alpha}_r = \frac{1}{|C_x|} \int_{C_x} \alpha_r \mathrm{d}a,$$

where  $C_x$  is the periodic cell in the  $(x_1, x_2)$ -plane, while  $|C_x|$  denotes its area. Thus,  $\check{\alpha}_r$  is a slowly changing function of the coordinates. We call  $\rho^g = |\check{\alpha}_r|/b$  the density of excess dislocations (or average dislocation density). This decomposition gives rise to the decomposition of the stress function  $\Psi$  and the plastic slip  $\beta$  as well

$$\Psi = \check{\Psi} + \acute{\Psi},$$

$$\beta = \check{\beta} + \acute{\beta}.$$
(3.16)

Note that function  $\beta$  defined in (3.14) is non-periodic and equals the sum of generalized functions concentrated on the cut lines  $\Lambda_i$ . Therefore, the integral over  $C_x$  of  $\beta$  equals the sum of line integrals over those segments  $\Lambda_i$  lying within this cell. It is easy to see that (cf. (Nye, 1953))

$$\breve{\alpha}_r = \breve{\beta}_{,1}.$$

Inserting the decomposed dislocation density (3.15) and the decomposed stress function (3.16)<sub>1</sub> into the energy functional (3.11), we get  $J = J_1 + J_2$ , where

$$J_1 = \int_{\mathcal{A}} \left[ -\frac{1}{2}\mu \gamma^2 - \mu \gamma x_1 \breve{\alpha}_r + \frac{1}{2\mu} \left( \nabla \breve{\Psi} \right)^2 + \breve{\alpha}_r \breve{\Psi} \right] da,$$

56

while

$$J_{2} = \int_{\mathcal{A}} (-\mu \gamma x_{1} \acute{\alpha}_{r} + \acute{\alpha}_{r} \check{\Psi}) da + \int_{\mathcal{A}} \left( \frac{1}{\mu} \nabla \check{\Psi} \cdot \nabla \acute{\Psi} + \check{\alpha}_{r} \acute{\Psi} \right) da + \int_{\mathcal{A}} \left[ \frac{1}{2\mu} \left( \nabla \acute{\Psi} \right)^{2} + \acute{\alpha}_{r} \acute{\Psi} \right] da. \quad (3.17)$$

Based on this decomposition, the minimization of J splits into the minimization of  $J_1$  among  $\check{\Psi}$  and then  $J_2$  among  $\check{\Psi}$ , provided  $\check{\Psi}$  is known. It is easy to show that the negative minimum value of  $J_1$  coincides with the energy of average elastic strain

$$-\underline{J}_1 = \int_{\mathcal{A}} \frac{1}{2} \mu (\gamma - \breve{\beta})^2 da. \tag{3.18}$$

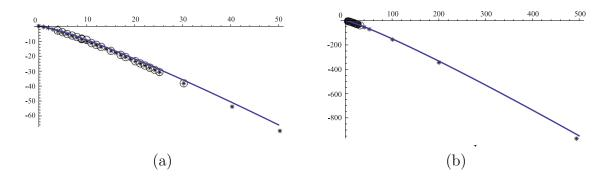


Figure 3.6.: (a) Dependence of interaction energy on the total number of dislocations N in continuum theory of dislocation (solid line) and Weinberger's numerical results (dots) (a) for small N and (b) for large N. Image reprinted by permission

Concerning the functional  $J_2$  we see that, due to the Euler equation for  $\check{\Psi}$ , the second integral in (3.17) vanishes. The first integral is small and can be neglected. The minimization of the last integral in (3.17) among periodic functions  $\check{\Psi}$  for the hexagonal periodic dislocation structure has been solved by Berdichevsky (2017). The combination of his result with (3.18) leads to the following statement: the energy density of crystal containing excess dislocations equals the sum of the energy density of macroscopic elastic strain and energy density of excess dislocations  $\psi_m(\rho^g)$ 

$$\psi = \frac{\mu}{2} \left( \gamma - \breve{\beta} \right)^2 + \psi_m(\rho^g),$$

where  $\rho^g = |\breve{\beta}_{,1}/b|$  and

$$\psi_m(\rho^g) = \mu b^2 \rho^g \left[ \psi^* + \frac{1}{4\pi} \ln \frac{1}{b^2 \rho^g} \right]. \tag{3.19}$$

Here  $\psi^*$  is a parameter depending on the periodic dislocation structure. For the hexagonal periodic dislocation structure  $\psi^* = -0.105$ . From (3.19), Berdichevsky (2017) extracted the interaction energy  $E_{int}$ , the subtraction of self-energy from the total energy of dislocations, as a function of dislocation number N and compared with the numerical results by Weinberger (2011) as shown in Fig. 3.6. For the number of

dislocations in the range between  $0 \sim 500$ , the results by two methods match well. However, the formula (3.19) has an advantage of low cost in computation, even if the crystal possesses large numbers of dislocation. Note that concerning the practical dislocation density is  $10^{14} \text{m}^{-2} \sim 10^{16} \text{m}^{-2}$  and the cross-section area of the sample is  $10 \mu \text{m} \times 10 \mu \text{m}$ , there are thousands of dislocations in crystals.

### 3.2.3. Extrapolation of the energy density of excess dislocations:

According to (3.19), the dimensionless energy density of excess dislocations can be written as

$$f(y) \equiv \psi_m/\mu = y(\psi^* - \frac{1}{4\pi} \ln y),$$
 (3.20)

where  $y = b^2 \rho^g$  is the dimensionless dislocation density. The plot of this function for  $y \in (0,1)$  is shown in Fig. 3.7. Function (3.20) possesses three remarkable properties.

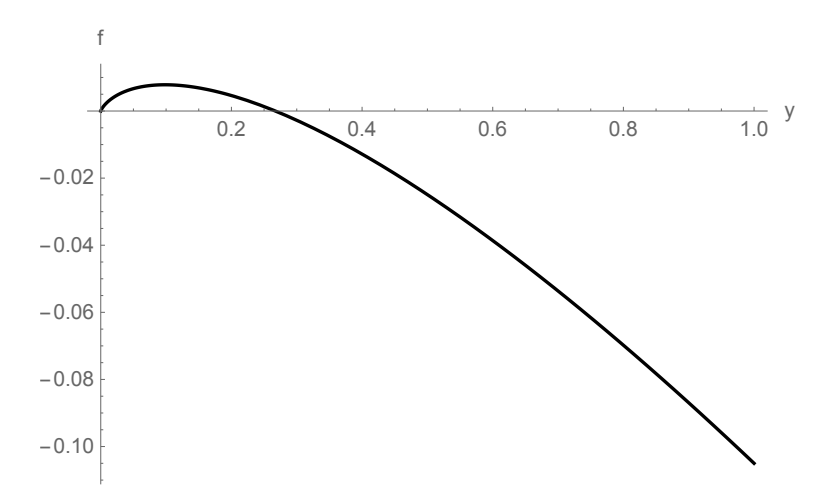


Figure 3.7.: Dimensionless energy density  $f = \psi_m/\mu$  versus dimensionless dislocation density  $y = b^2 \rho^g$ .

First,  $f'(0) = \infty$ . Second, f(y) is concave. Third, f(y) tends to  $-\infty$  when  $y \to \infty$ . These properties make the application of (3.20) to the determination of average plastic slip via energy minimization within the continuum approach problematic. For the well-posedness of the boundary value problems within the continuum approach requires the convexity of the energy density and the regularity of its derivative with respect to  $\rho^g$  (the latter is needed for the regularity of the back-stress). Looking more closely at the assumptions made in deriving formula (3.19), we see that these assumptions can be violated for the extremely small or large dislocation densities. Such extreme values of dislocation densities may occur near the head and the tail of the dislocation-free zone, so the local periodicity is no longer valid there. Therefore the energy density (3.19) must be extrapolated to these extremely small or large dislocation densities.

We propose the following extrapolation for the free energy density

$$\psi_m(\rho^g) = \mu b^2 \rho^g \left( \psi^* + \frac{1}{4\pi} \ln \frac{1}{k_0 + b^2 \rho^g} \right) + \frac{1}{8\pi} \mu k_1 (b^2 \rho^g)^2.$$
 (3.21)

with  $k_0$  and  $k_1$  being two new material constants. The small constant  $k_0$  corrects the behavior of the derivative of energy at  $\rho^g = 0$ , while the last term containing  $k_1$  corrects the behavior of the energy at large density of the excess dislocations. We choose  $k_0$  and  $k_1$  so that: (i) the energy density is close to the asymptotic exact energy density for moderate dislocation densities, (ii)  $\psi_m(\rho^g)$  is the convex function for all positive  $\rho^g$ . The latter requirement guarantees the existence of the energy minimizer. To investigate the convexity, we compute the second derivative of

$$f(y) \equiv \psi_m / \mu = y \left( \psi^* + \frac{1}{4\pi} \ln \frac{1}{k_0 + y} \right) + \frac{1}{8\pi} k_1 y^2$$
 (3.22)

as function of  $y = b^2 \rho^g$ . The simple calculation shows that

$$\frac{d^2f}{dy^2} = \frac{k_1y^2 + (2k_0k_1 - 1)y + k_1k_0^2 - 2k_0}{4\pi(k_0 + y)^2}.$$

For function  $\psi_m$  to be convex, the numerator must be positive for y > 0. Since the roots of this quadratic function are

$$y_{1,2} = \frac{1 - 2k_0k_1 \pm \sqrt{1 + 4k_0k_1}}{2k_1},$$

it is sufficient to require the largest root to be negative. This gives the following constraint for the coefficients  $k_0$  and  $k_1$ 

$$k_0 k_1 > 2$$
.

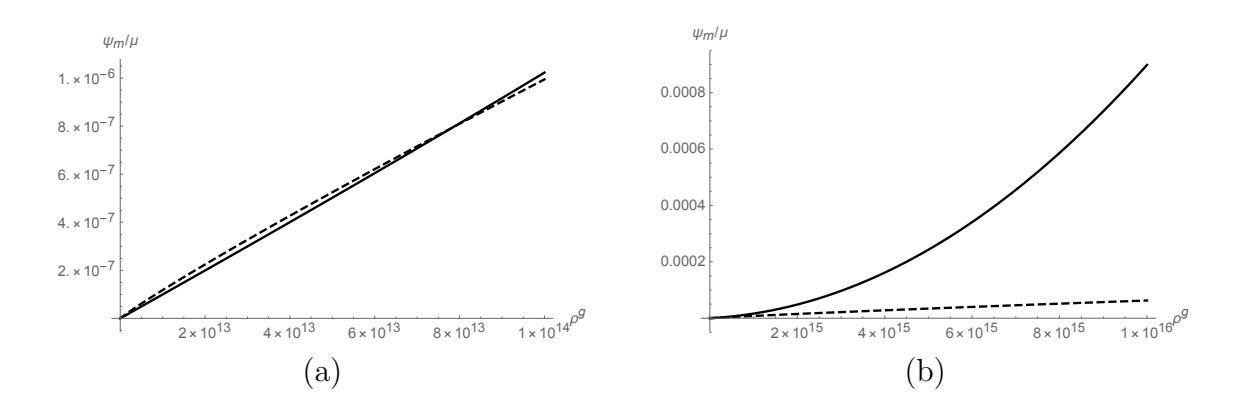


Figure 3.8.: The dimensionless energy density  $\psi_m/\mu$  versus the density of excess dislocations  $\rho^g$ : (i) (3.19) (dashed line), (ii) (3.21) (bold line).

Fig. 3.8 shows the comparison between two dimensionless energy densities  $\psi_m/\mu$  defined in accordance with (3.19) and (3.21) within the range  $\rho^g \in (0, 10^{14}/\text{m}^2)$  (on the left) and the range  $\rho^g \in (0, 10^{16}/\text{m}^2)$  (on the right). Here we choose  $b = 10^{-10}\text{m}$ ,  $k_0 = 10^{-6}$ ,  $k_1 = 2.1 \times 10^6$ . We see that the two energy densities are nearly the same in the range  $\rho^g \in (0, 10^{14}/\text{m}^2)$ , but differ essentially for  $\rho^g$  larger than  $10^{14}/\text{m}^2$ .

# 3.3. Anti-plane Constrained Shear Deformation and Numerical Simulations

### Thermodynamic dislocation theory in anti-plane shear deformation:

Now let us briefly go through the thermodynamic dislocation theory discussed in Sec. 2.3.3, and incorporate the formula for the energy density in it. We restrict ourself to the isothermal processes, so the kinetic-vibrational temperature T is assumed to be constant and can be dropped in the list of arguments of the free energy density. Our main assumption for the free energy density is

$$\psi = \frac{1}{2}\mu(\gamma - \check{\beta})^2 + \gamma_D \rho^r + \psi_m(\rho^g) - \chi(-\rho \ln(a^2 \rho) + \rho)/L, \tag{3.23}$$

where  $\rho = \rho^r + \rho^g$  is the total density of dislocations, and a the mean distance between dislocations in the saturated state. The first term in (3.23) describes the energy density of crystal due to the macroscopic elastic strain, and the breve () over  $\beta$  will be omitted for short from the average plastic slip. The second term is the energy density of redundant dislocations, with  $\gamma_D$  being the energy of the dislocation dipole per unit length. The third term is the energy density of excess dislocations, where  $\psi_m(\rho^g)$  is the extrapolated energy density taken in accordance with (3.21). The last term has been introduced by Langer (2016), with  $S_C = -\rho \ln(a^2 \rho) + \rho$  being the configurational entropy of dislocations. With this free energy density, we can now write down the energy functional of the crystal

$$I[\beta(\mathbf{x},t),\rho^r(\mathbf{x},t),\chi(\mathbf{x},t))] = \int_{A} \psi(\varepsilon^e,\rho^r,\rho^g,\chi) da.$$
 (3.24)

Note that the average plastic slip satisfies the kinematic boundary condition

$$\beta(0, x_2, t) = \beta(c, x_2, t) = 0. \tag{3.25}$$

Under the increasing overall shear strain  $\gamma(t)$ , the shear stress also increases, and when it reaches the Taylor stress, dislocation dipoles dissolve into freely moving dislocations. The latter dislocations move under the action of shear stress until they are trapped again by dislocations of opposite sign. During this motion, dislocations always experience the resistance causing the energy dissipation. As proposed before, the dissipation potential is in the form

$$D(\dot{\beta}, \dot{\rho}, \dot{\chi}) = \tau_Y |\dot{\beta}| + \frac{1}{2} d_\rho \dot{\rho}^2 + \frac{1}{2} d_\chi \dot{\chi}^2, \tag{3.26}$$

where  $\tau_Y$  is the flow stress during plastic yielding,  $d_{\rho}$  and  $d_{\chi}$  are given functions in (2.51). The first term in (3.26) is the plastic power which is assumed to be linear with respect to the plastic slip rate (Puglisi & Truskinovsky, 2005). The other two terms describe the dissipation caused by the multiplication of dislocations and the increase of configurational temperature (Langer *et al.*, 2010).

Since the dislocation mediated plastic flow is an irreversible process, we derive the governing equations from the following variational principle: the true average plastic slip  $\check{\beta}(\mathbf{x},t)$ , the true density of redundant dislocations  $\check{\rho}^r(\mathbf{x},t)$ , and the true configurational temperature  $\check{\chi}(\mathbf{x},t)$  obey the variational equation

$$\delta I + \int_{\mathcal{A}} \left( \frac{\partial D}{\partial \dot{\beta}} \delta \beta + \frac{\partial D}{\partial \dot{\rho}} \delta \rho + \frac{\partial D}{\partial \dot{\chi}} \delta \chi \right) da = 0$$
 (3.27)

for all variations of admissible fields  $\beta(\mathbf{x},t)$ ,  $\rho^r(\mathbf{x},t)$ , and  $\chi(\mathbf{x},t)$  satisfying the constraints (3.25). Taking the variation of I with respect to three unknown functions  $\beta$ ,  $\rho^r$ , and  $\chi$  and requiring that Eq. (3.27) is satisfied for their admissible variations and in addition with (2.54), we get four equations

$$\tau + \frac{1}{b} (\varsigma \operatorname{sign} \beta_{,1})_{,1} - \tau_{Y} = 0,$$

$$\dot{\tau}_{Y} = \mu \left[ \frac{q_{0}}{t_{0}} - \frac{q(\tau_{Y}, \rho)}{t_{0}} \right],$$

$$\dot{\chi} = K_{\chi} \frac{\tau_{Y} q(\tau_{Y}, \rho)}{\mu t_{0}} \left[ 1 - \frac{\chi}{\chi_{0}} \right],$$

$$\dot{\rho} = k_{\rho} \frac{\tau_{Y}}{\gamma_{D}} \frac{q(\tau_{Y}, \rho)}{t_{0}} \left[ 1 - \frac{\rho}{\rho^{ss}(\chi)} \right],$$
(3.28)

where  $\tau = \mu(\gamma - \beta)$  is the shear stress, while  $\varsigma = \partial \psi / \partial \rho^g$ . Eq. (3.28)<sub>1</sub>, valid under the condition  $\dot{\beta} > 0$ , can be interpreted as the balance of microforces acting on dislocations, with the second term taken with minus sign being the back-stress. This equation is subjected to the Dirichlet boundary condition (3.25) while the other three equations are subjected to initial conditions. Eq. (3.28)<sub>2</sub> is a rate form of Hooke's law involving Orowan's equation and the kinetics of dislocation depinning mechanism represented by two formula,

$$q(\tau_Y, \rho) = b\sqrt{\rho} [f_P(\tau_Y, \rho) - f_P(-\tau_Y, \rho)],$$

$$f_P(\tau_Y, \rho) = \exp\left[-\frac{1}{\Theta} e^{-\tau_Y/\tau_T(\rho)}\right],$$
(3.29)

where  $\Theta$  is a dimensionless temperature given as  $\Theta = T/T_P$ . The rate of shear strain is expressed by  $\dot{\gamma} = q_0/t_0$  with  $t_0 = 10^{-12}$ s being the characteristic microscopic time scale. Note that in the absence of the back stress, the rate of plastic deformation  $\beta$  equals to  $q/t_0$ , but when the effect of excess dislocations taken into account,  $\beta$  is not necessarily so. Eq.  $(3.28)_3$  is the equation of motion for the effective (configurational) temperature  $\chi$ . It is a statement of the first law of thermodynamics for the configurational subsystem.  $K_{\chi}$  is inversely proportional to the effective specific heat, and  $\chi_0$  the steady-state value of the effective temperature  $\chi$ . Eq. (3.28)<sub>4</sub> describes the flow of energy through the system of dislocations, as constrained by the second law of thermodynamics, where the second law implies that the difference between the power delivered to the system and the rate at which energy is stored in the form of dislocations is positive.  $\rho^{ss}(\chi) = (1/a^2)e^{-\gamma_D L/\chi}$  is the steady-state value of dislocation density  $\rho$  at given  $\chi$ , and the coefficient  $k_{\rho}$  denotes a dimensionless energy conversion factor. In general, the solution of the problem is sought by solving (3.28) that is a system of coupled partial differential equations satisfying the boundary conditions and initial conditions. However, in what follows of this chapter, we separate (3.28) into two parts, one part is the decoupled equation, and the other one is a system of ordinary differential equations, represented as follow

Decoupled equation

A system of equations

$$\begin{split} \tau + \frac{1}{b}(\varsigma \operatorname{sign}\beta_{,1})_{,1} - \tau_Y &= 0, \\ \dot{\tau}_Y &= \mu [\frac{q_0}{t_0} - \frac{q(\tau_Y, \rho)}{t_0}], \\ \dot{\chi} &= K_\chi \frac{\tau_Y q(\tau_Y, \rho)}{\mu \, t_0} [1 - \frac{\chi}{\chi_0}], \\ \dot{\rho} &= k_\rho \frac{\tau_Y}{\gamma_D} \frac{q(\tau_Y, \rho)}{t_0} [1 - \frac{\rho}{\rho^{ss}(\chi)}]. \end{split}$$

This separation has a benefit that reduces the complexity of the computation, from the partial differential equation to ordinary differential equation. Furthermore, by means of the separation, the onset of dislocation pile-ups can be analytically computed, and the size effect can be observed from the solving process. However, this method may lead to a tiny discrepancy from the exact solution, for  $\tau$  is no longer coupled with  $\tau_Y$  in each spatial coordinate. We suppose that due to the relatively large dislocation free zone (discussed later), the small region of non-uniformity of  $\beta$  affects little to the result.

We turn back to the single crystal layer undergoing an anti-plane shear deformation with the increasing overall shear strain  $\gamma(t)$  such that  $\dot{\gamma}$ =const. We aim at determining the average plastic slip, the densities of total and excess screw dislocations, the configurational temperature, and the stress-strain curve as a function of  $\gamma(t)$  by the thermodynamic dislocation theory proposed.

When the applied shear stress exceeds Taylor's stress, dislocation dipoles dissolve into freely moving dislocations. This applied stress drive the positive dislocations to the left and the negative ones to the right. After a short time, these free dislocations will either be trapped by the dislocations of opposite sign or be blocked near the grain boundaries acting as the obstacles. Thus, the dislocations of the same sign piling up against the left and right boundaries become excess dislocations occupying the boundary layers. We assume that the average plastic slip  $\beta$  is nearly uniform in the middle of the specimen. Neglecting a small non-uniformity of  $\beta$  in the boundary layers, we proceed the determination of  $\tau_Y$ ,  $\rho$ , and  $\chi$  in the first approximation to the solution of  $(3.28)_2 \sim (3.28)_4$ . After knowing  $\tau_Y$ ,  $\rho$ , and  $\chi$ , the variational equation (3.27) reduces to minimizing the following "relaxed" energy functional

$$I_{d} = hL \int_{0}^{c} \left[ \frac{1}{2} \mu \left( \gamma - \beta \right)^{2} + \mu f(b|\beta, 1|) + \tau_{Y}(\gamma) \beta \right] dx_{1}$$

among  $\beta$  satisfying (3.25), provided the sign of  $\beta$  is positive during the loading course. Here we neglect the end-effect at  $x_2 = 0$  and  $x_2 = h$  and assume that  $\beta$  depends only on  $x_1$ .

It is convenient to introduce the following dimensionless coordinates and quantities

$$\tilde{I}_d = \frac{I_d}{\mu b L h}, \quad \tilde{x} = \frac{x_1}{b}, \quad \tilde{c} = \frac{c}{b}, \quad g(\gamma) = \frac{\tau_Y(\gamma)}{\mu},$$

in terms of which the above functional becomes

$$I_d = \int_0^c \left[ \frac{1}{2} (\gamma - \beta)^2 + f(|\beta'|) + g(\gamma)\beta \right] dx,$$

where the prime ()'denotes the derivative of a function with respect to its argument. Since we shall deal only with the dimensionless quantities, the tilde over the variables,  $\tilde{()}$ , will be omitted for short and  $x_1$  is replaced by x for convenience. Up to an unessential constant, this functional can be reduced to

$$I_d = \int_0^c \left[ \frac{1}{2} (\gamma_l - \beta)^2 + f(|\beta'|) \right] dx, \tag{3.30}$$

where  $\gamma_l(\gamma) = \gamma - g(\gamma)$ .

Following the method of solution of the dislocation pile-up problem developed in Berdichevsky & Le (2007) (see also Le & Sembiring (2008a,b, 2009); Kochmann & Le (2009a); Kaluza & Le (2011); Le & Nguyen (2012, 2013); Le & Günther (2014); Le & Piao (2016); Le & Tran (2018)), we look for the minimizer in the form

$$\beta(x) = \begin{cases} \beta_1(x) & \text{for } x \in (0, l), \\ \beta_m & \text{for } x \in (l, c - l), \\ \beta_1(c - x) & \text{for } x \in (c - l, c), \end{cases}$$

where  $\beta_1(x)$  is an unknown increasing function,  $\beta_m$  is a constant, l an unknown length,  $0 \le l \le c/2$ , and  $\beta_1(l) = \beta_m$  at x = l. With this Ansatz, the functional becomes

$$I_d = 2 \int_0^l \left[ \frac{1}{2} (\gamma_l - \beta_1)^2 + f(\beta_1') \right] dx + \frac{1}{2} (\gamma_l - \beta_m)^2 (c - 2l).$$
 (3.31)

Varying this energy functional with respect to  $\beta_1$ , we get the equation

$$-f''(\beta_1')\beta_1'' + \beta_1 = \gamma_l(\gamma) \tag{3.32}$$

in the interval (0, l) which is subjected to the boundary conditions

$$\beta_1(0) = 0, \quad \beta_1(l) = \beta_m.$$

The variation of (3.31) with respect to l and  $\beta_m$  yield the two additional boundary conditions at x = l

$$\beta_1'(l) = 0,$$

$$2f'(0) - (\gamma_l(\gamma) - \beta_m)(c - 2l) = 0.$$
(3.33)

The first condition of (3.33) means the continuity of the dislocation density. It becomes clear from this construction that the above variational problem has no solution for the unmodified energy density f(y) from (3.20). For the modified function f(y) from (3.21), the variational problem is well-posed, and there exists a unique minimizer.

It is evident that  $l \to 0$  when  $\beta_m \to 0$ . In this limit, we can find the critical value  $\gamma_c$ , at which the excess dislocations begin to pile up, as the root of the equation

$$\gamma - g(\gamma) = 2(\psi^* - \frac{1}{4\pi} \ln k_0)/c. \tag{3.34}$$

This equation shows clearly the size effect. For  $\gamma > \gamma_c$ , the system (3.32)~(3.33) has a non-trivial solution. Since the integrand in functional (3.31) does not depend on x, Euler's equation (3.32) admits the first integral

$$\frac{1}{2}(\gamma_l - \beta_1)^2 + f(\beta_1') - \beta_1' f'(\beta_1') = C.$$

With f(y) from (3.22) and with the boundary conditions  $\beta'_1(l) = 0$  and  $\beta_1(l) = \beta_m$ , this equation reduces to

$$\frac{(\beta_1')^2}{4\pi} \left( k_1 - \frac{2}{k_0 + \beta_1'} \right) = (\gamma_l - \beta_1)^2 - (\gamma_l - \beta_m)^2.$$
 (3.35)

Due to the convexity of  $f(\beta')$ , the left-hand side of (3.35) is a monotonously increasing function of  $\beta'_1$ . Therefore, for each  $\beta_1 < \beta_m$ , there exists a unique root  $\beta'_1$  of this equation. The numerical solution of (3.35) will be discussed in the subsequent numerical simulation. After finding the average plastic slip, we calculate the average shear stress according to

$$\tau_a = \frac{1}{c} \int_0^c \mu(\gamma - \beta(x)) dx$$
$$= \frac{\mu}{c} \left[ \gamma c - 2 \int_0^l \beta_1(x) dx - \beta_m(c - 2l) \right]. \tag{3.36}$$

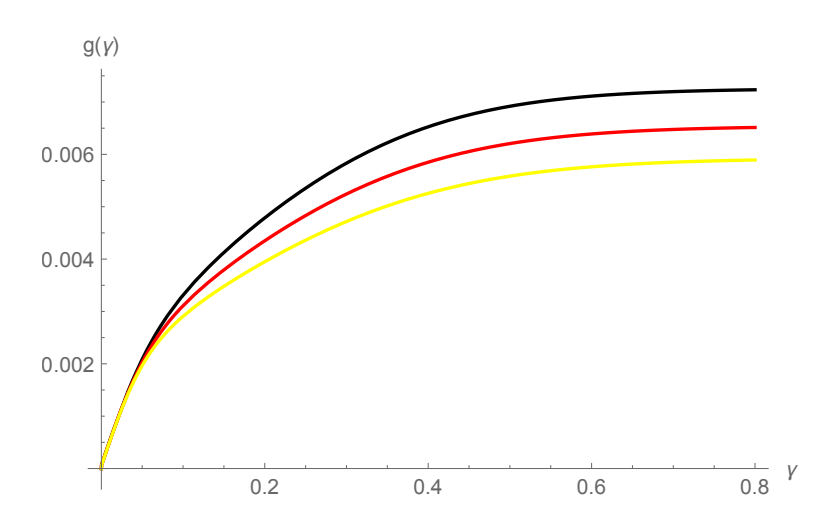


Figure 3.9.: Functions  $g(\gamma) = \tau_Y(\gamma)/\mu$ : (i)  $\tilde{q}_0 = 10^{-12}$  (black), (ii)  $\tilde{q}_0 = 10^{-14}$  (red), (i)  $\tilde{q}_0 = 10^{-16}$  (yellow).

### Numerical simulations:

Assume that the crystal is loaded with the constant shear strain rate  $\dot{\gamma}$ . As discussed, the first task is then to solve the system  $(3.28)_2 \sim (3.28)_4$ . Since the shear strain rate  $\dot{\gamma}$  is constant and only  $g(\gamma) = \tau_Y(\gamma)/\mu$  is required for the next task, we choose  $\gamma$  as the independent variables and rewrite this system of equations in terms of the following dimensionless quantities

$$g(\gamma) = \frac{\tau_Y(\gamma)}{\mu}, \quad \tilde{\rho} = a^2 \rho, \quad \tilde{\chi} = \frac{\chi}{e_D}, \quad \tilde{\rho}^{ss}(\tilde{\chi}) = e^{-1/\tilde{\chi}}.$$

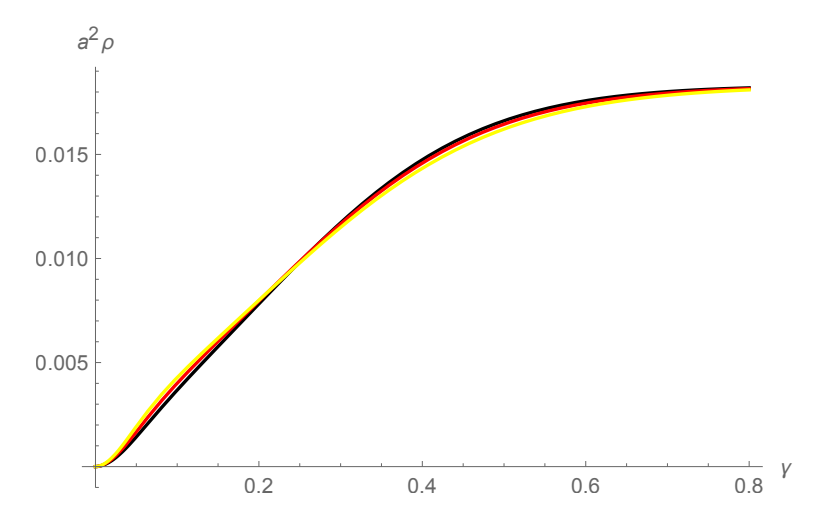


Figure 3.10.: Normalized total density of dislocations  $\tilde{\rho}(\gamma) = a^2 \rho$ : (i)  $\tilde{q}_0 = 10^{-12}$  (black), (ii)  $\tilde{q}_0 = 10^{-14}$  (red), (i)  $\tilde{q}_0 = 10^{-16}$  (yellow).

The system of ODEs becomes

$$\frac{\mathrm{d}g}{\mathrm{d}\gamma} = 1 - \frac{\tilde{q}(g,\tilde{\rho})}{\tilde{q}_0}, 
\frac{\mathrm{d}\tilde{\chi}}{\mathrm{d}\gamma} = K_{\chi}g\frac{\tilde{q}(g,\tilde{\rho})}{\tilde{q}_0} \left[ 1 - \frac{\tilde{\chi}}{\tilde{\chi}^{ss}(\tilde{q})} \right], 
\frac{\mathrm{d}\tilde{\rho}}{\mathrm{d}\gamma} = \frac{K_{\rho}g}{\tilde{\nu}(\Theta,\tilde{\rho},\tilde{q}_0)^2} \frac{\tilde{q}(g,\tilde{\rho})}{\tilde{q}_0} \left[ 1 - \frac{\tilde{\rho}}{\tilde{\rho}^{ss}(\tilde{\chi})} \right].$$
(3.37)

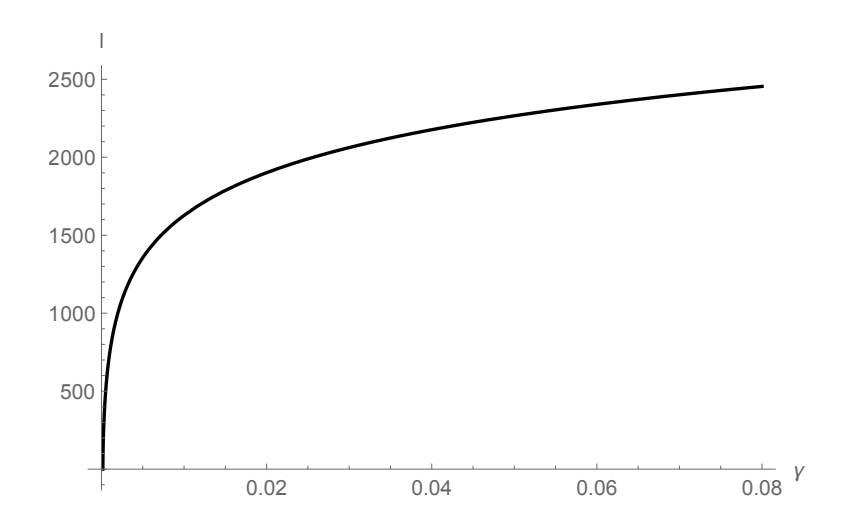


Figure 3.11.: Relative thickness of the boundary layers  $l(\gamma)$ .

Here  $\tilde{q}_0 = (a/b)\dot{\gamma}t_0$ ,  $r = (b/a)\mu_T/\mu$  and  $K_\rho$  is a new dimensionless conversion factor that proportional to  $k_\rho$  (see (2.79) and (2.80) in Sec. 2.3.3). For the loading process, we take

$$\begin{split} \tilde{q}(g,\tilde{\rho}) &= \sqrt{\tilde{\rho}} \exp\left[-\frac{1}{\Theta} e^{-g/(r\sqrt{\tilde{\rho}})}\right], \\ \tilde{\nu}(\Theta,\tilde{\rho},\tilde{q}_0) &= \ln\left(\frac{1}{\Theta}\right) - \ln\left[\frac{1}{2}\ln\left(\frac{\tilde{\rho}}{\tilde{q}_0^2}\right)\right]. \end{split}$$

Note that the second term in (3.29) is neglected here as small for this loading case. Let T=298 K. The parameters for copper at this room temperature are chosen as follows (Langer *et al.*, 2010)

$$r = 0.0323, \quad \Theta = 0.0073, \quad K = 350, \quad K_{\rho} = 96.87, \quad \tilde{\chi} = 0.25.$$

We choose also the initial conditions

$$g(0) = 0$$
,  $\tilde{\rho}(0) = 10^{-6}$ ,  $\tilde{\chi}(0) = 0.18$ .

The plots of functions  $g(\gamma)$  found by the numerical integration of (3.37) for three different resolved shear strain rates are shown in Fig. 3.9. It can be seen that  $g(\gamma)$  is rate-sensitive. Besides, it is also temperature-sensitive. Fig. 3.10 shows the evolution of the normalized total density of dislocations  $a^2\rho$  versus  $\gamma$  for the above shear strain rates.

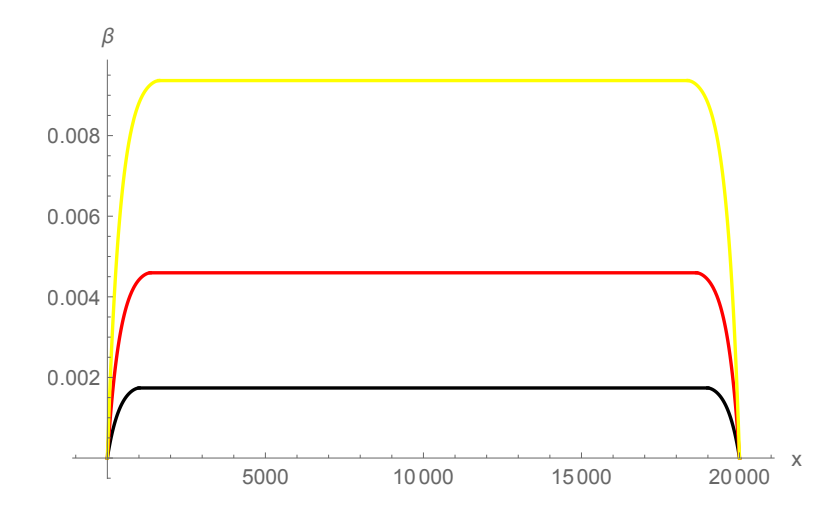


Figure 3.12.: The plastic slip  $\beta(x)$ : (i)  $\gamma = 0.002$  (black), (ii)  $\gamma = 0.005$  (red), (iii)  $\gamma = 0.01$  (yellow).

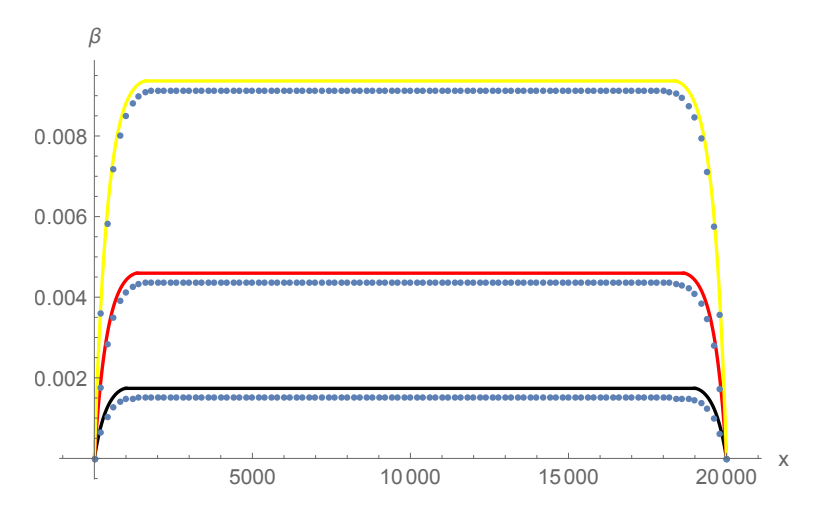


Figure 3.13.: Comparison of the plastic slip at  $\gamma = 0.002$ ,  $\gamma = 0.005$  and  $\gamma = 0.01$  by two methods: (i) Results by present method (solid line), (ii) Results by solving (3.28) (Le *et al.*, 2018) (dots).

Having found  $g(\gamma)$ , we turn now to the determination of the plastic slip  $\beta(x)$  from the energy minimization problem (3.30). In this problem, let us fix  $\tilde{q}_0 = 10^{-12}$  and choose the following parameters for copper

$$b = 0.255 \,\mathrm{nm}, \quad a = 2.55 \,\mathrm{nm}, \quad c = 5.1 \,\mu\mathrm{m}, \quad \nu = 0.355.$$

We also choose  $k_0 = 10^{-6}$ ,  $k_1 = 2.1 \times 10^6$ . With these parameters and with the above function  $g(\gamma)$  we find from equation (3.34) that  $\gamma_c = 0.00016$ . To solve equation (3.35), we reduce it to the following cubic equation

$$k_1q^3 + (k_0k_1 - 2)q^2 - 4\pi\alpha q - 4\pi k_0\alpha = 0,$$

with  $q = \beta'_1$  and  $\alpha = (\gamma_l - \beta_1)^2 - (\gamma_l - \beta_m)^2$ . Due to the convexity of  $f(\beta'_1)$  for the chosen set of parameters, this cubic equation has only one positive real root that we denote by

$$\beta_1' = p(\alpha) = p((\gamma_l - \beta_1)^2 - (\gamma_l - \beta_m)^2).$$

Integrating this equation numerically, we find

$$x = \int_0^{\beta_1} \frac{\mathrm{d}z}{p((\gamma_l - z)^2 - (\gamma_l - \beta_m)^2)},\tag{3.38}$$

which is the inverse function of  $\beta_1(x)$ . The length of the boundary layer equals

$$l(\beta_m) = \int_0^{\beta_m} \frac{dz}{p((\gamma_l - z)^2 - (\gamma_l - \beta_m)^2)}.$$
 (3.39)

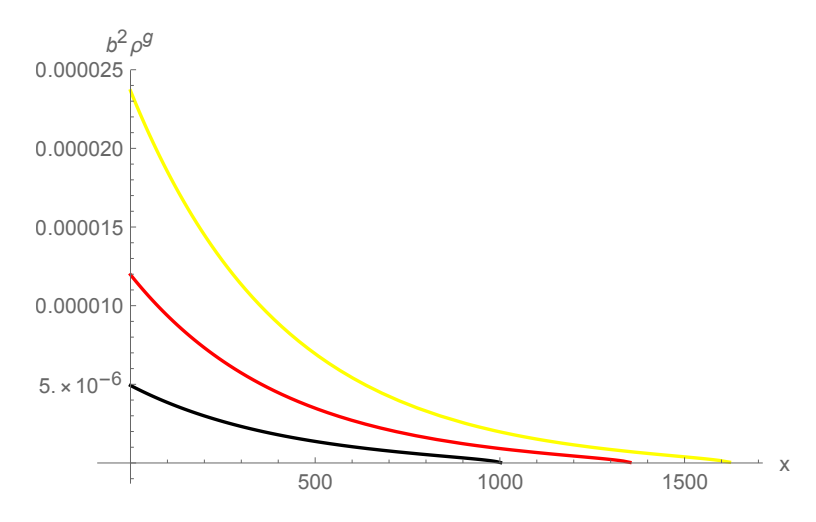


Figure 3.14.: The normalized density of excess dislocations  $b^2 \rho^g = \beta'$ : (i)  $\gamma = 0.002$  (black), (ii)  $\gamma = 0.005$  (red), (iii)  $\gamma = 0.01$  (yellow).

Substituting function  $l(\beta_m)$  from (3.39) into (3.33)<sub>2</sub>, we get an equation to determine  $\beta_m$  in terms of  $\gamma$ . Then, with this  $\beta_m(\gamma)$ , we find also the length  $l(\gamma) = l(\beta_m(\gamma))$  of the boundary layer. The plot of function  $l(\gamma)$  is shown in Fig. 3.11, from which it is seen that  $l(\gamma)$  is a monotonously increasing function of  $\gamma$ . However, for the whole range of  $\gamma \in (\gamma_c, 0.08)$  the relative thickness of the boundary layers l remains small compared to  $\bar{c} = 2 \times 10^4$ . Next, we find with (3.38) the plastic slip as a function of x at three chosen values of  $\gamma > \gamma_c$ . Their plots are shown in Fig. 3.12. We see that the plastic slip is constant in the middle of the specimen, and changes rapidly only in two thin boundary layers where the positive and negative excess dislocations pile up against the grain boundaries. Le & Tran (2018) plotted the plastic slip numerically by solving the system of partial differential equations (3.28). When we compare two results, one can observe that two simulations match well, as shown in Fig. 3.13, except the region

near the joint connecting the dislocation free-zone and dislocation pile-ups.

The number of excess dislocations increases with increasing shear strain. It is interesting to know the distribution of normalized density of excess dislocations  $b^2 \rho^g = \beta_1'$ . Their distributions at three chosen values of  $\gamma > \gamma_c$  in the left boundary layer are shown in Fig. 3.14. In the right boundary layer, the excess dislocations of opposite sign are symmetrically distributed. Using the implicit equation (3.38), we reduce equation (3.36) for the average dimensionless shear stress to

$$\tau/\mu = \gamma - \frac{1}{c} \left[ 2 \int_0^{\beta_m} \frac{\beta d\beta}{p((\gamma_l - \beta)^2 - (\gamma_l - \beta_m)^2)} + \beta_m(c - 2l) \right].$$

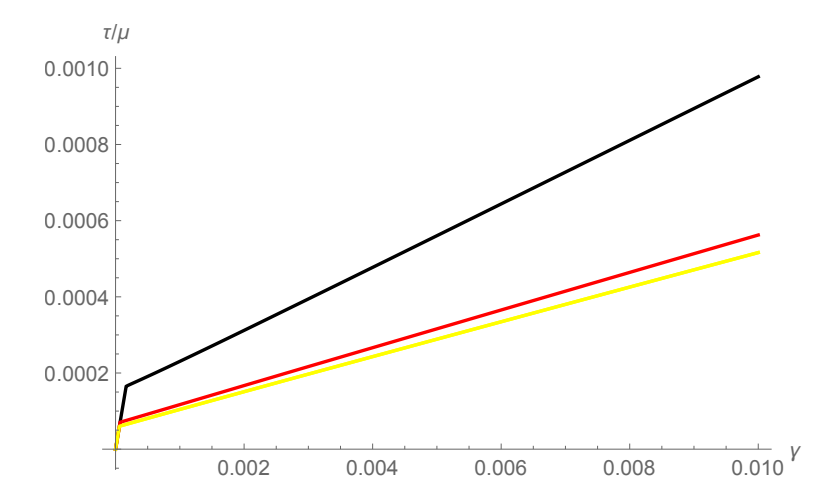


Figure 3.15.: Dimensionless average shear stress versus shear strain curve: (i) present theory: c = 5.1 micron (black), c = 51 micron (red) (ii) LBL-theory (yellow).

The dimensionless shear stress versus the shear strain curve computed in accordance with this equation is shown in Fig. 3.15 for two chosen widths of the sample: (i) c=5.1 micron (black), (ii) c=51 micron (red). For comparison, we also show the stress-strain curve  $g(\gamma)$  computed in accordance with the LBL-theory (yellow). We see that, in addition to the isotropic work-hardening caused by the redundant dislocations, there is a kinematic work-hardening caused by the pile-up of excess dislocations against the grain boundaries. The difference due to this kinematic work-hardening becomes remarkable at large strains. Besides, it is seen that this kinematic work-hardening decreases when the thickness of the specimen increases, thus exhibiting the size effect (cf. Berdichevsky & Le (2007); Le & Sembiring (2008a,b, 2009); Kochmann & Le (2009a); Kaluza & Le (2011); Le & Nguyen (2012, 2013); Le & Günther (2014); Le & Piao (2016); Le & Tran (2018)). For single crystals of macroscopic sizes, the kinematic work-hardening is negligibly small, and the stress-strain curve approaches that of LBL-theory.

Different boundary conditions are shortly discussed. The task we have investigated is solving the minimization problem of energy functional (3.24) subjected to the Dirichlet boundary conditions (3.25) at two ends. This boundary condition leads to dislocation pile-ups in the boundary layers, and a dislocation free zone forms between those two layers. Suppose now there is an imaginary boundary at  $x_1 = c/2$ , then this boundary

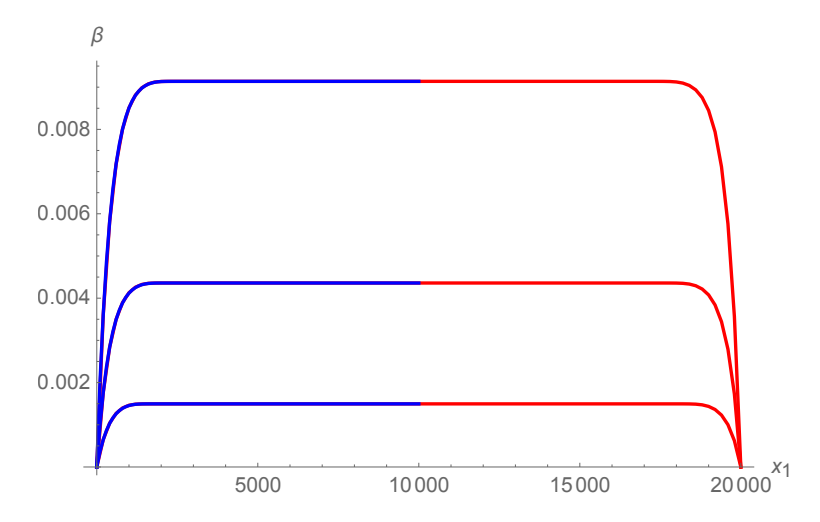


Figure 3.16.: Comparison of the plastic slip driven by Dirichlet-Dirichlet boundary condition in the interval  $x_1 \in (0, c)$  (red) and that by Dirichlet-Neumann boundary condition in the interval  $x_1 \in (0, c/2)$  (blue).

can be regarded as being subjected to homogeneous Neumann boundary condition because the number of dislocations is proportional to the curl of plastic slip, and  $\partial \beta(c/2, x_2)/\partial x_1 = 0$  implies the dislocation free condition at  $(c/2, x_2)$ . Comparing the plastic slip driven by two Dirichlet boundary conditions with that by Dirichlet-Neumann boundary conditions (3.40), one see from Fig. 3.16 that they coincide to each other. The blue curves indicate the plastic slip subjected to Dirichlet-Neumann boundary condition in the interval  $x_1 \in (0, c/2)$ , and the red curves are those presented in Fig. 3.12.

$$\beta(0, x_2) = 0, \quad \frac{\partial \beta(c/2, x_2)}{\partial x_1} = 0.$$
 (3.40)

Le & Tran (2018) investigated the problem of crystal sample undergoing the antiplane constrained shear with boundary condition (3.41), while it considered not only the loading process but also unloading, and further reloading in the opposite direction. As a consequence, the response of the stress-strain curve shows clearly the Bauschinger effect. Following the idea, we compare the Bauschinger effects by the same loading process (Loading, Reversal, and Reloading) but with different boundary conditions as (3.42),

Dirichlet-Dirichlet: 
$$\beta(0, x_2) = 0$$
,  $\beta(c, x_2) = 0$ , (3.41)

Dirichlet-Neumann: 
$$\beta(0, x_2) = 0$$
,  $\frac{\partial \beta(c, x_2)}{\partial x_1} = 0$ . (3.42)

The blue curve in Fig. 3.17 represents the Bauschinger effect caused by (3.41) and the red curve indicates that by (3.42). The flow stress  $\tau_Y/\mu$  versus  $\gamma$  (isotropic hardening) is plotted for comparison by the dashed black curve. It turns out that the crystal sample under (3.41), by which two pile-ups of dislocation take place, is hardened most and shows strongest Bauschinger effect, while it is less hardened for the sample under (3.42) because there is only one boundary that dislocations pill-ups.

3.4. Conclusion 69

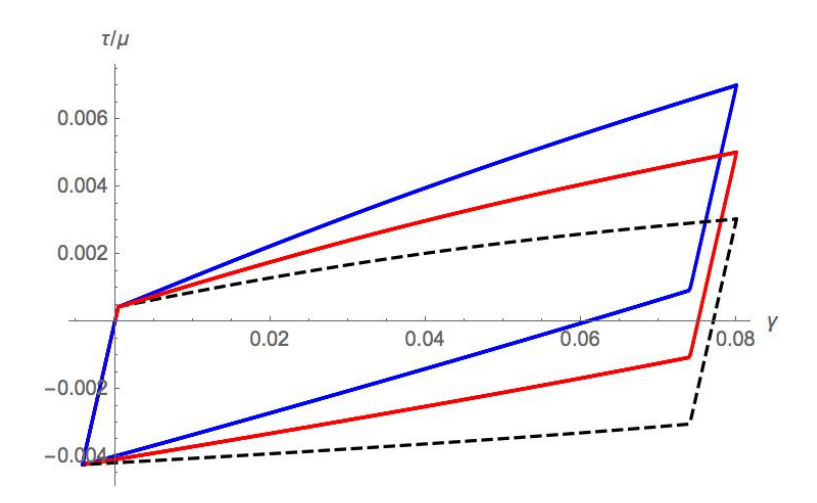


Figure 3.17.: Stress-strain curves at the strain rate  $\tilde{q_0} = 10^{-13}$ , for room temperature: (a) with Dirichlet-Dirichlet boundary conditions (blue), Eq. (3.41), (b) with Dirichlet-Neumann boundary conditions (red), Eq. (3.42), (c) flow stress  $\tau_Y/\mu$  versus strain  $\gamma$  (dashed black).

## 3.4. Conclusion

In this chapter, the asymptotically exact energy density of excess screw dislocation found by the averaging procedure is extrapolated to the extremely small or large dislocation density. This energy density is used in applying the thermodynamic dislocation theory for non-uniform plastic deformations of crystals undergoing anti-plane constrained shear. We decoupled the equation for microforce equilibrium from the system of governing equations under the assumption that the decoupling weakly influences the result. Under the corresponding deformation, the excess dislocations pile up in thin boundary layers near the grain boundaries. The stress-strain curves exhibit both the isotropic hardening and kinematic hardening and show the size effect. For single crystals of macroscopic sizes, the kinematic work-hardening is negligibly small, and the stress-strain curve approaches that of LBL-theory. At last, different boundary conditions are investigated, and its effect on the kinematic hardening and Bauschinger effect are studied.

# 4. Thermodynamic Dislocation Theory: Size Effect in Torsion

#### 4.1. Introduction

The purpose of this chapter is to explore the use of TDT for non-uniform plastic deformations (Le, 2018; Le & Piao, 2018; Le & Tran, 2018) in modeling twisted copper wires. Our challenge is to simulate the torque-twist curves that show the hardening behavior and the size effect. We also want to compare these torque-twist curves with those obtained by a simple extension of the LBL theory (Le et al., 2018) in which the excess dislocations are ignored, by the micro-torsion tests reported in (Liu et al., 2012) and by an empirical formula proposed therein. To make this comparison possible, we will need to identify from the experimental data obtained in (Liu et al., 2012) a list of material parameters for twisted copper wires. For this purpose, we will use the large scale least-squares analysis described in (Le et al., 2017, 2018; Le & Tran, 2017). The comparison shows that: (i) the LBL-theory cannot predict the torque-twist curves and the size effect for wires in the micrometer range, (ii) the empirical formula proposed in (Liu et al., 2012) is not based on the solution of the coupled boundary-value problem of dislocated crystal in equilibrium and therefore does not allow to find both the stress distribution and the dislocation densities inside the bar, (iii) the TDT provides an accurate prediction of the torque-twist curves and the size effect as well as enables one to find the distributions of stress, strain, and dislocation densities. Regarding the distribution of the excess dislocation density: It is still early to judge its validity by comparing it with the available results in the literature, neither with the experimental data obtained by the EBSD measurement (Ziemann et al., 2015), nor with the discrete dislocation dynamics simulations (Senger et al., 2011) (see the discussion in Section 4.4 and in the conclusion).

# 4.2. Theory of Torsion

## 4.2.1. Torsion of prismatic bar:

#### General cross-section:

A prismatic bar is a bar in which there is a uniform cross-section throughout. The deformation of the twisted bar is assumed to have rotation  $\omega z$  in the cross-section and warping for a non-circular cross-section in the bar axis. In torsion problem, we denote three axes of the Cartesian coordinate by x, y, z and the twist (the angle of twist per unit length) by  $\omega$ . The displacement components  $u_x$ ,  $u_y$  in the plane corresponding to

the rotation are then

$$u_x = -\omega yz, \quad u_y = \omega xz,$$

and the warping displacement  $u_z$  along z-direction is proportional to the twist, but independent of z,

$$u_z = \omega \varphi(x, y),$$

where  $\varphi(x,y)$  is referred to as the warping function. Then the strain components from these displacements are

$$\varepsilon_{xx} = \varepsilon_{yy} = \varepsilon_{zz} = 0,$$

and

$$\varepsilon_{xz} = \frac{1}{2}\omega \left(\frac{\partial \varphi}{\partial x} - y\right), \quad \varepsilon_{yz} = \frac{1}{2}\omega \left(\frac{\partial \varphi}{\partial y} + x\right),$$

$$\varepsilon_{xy} = \frac{1}{2}\left(\frac{\partial u_x}{\partial y} + \frac{\partial u_y}{\partial x}\right) = 0.$$

By constitutive equation for the isotropic linear elastic material, the stress components are

$$\begin{split} &\sigma_{xx} = \sigma_{yy} = \sigma_{zz} = \sigma_{xy} = 0, \\ &\sigma_{xz} = 2\mu\varepsilon_{xz} = \mu\omega\left(\frac{\partial\varphi}{\partial x} - y\right), \quad \sigma_{yz} = 2\mu\varepsilon_{yz} = \mu\omega\left(\frac{\partial\psi}{\partial y} + x\right). \end{split}$$

The equilibrium equation in the absence of body force is presented as

$$\frac{\partial \sigma_{xz}}{\partial x} + \frac{\partial \sigma_{yz}}{\partial y} = 0. \tag{4.1}$$

This equilibrium equation (4.1) requires the warping function to satisfy the Laplace's equation

$$\nabla^2 \varphi = 0, \quad \text{in} \quad \mathcal{A}$$

where the boundary  $\partial \mathcal{A}$  fulfills traction free condition on the surface,  $\boldsymbol{\sigma} \cdot \mathbf{n} = 0$ , such that

$$\left(\frac{\partial \varphi}{\partial x} - y\right) n_x + \left(\frac{\partial \psi}{\partial y} + x\right) n_y = 0, \tag{4.2}$$

for which

$$n_x = \frac{\mathrm{d}y}{\mathrm{d}s}, \quad n_y = -\frac{\mathrm{d}x}{\mathrm{d}s}.\tag{4.3}$$

Here, ds is an increment of arc length. An alternative way by introducing a stress function  $\Phi$  (Prandtl's stress function) can make the boundary condition much simpler,

$$\frac{\partial \Phi}{\partial y} = \sigma_{xz} = \mu \omega \left( \frac{\partial \varphi}{\partial x} - y \right), \quad -\frac{\partial \Phi}{\partial x} = \sigma_{yz} = \mu \omega \left( \frac{\partial \psi}{\partial y} + x \right). \tag{4.4}$$

Differentiating  $\partial \Phi/\partial y$  and  $\partial \Phi/\partial x$  with respect to x and y, respectively, in order to eliminate the warping function, and subtracting the two terms, we obtain a Poisson equation as

$$\nabla^2 \Phi = -2\mu\omega, \quad \text{in} \quad \mathcal{A}. \tag{4.5}$$

Substituting (4.3) and (4.4) into (4.2), we have

$$\frac{\partial \Phi}{\partial y} \frac{\partial y}{\partial s} + \frac{\partial \Phi}{\partial x} \frac{\partial x}{\partial s} = \frac{\partial \Phi}{\partial s} = 0,$$

which implies that the stress function  $\Phi$  must be subjected to a homogeneous Dirichlet boundary condition

$$\Phi = 0, \quad \text{on} \quad \partial \mathcal{A}.$$
(4.6)

Note that Poisson equation, (4.5) and (4.6), with different shapes of cross-section (ellipse, rectangular, triangular) can be solved by the use of Green's function. The torque is given by

$$T_c = \int_{\mathcal{A}} (\sigma_{xz} y - \sigma_{yz} x) da. \tag{4.7}$$

Inserting (4.4) into (4.7) and applying the integration by parts and (4.6), the torque in terms of the stress function is expressed as

$$T_c = 2 \int_A \Phi(x, y) da. \tag{4.8}$$

#### Special case with circular cross-section:

If the cross section is circular, the problem becomes simpler because the warping function vanishes. It is convenient to use circular cylindrical coordinate  $(r, \theta, z)$ , and the only non-zero component of the displacement is the circumferential displacement in the form

$$u_{\theta} = r\omega z$$
.

Therefore, the non-zero strain and stress components for isotropic linear material are

$$\varepsilon_{\theta z} = \varepsilon_{z\theta} = \frac{1}{2}r\omega, \quad \sigma_{\theta z} = \sigma_{z\theta} = \mu r\omega.$$

Since the torque represents the resultant of the shear stress distribution over the circular cross-section, it follows that

$$T_c = \int_{\mathcal{A}} \sigma_{\theta z} r da = \int_{\mathcal{A}} \mu \omega r^2 da = 2\pi \int_0^R \mu \omega r^3 dr.$$
 (4.9)

#### 4.2.2. Configuration of screw dislocations in torsion:

In both bending and indentation indicated in Fig. 2.9, the edge dislocations are accumulated in order to accommodate the plastic deformation (Arsenlis, 1999; Nix &

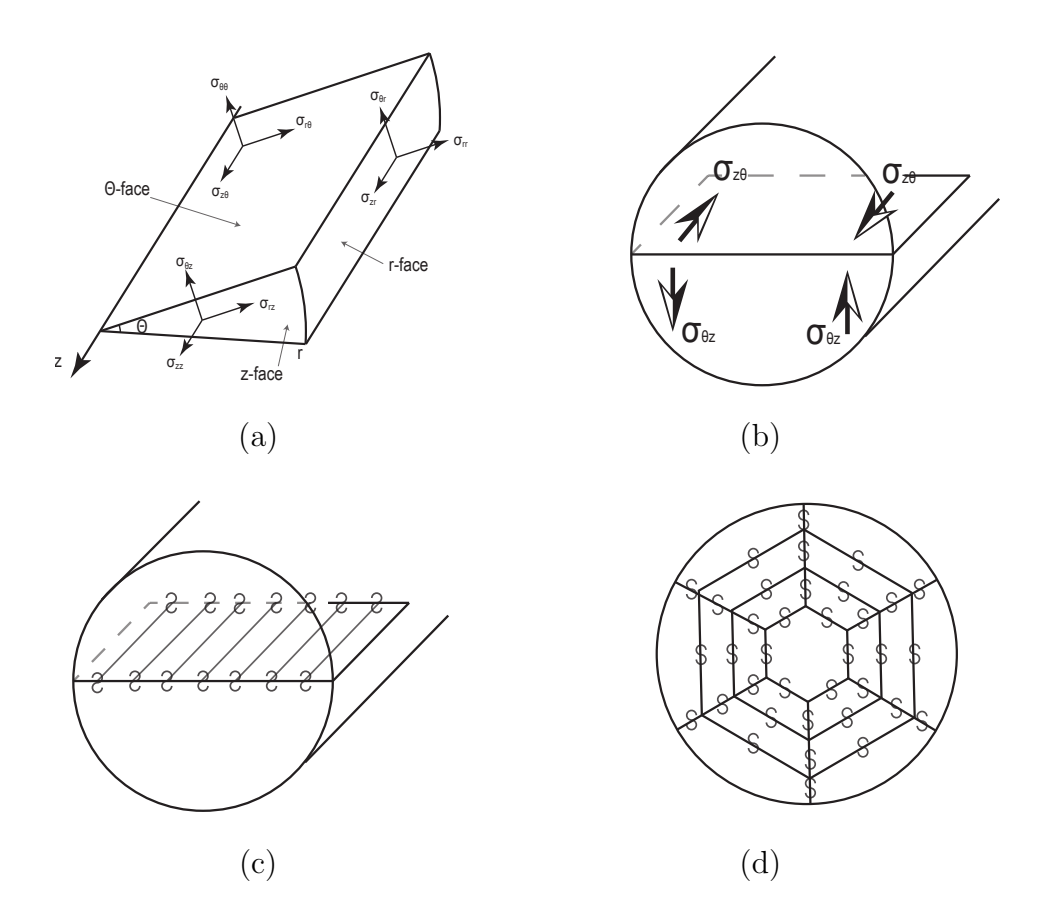


Figure 4.1.: Configurations of excess screw dislocation in torsion loaded wire: (a) stress components in the cylindrical polar coordinate, (b) Stress acting on planes parallel and perpendicular to wire axis, (c) Screw dislocations parallel to wire axis on  $\theta$ -face (Weertman, 2002), (d) Screw dislocations perpendicular to wire axis on z-face (Weertman, 2002).

Gao, 1997), and the images of the plastic deformation in both tests were observed by scanning electron microscopy (SEM) (Demir et al., 2010a; Moser et al., 2005). In torsion, it is believed that excess dislocations coaxial with the wire axis appear in the form of the screw (Gao et al., 1999). Weinberger & Cai (2010) reported that for properly oriented nanowire under torsion, the favored mechanism of plastic deformation is the Eshelby dislocations (Eshelby, 1953). However, there are different viewpoints that screw excess dislocations may lie in the planes perpendicular to the wire axis (Weertman, 2002). Fig. 4.1(a) shows the stress components in the cylindrical polar coordinate  $(r, \theta, z)$ , and Fig. 4.1(b) shows the non-zero components of a wire under torsion,  $\sigma_{\theta z}$ , and  $\sigma_{z\theta}$ , acting on the perpendicular (z-face) and parallel ( $\theta$ -face) planes to wire axis. Following Weertman (2002), screw dislocations may form a dislocation array on the plane parallel to the wire axis as Fig. 4.1(c) and a dislocation net on the plane perpendicular to the wire axis as Fig. 4.1(d). It was further stated that under the assumption that the solid possesses zero yield stress, the dislocations are driven into the center of the wire from the outer surface.

Senger et al. (2011) analyzed the evolution of dislocation microstructure in torsion loaded single-crystalline aluminum wires by discrete dislocation dynamics (DDD) simulations. Authors found that for wire axis oriented in the  $\langle 234 \rangle$ , which almost lie on the glide plane, screw dislocations roughly equivalent long with the sample height are

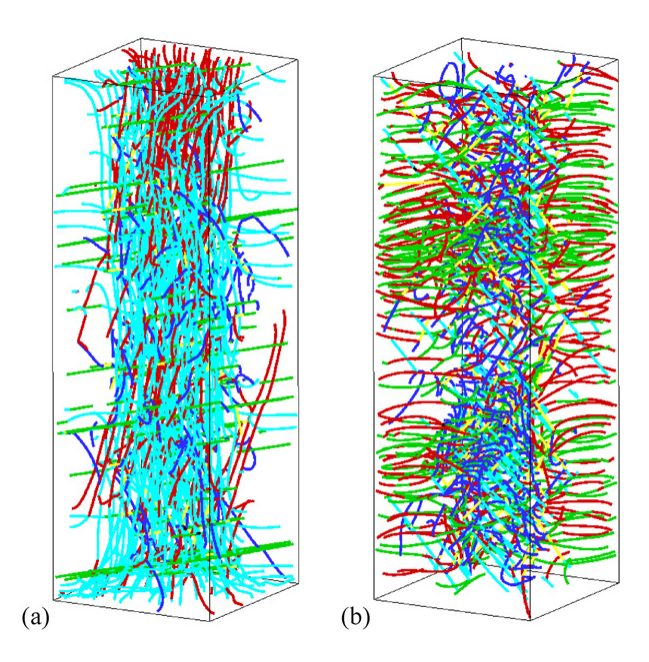


Figure 4.2.: Dislocation microstructure in the sample of micro-scale  $(1 \times 1 \times 3 \mu m^3)$ : (a) wire axis oriented in the  $\langle 234 \rangle$  which almost parallel to glide plane, (b) wire axis oriented in the  $\langle 100 \rangle$ . (Senger *et al.*, 2011). Images reprinted by permission

generated parallel to the wire axis as shown in Fig. 4.2(a). While when the wire is oriented in the  $\langle 100 \rangle$ , dislocations perpendicular to wire axis are observed as indicated in Fig. 4.2(b), where  $\langle \rangle$  refers to directions of the same type in Miller indices. One question may arise that how two configurations of dislocation affect the torque-twist response. In Fig. 4.3, the authors compared normalized torsion moment as a function of the plastic torsion angle  $\phi_{\rm pl}$  for two orientations (red:  $\langle 234 \rangle$  and blue:  $\langle 100 \rangle$ ). Fig. 4.3(a) indicates the case with cross slip activated, while Fig. 4.3(b) is the one without the cross slip behavior. As we can observe, despite different configurations of screw dislocation, the corresponding torque-twist curves look similar in two cases, except a small discrepancy appearing in the region of small-angle that the torque caused by screw dislocations perpendicular to wire axis is more significant than that parallel to the axis.

# 4.3. Thermodynamic Dislocation Theory in Torsion:

Suppose a thin polycrystalline copper wire with a circular cross-section  $\mathcal{A}$ , of radius R and length L, is subjected to torsion (see the wire with its cross-section in Fig. 4.4). As discussed, for this particular geometry of the wire and under the condition  $R \ll L$  it is natural to assume that the circumferential displacement is  $u_{\theta} = \omega r z$ , with  $\omega$  being the twist angle per unit length, while the displacement  $u_z$  does not depend on the warping function and is vanished. Thus, the total shear strain of the wire  $\gamma = 2\varepsilon_{\theta z} = \omega r$  and the shear strain rate  $\dot{\gamma} = \dot{\omega}r$  turn out to be non-uniform as they are linear functions of radius r.

Now, let this system be driven at a constant twist rate  $\dot{\omega} \equiv \varpi_0/t_0$ , where  $t_0$  is a

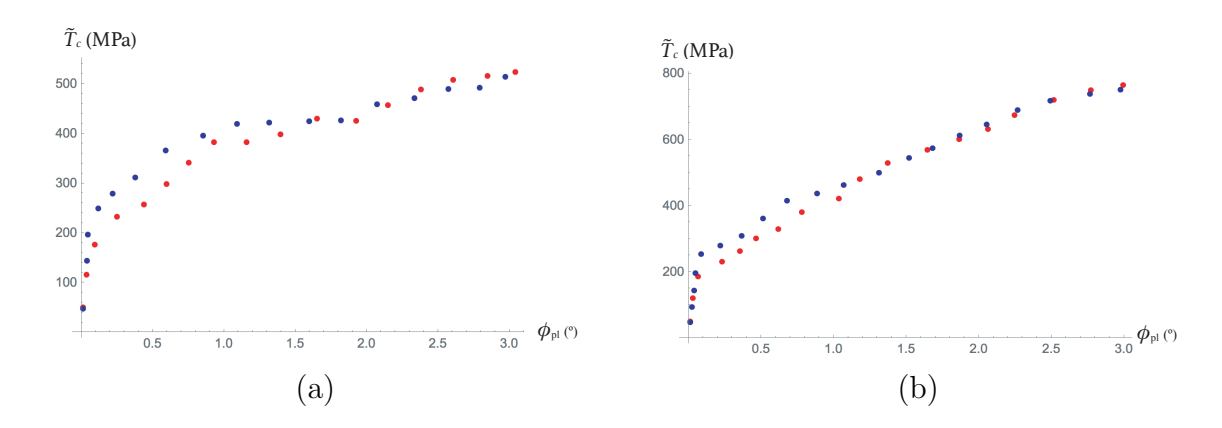


Figure 4.3.: Comparison of torque-twist curves by two different configuration of screw dislocations, red for  $\langle 234 \rangle$  (screw dislocations parallel to wire axis) orientation and blue for  $\langle 100 \rangle$  (screw dislocations perpendicular to wire axis):

(a) with the cross slip activated, (b) without the cross slip activated. The data are taken from (Senger *et al.*, 2011).

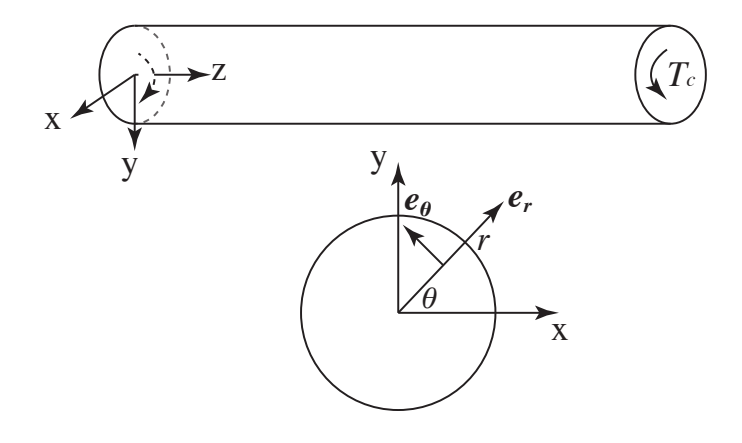


Figure 4.4.: Torsion of a wire.

characteristic microscopic time scale. Since the system experiences a steady-state torsional deformation, we can replace the time t by the total twist angle (per unit length)  $\omega$  so that

$$t_0 \partial/\partial t \to \varpi_0 \partial/\partial \omega.$$
 (4.10)

In what follows, we build up equations of motion for wires under torsion based on Sec. 2.3.3.

#### The microforce equilibrium:

The equation for the plastic distortion  $\beta$  reads

$$\tau - \tau_B - \tau_Y = 0, \tag{4.11}$$

with  $\tau(r,t) = \sigma_{\theta z}$  being the shear stress. This equation is the equilibrium of microforces acting on excess dislocations, where the first term  $\tau = \mu(\gamma - \beta) = \mu(\omega r - \beta)$  is the applied shear stress, the second term the back-stress due to the interaction of excess dislocations, and the last one the flow stress. Note that if the inertia of dislocations

is essential and should be included, dynamic non-local flow rules are suggested where the left-hand side of Eq. (4.11) is used as the driving force (Le & Stumpf, 1996). In this sense, this equation can be interpreted as a balance of micromomentum for stationary plastic distortion fields. Since dislocations can reach the free boundary and form an array of dislocations there, we add the surface energy (Huang *et al.*, 2010; Le & Nguyen, 2012) to the energy functional (per unit length)

$$I = \int_{\mathcal{A}} \psi(\gamma - \beta, \rho^r, \rho^g, \chi) da + \int_{\partial \mathcal{A}} \Gamma(\beta) ds,$$

where

$$\psi(\gamma - \beta, \rho^r, \rho^g, \chi) = \frac{1}{2}\mu(\gamma - \beta)^2 + \gamma_D \rho^r + \psi_m(\rho^g) - \chi(-\rho \ln(a^2 \rho) + \rho)/L$$

is the bulk free energy density of macroscopically isotropic material, with  $\gamma_D = e_D/L$ , and

$$\Gamma(\beta) = \frac{\mu b}{4\pi} \beta \left( \ln \frac{e\beta_*}{\beta} + \frac{1}{2} \varkappa \beta \right) \tag{4.12}$$

the modified Read-Shockley surface energy density of an array of screw dislocations (having the surface dislocation density  $\beta/b$  and forming the twist boundary). The logterm in (4.12) was obtained by Read & Shockley (1950), while the  $\beta^2$ -term by Vitek (1987). The state variables that describe this system are the elastic strain  $\gamma - \beta$ , the densities of redundant dislocations  $\rho^r$  and excess dislocations  $\rho^g$ , and the disorder temperature  $\chi$  (cf. (Langer, 2016; Kröner, 1992)). The ordinary temperature is discarded from the state variables, for it is assumed to be constant. All four quantities,  $\gamma - \beta$ ,  $\rho^r$ ,  $\rho^g$ , and  $\chi$ , are functions of r and  $\omega$ . We also introduce the dissipation function

$$D(\dot{\beta}, \dot{\rho}, \dot{\chi}) = \tau_Y \dot{\beta} + \frac{1}{2} d_\rho \dot{\rho}^2 + \frac{1}{2} d_\chi \dot{\chi}^2.$$

We require that the equations (4.11), (4.23) and (4.25) obey the variational equation, (see Sec. 2.3.2)

$$\delta I + \int_{\mathcal{A}} \left( \frac{\partial D}{\partial \dot{\beta}} \delta \beta + \frac{\partial D}{\partial \dot{\rho}} \delta \rho + \frac{\partial D}{\partial \dot{\chi}} \delta \chi \right) da = 0.$$
 (4.13)

Let us show the derivation of (4.11) and corresponding boundary condition at the free boundary r=R by solving the variational equation (4.13) with regard to plastic slip  $\beta$  using the standard calculus of variations. Eliminating the term containing the variation of  $\rho^r$  and  $\chi$  from (4.13) and divided by  $2\pi$ , we obtain

$$\int_{0}^{R} \left[ \mu \left( \beta - r \omega \right) \delta \beta + \tau_{Y} \delta \beta + \left( \frac{\partial \psi_{m}}{\partial \rho^{g}} + \chi \ln(a^{2} \rho) + d_{\rho} \dot{\rho} \right) \delta \rho^{g} \right] r dr + r \left. \frac{\partial \Gamma}{\partial \beta} \right|_{r=R} \delta \beta - r \left. \frac{\partial \Gamma}{\partial \beta} \right|_{r=0} \delta \beta = 0. \quad (4.14)$$

We assume that the active slip planes are perpendicular to the vector  $\mathbf{e}_{\theta}$ , then all screw excess dislocations lie parallel to the wire axis, and the only non-zero component of the tensor of dislocation density,  $\alpha_{ij} = \epsilon_{jkl}\beta_{il,k}$ , is

$$\alpha_{zz} = \beta_{,r} + \beta/r.$$

Supposed that  $dB = \alpha_{zz}da$  repents the resultant Burgers vector of an infinitesimal area da of the cross-section, the areal screw dislocation density becomes

$$\rho^g = \frac{1}{b} \left| \alpha_{zz} \right| = \frac{1}{b} \left| \beta_{,r} + \frac{\beta}{r} \right|, \tag{4.15}$$

where b is the magnitude of the Burgers vector. The variation with respect to  $\rho^r$  from (2.44), which is free from the coordinate system, follows the relation,

$$\chi \ln(a^2 \rho) + d_\rho \dot{\rho} = -\gamma_D, \tag{4.16}$$

Inserting (4.15) and (4.16), as well as the boundary condition at the center  $\beta(0) = 0$ , into (4.14), the functional becomes

$$\int_{0}^{R} \left[ \mu \left( \beta - r \omega \right) + \tau_{Y} - \frac{1}{b} \frac{\partial^{2} \psi_{m}}{\partial (\rho^{g})^{2}} \frac{\partial \rho^{g}}{\partial r} \right] \delta \beta \, r \mathrm{d}r + r \left[ \frac{1}{b} \left( \frac{\partial \psi_{m}}{\partial \rho^{g}} - \gamma_{D} \right) + \frac{\partial \Gamma}{\partial \beta} \right] \Big|_{r=R} = 0.$$

Suppose that  $\beta$  takes positive, which describes the loading process only, then

$$\frac{\partial \rho^g}{\partial r} = \frac{1}{b} (\beta'' + \beta'/r - \beta/r^2). \tag{4.17}$$

As a result, from the variation of  $\beta$  on the interval (0, R), we obtain (4.11) and formula for back stress

$$\tau_B = -\frac{1}{b^2} \frac{\partial^2 \psi_m}{\partial (\rho^g)^2} (\beta_{,rr} + \beta_{,r}/r - \beta/r^2).$$

The free energy density of screw excess dislocations  $\psi_m$  has been developed in the previous chapter by extrapolating the Berdichevsky's energy at the extremely small or large dislocation densities to guarantee the existence of solution within TDT, and it is given by (see Sec. 3.2.3)

$$\psi_m(\rho^g) = \mu b^2 \rho^g \left( \psi^* + \frac{1}{4\pi} \ln \frac{1}{k_0 + b^2 \rho^g} \right) + \frac{1}{8\pi} \mu k_1 (b^2 \rho^g)^2, \tag{4.18}$$

with  $\psi^* = -0.105$ ,  $k_0$  being a small constant correcting the behavior of the derivative of energy at  $\rho_g = 0$ , and  $k_1$  another constant correcting the behavior of the energy at large densities of the excess dislocations. Using (4.18) we find that  $\tau_B$  is given by

$$\tau_B = -\mu b^2 \frac{k_1 \xi^2 + (2k_0 k_1 - 1)\xi + k_1 k_0^2 - 2k_0}{4\pi (k_0 + \xi)^2} (\beta_{,rr} + \beta_{,r}/r - \beta/r^2),$$

where  $\xi = b|\beta_{,r} + \beta/r|$ . The variation with respect to  $\beta$  on the surface from (4.13) gives rise to the natural boundary condition at r = R,

$$\left. \left( \frac{\partial \psi_m}{\partial \rho^g} + b \frac{\partial \Gamma}{\partial \beta} \right) \right|_{r=R} = \gamma_D.$$
(4.19)

With  $\psi_m$  from (4.18) and  $\Gamma$  from (4.12), we get

$$\frac{\partial \psi_m}{\partial \rho^g} = \mu b^2 \left[ -\frac{\xi}{4\pi (k_0 + \xi)} - \frac{\ln(k_0 + \xi)}{4\pi} + \frac{k_1 \xi}{4\pi} - 0.105 \right],$$

and

$$b\frac{\partial\Gamma}{\partial\beta} = \frac{1}{4\pi}\mu b^2 \left(\ln\frac{\beta_*}{\beta} + \varkappa\beta\right).$$

### Equation of motion for flow stress:

To derive the equations of motion for the system we begin with Hooke's law in rate form

$$\frac{\partial \tau}{\partial t} = \mu \left( \frac{\partial \gamma}{\partial t} - \frac{\partial \beta}{\partial t} \right),\tag{4.20}$$

with  $\beta(r,t) = 2\varepsilon_{\theta z}^p$  the plastic distortion, and  $\mu$  the shear modulus. Let us first ignore the excess dislocations. The central, dislocation-specific ingredient of TDT (Langer *et al.*, 2010) is the thermally activated depinning formula for  $q(\tau,\rho)/t_0$  representing the plastic distortion rate  $\dot{\beta}$  as a function of the stress  $\tau$  and the total dislocation density  $\rho$ 

$$\frac{q(\tau,\rho)}{t_0} = \frac{1}{t_0} b \sqrt{\rho} [f_P(\tau,\rho) - f_P(-\tau,\rho)], \tag{4.21}$$

where

$$f_P(\tau, \rho) = \exp\left[-\frac{1}{\Theta}e^{-\tau/\tau_T(\rho)}\right].$$

As argued in Langer et al. (2010), Eq. (4.21) is an Orowan relation of the form  $\dot{\beta} = \rho b v$  in which the speed of the dislocations v is given by the distance between them multiplied by the rate at which they are depinned from each other. That rate is approximated here by the activation terms  $f_P(\tau, \rho)$  and  $-f_P(-\tau, \rho)$ , in which the energy barrier  $e_P = k_B T_P$  (implicit in the scaling of  $\Theta = T/T_P$ ) is reduced by the stress-dependent factor  $e^{-\tau/\tau_T(\rho)}$ , where  $\tau_T(\rho) = \mu_T b \sqrt{\rho}$  is the Taylor stress with  $\mu_T$  being proportional to  $\mu$ . The pinning energy  $e_P$  is large, of the order of electron volts, so that  $\Theta$  is very small. As a result,  $q(\tau, \rho)$  is an extremely rapidly varying function of  $\tau$  and  $\Theta$ . This strongly nonlinear behavior is the key to understanding yielding transitions and shear banding as well as many other important features of crystal plasticity. For example, the extremely slow variation of the steady-state flow stress as a function of strain rate discussed in (Langer et al., 2010) is the converse of the extremely rapid variation of q as a function of  $\tau$  in Eq. (4.21).

Replacing  $\dot{\gamma}$  in Eq. (4.20) by  $(\varpi_0/t_0)r$ ,  $\dot{\beta}$  by  $q(\tau,\rho)/t_0$ , and the partial time derivative by  $(\varpi_0/t_0) \partial/\partial \omega$ , we arrive at

$$\frac{\partial \tau}{\partial \omega} = \mu \left[ r - \frac{q(\tau, \rho)}{\varpi_0} \right].$$

As mentioned before, for the theory ignoring the excess dislocations  $q(\gamma)/t_0$  equals the plastic distortion rate  $\dot{\beta}$ . However, if the excess dislocations are accounted for,  $q(\gamma)/t_0$  does not equal  $\dot{\beta}$ , and we associate (4.21) to the plastic shear rate caused by the depinning of redundant dislocations only. In this case, the equation for the flow stress in rate form is proposed as follows

$$\frac{\partial \tau_Y}{\partial \omega} = \mu \left[ r - \frac{q(\tau_Y, \rho)}{\varpi_0} \right]. \tag{4.22}$$

Here, the flow stress  $\tau_Y$  is interpreted as the stress required to separate redundant dislocations from each other.

#### Equation of motion for the dislocation density:

It has been shown in Sec. 2.3.2 that the variation of (4.13) with respect to  $\rho$  and  $\chi$  yields

two governing equations, provided the coefficients  $d_{\rho}$  and  $d_{\chi}$  appropriately chosen. The equation for the total dislocation density  $\rho = \rho^r + \rho^g$  describes the energy flow. It says that some fraction of the power delivered to the system by external driving force is converted into the energy of dislocations, and that that energy is dissipated according to a detailed-balance analysis involving the disorder temperature  $\chi$ . In terms of the twist angle  $\omega$ , this equation reads:

$$\frac{\partial \rho}{\partial \omega} = K_{\rho} \frac{\tau_{Y} q}{a^{2} \nu(\Theta, \rho, \varpi_{0} r)^{2} \mu \varpi_{0}} \left[ 1 - \frac{\rho}{\rho^{ss}(\chi)} \right], \tag{4.23}$$

with  $\rho^{ss}(\chi) = (1/a^2)e^{-e_D/\chi}$  being the steady-state value of  $\rho$  at given  $\chi$ ,  $e_D$  a characteristic formation energy for dislocations, and a denoting the average spacing between dislocations in the limit of infinite  $\chi$  (a is a length of the order of tens of atomic spacings). Note that Eq. (4.23) reduces to the equation proposed by Langer et~al. (2010) if the density of excess dislocations  $\rho^g$  vanishes. The coefficient  $K_\rho$  is an energy conversion factor that, according to arguments presented in (Langer et~al., 2010; Langer, 2017a), should be independent of both strain rate and temperature. The other function that appears in the prefactor in Eq. (4.23) is

$$\nu(\Theta, \rho, q_0) \equiv \ln\left(\frac{1}{\Theta}\right) - \ln\left[\ln\left(\frac{b\sqrt{\rho}}{q_0}\right)\right]. \tag{4.24}$$

#### Equation of motion for the effective temperature:

The equation for the disorder temperature  $\chi$  is a statement of the first law of thermodynamics for the configurational subsystem (Langer *et al.*, 2010):

$$\frac{\partial \chi}{\partial \omega} = K_{\chi} \frac{\tau_{Y} e_{D} q}{\mu \varpi_{0}} \left( 1 - \frac{\chi}{\chi_{0}} \right). \tag{4.25}$$

Here,  $\chi_0$  is the steady-state value of  $\chi$  for strain rates appreciably smaller than inverse atomic relaxation times. Since the maximum shear strain rate (reached the outer radius of the bar) for the small twist rate in our torsion test is small, we assume that the conversion factor  $K_{\chi}$  is a constant.

In this chapter, we will also consider a simple extension of LBL-theory to non-uniform deformations proposed in (Le *et al.*, 2018), where the excess dislocations are ignored. Since the back-stress  $\tau_B = 0$  in this case, we identify  $\tau_Y$  with  $\tau$  in Eqs. (4.22), (4.23), and (4.25). This system of equations becomes close, and after its integration, we use  $\tau_Y = \tau$  to compute the torque.

#### Method of solution:

For the purpose of numerical integration of the system (4.22), (4.23), (4.25), and (4.11) let us introduce the following variables and quantities

$$\tilde{r} = r/R, \quad \tilde{\tau} = \tau/\mu, \quad \tilde{\tau}_Y = \tau_Y/\mu, \quad \tilde{\tau}_B = \tau_B/\mu,$$

$$\tilde{\omega} = R\omega, \quad \tilde{\chi} = \frac{\chi}{e_D}, \quad \eta = \frac{b}{R}, \quad \tilde{\rho} = a^2 \rho.$$

The variable  $\tilde{r}$  changes from 0 to 1. The dimensionless quantity  $\tilde{\omega}$  has the meaning of the maximum shear strain achieved at the outer radius. The calculation of the

dimensionless torque  $\tilde{T}_c = T_c/R^3$  as the function of  $\tilde{\omega} = \omega R$  is convenient for the later comparison with the experimental data from (Liu *et al.*, 2012). Then we rewrite Eq. (4.21) in the form

$$q(\tau_Y, \rho) = \frac{b}{a}\tilde{q}(\tilde{\tau}_Y, \tilde{\rho}),$$

where

$$\tilde{q}(\tilde{\tau}_Y, \tilde{\rho}) = \sqrt{\tilde{\rho}} [\tilde{f}_P(\tilde{\tau}_Y, \tilde{\rho}) - \tilde{f}_P(-\tilde{\tau}_Y, \tilde{\rho})].$$

We set  $\tilde{\mu}_T = (b/a)\mu_T = \mu s$ , and assume that s is independent of temperature and strain rate. Then

$$\tilde{f}_P(\tilde{\tau}_Y, \tilde{\rho}) = \exp\left[-\frac{1}{\Theta}e^{-\tilde{\tau}_Y/(s\sqrt{\hat{\rho}})}\right].$$

We define  $\tilde{\varpi}_0 = (a/b)R\varpi_0$  so that  $q/(R\varpi_0) = \tilde{q}/\tilde{\varpi}_0$ . Function  $\nu$  in Eq. (4.24) becomes

$$\tilde{\nu}(\Theta, \tilde{\rho}, \tilde{\varpi}_0 \tilde{r}) \equiv \ln \left(\frac{1}{\Theta}\right) - \ln \left[\ln \left(\frac{\sqrt{\tilde{\rho}}}{\tilde{\varpi}_0 \tilde{r}}\right)\right].$$

The dimensionless steady-state quantities are

$$\tilde{\rho}^{ss}(\tilde{\chi}) = e^{-1/\tilde{\chi}}, \quad \tilde{\chi}_0 = \chi_0/e_D.$$

Since  $t_0^{-1}$  is a microscopic attempt frequency, of the order  $10^{12} \,\mathrm{s}^{-1}$ , we take  $(a/b)t_0 = 10^{-12} \mathrm{s}$ .

In terms of the introduced quantities, the governing equations read

$$\begin{split} &\tilde{\omega}\tilde{r}-\beta-\tilde{\tau}_B-\tilde{\tau}_Y=0,\\ &\frac{\partial\tilde{\tau}_Y}{\partial\tilde{\omega}}=\tilde{r}-\frac{\tilde{q}(\tilde{\tau}_Y,\tilde{\rho})}{\tilde{\varpi}_0},\\ &\frac{\partial\tilde{\rho}}{\partial\tilde{\omega}}=K_{\rho}\,\frac{\tilde{\tau}_Y\,\tilde{q}}{\tilde{\nu}(\Theta,\tilde{\rho},\tilde{\varpi}_0\tilde{r})^2\,\tilde{\varpi}_0}\,\Big[1-\frac{\tilde{\rho}}{\tilde{\rho}^{ss}(\tilde{\chi})}\Big],\\ &\frac{\partial\tilde{\chi}}{\partial\tilde{\omega}}=K_{\chi}\,\frac{\tilde{\tau}_Y\,\tilde{q}}{\tilde{\varpi}_0}\,\Big(1-\frac{\tilde{\chi}}{\tilde{\chi}_0}\Big), \end{split}$$

where  $\tilde{\tau}_B$  is equal to

$$\tilde{\tau}_B = -\frac{k_1 \xi^2 + (2k_0 k_1 - 1)\xi + k_1 k_0^2 - 2k_0}{4\pi (k_0 + \xi)^2} \eta^2 (\beta_{,\tilde{r}\tilde{r}} + \beta_{,\tilde{r}}/\tilde{r} - \beta/\tilde{r}^2), \tag{4.26}$$

with  $\xi = \eta |\beta_{\tilde{r}} + \beta/\tilde{r}|$ .

We use the method of lines to discretize the equations in the interval (0, 1). By dividing it into n sub-intervals of equal length  $\Delta \tilde{r} = 1/n$ , we approximate the first and second spatial derivative of  $\beta(\tilde{r})$  in equation (4.26) by the finite differences

$$\frac{\partial \beta}{\partial \tilde{r}}(\tilde{r}_i) = \frac{\beta_{i+1} - \beta_{i-1}}{2\Delta \tilde{r}},$$

$$\frac{\partial^2 \beta}{\partial \tilde{r}^2}(\tilde{r}_i) = \frac{\beta_{i+1} - 2\beta_i + \beta_{i-1}}{(\Delta \tilde{r})^2},$$

where  $\beta_i = \beta(\tilde{r}_i)$ . For the end-point  $\tilde{r} = 1$ , we introduce  $\beta_{n+1}$  at a fictitious point  $\tilde{r}_{n+1} = (n+1)\Delta \tilde{r}$  and pose the discretized boundary condition

$$f_1(\xi_n) + f_2(\beta_n) = \tilde{\gamma}_D, \tag{4.27}$$

with  $\xi_n = \eta \frac{\beta_{n+1} - \beta_{n-1}}{2\Delta \tilde{r}}$ ,  $\tilde{\gamma}_D = \gamma_D / (\mu b^2)$ 

$$f_1(\xi) = -\frac{\xi}{4\pi(k_0 + \xi)} - \frac{\ln(k_0 + \xi)}{4\pi} + \frac{k_1 \xi}{4\pi} - 0.105, \tag{4.28}$$

and

$$f_2(\beta) = \frac{1}{4\pi} \left( \ln \frac{\beta_*}{\beta} + \varkappa \beta \right). \tag{4.29}$$

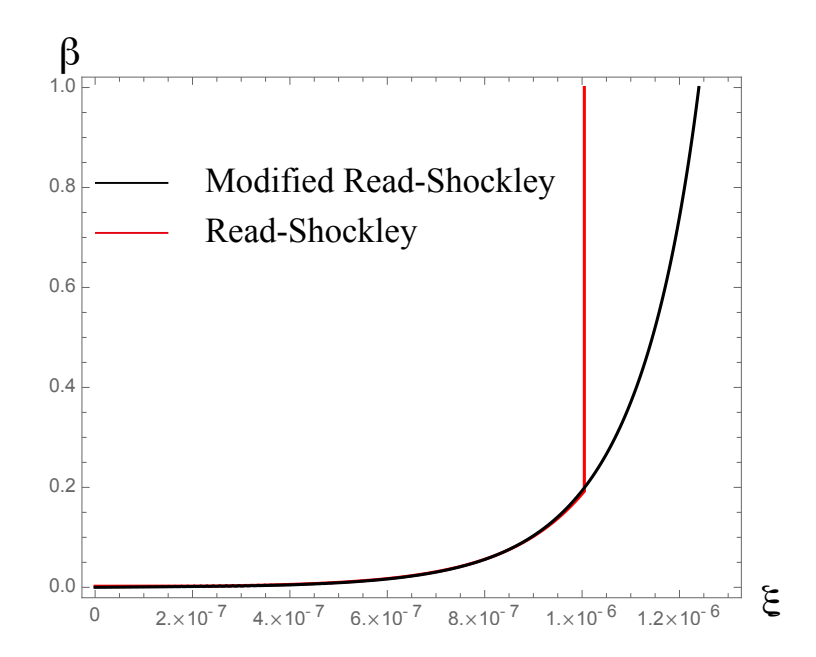


Figure 4.5.: Solution of Eq. (4.27) with (i) original Read-Shockley's  $f_2(\beta) = \frac{1}{4\pi} \ln(\beta_*/\beta)$  for  $\beta < \beta_*$  and 0 otherwise: red, (ii) modified  $\tilde{f}_2(\beta)$  from (4.30): black.

To avoid the singularity of  $f_2(\beta)$  at  $\beta = 0$ , which is difficult to handle numerically, we replace  $f_2(\beta)$  from (4.29) by

$$\tilde{f}_2(\beta) = \frac{1}{4\pi} \left( \ln \frac{\beta_*}{\beta + \delta} + \varkappa \beta \right), \tag{4.30}$$

with  $\delta$  being a small positive number, such that Eq. (4.27) yields the curve in the  $(\xi, \beta)$ plane starting from the origin (see Fig. 4.5). With  $f_1(\xi)$  and  $\tilde{f}_2(\beta)$  from Eq. (4.28)
and Eq. (4.30), respectively, we find that  $\delta = \beta_*/(k_0 \exp(4\pi(\tilde{\gamma}_D + 0.105)))$ . With  $\beta_{n+1}$ found from (4.27), it is possible again to discretize the first and second derivative
of  $\beta(\tilde{r})$  at  $\tilde{r} = 1$  and write the finite difference equation for  $\beta(\tilde{r})$  at that point. In
this way, we reduce the four partial differential equations to a system of 4n ordinary
differential-algebraic equations that will be solved by Matlab-ode15s.

After finding the plastic distortion  $\beta(\tilde{r})$ , we compute the dimensionless torque as a function of the twist angle according to

$$\tilde{T}_c = T_c/R^3 = 2\pi\mu \int_0^1 [\tilde{\omega}\tilde{r} - \beta(\tilde{r})]\tilde{r}^2 d\tilde{r}.$$

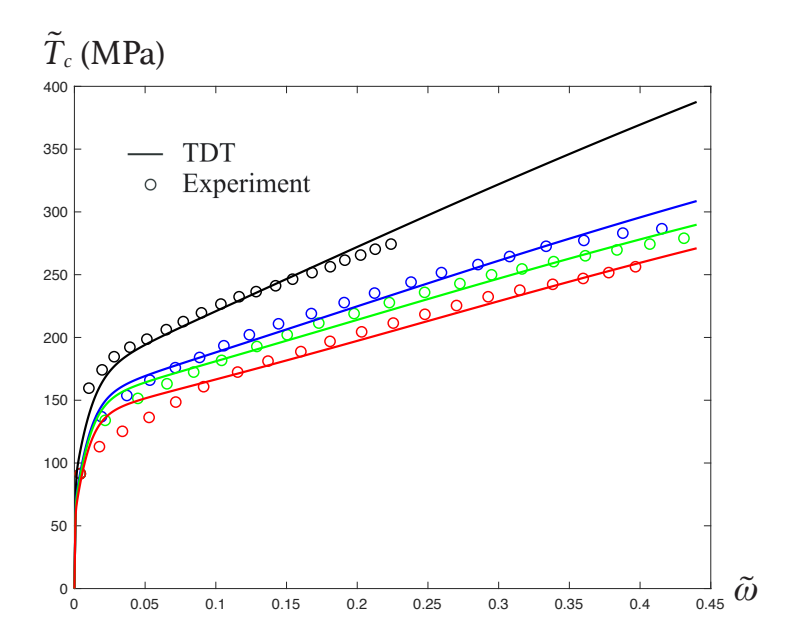


Figure 4.6.: Torque-twist curves with twist rate  $L\dot{\omega} = \frac{\pi}{30}/\mathrm{s}$  and for room temperature, for four different radii R=9 micron (black), R=15 micron (blue), R=21 micron (green) and R=52.5 micron (red): (i) TDT (bold lines), (ii) experimental points taken from Liu *et al.* (2012) (circles).

#### 4.4. Parameter Identification and Numerical Simulations

The experimental data of Liu et al. (2012) include four torque-twist curves for polycrystalline copper wires with different radii R=9 micron, R=15 micron, R=21 micron, and R=52.5 micron. It was mentioned in (Liu et al., 2012) that all wires were annealed for 2.4 hours in a vacuum furnace with argon shielding at 410° C to ensure that each sample had the same mean grain size. Torsion tests were performed at room temperature, and for all tests, the twist rate  $L\dot{\omega}$  was  $\pi/30$  per second (6°/s). We show these data together with our theoretical results based on the TDT in Fig. 4.6. In this figure, the circles represent the experimental data in (Liu et al., 2012), while the bold lines are our theoretical simulation based on the TDT. For comparison, we show in Fig. 4.7 the torque-twist curves simulated by the TDT (bold lines) and the LBL-theory (dashed lines) in the larger range of the twist angle  $\tilde{\omega} \in (0, 2.5)$ .

In order to compute the theoretical torque-twist curves, we need values for ten system-specific parameters. The ten basic parameters are the following: the activation temperature  $T_P$ , the stress ratio s, the steady-state scaled disorder temperature  $\tilde{\chi}_0$ , the two dimensionless conversion factors  $K_\rho$  and  $K_\chi$ , the two coefficients  $k_0$ , and  $k_1$  defining the function  $\tilde{\tau}_B$  in Eq. (4.26), and the three coefficients  $\beta_*$ ,  $\varkappa$ , and  $\tilde{\gamma}_D$  entering Eq. (4.27). We also need initial values of the scaled dislocation density  $\tilde{\rho}_i$  and the scaled disorder temperature  $\tilde{\chi}_i$ ; all of which characterize the microstructure of the material prior to the plastic deformation and are determined by the sample preparation depending on many factors. For example, the history of metal forming, sample preparation by cutting the metal piece that produces plastic deformation, and heat treatment may affect grain size, the initial dislocation density  $\tilde{\rho}_i$ , and the initial disorder temperature  $\tilde{\chi}_i$ , which may vary from sample to sample. Note that the size of the sample can also play a role in this history of preparation. Our assumption is that the grain size is

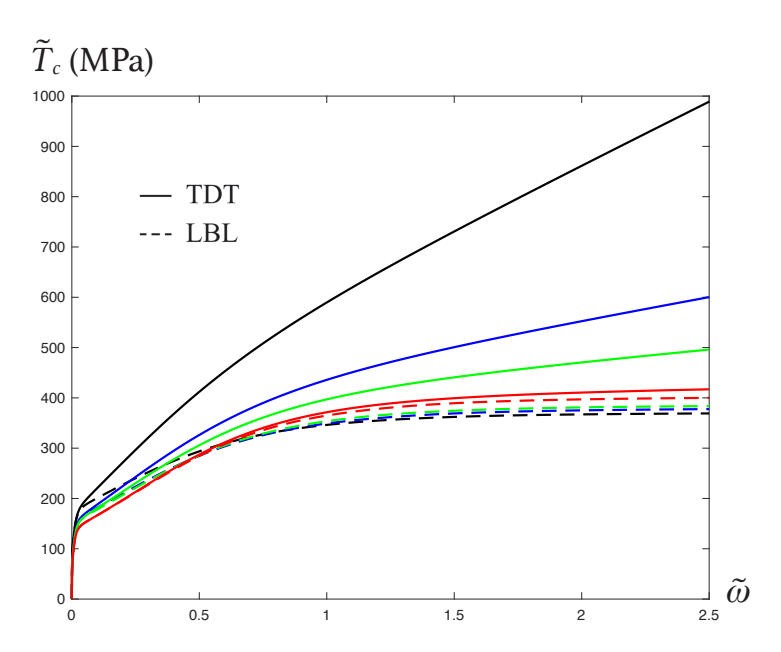


Figure 4.7.: Torque-twist curves with twist rate  $L\dot{\omega}=\frac{\pi}{30}/\mathrm{s}$  and for room temperature, for four different radii R=9 micron (black), R=15 micron (blue), R=21 micron (green) and R=52.5 micron (red): (i) TDT (bold lines), (ii) LBL-theory (dashed lines).

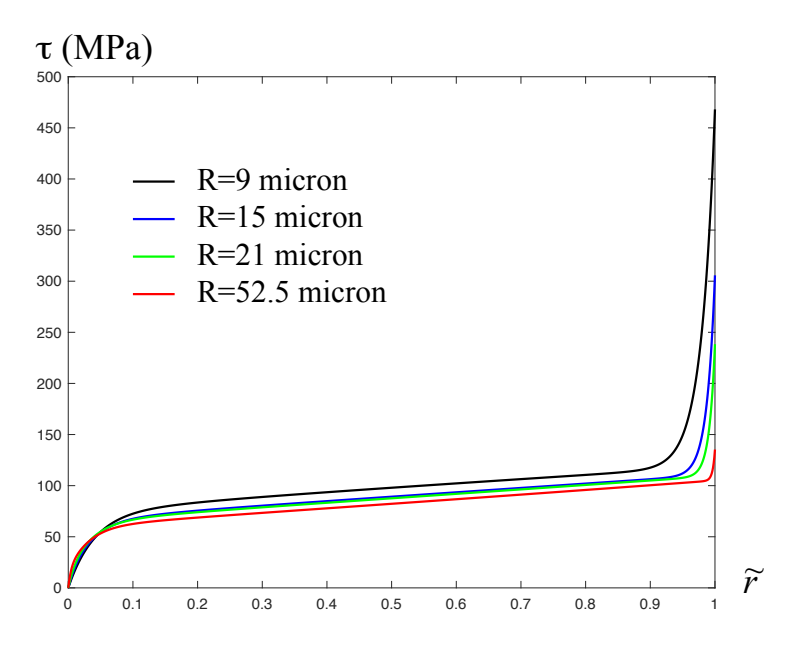


Figure 4.8.: Stress distributions  $\tau(\tilde{r})$  at twist rate  $L\dot{\omega}=\frac{\pi}{30}/\mathrm{s}$  and for room temperature, at  $\tilde{\omega}=0.198$  and for four different radii R=9 micron (black), R=15 micron (blue), R=21 micron (green), and R=52.5 micron (red).

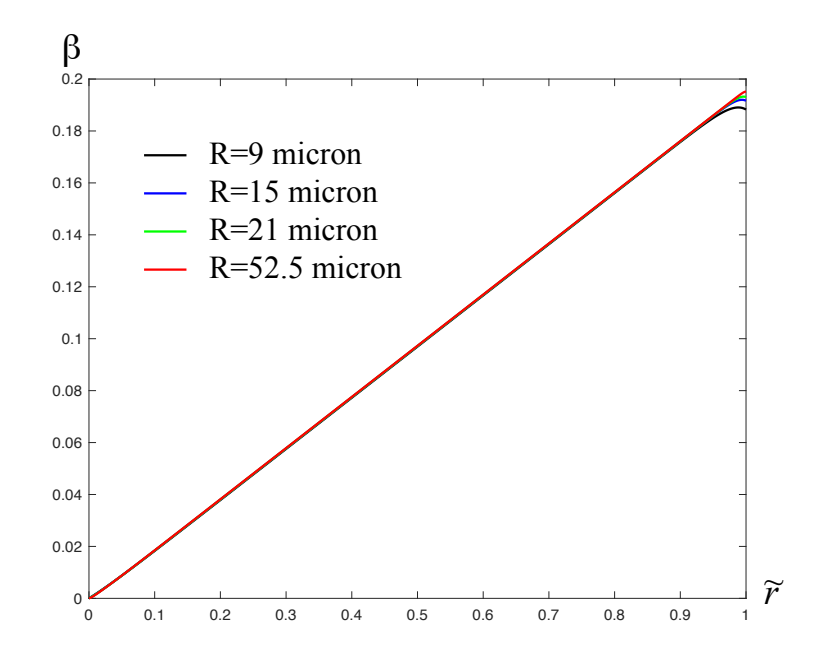


Figure 4.9.: Plastic distortion  $\beta(\tilde{r})$  at twist rate  $L\dot{\omega} = \frac{\pi}{30}/s$  and for room temperature, at  $\tilde{\omega} = 0.198$  and for four different radii R = 9 micron (black), R = 15 micron (blue), R = 21 micron (green), and R = 52.5 micron (red).

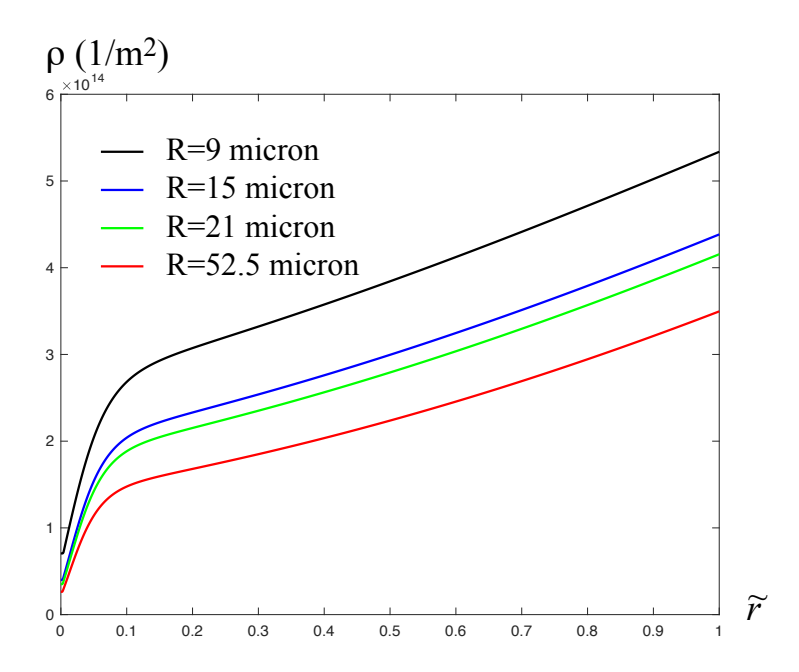


Figure 4.10.: Total density of dislocations  $\rho(\tilde{r})$  at twist rate  $L\dot{\omega}=\frac{\pi}{30}/\mathrm{s}$  and for room temperature, at  $\tilde{\omega}=0.198$  and for four different radii R=9 micron (black), R=15 micron (blue), R=21 micron (green), and R=52.5 micron (red).

			10 /	
$R(\mu m)$	9	15	21	52.5
$ ilde{ ho}_i$	$4.589 \times 10^{-4}$	$2.605 \times 10^{-4}$	$2.282 \times 10^{-4}$	$1.707 \times 10^{-4}$
$\tilde{\chi}_i$	0.158	0.151	0.149	0.143

Table 4.1.: The initial values of  $\tilde{\rho}_i$  and  $\tilde{\chi}_i$ 

characterized by the initial disorder temperature. Perhaps, more information from the microstructure is required for the initially textured materials under torsion, but we will not address this topic here. Thus, for four samples, we will need to identify eight initial values.

The other parameters required for numerical simulations but known from the experiment are: the ambient temperature  $T=298\mathrm{K}$ , the shear modulus  $\mu=48\mathrm{GPa}$ , the length  $L=25\mathrm{mm}$  of the wires, the magnitude of Burgers vector  $b=2.55\mathrm{\mathring{A}}$ , the twist rate  $L\dot{\omega}=\pi/30/\mathrm{s}$ , and consequently,  $\varpi_0=0.419\times10^{-12}/\mathrm{m}$ . We take a=10b, which is close to the distance between dislocations in the saturated state.

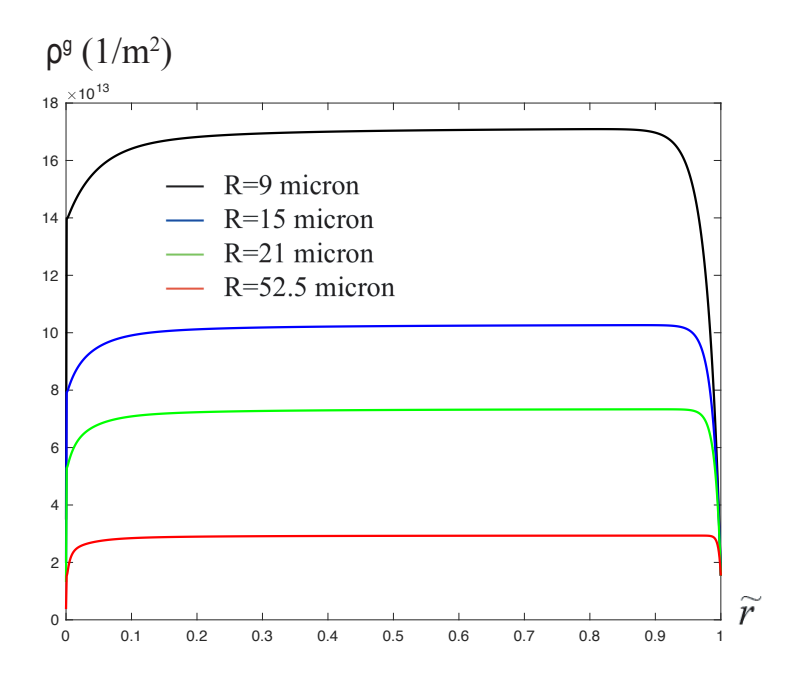


Figure 4.11.: Density of excess dislocations  $\rho^g(\tilde{r})$  at twist rate  $L\dot{\omega}=\frac{\pi}{30}/\mathrm{s}$  and for room temperature, at  $\tilde{\omega}=0.198$  and for four different radii R=9 micron (black), R=15 micron (blue), R=21 micron (green), and R=52.5 micron (red).

In the papers dealing with the uniform deformations (Langer et al., 2010; Langer, 2015, 2016, 2017a), it was possible to begin evaluating the parameters by observing steady-state stresses  $\sigma_{ss}$  at just a few strain rates  $q_0$  and ambient temperatures  $T_0 = T_P \tilde{\Theta}_0$ . Knowing  $\sigma_{ss}$ ,  $T_0$  and  $q_0$  for three stress-strain curves, one could solve equation

$$\sigma = \sigma_T(\tilde{\rho})\nu(\tilde{\Theta}, \tilde{\rho}, q_0),$$

which is the inverse of Eq. (4.21) for  $T_P$ , s, and  $\tilde{\chi}_0$ , and check for consistency by looking at other steady-state situations. With that information, it was relatively easy to evaluate  $K_\rho$  and  $K_\chi$  by directly fitting the full stress-strain curves. This strategy does not work here because the stress state of twisted bars is non-uniform. We may still have local steady-state stresses as a function of the radius r, but it is impossible

to extract this information from the experimental torque-twist curve. Furthermore, the similar parameters for copper found in (Langer *et al.*, 2010; Langer, 2015, 2016, 2017a) cannot be used here, since we are dealing with torsional deformations having the energy barrier  $T_P$  and other characteristics different from those identified in the above references.

To counter these difficulties, we have resorted to the large-scale least-squares analysis developed in (Le & Tran, 2017). That is, we have solved the discretized system of ordinary differential-algebraic equations (DAE) numerically, provided a set of material parameters, and initial values are known. Based on this numerical solution we then computed the sum of the squares of the differences between our theoretical torque-twist curves and a large set of selected experimental points and minimized this sum in the space of the unknown parameters. The DAEs were solved numerically using the Matlab-ode15s, while the finding of least squares was realized with the Matlab-globalsearch. To keep the calculation time manageable and simultaneously ensure the accuracy, we have chosen n = 1000 and the  $\tilde{\omega}$ -step equal to  $0.44 \times 10^{-4}$ .

We have found that the torque-twist curves taken from Liu et al. (2012) can be fitted with a single set of system-specific parameters. These are:  $T_P = 19205 \,\mathrm{K}, s = 0.0686, \, \chi_0 = 0.2089, \, K_\rho = 57.02, \, K_\chi = 242.8, \, k_0 = 6.386 \times 10^{-7}, \, k_1 = 6.947 \times 10^6, \, \beta_* = 0.192, \, \varkappa = 0.198, \, \tilde{\gamma}_D = 1.462$ . The identified initial values for the four samples are shown in Table 4.1. To obtain the actual initial dislocation densities, we must divide these values by  $a^2$ , resulting in the order of  $10^{13}$  dislocations per square meter. We observe that the initial dislocation density and the disorder temperature decrease with increasing radius. As already discussed, the initial dislocation densities depend on many factors, some of which are unknown. In addition, (Liu et al., 2012) did not provide information about initial dislocation densities. Therefore, identifying these parameters on the basis of least squares analysis seems to be the only way to estimate them.

The agreement between theory and experiment seems to be well within the bounds of experimental uncertainties. There are only two visible discrepancies: (i) near the yielding transition, the torques are slightly above those predicted by theory for R=9 micron and R=15 micron, (ii) at large twist angles, the torques are slightly below those predicted by theory for R=21 micron and R=52.5 micron. The comparison also shows that the LBL-theory fails in predicting the torque twist curves and the size effect, except in the vicinity of the yielding transition where the density of excess dislocations is negligibly small. Indeed, looking at the torque-twist curves predicted by the LBL-theory in Fig. 4.7 we see that the differences in torque due to the different initial dislocation density and disorder temperature do not increase as the twist angle increases. Besides, all torque-twist curves approach the steady-state at large twist angles. This contradicts the behavior of the experimental torque-twist curves obtained in (Fleck et al., 1994; Liu et al., 2012).

Liu et al. (2012) proposed the following empirical formula

$$\tilde{T}_c = \frac{6\pi\Sigma_0\tilde{\omega}^N}{N+3} \left\{ \left[ \frac{1}{3} + \left(\frac{l}{R}\right)^2 \right]^{(N+3)/2} - \left(\frac{l}{R}\right)^{N+3} \right\}$$

for the torque-twist curves containing the internal length scale l, the reference stress  $\Sigma_0$  and the hardening parameter N. By choosing appropriate parameters, they can fit the experimental torque-twist curves in Fig. 4.6 (we do not show their curves to avoid

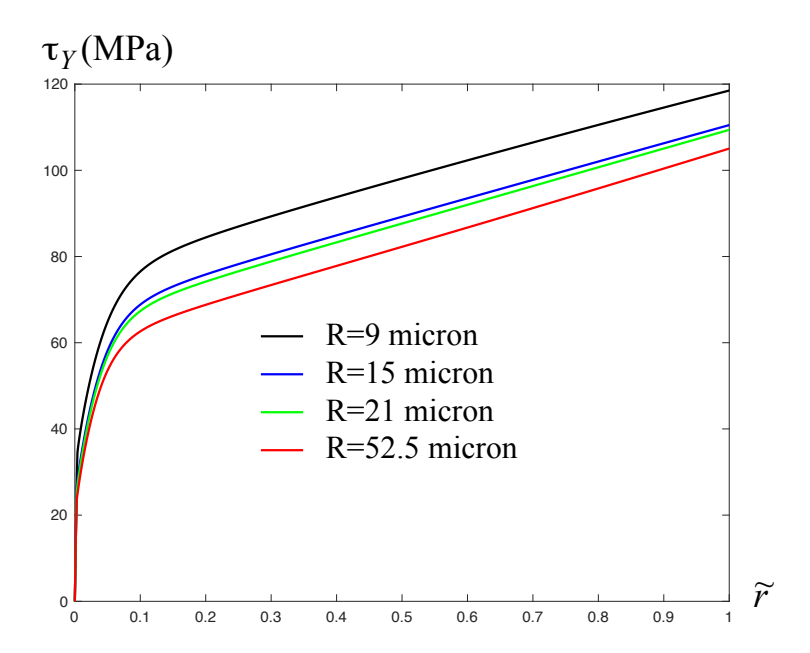


Figure 4.12.: Distributions of flow stress  $\tau_Y(\tilde{r})$  at twist rate  $L\dot{\omega} = \frac{\pi}{30}/\text{s}$  and for room temperature, at  $\tilde{\omega} = 0.198$  and for four different radii R = 9 micron (black), R = 15 micron (blue), R = 21 micron (green), and R = 52.5 micron (red).

the strong overlap). Unfortunately, this empirical formula is not based on the solution of the boundary-value problem of the equilibrium of crystals containing dislocations and therefore does not allow to find both the stress distribution and the dislocation densities within the wire.

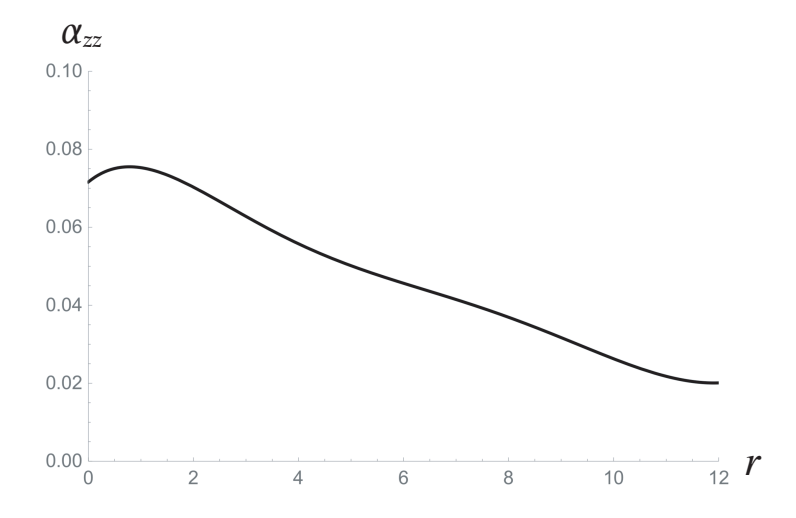


Figure 4.13.: Distributions of  $\alpha_{zz} = \omega_{,r} + \omega/r$ , where  $\omega$  is the average misalignment taken from Figure 7b of (Ziemann *et al.*, 2015) for  $\gamma_{pl}(R) = 0.01$ .

The results of numerical simulations for other quantities are shown in Figs. 4.8-4.16. We plot in Fig. 4.8 the shear stress distributions  $\tau(\tilde{r}) = \mu(\tilde{\omega}\tilde{r} - \beta)$  at  $\tilde{\omega} = 0.198$ . Contrary to the similar distribution obtained by the phenomenological theory of ideal plasticity, the stress in the plastic zone does not remain constant but rises with increasing  $\tilde{r}$  and reaches a maximum at  $\tilde{r} = 1$ . The slope of this stress distribution is small in the middle ring  $(\tilde{r}_1, \tilde{r}_2)$   $(0 < \tilde{r}_1 < \tilde{r}_2 < 1)$  of the cross-section but increases rapidly near the free boundary. Another interesting behavior is that the stress near the center is

highest for the largest wire, while it is lowest in the periphery. This behavior can later be explained by the presence of back stress. Fig. 4.9 shows distributions of the plastic distortion  $\beta(\tilde{r})$  at the above twist angle  $\tilde{\omega} = 0.198$ . Remarkably, all four distributions of plastic distortion are nearly linear and almost indistinguishable functions of  $\tilde{r}$  except very near the free boundary  $\tilde{r} = 1$ . Since the latter attracts excess dislocations,  $\beta(\tilde{r})$ should decrease in this region, leading to the decreasing density of excess dislocations. Besides, due to the different values of the factor  $\eta$  for different radii, the density of excess dislocations derivable from  $\beta(\tilde{r})$  depends on the radius of the wire as will be seen later. Fig. 4.10 shows the total densities of dislocations at the above twist angle  $\tilde{\omega} = 0.198$ . Note that the total density of dislocations is highest for the wire with the smallest radius. The entanglement of dislocations and the initial dislocation density and disorder temperature play a decisive role here. The higher dislocation density leads to the stronger entanglement and the higher yield stress, which, together with the higher disorder temperature, causes a stronger dislocation multiplication. Fig. 4.11 presents the density of excess dislocations at the above twist angle  $\tilde{\omega} = 0.198$ . Under the applied shear stress excess dislocations of the positive sign move to the center of the wire and pile up against the middle ring  $(\tilde{r}_1, \tilde{r}_2)$  (cf. (Weinberger, 2011; Kaluza & Le, 2011; Le & Piao, 2016; Liu et al., 2018)). The highest and almost constant density of excess dislocations is achieved in the middle ring, while this density rapidly decreases as  $\tilde{r}$  approaches 0 or 1.

The formation and accumulation of excess dislocations in twisted wires can be explained as follows. Since the flow stress during the plastic deformation exceeds the Taylor stress, redundant dislocations in the form of dislocation dipoles begin to dissolve according to the kinetics of thermally activated dislocation depinning (Langer et al., 2010). Under the applied shear stress, positive dislocations then move towards the center and negative dislocations towards the boundary. For the dissolved dislocation dipoles within the sample and far from the free boundary, these freely moving dislocations are soon trapped by dislocations of the opposite sign. But the dislocation dipoles near the free boundary behave differently. Now the positive dislocations move inwards and become excess dislocations, while the negative dislocations leave the sample and become image dislocations. At small angles of twist, the applied shear stress near the center is still small and cannot move dislocations. Therefore, excess dislocations occupy a small outer ring  $(\tilde{r}_1,1)$   $(0 < \tilde{r}_1 < 1)$ . As the angle of twist increases, the shear stress increases as well, and when it becomes large enough, it can drive these excess dislocations to the center. Thus, we can say that the dissolution of dipoles near the free boundary results in excess dislocations of positive sign. They then move to the center and pile up against the middle ring, increasing the kinematic hardening. As far as the experimental measurement of excess dislocations is concerned, the interesting work of Ziemann et al. (2015) for twisted Au microwires should be mentioned. Here, the cross-sections of the individual (100) oriented grains of 25 micron Au microwires were characterized by Laue micro diffraction. The diffraction data were used to calculate the misalignment of each data point with respect to the neutral fiber at the center of the cross-section from which some qualitative information could be obtained on the density of excess dislocations. Unfortunately, as mentioned by Ziemann et al. (2015), "the misorientation data do not allow to distinguish between pure elastic distortions and distortions caused by dislocations", so the quantitative determination of the excess dislocation density as the curl of the plastic distortion (or, equivalently, the curl of the elastic distortion taken with minus sign) could not yet be performed. Provided the measured average misalignment represent the true lattice rotation  $\omega$ , we can compute the density of excess dislocation according to  $\rho^g = |\omega_r + \omega/r|/b$ . The

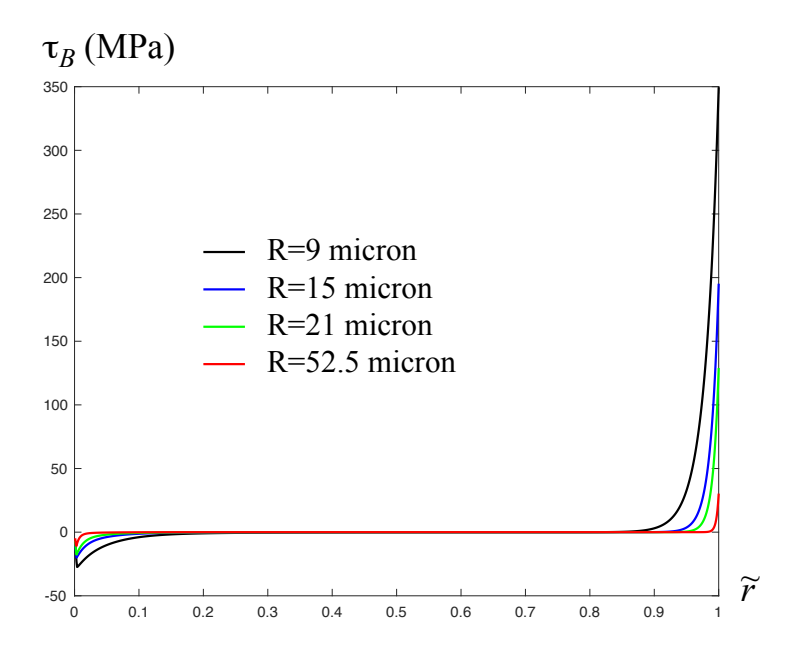


Figure 4.14.: Distributions of back stress  $\tau_B(\tilde{r})$  at twist rate  $L\dot{\omega} = \frac{\pi}{30}/\text{s}$  and for room temperature, at  $\tilde{\omega} = 0.198$  and for four different radii R = 9 micron (black), R = 15 micron (blue), R = 21 micron (green), and R = 52.5 micron (red).

plot of  $\alpha_{zz} = \omega_{,r} + \omega/r$  computed from one representative curve taken from Ziemann et al. (2015) is shown in Fig. 4.13. We see that this plot agrees qualitatively with our distribution in the sense that  $\alpha_{zz}$  achieves a maximum in the middle ring and decreases when r goes to zero and R. We also tried to compare our result with that obtained by discrete dislocation dynamics (DDD) simulations reported in (Senger et al., 2011). However, since the quantitative distribution of the excess dislocations in (Senger et al., 2011) is absent, no comparison is possible so far.

It is interesting to examine the influence of the size of samples and the initial values of dislocation density and disorder temperature on the flow and back stress. Figs. 4.12 and 4.14 show the distributions of flow and back stress, respectively, at  $\tilde{\omega} = 0.198$ . The flow stress depends linearly on  $\tilde{r}$  in a small elastic zone near the center of the wire. In the plastic zone, it is largest for the smallest wire. This behavior should be explained by the entanglement of dislocations as well as the initial dislocation density and disorder temperature. As shown in Table 4.1, the initial dislocation density  $\tilde{\rho}_i$  and the initial disorder temperature  $\tilde{\chi}_i$  are the highest for the smallest wire. Thus, the Taylor stress for the smallest wire is highest, and the entanglement of dislocations leads to the highest flow stress for the smallest wire. The back stress vanishes in the middle ring  $(\tilde{r}_1, \tilde{r}_2)$  of the cross-section because the density of excess dislocations is nearly constant there and changes rapidly near the center  $(0, \tilde{r}_1)$  and the periphery  $(\tilde{r}_2, 1)$  as seen in Fig. 4.14. The distribution of back stress shows the influence of the sample size. Since nearly the same number of excess dislocations is distributed in the wires, that wire with the smallest cross-section area must have the largest magnitude of the back stress. Note however that, as the excess dislocations pile up against the middle ring  $(\tilde{r}_1, \tilde{r}_2)$ , the back stress is positive in the periphery  $(\tilde{r}_2, 1)$  and negative near the center  $(0, \tilde{r}_1)$  of the wires. This leads to the different behavior of the stress there, as can be seen in Fig. 4.8. Figs. 4.15 and 4.16 show the contribution of the flow stress and back stress to the torque versus the twist angle. While the contribution of flow stress to

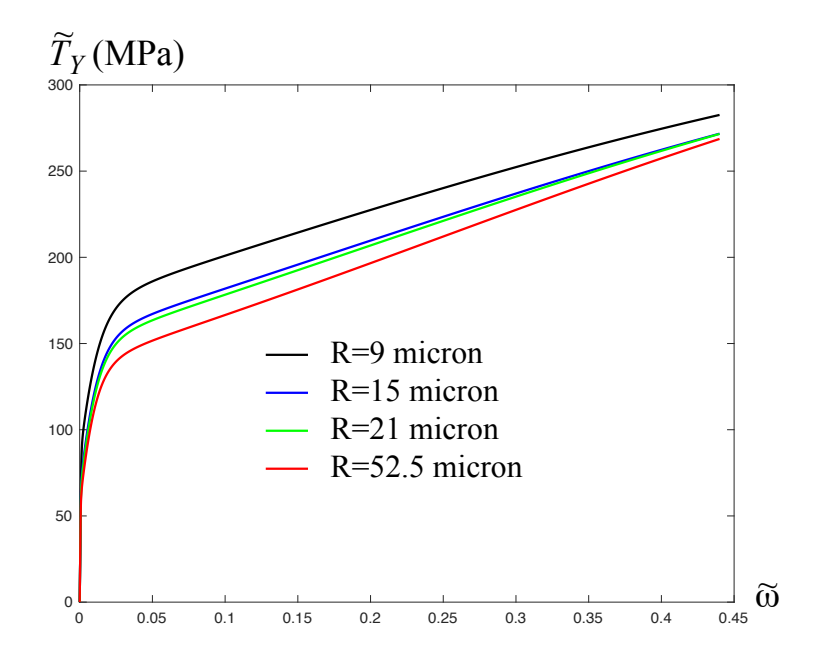


Figure 4.15.: Contribution of flow stress  $\tau_Y(\tilde{r})$  to the torque versus twist angle at twist rate  $L\dot{\omega} = \frac{\pi}{30}/\text{s}$  and for room temperature, at four different radii R=9 micron (black), R=15 micron (blue), R=21 micron (green), and R=52.5 micron (red).

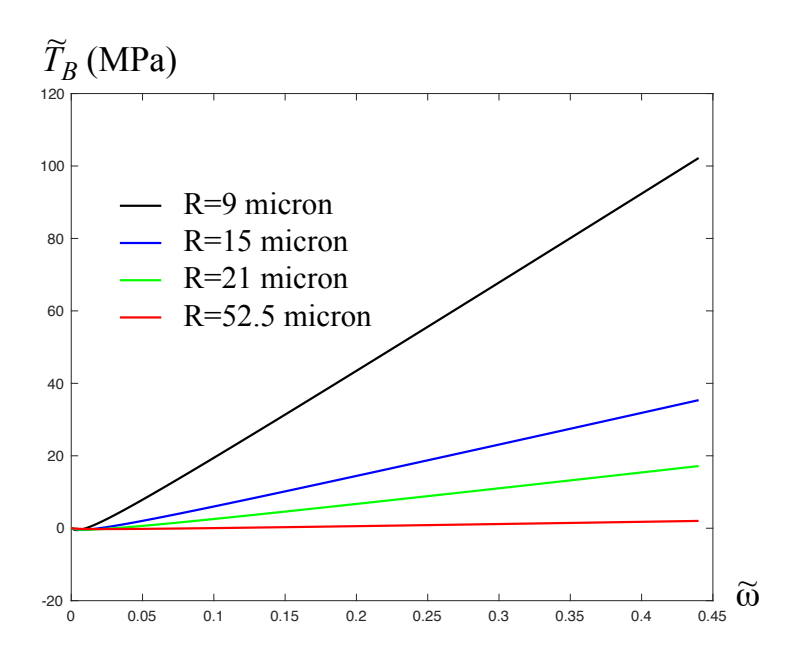


Figure 4.16.: Contribution of back stress  $\tau_B(\tilde{r})$  to the torque versus twist angle at twist rate  $L\dot{\omega}=\frac{\pi}{30}/\mathrm{s}$  and for room temperature, at four different radii R=9 micron (black), R=15 micron (blue), R=21 micron (green), and R=52.5 micron (red).

torque is controlled by the entanglement of dislocations, which depends on the initial dislocation density and disorder temperature (in short, on the microstructure of the material), the contribution of back stress is controlled by the nucleation and pile-up of excess dislocations, which depend on the radius of the wire. The torque generated by the back stress from the pile-up of excess dislocations contributes a maximum of 26% to the total torque in the range of the considered twist angles. Note that as the twist angle increases, the differences in torque generated by the flow stress decrease, while the differences in torque generated by excess dislocations increase almost linearly as seen in Fig. 4.16.

At last, it is mentioned that the comparison between the experimental data and the simulation by TDT matches well shown in Fig. 4.6. However, one may observe that a small discrepancy happens at the beginning of plastic deformation and disappear in the latter. It is probably due to the assumption that all screw excess dislocations lie parallel to the wire axis. As discussed in Fig. 4.3, the different configuration types of screw dislocations may affect the torque-twist response in the yielding transition. Therefore, it would be interesting for further investigations on the twisted wire containing the grains in which both parallel and perpendicular screw excess dislocations to wire axis exist.

## 4.5. Conclusion

The results obtained show the principal applicability of TDT to torsion tests. We found that the behavior of the torque-twist curves is controlled not only by the microstructure of material (the grain size, the initial dislocation density, and the initial disorder temperature), which affects isotropic hardening but above all the sample size, which affects the nucleation and pile-up of excess dislocations and kinematic hardening. For wires of micron sizes under torsion, the back stress contributes at most 26% to the torque for  $\tilde{\omega} < 0.44$ , but this contribution increases almost linearly with the increasing twist angle. It is still early to assess the validity of the distribution of excess dislocations by comparing it with the available results in the literature, neither with the experimental data obtained by the EBSD measurement nor with the discrete dislocation dynamics simulations, so more careful theoretical and experimental investigations are required.

# 5. Thermodynamic Dislocation Theory in Macro-scale

#### 5.1. Introduction

The aim of this chapter is to explore the use of a simple extension of TDT in modeling the twisted bars made of single crystal copper and polycrystal aluminum alloy. For bars of macro sizes, the theory takes into account the spatial variation of state variables and ignores the excess dislocations. Our challenge is to simulate the torque-twist curves exhibiting the hardening and thermal softening behaviors, respectively, and to compare them with the experimental results provided by Horstemeyer et al. (2002) (hardening) and by Zhou & Clode (1998) (thermal softening). To make this comparison possible, we need to identify from the experimental data a list of material parameters for each material under torsion. For this purpose, we will use the large scale least-squares analysis described in (Le & Tran, 2017). We start in Sec. 5.2 with a brief summary of the proposed equations of motion discussed in the previous chapters. In addition, an equation for the ordinary temperature is taken into account for inhomogeneous temperature distribution in the sample body. Two applications, the hardening and thermal softening behaviors in the twisted bar, are investigated in Sec. 5.3 and Sec. 5.4. In each section, we discretize the corresponding system of governing equations and develop the numerical method for its solution. The parameter identification based on the large scale least-squares analysis and results of numerical simulations are presented. Finally, Sec. 5.5 concludes the chapter.

# 5.2. Equations of Motion

#### Description of experiments and sample bars:

Horstemeyer et al. (2002) and Zhou & Clode (1998) investigated torsion experiments on solid specimens with a geometric shape of a stepped cylinder (see Fig. 5.1), and discovered the hardening and thermal softening behaviors of twisted bars, respectively. In the hardening experiment, two samples of single crystal copper with bar axis parallel to  $\langle 110 \rangle$  crystallographic direction are used. In the experiment for thermal softening, five polycrystal samples of aluminum alloy 5252 performed at the elevated temperature and at different strain rates are used. Both ends of the specimen, subjected to torsion (see Fig. 5.2), have a larger radius, and the gauge section has a relatively thin circular cross-section of radius R and length L. For this particular geometry of bars and under the condition  $R \ll L_t$ , it is natural to assume that the circumferential displacement is  $u_{\theta} = \omega r z$ , with  $\omega$  being the twist angle per unit length. Thus, the total shear strain of the bar  $\gamma = 2\varepsilon_{\theta z} = \omega r$  and the shear strain rate  $\dot{\gamma} = \dot{\omega} r$  turn out to be non-uniform as they are linear functions of radius r. Now, let this system be driven at a constant twist rate  $\dot{\omega} \equiv \varpi_0/t_0$ , where  $t_0$  is a characteristic microscopic time scale. Since the system experiences a steady-state torsional deformation, we can replace the time t by

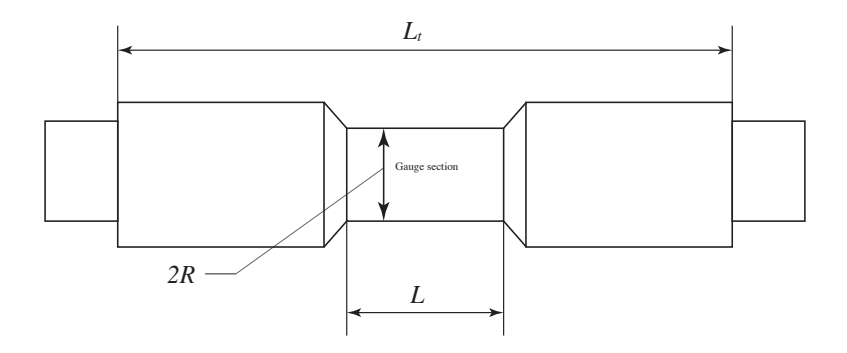


Figure 5.1.: The geometry of a solid bar.

the total twist angle (per unit length)  $\omega$  so that

$$t_0 \partial/\partial t \to \varpi_0 \partial/\partial \omega$$
.

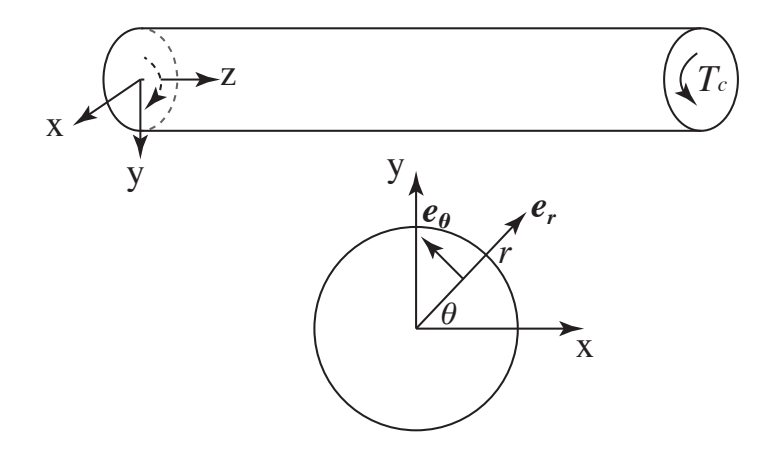


Figure 5.2.: Gauge section of crystal sample.

Microforce equilibrium: It turns out that the influence of excess dislocations to microforce equilibrium can be ignored not only in the uniform deformation but also in the sample of macro scales undergoing a non-uniform deformation. Therefore, the back-stress  $\tau_B$  vanishes in this problem, and apparently, the equilibrium of microforces becomes

$$\tau = \tau_Y$$
.

In what follows, we identify  $\tau_Y$  with  $\tau$  in the related governing equations, and it is valid in both applications in Sec. 5.3 and Sec. 5.4.

The equations of motion for the flow stress, total dislocation density, and the effective temperature are identical to those in Sec. 4.3. Here we briefly annotate governing equations, and for more details, see Sec. 4.3 and Sec. 2.3.3.

**Flow stress:** The equation of motion for flow stress starts from the Hooke's law in rate form. By introducing the dimensionless plastic distortion rate  $q(\tau, \rho)$ , the governing

equation reads

$$\frac{\partial \tau}{\partial \omega} = \mu \left[ r - \frac{q(\tau, \rho)}{\varpi_0} \right],\tag{5.1}$$

with  $\tau(r,t) = \sigma_{\theta z}$  being the shear stress and  $\mu$  the shear modulus. The dimensionless plastic strain rate, as a function of stress  $\tau$  and total dislocation density  $\rho$ , involves thermally activated depinning mechanism introduced by Langer *et al.* (2010) as

$$q(\tau, \rho) = b\sqrt{\rho}[f_P(\tau, \rho) - f_P(-\tau, \rho)], \tag{5.2}$$

where

$$f_P(\tau, \rho) = \exp\left[-\frac{1}{\Theta}e^{-\tau/\tau_T(\rho)}\right].$$

The central idea of (5.2) is that the energy barrier, which prevents the dissolution of dislocations from dipoles, is reduced by applied stress owing to the stress-dependent factor  $e^{-\tau/\tau_T(\rho)}$ , and in addition, the increasing ambient temperature  $(T = \Theta T_P)$  helps dislocations depinning from pinning sites. Here,  $\tau_T(\rho) = \mu_T b \sqrt{\rho}$  is the Taylor stress with  $\mu_T$  being proportional to  $\mu$ .

**Dislocation density:** The equation of motion for total dislocation density  $\rho$  describes energy flow, and it emerges from the second law of thermodynamics that the total entropy of two subsystems is never negative. In terms of the twist  $\omega$ , this equation reads:

$$\frac{\partial \rho}{\partial \omega} = K_{\rho} \frac{\tau \, q}{a^2 \nu(\Theta, \rho, \varpi_0 r)^2 \, \mu \, \varpi_0} \left[ 1 - \frac{\rho}{\rho^{ss}(\chi)} \right],\tag{5.3}$$

with  $\rho^{ss}(\chi) = (1/a^2)e^{-e_D/\chi}$  being the steady-state value of  $\rho$  at given  $\chi$ ,  $e_D$  a characteristic formation energy for dislocations, and a denoting the average spacing between dislocations in the limit of infinite  $\chi$  (a is a length of the order of tens of atomic spacings). The coefficient  $K_{\rho}$  is an energy conversion factor that should be independent of both strain rate and temperature. The other quantity that appears in the prefactor in Eq. (5.3) is

$$\nu(\Theta, \rho, \varpi_0 r) \equiv \ln\left(\frac{1}{\Theta}\right) - \ln\left[\ln\left(\frac{b\sqrt{\rho}}{\varpi_0 r}\right)\right]. \tag{5.4}$$

The effective temperature: The equation of motion for effective temperature  $\chi$  is a statement of the first law of thermodynamics for the configurational subsystem (Langer *et al.*, 2010):

$$\frac{\partial \chi}{\partial \omega} = K_{\chi} \frac{\tau e_D q}{\mu \varpi_0} \left( 1 - \frac{\chi}{\chi_0} \right). \tag{5.5}$$

Here,  $\chi_0$  is the steady-state value of  $\chi$  for strain rates appreciably smaller than inverse atomic relaxation times, i.e., much smaller than  $t_0^{-1}$ . The dimensionless factor  $K_{\chi}$  is inversely proportional to the effective specific heat  $c_{eff}$ . Since the maximum strain rate (reached the outer radius of the bar) for the small twist rate in our torsion test is small, we assume that  $K_{\chi}$  is a constant.

The ordinary temperature: As the first law of thermodynamics states, the irreversible external work done to the material system is partly stored in the dislocation energy, and the rest is dissipated into the heat. If applied strain rate is small and the material is of high thermal conductivity, such as copper, the heat is conducted fast through the body so that there is no significant temperature change inside. While at a relatively high strain rate of the deformation in the material of low thermal conductivity, the generated heat by plastic deformation causes inhomogeneous temperature distribution in the material body. Therefore, the equation of motion for ordinary temperature  $\Theta = T/T_P$  is required to describe this process, and it reads

$$\frac{\partial \Theta}{\partial \omega} = K_1(\Theta) \frac{\tau q}{\mu(\Theta)\varpi_0} - \frac{K_2}{\varpi_0} (\Theta - \Theta_0). \tag{5.6}$$

Here,  $K_1(\Theta) = \beta_Q \mu(\Theta)/(T_P c_p \rho_d)$  is a thermal energy conversion factor, with  $c_p$  being the thermal heat capacity per unit mass,  $\rho_d$  the mass density, and  $0 < \beta_Q < 1$  a dimensionless factor known as the Taylor-Quinney factor. Rittel et al. (2017) reported that the Taylor-Quinney factor varies greatly with investigated material and the loading mode, hence we bring this factor into the parameter  $K_1$  that to be identified. The first term on the right-hand side of Eq. (5.6) represents the portion of plastic power dissipated into heat. As indicated here,  $K_1(\Theta)$  will be found to be temperature-dependent.  $K_2$  is a thermal transport coefficient that controls how rapidly the system relaxes toward the ambient temperature  $T_0$ , that is,  $\Theta \to \Theta_0 = T_0/T_P$ . This coefficient turns out to be small for the situations reported here. Nevertheless, it cannot be neglected, especially for small twist rates. In principle, after long enough times of steady deformation, systems must reach steady-state temperatures determined by the balance between heating and cooling terms in Eq. (5.6).

# 5.3. Hardening of Copper Bars in Torsion

#### 5.3.1. Discretization and parameter identification

#### Discretization:

Torsion experiment of copper bars under a low strain rate (Horstemeyer et al., 2002) leads the sample free from temperature variation in the material body. Therefore, the equation of motion for ordinary temperature (5.6) is not under consideration. For the purpose of numerical integration of the system of equations (5.1)-(5.5), let us introduce the following variables and quantities

$$\tilde{r} = r/R, \quad \tilde{\tau} = \tau/\mu, \quad \tilde{\rho} = a^2 \rho, \quad \tilde{\chi} = \frac{\chi}{e_D}, \quad \phi = R\omega/\eta, \quad \eta = \frac{\pi R}{180^{\circ} L}.$$
 (5.7)

The variable  $\tilde{r}$  changes from zero to 1. The variable  $\phi$  has the meaning of the total twist angle measured in degree (in (Horstemeyer *et al.*, 2002)  $\phi$  changes from zero to  $\phi_* = 73.35^{\circ}$ ). The calculation of the torque as a function of  $\phi$  is convenient for the later comparison with the torque-twist curve from (Horstemeyer *et al.*, 2002). Then we rewrite Eq. (5.2) in the form

$$q(\tau, \rho) = -\frac{b}{a}\tilde{q}(\tilde{\tau}, \tilde{\rho}), \tag{5.8}$$

where

$$\tilde{q}(\tilde{\tau}, \tilde{\rho}) = \sqrt{\tilde{\rho}} [\tilde{f}_P(\tilde{\tau}, \tilde{\rho}) - \tilde{f}_P(-\tilde{\tau}, \tilde{\rho})]. \tag{5.9}$$

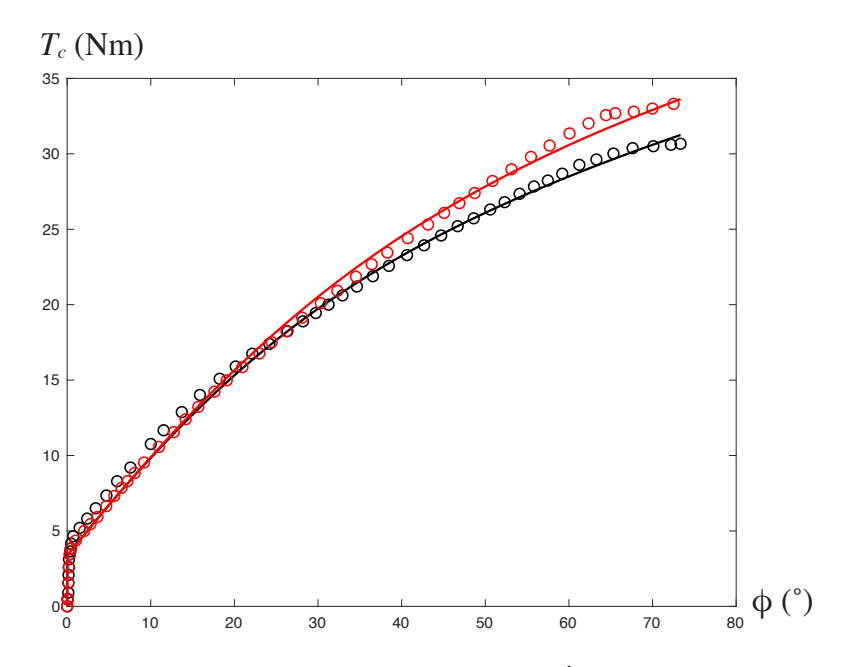


Figure 5.3.: The torque-twist curves at the twist rate  $\dot{\phi} = 0.25^{\circ}/\text{s}$  and for room temperature: (i) sample 1: TDT-theory: black curve, experiment (Horstemeyer et al., 2002): black circles (ii) sample 2: TDT-theory: red/dark gray curve, experiment (Horstemeyer et al., 2002): red/dark gray circles

We set  $\tilde{\mu}_T = (b/a)\mu_T = \mu s$  and assume that s is independent of temperature and strain rate. Then

$$\tilde{f}_P(\tilde{\tau}, \tilde{\rho}) = \exp\left[-\frac{1}{\Theta}e^{-\tilde{\tau}/(s\sqrt{\tilde{\rho}})}\right].$$
 (5.10)

We define  $\tilde{\varpi}_0 = (a/b)R\varpi_0$  so that  $q/(R\varpi_0) = \tilde{q}/\tilde{\varpi}_0$ . Function  $\nu$  in Eq. (5.4) becomes

$$\tilde{\nu}(\Theta, \tilde{\rho}, \tilde{\varpi}_0 \tilde{r}) \equiv \ln\left(\frac{1}{\Theta}\right) - \ln\left[\ln\left(\frac{\sqrt{\tilde{\rho}}}{\tilde{\varpi}_0 \tilde{r}}\right)\right]. \tag{5.11}$$

The dimensionless steady-state quantities are

$$\tilde{\rho}^{ss}(\tilde{\chi}) = e^{-1/\tilde{\chi}}, \quad \tilde{\chi}_0 = \chi_0/e_D. \tag{5.12}$$

Using  $\tilde{q}$  instead of q as the dimensionless measure of plastic strain rate means that we are effectively rescaling  $t_0$  by a factor b/a. Since  $t_0^{-1}$  is a microscopic attempt frequency, of the order  $10^{12}\,\mathrm{s}^{-1}$ , we take  $(a/b)t_0=10^{-12}\mathrm{s}$ .

In terms of the introduced quantities, the governing equations read

$$\frac{\partial \tilde{\tau}}{\partial \phi} = \eta \left[ \tilde{r} - \frac{\tilde{q}(\tilde{\tau}, \tilde{\rho})}{\tilde{\omega}_{0}} \right], 
\frac{\partial \tilde{\rho}}{\partial \phi} = \eta K_{\rho} \frac{\tilde{\tau} \, \tilde{q}}{\tilde{\nu}(\Theta, \tilde{\rho}, \tilde{\omega}_{0}\tilde{r})^{2} \, \tilde{\omega}_{0}} \left[ 1 - \frac{\tilde{\rho}}{\tilde{\rho}^{ss}(\tilde{\chi})} \right], 
\frac{\partial \tilde{\chi}}{\partial \phi} = \eta K_{\chi} \frac{\tilde{\tau} \, \tilde{q}}{\tilde{\omega}_{0}} \left( 1 - \frac{\tilde{\chi}}{\tilde{\chi}_{0}} \right).$$
(5.13)

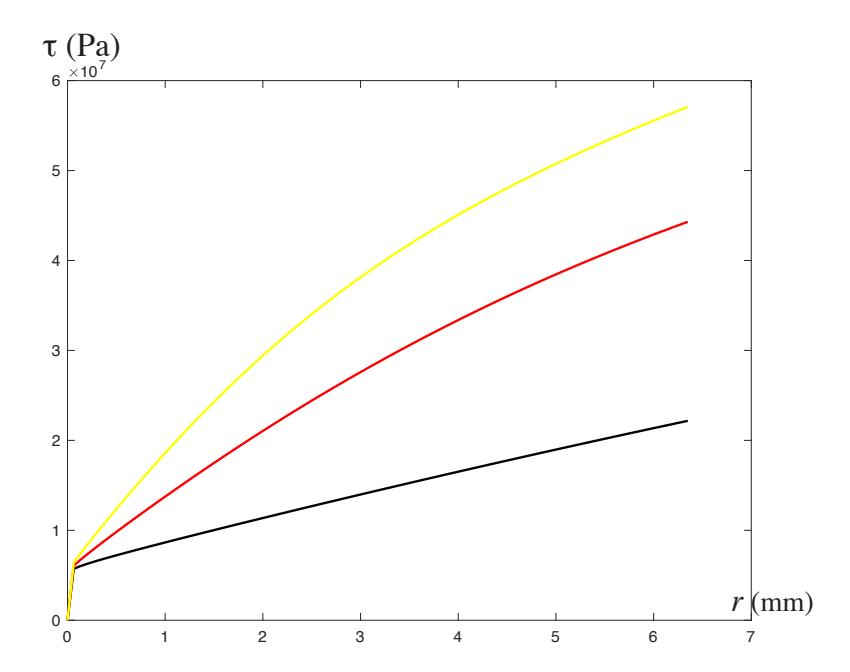


Figure 5.4.: Stress distribution  $\tau(r)$  at the twist rate  $\dot{\phi} = 0.25^{\circ}/\text{s}$  and for room temperature: (i)  $\phi = 10^{\circ}$  (black), (ii)  $\phi = 30^{\circ}$  (red/dark gray), (iii)  $\phi = 50^{\circ}$  (yellow/light gray).

To solve this system of differential equations subject to initial conditions numerically, we discretize the equations in the interval  $(0 < \tilde{r} < 1)$  by dividing it into n subintervals of equal length  $\Delta \tilde{r} = 1/n$  and writing the corresponding equations at n nodes  $\tilde{r}_i = i\Delta \tilde{r}, i = 1, ..., n$ . In this way, we reduce the three differential equations depending on  $\tilde{r}$  to a system of 3n ordinary differential equations at n nodes that will be solved by Matlab-ode15s.

The torque as function of the twist angle can be easily computed by the following formula, once the governing equations are solved

$$T_c = 2\pi\mu R^3 \int_0^1 \tilde{\tau}\tilde{r}^2 d\tilde{r}. \tag{5.14}$$

## Parameter identification:

Following the procedure in Sec. 4.4, we list the five system-specific parameters and two initial conditions from each sample required to simulate the theoretical torque-twist curves. The five basic parameters are the following: the activation temperature  $T_P$ , the stress ratio s, the steady-state scaled effective temperature  $\tilde{\chi}_0$ , and the two dimensionless conversion factors  $K_\rho$  and  $K_\chi$ . We also need initial values of the scaled dislocation density  $\tilde{\rho}_i$  and the effective disorder temperature  $\tilde{\chi}_i$ ; all of which are determined by the sample preparation. The other parameters required for numerical simulations but known from the experiment are: the ambient temperature  $T=298\mathrm{K}$ , the shear modulus  $\mu=48\mathrm{GPa}$ , the length  $L=17.6\mathrm{mm}$  and radius  $R=6.35\mathrm{mm}$  of the bar, the length of Burgers vector  $b=2.55\mathrm{\mathring{A}}$ , the twist rate  $\dot{\phi}=0.25^\circ/\mathrm{s}$ , and consequently,  $\tilde{\omega}_0=1.57427\times10^{-15}/\mathrm{s}$ . Since a corresponds to the smallest admissible distance between dislocations in the state of maximum disorder in crystal, we take a=10b. Note that a only affects the dislocation density, not the torque-twist curves.

It is believed that the energy barrier  $T_P$  and other characteristics in torsion deformation

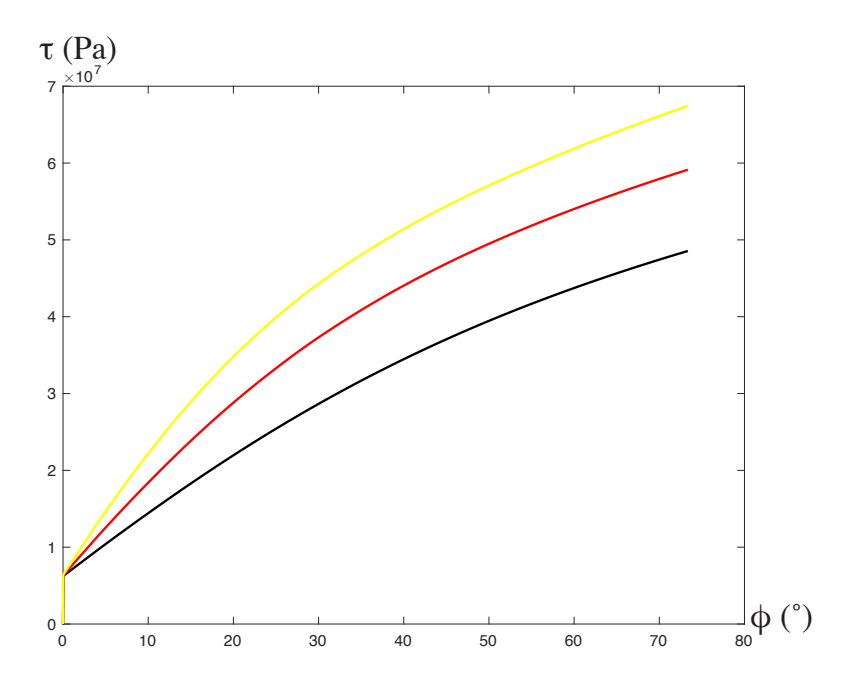


Figure 5.5.: Stress-twist curves at particular position of r at the twist rate  $\dot{\phi} = 0.25^{\circ}/\text{s}$  and for room temperature: (i) r = 3.18mm (black), (ii) r = 4.76mm (red/dark gray), (iii) r = 6.35mm (yellow/light gray).

of the single crystal may differ from those of polycrystals. Therefore, although the same materials are used in the experiment and the same deformation mode are applied, the parameters found in the previous chapter can not be used here. For the same reason that the deformation in this work is non-uniform and no steady-state situation appears in the experimental torque-twist curve, we cannot utilize the strategy used in (Langer et al., 2010) that directly evaluate some required parameters from the experiment.

#### Large scale least-squares:

We have resorted to the large scale least-squares analyses (Le & Tran, 2017) in order to find the parameters. That is, we have solved the system of ordinary differential equations (ODEs) numerically, provided a set of material parameters is known. Based on this numerical solutions, we then computed the sum of the squares of the differences between our theoretical torque-twist curves and a large set of selected experimental points and minimized this sum in the space of the parameters. We form the sum of squares as

$$f_{min}(T_P, s, \tilde{\chi}_0, K_\rho, K_\chi, \tilde{\chi}_i, \tilde{\rho}_i) = \sum_{i=1}^N (T_c^*(\phi_i) - (T_c^{ex})_i)^2$$

where  $(T_c^{\text{ex}})_i$  denotes the data points of torque measured in the experiment at selected twist angle  $\phi_i$  and  $(T_c^*)_i$  corresponds to the numerical output of the torque at  $\phi_i$ . N is the total number of points. Note that, solving the system of equation (5.13) with given seven parameters provides us the flow stress in terms of the twist angle in degree and by (5.14) we compute the torque at desired twist angle. The parameters are supposed to make  $f_{min}$  as small as possible. Since  $f_{min}$  has many local minima, the parameters for global minimum cannot be guaranteed. However, we will see that the found values are reliable, for the corresponding  $f_{min}$  is small enough. The ODEs were solved numerically using the Matlab-ode15s, while the finding of least squares was realized with the Matlab-globalsearch. To keep the calculation time manageable and

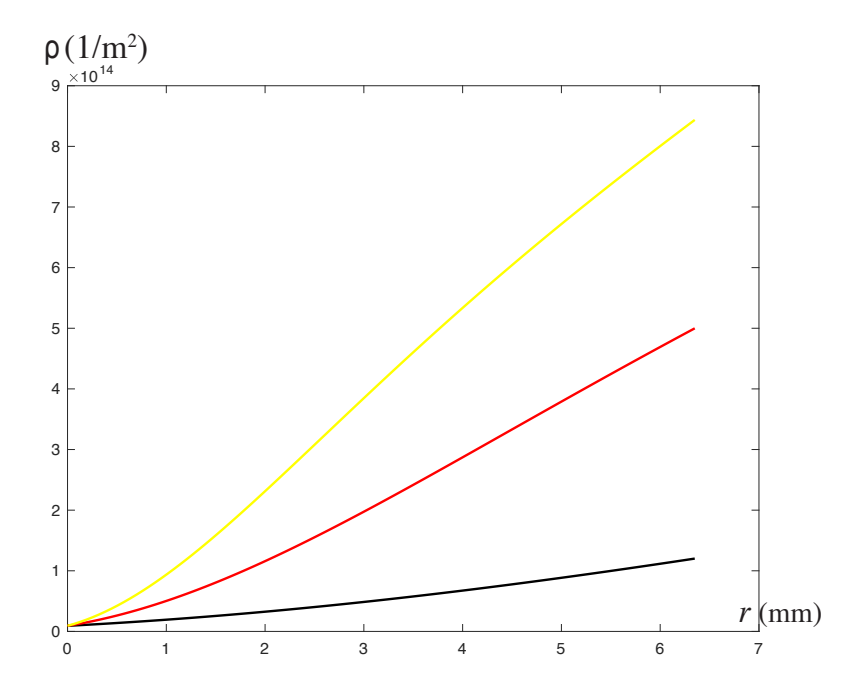


Figure 5.6.: Total density of dislocations  $\rho(r)$  at the twist rate  $\dot{\phi} = 0.25^{\circ}/\text{s}$  and for room temperature: (i)  $\phi = 10^{\circ}$  (black), (ii)  $\phi = 30^{\circ}$  (red/dark gray), (iii)  $\phi = 50^{\circ}$  (yellow/light gray).

simultaneously ensure the accuracy, we have chosen n=1000 and the  $\phi$ -step equal to  $\phi_*/7335$ . We have found that the torque-twist curves for both samples taken from (Horstemeyer et~al., 2002) can be fitted with just a single set of system parameters. These are:  $T_P=26976\,\mathrm{K}$ , s=0.0152,  $\chi_0=0.2496$ ,  $K_\rho=50.3$ ,  $K_\chi=377$ . The initial parameters for sample 1 are:  $\tilde{\rho}_{i1}=6.04\times10^{-5}$ ,  $\tilde{\chi}_{i1}=0.187$ , while for sample 2 we have:  $\tilde{\rho}_{i2}=6\times10^{-5}$ , and  $\tilde{\chi}_{i2}=0.2$ . The precision of the fit could be measured by the minimum of the sum of squares, which is equal to  $f_{min}=48.442\,\mathrm{N^2m^2}$  in this case. Note that  $f_{min}$  also depends on the number of points selected from the experimental torque-twist curves. The mean square of the deviation (or the square of the error per point) can be characterized by  $f_{min}/N$ . We took 48 points from each curve of (Horstemeyer et~al., 2002), so the mean square of the deviation is approximately 0.5 N<sup>2</sup>m<sup>2</sup>. Numerous numerical results of the least-squares analysis with the disturbed torque-twist curves (not shown here) confirm that our method for parameter identification is robust against small experimental uncertainties.

#### 5.3.2. Numerical simulations:

With the identified parameters, we can now simulate the torque-twist curves for the single crystal copper bars. The result is presented in Fig. 5.3. In this figure, the circles represent the selected experimental points in (Horstemeyer *et al.*, 2002) while the solid curves are our theoretical simulation. One can see that even the initial yielding transition appears to be described accurately by this theory. There are only two visible discrepancies: for sample 1 and for  $\phi \in (0^{\circ}, 25^{\circ})$ , the torques are slightly above those predicted by the theory, and for large twist angles  $(\phi > 70^{\circ})$  they are slightly below those predicted by the theory. For sample 2, the torques are slightly above those predicted by the theory for  $\phi \in (60^{\circ}, 70^{\circ})$ . Nothing about this result leads us to believe that there are relevant physical ingredients missing in the theory.

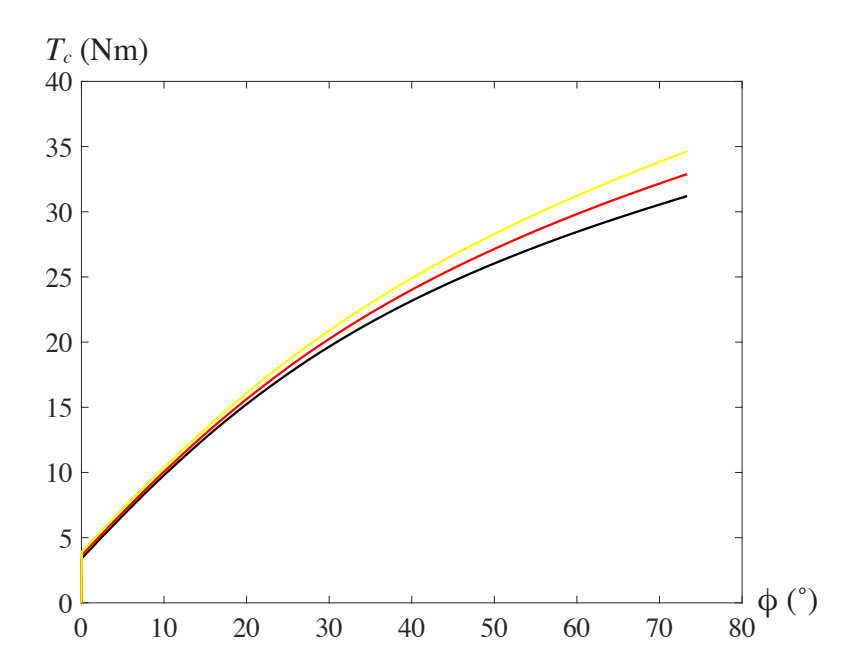


Figure 5.7.: The torque-twist curves for the bars twisted at different twist rates and for room temperature: (i)  $\dot{\phi} = 0.25^{\circ}/\text{s}$  (black), (ii)  $\dot{\phi} = 2.5^{\circ}/\text{s}$  (red/dark gray), (iii)  $\dot{\phi} = 25^{\circ}/\text{s}$  (yellow/light gray).

The results of numerical simulations for other quantities using the above set of parameters and the initial values of sample 1 are shown in Figs. 5.4-5.8. We plot in Fig. 5.4 the shear stress distribution  $\tau$  at three different twist angles  $\phi = 10^{\circ}$  (black),  $\phi = 30^{\circ}$  (red/dark gray), and  $\phi = 50^{\circ}$  (yellow/light gray). In a small elastic zone near the center of the cross-section, the stress depends linearly on r. In the plastic zone, the stress does not remain constant, but increases with increasing r and reaches a maximum at r = R, as opposed to the similar distribution obtained by the phenomenological theory of ideal plasticity. This exhibits the hardening behavior due to the entanglement of dislocations. In Fig. 5.5, it shows that the stress at three particular positions of r axis increase as the twist angle increases. It is not only those three points but all points in the cross-section showing the hardening behavior. However, it is not the case for the softening that will be shown in the next section. Fig. 5.6 presents the density of dislocations at the above three different twist angles. The density of dislocations is an increasing function of r and achieves the highest value at r = R.

Another interesting question is how strongly the twist rate and ambient temperature affect the torque-twist curve. Fig. 5.7 shows the three torque-twist curves for three samples loaded at the room temperature and three different twist rates  $\dot{\phi}=0.25^{\circ}/\text{s}$  (black),  $\dot{\phi}=2.5^{\circ}/\text{s}$  (red/dark gray), and  $\dot{\phi}=25^{\circ}/\text{s}$  (yellow/light gray). The radius of the samples is R=6.35mm, while all other parameters remain unchanged. We see that the twist rate affects the strain hardening: the higher the twist rate, the higher the slope of the torque-twist curve. Fig. 5.8 shows the three torque-twist curves for three samples loaded at the same twist rate  $\dot{\phi}=0.25^{\circ}/\text{s}$  but at three different ambient temperatures:  $T=25^{\circ}\text{C}$  (black),  $T=250^{\circ}\text{C}$  (red/dark gray), and  $T=500^{\circ}\text{C}$  (yellow/light gray). Thus, the higher the temperature, the lower the slope of the torque-twist curve and the smaller the hardening. As far as the size effect is concerned, we could not find reliable experimental data for single crystal copper under torsion at different bar radii, in contrast to twisted polycrystalline copper wires of different radii

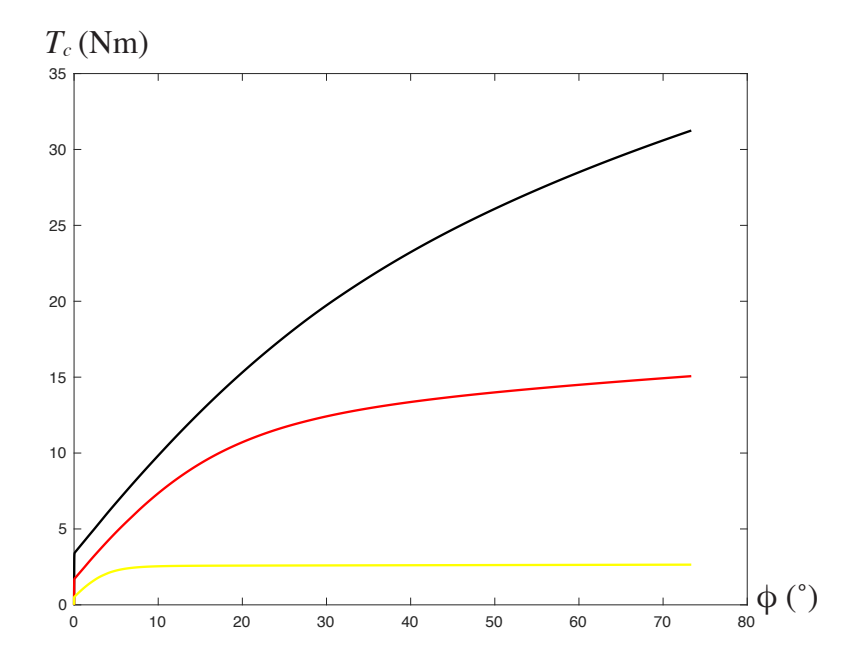


Figure 5.8.: The torque-twist curves for the bars twisted at the same twist rate  $\dot{\phi}=0.25^{\circ}/\mathrm{s}$  and for three different ambient temperatures: (i)  $T=25^{\circ}\mathrm{C}$  (black), (ii)  $T=250^{\circ}\mathrm{C}$  (red/dark gray), (iii)  $T=500^{\circ}\mathrm{C}$  (yellow/light gray).

(Liu et al., 2012).

# 5.4. Thermal Softening during High-temperature Torsion of Aluminum Bars

## 5.4.1. Discretization and parameter identification

#### Discretization:

The experiment (Zhou & Clode, 1998) was performed over a wide range of strain rate, and the inhomogeneous temperature distribution is observed in the sample body. Hence, we need to add (5.6) into the governing equations. For the purpose of numerical integration of the system of equations (5.1)-(5.6), let us introduce the following dimensionless variables and quantities

$$\tilde{r} = r/R, \quad \tilde{\rho} = a^2 \rho, \quad \tilde{\chi} = \frac{\chi}{e_D}, \quad \tilde{\omega} = R\omega.$$
 (5.15)

The dimensionless variable  $\tilde{r}$  changes from zero to 1. The dimensionless variable  $\tilde{\omega}$  has the meaning of the maximum shear strain achieved at the outer radius. Since shear modulus  $\mu(\Theta)$  varies with different temperature, the stress is kept unnormalized, which makes the normalization differ from those in Sec. 5.3. The calculation of the rescaled torque  $\tilde{T}_c = T_c/R^3$  as a function of  $\tilde{\omega} = \omega R$  is convenient for the later comparison with the experimental data from (Zhou & Clode, 1998). Then we rewrite Eq. (5.2) in

the form

$$q(\tau, \rho) = -\frac{b}{a}\tilde{q}(\tau, \tilde{\rho}), \tag{5.16}$$

where

$$\tilde{q}(\tau,\tilde{\rho}) = \sqrt{\tilde{\rho}} [\tilde{f}_P(\tau,\tilde{\rho}) - \tilde{f}_P(-\tau,\tilde{\rho})]. \tag{5.17}$$

We set  $\tilde{\mu}_T = (b/a)\mu_T = \mu(\Theta)s$  and assume that s is independent of temperature and strain rate. Then

$$\tilde{f}_P(\tau, \tilde{\rho}) = \exp\left[-\frac{1}{\Theta}e^{-\tau/(\mu(\Theta)s\sqrt{\tilde{\rho}})}\right].$$
 (5.18)

We define  $\tilde{\varpi}_0 = (a/b)R\varpi_0$  so that  $q/(R\varpi_0) = \tilde{q}/\tilde{\varpi}_0$ . Function  $\nu$  in Eq. (5.4) becomes

$$\tilde{\nu}(\Theta, \tilde{\rho}, \tilde{\varpi}_0 \tilde{r}) \equiv \ln\left(\frac{1}{\Theta}\right) - \ln\left[\ln\left(\frac{\sqrt{\tilde{\rho}}}{\tilde{\varpi}_0 \tilde{r}}\right)\right]. \tag{5.19}$$

The dimensionless steady-state quantities are

$$\tilde{\rho}_{ss}(\tilde{\chi}) = e^{-1/\tilde{\chi}}, \quad \tilde{\chi}_0 = \chi_0/e_D. \tag{5.20}$$

Using  $\tilde{q}$  instead of q as the dimensionless measure of plastic strain rate means that we are effectively rescaling  $t_0$  by a factor b/a. Since  $t_0^{-1}$  is a microscopic attempt frequency, of the order  $10^{12} \, \mathrm{s}^{-1}$ , we take  $(a/b)t_0 = 10^{-12} \mathrm{s}$ .

In terms of the introduced quantities the governing equations read

$$\frac{\partial \tau}{\partial \tilde{\omega}} = \mu(\Theta) \left[ \tilde{r} - \frac{\tilde{q}(\tau, \tilde{\rho})}{\tilde{\omega}_{0}} \right], 
\frac{\partial \tilde{\rho}}{\partial \tilde{\omega}} = K_{\rho} \frac{\tau \, \tilde{q}}{\mu(\Theta) \tilde{\nu}(\Theta, \tilde{\rho}, \tilde{\phi}_{0} \tilde{r})^{2} \, \tilde{\omega}_{0}} \left[ 1 - \frac{\tilde{\rho}}{\tilde{\rho}^{ss}(\tilde{\chi})} \right], 
\frac{\partial \tilde{\chi}}{\partial \tilde{\omega}} = K_{\chi} \frac{\tau \, \tilde{q}}{\mu(\Theta) \tilde{\omega}_{0}} \left( 1 - \frac{\tilde{\chi}}{\tilde{\chi}_{0}} \right), 
\frac{\partial \Theta}{\partial \tilde{\omega}} = K_{1}(\Theta) \frac{\tau \, \tilde{q}}{\mu(\Theta) \tilde{\omega}_{0}} - \frac{\tilde{K}_{2}}{\tilde{\omega}_{0}} (\Theta - \Theta_{0}),$$
(5.21)

where  $\tilde{K}_2 = (a/b)K_2$ . To solve this system of differential equations subject to initial conditions numerically, we discretize the equations in the interval  $(0 < \tilde{r} < 1)$  by dividing it into n sub-intervals of equal length  $\Delta \tilde{r} = 1/n$  and writing the corresponding equations at n nodes  $\tilde{r}_i = i\Delta \tilde{r}$ , i = 1, ..., n. In this way, we reduce the four differential equations depending on  $\tilde{r}$  to a system of 4n ordinary differential equations at n nodes that will be solved by Matlab-ode23s.

The torque as function of the twist angle can be computed by the following formula

$$T_c = 2\pi R^3 \int_0^1 \tau \tilde{r}^2 d\tilde{r}. \tag{5.22}$$

#### Parameter identification:

Since an additional governing equation is taken into account, eight system-specific parameters and two initial conditions for each sample need to be specified to simulate

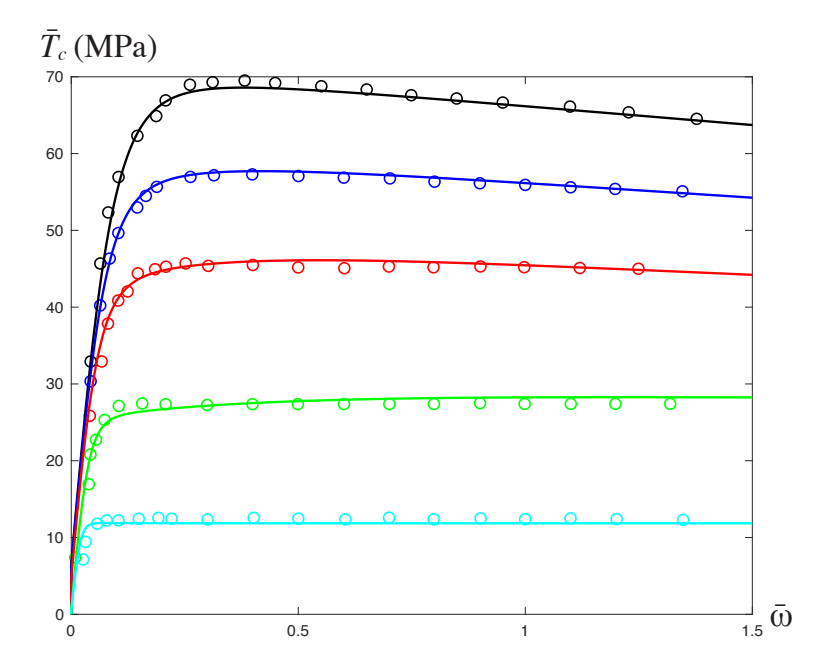


Figure 5.9.: Torque-twist curves for ambient temperature  $T_0 = 773 \,\mathrm{K}$ , and for five different twist rates  $R\dot{\omega} = 19.7/\mathrm{s}$  (black),  $R\dot{\omega} = 6.44/\mathrm{s}$  (blue),  $R\dot{\omega} = 1.84/\mathrm{s}$  (red),  $R\dot{\omega} = 0.21/\mathrm{s}$  (green) and  $R\dot{\omega} = 0.02/\mathrm{s}$  (cyan): (i) TDT (bold lines), (ii) experimental points taken from Zhou & Clode (1998) (circles).

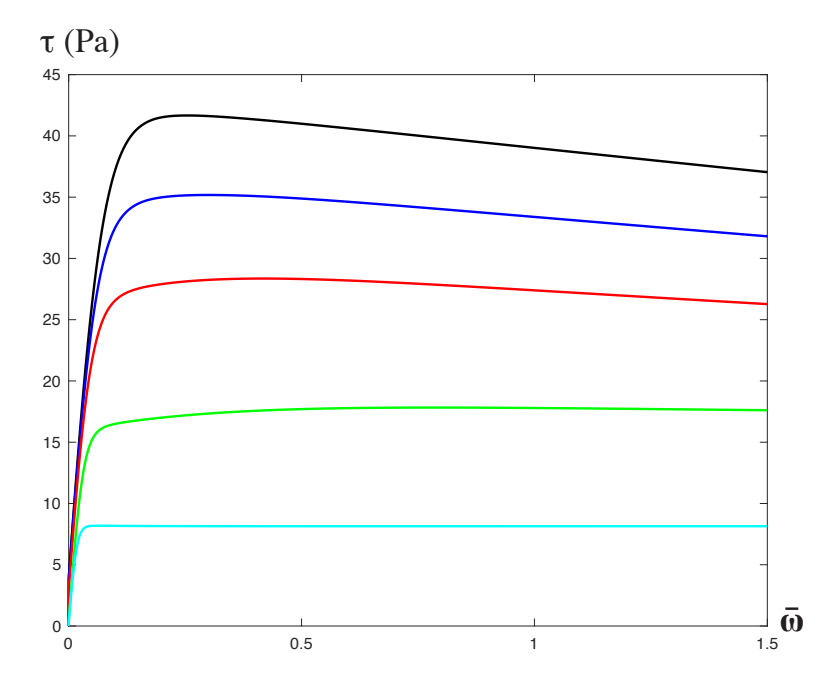


Figure 5.10.: Stress-twist curves at  $r=5 \mathrm{mm}$  for ambient temperature  $T_0=773 \mathrm{~K}$ , and for five different twist rates  $R\dot{\omega}=19.7/\mathrm{s}$  (black),  $R\dot{\omega}=6.44/\mathrm{s}$  (blue),  $R\dot{\omega}=1.84/\mathrm{s}$  (red),  $R\dot{\omega}=0.21/\mathrm{s}$  (green) and  $R\dot{\omega}=0.02/\mathrm{s}$  (cyan).

			, .	/ ( )	
$R\dot{\omega}$ (1/s)	19.7	6.44	1.84	0.21	0.02
$ ilde{ ho}_i$	$7.94 \times 10^{-5}$	$9.49 \times 10^{-5}$	$7.66 \times 10^{-5}$	$1.47 \times 10^{-6}$	$1 \times 10^{-6}$
$\tilde{\chi}_i$	0.245	0.24	0.234	0.225	0.2488

Table 5.1.: The initial values of  $\tilde{\rho}_i$  and  $\tilde{\chi}_i$ 

the theoretical torque-twist curves. These basic parameters include the following six: the activation temperature  $T_P$ , the stress ratio s, the steady-state scaled effective temperature  $\tilde{\chi}_0$ , and the three dimensionless conversion factors  $K_\rho$ ,  $K_\chi$ , and  $\tilde{K}_2$ . In addition, we need a formula for the thermal conversion factor  $K_1(\theta)$  in Eq. (5.6) which is assumed to be a linear function of  $\Theta$ 

$$K_1(\Theta) = K_0 \left[ 1 + c_1 T_P (\Theta - \Theta_0) \right].$$
 (5.23)

The numbers  $K_0$  and  $c_1$  are the two remaining parameters to be determined from the data. We also need initial values of the scaled dislocation density  $\tilde{\rho}_i$  and the effective disorder temperature  $\tilde{\chi}_i$ ; all of which are determined by the sample preparation. Concerning the initial values of the shear stress and the ordinary temperature, we assume that  $\tau_i = 0$  and  $\Theta_i = \Theta_0$ , where  $T_0 = T_P \Theta_0 = 773 \,\mathrm{K}$  is the ambient temperature. The other parameters required for numerical simulations but known from the experiment are: the length  $L = 10 \,\mathrm{mm}$  and radius  $R = 5 \,\mathrm{mm}$  of the bars, and the length of Burgers vector  $b = 2.86 \,\mathrm{Å}$ . Since a corresponds to the smallest admissible distance between dislocations in the state of maximum disorder in crystal, we take a = 10b.

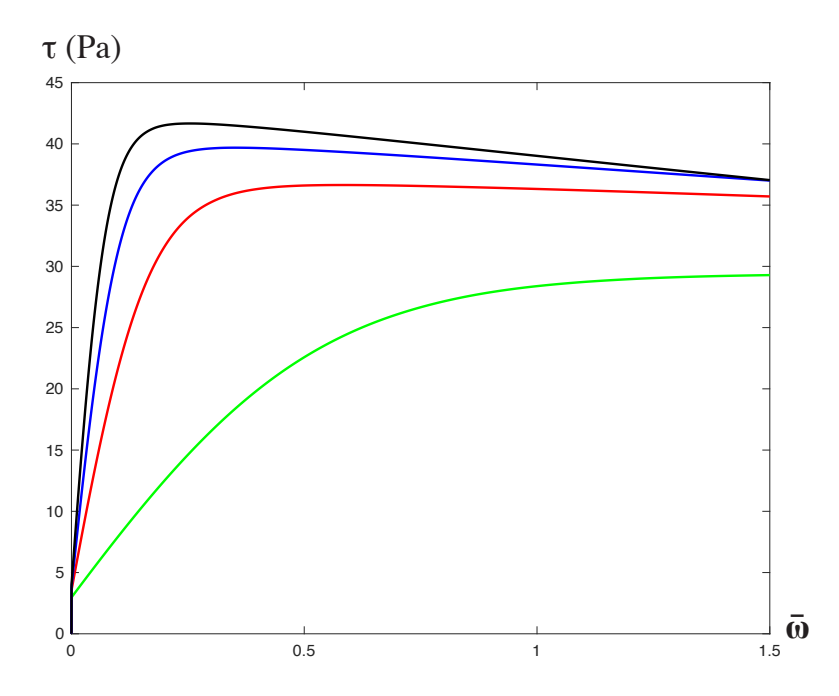


Figure 5.11.: Stress-twist curve for four different position in r axis at ambient temperature  $T_0 = 773 \,\mathrm{K}$  and twist rate  $R\dot{\omega} = 19.7/\mathrm{s}$ :  $r = 5 \mathrm{mm}$  (black),  $r = 3.5 \mathrm{mm}$  (blue),  $r = 2 \mathrm{mm}$  (red),  $r = 0.5 \mathrm{mm}$  (green).

Finally, for the temperature-dependent shear modulus  $\mu(\Theta)$  we use a formula proposed by Varshni (1970)

$$\mu(\Theta) = \mu_1 - \left[ \frac{S_v}{\exp(T_1/T_P \Theta) - 1} \right], \tag{5.24}$$

where  $\mu_1 = 28.8 \,\text{GPa}$ ,  $S_v = 3.44 \,\text{GPa}$ , and  $T_1 = 215 \,\text{K}$ . (These values taken from (Chen *et al.*, 1998) is actually for the aluminum alloy 5182, but since the chemical composition of the aluminum alloy 5252 is very close to that of 5182, we use the same parameters for our alloy.)

We apply the large-scale least-squares analyses utilized in Sec. 4.4 and Sec. 5.3 to find the required parameters. The ODEs were solved numerically using the Matlabode23s, while the finding of least squares was realized with the Matlab-globalsearch. To keep the calculation time manageable and simultaneously ensure the accuracy, we have chosen n=100 and the  $\tilde{\omega}$ -step equal to  $\tilde{\omega}_*/8000$ . Our results appear to be robust against the experimental uncertainties. We have found that the torque-twist curves for five samples taken from (Zhou & Clode, 1998) can be fitted with just a single set of system parameters. These are:  $T_P = 23628 \,\mathrm{K}, s = 0.052, \chi_0 = 0.2489, K_\rho =$ 10.16,  $K_{\chi} = 327.72$ ,  $K_0 = 0.152$ ,  $c_1 = 0.0057$ ,  $\tilde{K}_2 = 1.762 \times 10^{-13}$ . So far as we can tell, our values of  $K_0$  and  $c_1$  are consistent with values of the Taylor-Quinney factor  $\beta$  of the order of unity or less, at least in the range  $T < 900\,\mathrm{K}$  (which is close to the melting temperature). The identified initial values of dislocation densities and disorder temperatures for five samples are shown in Table 5.1, where the first row indicates the twist rates at which the samples are twisted. To obtain the actual initial dislocation densities, we must divide  $\tilde{\rho}_i$  by  $a^2$ , resulting in the order between  $10^{12}$  and  $10^{13}$  dislocations per square meter.

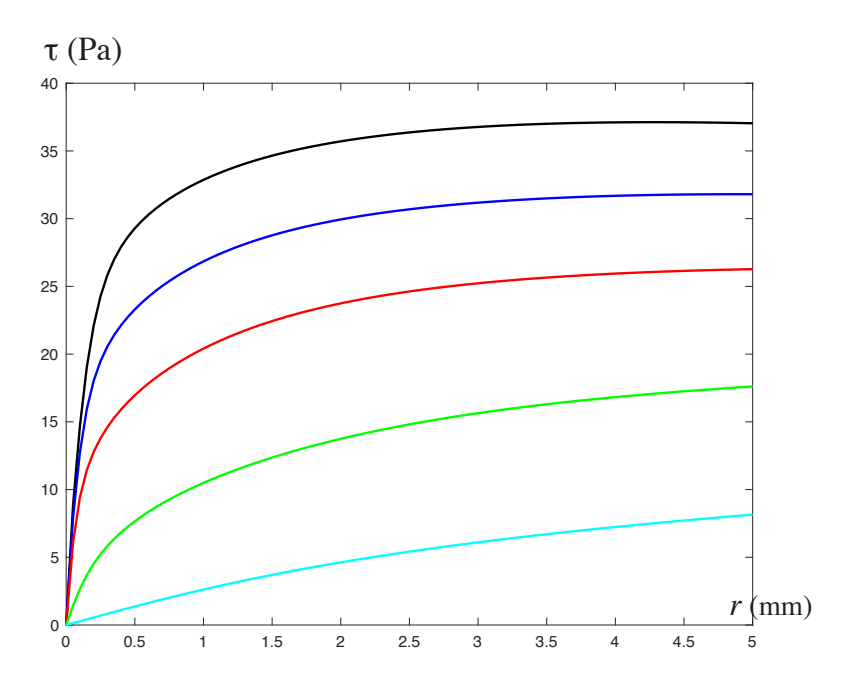


Figure 5.12.: Stress distributions  $\tau(r)$  at  $\bar{\omega}_* = 1.5$  for ambient temperature  $T_0 = 773$  K, and for five different twist rates  $R\dot{\omega} = 19.7/\text{s}$  (black),  $R\dot{\omega} = 6.44/\text{s}$  (blue),  $R\dot{\omega} = 1.84/\text{s}$  (red),  $R\dot{\omega} = 0.21/\text{s}$  (green) and  $R\dot{\omega} = 0.02/\text{s}$  (cyan).

### 5.4.2. Numerical simulations

With the identified parameters we can now simulate the torque-twist curves for bars made of aluminum alloy 5252 undergoing torsional deformations at five different twist

rates  $R\dot{\omega} = 19.7/\text{s}$ , 6.44/s, 1.84/s, 0.21/s, and 0.02/s, and for ambient temperature  $T_0 = 773 \,\text{K}$ . In order to compare with the experimental curves, we use the rescaled torque and twist angle (or effective strain) defined as followed (Zhou & Clode, 1998)

$$\bar{T}_c = \frac{12\sqrt{3}}{8\pi R^3} T_c, \quad \bar{\omega} = \frac{0.722R\omega}{\sqrt{3}}.$$
 (5.25)

Here, the bar accent () indicates the rescaled variables. The result is presented in Fig. 5.9. In this figure, the circles represent the selected experimental points in (Zhou & Clode, 1998) while the solid curves are our theoretical simulation. One can see that even the initial yielding transition appears to be described accurately by this theory. There is only one visible discrepancy: for the twist rate  $R\dot{\omega} = 0.21/s$  the torques are slightly above those predicted by the theory at small  $\bar{\omega}$ . Nothing about this result leads us to believe that there are relevant physical ingredients missing in the theory.

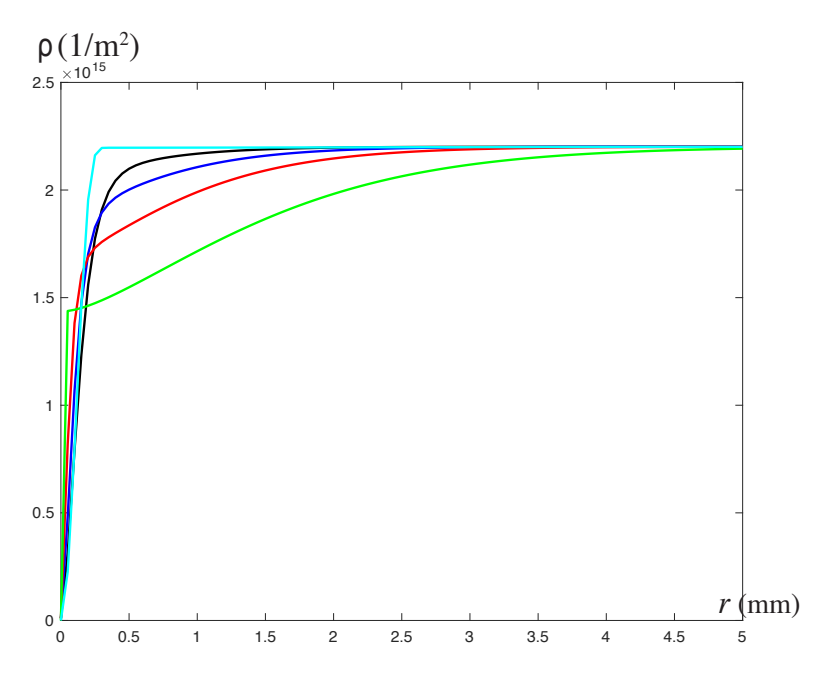


Figure 5.13.: Density of dislocations  $\rho(r)$  at  $\bar{\omega}_* = 1.5$  for ambient temperature  $T_0 = 773 \,\mathrm{K}$ , and for five different twist rates  $R\dot{\omega} = 19.7/\mathrm{s}$  (black),  $R\dot{\omega} = 6.44/\mathrm{s}$  (blue),  $R\dot{\omega} = 1.84/\mathrm{s}$  (red),  $R\dot{\omega} = 0.21/\mathrm{s}$  (green) and  $R\dot{\omega} = 0.02/\mathrm{s}$  (cyan).

The results of numerical simulations for other quantities are shown in Figs. 5.10-5.14. Fig. 5.10 shows the stress-twist curves at the end of cross-section, r=5mm, for five different twist rates. The shape of the outcomes is roughly the same as the results shown in Fig. 5.9 that for the highest three twist rates the stress-twist curves at r=5mm show thermal softening behavior, while in the rest two curves it is not remarkable. Fig. 5.11 also shows stress-twist curves but at different position of r for the twist rate  $R\dot{\omega}=19.7/\mathrm{s}$ . We can observe that the stress keeps increasing in the inner circle of the cross-section as can be seen from the green curve. When it comes to r=2mm, the stress-twist curve exhibits a steady-state respond. Probably, the hardening by dislocation entanglement and the thermal softening due to temperature increase cancel out. However, beyond a certain position in r, it shows clear thermal softening behavior as shown in the curves for r=3.5mm and r=5mm. We plot in Fig. 5.12 the shear stress distribution  $\tau(r)$  at the maximal twist angle  $\bar{\omega}_*=1.5$ . In a small elastic zone near the center of the cross-section, the stress depends linearly on r.

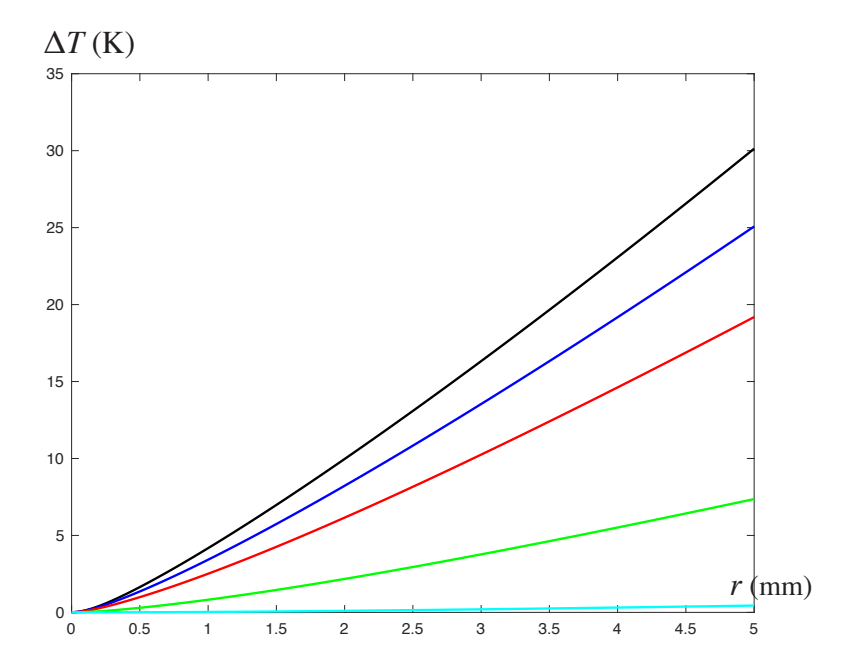


Figure 5.14.: Temperature rise  $\Delta T(r)$  at  $\bar{\omega}_* = 1.5$  for ambient temperature  $T_0 = 773$  K, and for five different twist rates  $R\dot{\omega} = 19.7/\text{s}$  (black),  $R\dot{\omega} = 6.44/\text{s}$  (blue),  $R\dot{\omega} = 1.84/\text{s}$  (red),  $R\dot{\omega} = 0.21/\text{s}$  (green) and  $R\dot{\omega} = 0.02/\text{s}$  (cyan).

In the plastic zone, the stress does not remain constant, but increases with increasing r and reaches a maximum at r = R, as opposed to the similar distribution obtained by the phenomenological theory of ideal plasticity. Fig. 5.13 presents the distributions of the density of dislocations  $\rho(r)$  at the maximal twist angle  $\bar{\omega}_* = 1.5$ . The density of dislocations is an increasing function of r but quickly achieves a nearly constant value in the outer ring  $r_0 < r < R$ , especially for the high twist rates.

Finally, we present in Fig. 5.14 the distribution of the temperature rise  $\Delta T(r)$  at the maximal twist angle  $\bar{\omega}_* = 1.5$ . The temperature rise is a monotonously increasing function of the radius and achieves the maximum at r = R. We see that the higher the twist rate, the higher is the temperature rise. At the highest twist rate  $R\dot{\omega} = 19.7/s$ , the temperature rise at the outer radius is about 30 K. Our theory predicts that the larger temperature increases occur at higher twist rates because the plastic power is larger there. This is confirmed by the calculations of the temperature distribution based on the finite element method provided in Zhou & Clode (1998).

As discussed, when experimental results show a steady-state response in stress-strain curve, parameters  $T_P$ , s, and  $\chi_0$  can be directly extracted. And it makes relatively easier to identify the parameters left. However, when it is not the case, all parameters must be identified using the introduced large-scale least-square method. For comparison, we show in Table 5.2 all values of 5 basic parameters identified from experiments in different circumstances (Dislocation type, chemical element, loading mode). Those basic parameters are believed to vary with type of dislocation, investigated material and loading mode, analogous to the Taylor-Quinney factor. Although each set of parameters are different, they are not randomly given, but remain in the same order. In some cases, like aluminum in two different circumstances, parameters are almost same. Nevertheless, it is still too early to draw a conclusion and, therefore, more investigation on those parameters are needed.

5.5. Conclusion 109

Experiment: Type of dislocation, material Parameters: and loading mode: Shi et al. (1997) Edge dislocation,  $T_P = 24000 \,\mathrm{K}, \, s = 0.040,$ Aluminum polycrystal,  $\chi_0 = 0.249, K_\rho = 24.25,$ Tension  $K_{\chi} = 300$ Screw dislocations, Zhou & Clode (1998)  $T_P = 23628 \,\mathrm{K}, s = 0.052,$ Aluminum polycrystal,  $\chi_0 = 0.2489, K_\rho = 10.16,$ Torsion  $K_{\rm v} = 327.72,$ Liu et al. (2012) Screw dislocation,  $T_P = 19205 \,\mathrm{K}, s = 0.0686,$ 

 $\chi_0 = 0.2089, K_\rho = 57.02,$ 

 $T_P = 26976 \,\mathrm{K}, s = 0.0152,$ 

 $\chi_0 = 0.2496, K_\rho = 50.3,$ 

 $K_{\chi} = 242.8$ 

 $K_{\rm v} = 377$ 

Table 5.2.: Comparison of Parameters

Copper polycrystal,

Screw dislocation,

Copper single-crystal,

Torsion

Torsion

#### 5.5. Conclusion

Horstemeyer et al. (2002)

The results show the principal applicability of a simple extension of TDT to twisted bars of macro sizes where excess dislocations and kinematic hardening can be ignored. Two applications, hardening and thermal softening of bars under torsion, are studies using TDT and the results are very satisfactory. Note that we are now using thermodynamic dislocation theory not only to verify its validity but also as a tool to discover the properties of structural materials. One of the main reasons for the success of this theory is the extreme sensitivity of the plastic strain rate to small changes in the temperature or the stress. This allows the yielding transition and strain hardening to be correctly captured, as can be seen in the torque-twist curves. The proposed theory can serve as a useful guide for the future experimental investigation on the sensitivity of torque-twist curves to twist rate and ambient temperature. In particular, it would be very interesting to perform torsion tests with extremely high twist rates when the samples are bonded to Kolsky bars (cf. (Marchand & Duffy, 1988)). In this case, our theory would predict the runaway instability and shear band formation due to the thermal softening.

## 6. Distribution of Dislocations in Twisted Bar

## 6.1. Introduction

The aim of this chapter is to find the dislocation distribution in equilibrium as a function of the given torque by continuum dislocation theory (Baitsch et al., 2015; Berdichevsky, 2006a; Berdichevsky & Le, 2007; Kochmann & Le, 2008, 2009a; Koster et al., 2015; Le, 2016a,b; Le & Günther, 2014; Le & Nguyen, 2013; Le & Sembiring, 2008a,b, 2009) and compare with the similar results obtained by numerical simulations in Weinberger (2011). To simplify the analysis, we assume that the crystal is elastically isotropic, and all dislocations are screw. Besides, the side boundary of the bar is traction free and may, therefore, attract dislocations. Various formulation of the defect energy appeared in the literature, such as quadratic defect energy (Wulfinghoff et al., 2013), rank-one (Kametani et al., 2012; Klusemann et al., 2013; Wulfinghoff et al., 2014) and logarithmic defect energy (Berdichevsky, 2006b), a nonlinear function that is product of linear and logarithmic function (Zaiser, 2015; Wulfinghoff & Böhlke, 2015; Berdichevsky, 2016). We adopt the defect energy formulation found by Berdichevsky (2016) that is asymptotically exact in the continuum limit. If the dissipation is neglected, the displacement and the plastic distortion should be found by the energy minimization. First, we show that the dislocation distribution minimizing the energy of the bar with zero torque is uniform. This agrees well with the result obtained by Weinberger (2011). Next, for the bar loaded by a non-zero torque, we find an energetic threshold for the dislocation nucleation. If the twist exceeds this threshold, excess dislocations appear to minimize the energy. It turns out that there is a dislocation-free zone at the outer ring of the bar's cross-section. The non-uniform distribution of dislocations in equilibrium, as well as the twist angle, are found in terms of the given torque. Furthermore, the evolution of plastic warping is compared with those reported in Kaluza & Le (2011) and Liu et al. (2018). In case the dissipation due to the resistance to dislocation motion is taken into account, the energy minimization should be replaced by a variational equation. The solution is shown to have an elastic core region in the middle of the cross-section. Dislocations are concentrated in a ring between two dislocation-free zones. This leads to the change of the stress distribution, increasing the dissipative threshold of the torque. We show that the dislocation-free zones, as well as the threshold in twist angle, depend on the radius of the bar's cross-section exhibiting the size effect. We compare the torque-twist curve with the experimental curve obtained in Horstemeyer et al. (2002) that shows a good agreement in the range of small plastic twist angles. We compare dislocation distributions in a bar of macroscale and a microwire, which shows that the size of samples influences the dislocation distribution.

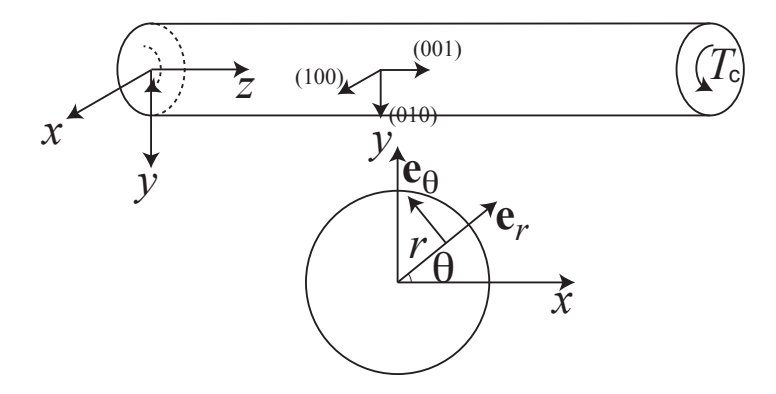


Figure 6.1.: A single crystal bar loaded in torsion and its cross section

## 6.2. Asymptotically Exact Energy of the Bar

Consider a single crystal bar (or wire) of length L loaded in torsion by given torques  $\pm T_c$  acting at its ends. Let  $\mathcal{A}$  be the cross-section of the bar by planes  $z=\mathrm{const.}$  For simplicity, we consider  $\mathcal{A}$  to be a circle of radius R (see Fig. 6.1). The side boundary of the bar  $\partial \mathcal{A} \times [0, L]$  is free from tractions. The length of the bar is assumed to be much larger than the radius  $(L \gg R)$  to neglect the end effects. If the torque  $T_c$  is sufficiently small, it is natural to assume that the bar deforms elastically so that the twist is proportional to the torque, provided the bar is initially dislocation-free. If  $T_c$  exceeds some critical value, then screw dislocations may appear. We assume that the active slip planes are perpendicular to the vectors  $\mathbf{e}_{\theta}$  in the cylindrical coordinate system, while the slip directions, as well as the dislocation lines, are parallel to the z-axis. Mention that this assumption is not likely to be realistic for single crystals. However, since the Burgers vector is parallel to a screw dislocation, any crystallographic plane containing the dislocation is a possible slip plane. Thus, the screw dislocations in single cubic primitive crystals with the Burgers vector parallel to [001] and slip planes of type  $\{mn0\}, m, n$  being any irreducible pair of integers, may approximately be regarded as showing a continuously varying crystal orientation (see Fig. 6.1). Likewise, the screw dislocations in single hcp-crystals with the Burgers vector parallel to [0001] and slip planes of type  $\{11\overline{2}0\}$  may also be considered as satisfying this assumption to some degree. Our aim is to determine the distribution of dislocations as a function of  $T_c$  by the continuum dislocation theory. For screw dislocations with the slip planes perpendicular to the vector  $\mathbf{e}_{\theta}$ , the tensor of plastic distortion,  $\beta_{ij}$ , has only one nonzero component  $\beta_{z\theta} \equiv \beta$ . Function  $\beta$  can be interpreted as the plastic warping, and, by the symmetry reasoning, we assume that  $\beta$  depends only on r-coordinate:  $\beta = \beta(r)$ . The only non-zero components of the plastic strain tensor are given by

$$\varepsilon_{\theta z}^p = \varepsilon_{z\theta}^p = \frac{1}{2}\beta(r).$$

For the bar of circular cross-section loaded in torsion, the only non-zero components of the displacement vector are  $u_{\theta}$ , which depends only on r and z:  $u_{\theta} = u_{\theta}(r, z)$ . With the previous equation, we obtain for the components of the elastic strain tensor

$$\begin{split} \varepsilon_{rr}^e &= \varepsilon_{\theta\theta}^e = \varepsilon_{rz}^e = \varepsilon_{zz}^e = 0, \\ \varepsilon_{r\theta}^e &= \frac{1}{2}(u_{\theta,r} - u_{\theta}/r), \quad \varepsilon_{\theta z}^e = \frac{1}{2}(u_{\theta,z} - \beta), \end{split}$$

where the comma in indices denotes the partial derivative with respect to the corresponding coordinate. The only non-zero component of the dislocation density tensor introduced by Nye (1953); Bilby (1955); Kröner (1955),  $\alpha_{ij} = \varepsilon_{jkl}\beta_{il,k}$ , is

$$\alpha_{zz} = \beta_{.r} + \beta/r.$$

Mention that  $\alpha_{zz}da$  presents the resultant Burgers vector of all excess dislocations, whose dislocation lines cross an infinitesimal area da perpendicular to the z-axis. Thus, the number of screw excess dislocations per unit area becomes

$$\rho = \frac{1}{h} |\alpha_{zz}| = \frac{1}{h} |\beta_{,r} + \beta/r|,\tag{6.1}$$

with b being the magnitude of Burgers vector. We require the dislocation density to remain finite everywhere including r = 0, so function  $\beta(r)$  must satisfy the regularity condition

$$\beta(0) = 0. \tag{6.2}$$

Hence, the center line of the bar can be considered as an obstacle hindering the motion of dislocations which have to pile up against it.

Following Kröner (1992), we regard the elastic strain  $\varepsilon_{ij}^e$  and the dislocation density  $\alpha_{ij}$  of excess dislocations as the state variables of the continuum dislocation theory. In addition to these state variables, one should also include the density of redundant dislocations  $\rho^r$  and the effective temperature  $\chi$  into the list of state variables. In the specific problem that the dissipation is neglected, we may first ignore the density of redundant dislocations and the effective temperature in the free energy. However, when the dissipation is taken into account, with the lack of those two state variables, the hardening behavior can not be properly described. The free energy per unit volume of the crystal with dislocations is allowed to depend only on the position vector  $\mathbf{x} = (x, y, z)$  as well as on these state variables. Provided that there are only excess dislocations, we lay down in the continuum limit

$$\psi(\mathbf{x}, \varepsilon_{ij}^e, \alpha_{ij}) = \psi_e(\varepsilon_{ij}^e) + \psi_m(\mathbf{x}, \alpha_{ij}). \tag{6.3}$$

The first term of (6.3) corresponds to the energy contribution due to the elastic strain that also includes the energy of interaction of dislocations, while the second term describes the self-energy of dislocations whose explicit dependence on  $\mathbf{x}$  accounts for the influence of the free boundary (Eshelby, 1953). Berdichevsky (2016) has solved the eigenstrain problem of a bar containing a large number of screw dislocations of the equal sign and found the free energy density of an elastically isotropic dislocated crystal bar which we present in the form

$$\psi(\mathbf{x}, \varepsilon_{ij}^e, \alpha_{ij}) = \frac{1}{2}\mu(\varepsilon_{r\theta}^e)^2 + \frac{1}{2}\mu(\varepsilon_{\theta z}^e)^2 + \frac{\mu b^2}{4\pi}f(r/R)\rho, \tag{6.4}$$

where  $\mu$  is the shear modulus,  $f(r/R) = \ln(1 - r^2/R^2) + \ln\frac{R}{r_0} + 1/4$ , with  $r_0$  being the cut-off radius of the dislocation core. The first two terms of (6.4) correspond to the energy contribution due to the elastic strain, the third term is the self-energy of dislocations, with  $\frac{\mu b^2}{4\pi} \ln(1 - r^2/R^2)$  being dislocation-boundary interaction energy and  $\frac{\mu b^2}{4\pi} (\ln\frac{R}{r_0} + 1/4)$  the self-energy of one dislocation without dislocation-boundary interaction. The summand 1/4 in the last term is due to the method of regularization

of plastic distortion within the cut-off radius of the dislocation core as a "smeared out" delta function, so altogether we can present this self-energy without dislocation-boundary interaction as  $\frac{\mu b^2}{4\pi} (\ln \frac{R}{r_0} + 1/4) = \frac{\mu b^2}{4\pi} \ln \frac{R}{r_c}$  and interpret  $r_c$  as the "effective" radius of the dislocation core. Note that function f(r/R) is well defined only for r having a distance larger than  $r_0/2$  to the side boundary r = R. For  $r \in (R - r_0/2, R)$  we set f(r/R) = 1/4. The plot of function f(x) for  $R/r_0 = 10^4$  is show in Fig. 6.2.

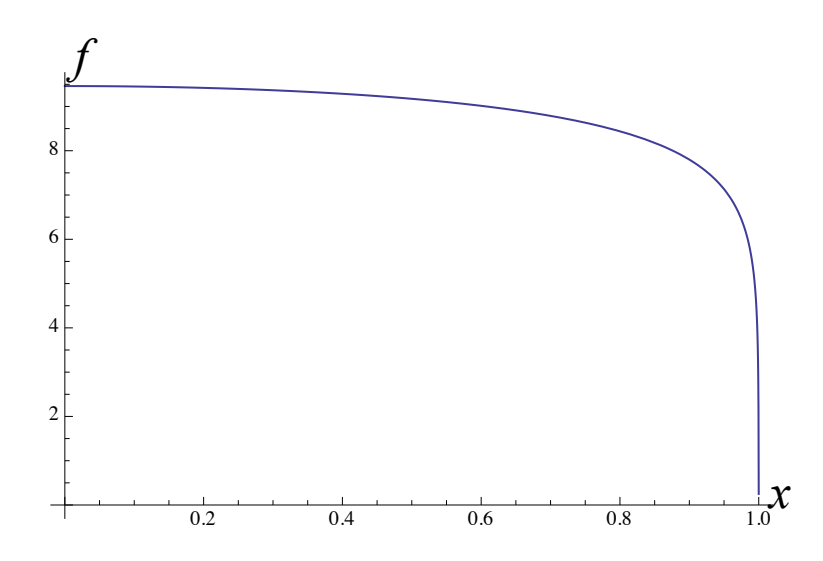


Figure 6.2.: Function f(x) for  $R/r_0 = 10^4$ .

According to Berdichevsky's classification, the first two terms are the main terms, while the last term belongs to the small correction term that is comparable with the error in obtaining the first two terms in the continuum limit for the ensemble of randomly distributed dislocations and should, therefore, be neglected. However, if we do averaging in the spatial way in which the volume of the bar is divided into a large number of boxes such that the number of dislocations in each box is proportional to the dislocation density times the box volume, the errors in obtaining all three terms through averaging have the same order of smallness that tends to zero as sizes of the boxes go to zero. Thus, the last term in the average energy density (6.4), although small compared to the first two due to the smallness of b, has the right of existence in the continuum theory obtained by the spatial averaging procedure. We will see that this small correction term enables one to uniquely determine the distribution of dislocations in terms of the torque.

We assume that the distributed tractions  $t_{\theta} = \pm t(r)$  leading to the torques  $\pm T_c$  act at the ends z = 0, L of the bar. Under the assumption of axial symmetry, the energy functional of the twisted bar reads

$$I(u_{\theta}, \beta) = 2\pi \int_{0}^{L} \int_{0}^{R} \left[ \frac{1}{2} \mu (u_{\theta,r} - \frac{1}{r} u_{\theta})^{2} + \frac{1}{2} \mu (u_{\theta,z} - \beta)^{2} + \frac{\mu b}{4\pi} f(r/R) |\beta_{,r} + \beta/r| \right] r dr dz - 2\pi \int_{0}^{R} t(r) [u_{\theta}(r, L) - u_{\theta}(r, 0)] r dr.$$
 (6.5)

We consider first the case of a free bar with zero traction t(r) = 0 causing no torque.

In this case, the true displacement and plastic warping minimize the energy functional

$$I(u_{\theta}, \beta) = 2\pi \int_{0}^{L} \int_{0}^{R} \left[ \frac{1}{2} \mu (u_{\theta,r} - \frac{1}{r} u_{\theta})^{2} + \frac{1}{2} \mu (u_{\theta,z} - \beta)^{2} + \frac{\mu b}{4\pi} f(r/R) |\beta_{,r} + \beta/r| \right] r dr dz$$
 (6.6)

among all admissible  $u_{\theta}$  and  $\beta$ . Since functional (6.6) is non-negative, the minimizer vanishes identically:  $u_{\theta} = 0$  and  $\beta = 0$ . There is another interesting question in the case of zero torque, first raised by Eshelby (1953) and studied later in Weinberger (2011): provided N screw dislocations exist in the free unloaded bar, how to find the energy minimizing dislocation distribution. Within the proposed theory, the problem reduces to finding  $u_{\theta}$  and  $\beta$  that minimize (6.6) under the constraint

$$2\pi \int_{0}^{R} \rho r dr = \frac{2\pi}{b} \int_{0}^{R} |\beta_{,r} + \beta/r| r dr = N.$$
 (6.7)

This problem can be solved by the variational-asymptotic method (see, e.g., Le (1999)). Since the last term in functional (6.6) is small due to the smallness of b, we neglect it in the first approximation. Then the minimizer that makes the two first terms vanishing reads

$$u_{\theta} = \omega_0 r z, \quad \beta = \omega_0 r,$$
 (6.8)

where  $\omega_0$  can be interpreted as the twist per unit length due to screw dislocations in the free bar. This leads to the uniform dislocation distribution  $\rho = 2\omega_0/b$ .<sup>1</sup> Assuming that  $\omega_0 > 0$  and substituting  $\rho$  into (6.7), we obtain

$$2\pi \int_0^R 2\omega_0/br dr = \frac{2\omega_0}{b}\pi R^2 = N \quad \Rightarrow \quad \omega_0 = \frac{Nb}{2\pi R^2}.$$

If we denote the dimensionless twist per unit length as  $\tilde{\omega}_0 = \omega_0/(b/\pi R^2)$ , then  $\tilde{\omega}_0 = N/2$ . This agrees well with the result obtained by Weinberger (2011) for large N, as shown in Fig. 6.3. Note that, here the notations for denoting the dimensionless energy  $\bar{\mathcal{E}}$  and the normalized twist per unit length  $\bar{\beta}$  in Weinberger (2011) were used. The minimum of energy is found by substituting (6.8) into the energy functional (6.6) where the last term should now be kept because it becomes at this step the principal term. This yields the energy per unit length

$$\mathcal{E} = 2\pi \frac{\mu b^2}{4\pi} \int_0^R 2\omega_0/bf(r/R)rdr = \frac{\mu b^2}{2\pi} (\frac{N}{2}\epsilon_0 + \bar{\mathcal{E}}),$$

where  $\epsilon_0 = \ln \frac{R}{r_0} + 1/4 = \ln \frac{R}{r_c}$  and

$$\bar{\mathcal{E}} = N \int_0^1 \ln(1 - \tilde{r}^2) \tilde{r} d\tilde{r} = -\frac{N}{2}.$$

The comparison with the dimensionless energy  $\bar{\mathcal{E}}$  obtained by Weinberger (2011) is shown in the same Figure, where  $\tilde{r}$  is the dimensionless radius. In contrast to the twist, there is a difference in the slope of  $\bar{\mathcal{E}}$ : in our continuum theory, this slope is -1/2, while Weinberger's numerical simulations give -2 for large N.

<sup>&</sup>lt;sup>1</sup>The more accurate analysis shows that this uniform dislocation distribution for the free bar is asymptotic exact in the limit  $N \to \infty$ .

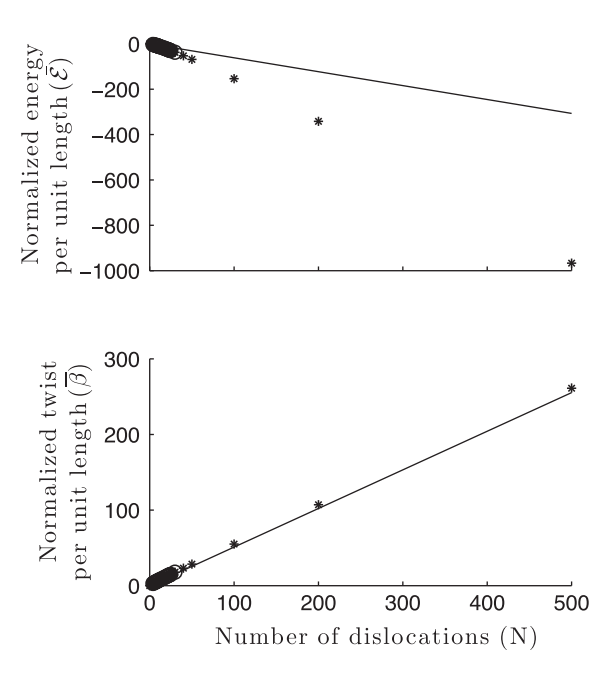


Figure 6.3.: The normalized energy and normalized twist per unit length as functions of the number of dislocations: (i) bold line: The proposed continuum theory, (ii) points: numerical simulations Weinberger (2011).

Assume now that a non-zero torque  $T_c$  is applied. In this case, the true displacement and plastic warping should be found from minimizing functional (6.5). This variational problem can again be solved by the variational-asymptotic method. In the first step, we keep in (6.5) only the first term as the main asymptotic term (Le, 1999). Then the true displacement  $u_{\theta}$  reads

$$u_{\theta}(r,z) = \omega r z,$$

where  $\omega = \phi/L$  corresponds to the twist of the bar per unit length, and  $\phi$  being the total twist angle. Except for the two edges of the bar where  $u_{\theta}$  and  $\beta$  may depend on the detailed distribution of t(r), the energy per unit length in the main part of the bar reduces then to

$$I(\beta) = 2\pi \int_0^R \left[ \frac{1}{2} \mu (r\omega - \beta)^2 + \frac{\mu b}{4\pi} f(r/R) |\beta_{,r} + \beta/r| \right] r dr.$$
 (6.9)

If the resistance to dislocation motion is negligible (and, hence, the dissipation is zero), the true plastic warping minimizes functional (6.9) among all admissible function  $\beta(x)$  satisfying the regularity condition (6.2).

If the resistance to dislocation motion cannot be neglected, then the energy minimization must be replaced by the variational equation (Sedov, 1965)

$$\delta I + 2\pi \int_0^R \frac{\partial D}{\partial \dot{\beta}} \delta \beta r dr = 0, \tag{6.10}$$

where, in case of rate-independent theory,

$$D(\dot{\beta}) = K|\dot{\beta}|.$$

Function  $D(\dot{\beta})$  represents the dissipation potential due to plastic warping, with K being called critical resolved shear stress, and the dot above a function denoting its time derivative. For  $\dot{\beta}=0$  the variational equation (6.10) needs not be satisfied: it is replaced by the equation  $\dot{\beta}=0$ . Note that the dissipation terms due to redundant dislocations and the effective temperature are not taken into account.

## 6.3. Dislocation Distribution at Zero Dissipation

We first analyze the situation when the resistance to dislocation motion is negligible (and, hence, the dissipation is zero). In this case, the determination of  $\beta(r)$  reduces to the minimization problem (6.9). It is convenient to introduce the following dimensionless variable and quantities

$$\tilde{r} = \frac{r}{R}, \quad \tilde{\omega} = R\omega, \quad \tilde{I} = \frac{I}{2\pi\mu R^2}, \quad c_0 = \frac{b}{4\pi R}.$$
 (6.11)

The dimensionless variable  $\tilde{r}$  changes in the interval (0,1). Assuming for definiteness that the dimensionless dislocation density  $\beta_{,\tilde{r}} + \beta/\tilde{r}$  is positive, functional (6.9) reduces to

$$\tilde{I}(\beta) = \int_0^1 \left[ \frac{1}{2} (\tilde{r}\tilde{\omega} - \beta)^2 + c_0 f(\tilde{r}) (\beta_{,\tilde{r}} + \beta/\tilde{r}) \right] \tilde{r} d\tilde{r}, \tag{6.12}$$

where  $f(\tilde{r}) = \ln(1 - \tilde{r}^2) + \epsilon_0$ . We minimize functional (6.12) among functions  $\beta(\tilde{r})$  satisfying the regularity condition  $\beta(0) = 0$ . Because the last gradient term is linear in  $\beta_{\tilde{r}}$ , we allow the plastic warping to have jumped at some point  $\tilde{r} = l$ .

Under the action of sufficiently large Peach-Koehler force due to the positive torque (see, e.g., Le (2010)) positive excess dislocations move toward the middle line of the bar, while the negative move to the free boundary and disappear. Supposed that only excess dislocations inside the bar are considered, then the motion of the negative dislocations lead the bar to have a dislocation-free zone near the side boundary:  $\beta_{,\tilde{r}} + \beta/\tilde{r} = 0$ . In the dislocation-free zone, the equation is satisfied only if  $\beta = \beta_0/\tilde{r}$  for some constant  $\beta_0$ . This leads to the following Ansatz for the minimizer

$$\beta(\tilde{r}) = \begin{cases} \beta_1(\tilde{r}) & \text{for } \tilde{r} \in (0, l), \\ \beta_0/\tilde{r} & \text{for } \tilde{r} \in (l, 1), \end{cases}$$

$$(6.13)$$

where l is an unknown length,  $0 \le l \le 1$ . We admit that  $\beta(\tilde{r})$  may have a jump at  $\tilde{r} = l$ . We have to find  $\beta_1(\tilde{r})$  and the constants,  $\beta_0$ , and l. Thus, the functional becomes

$$\tilde{I} = \int_0^l \left[ \frac{1}{2} (\tilde{r}\tilde{\omega} - \beta_1)^2 + c_0 f(\tilde{r}) \left( \beta_{1,\tilde{r}} + \frac{\beta_1}{\tilde{r}} \right) \right] \tilde{r} d\tilde{r} + \int_l^1 \frac{1}{2} \left( \tilde{r}\tilde{\omega} - \frac{\beta_0}{\tilde{r}} \right)^2 \tilde{r} d\tilde{r}.$$
 (6.14)

Varying energy functional (6.14) with respect to  $\beta_1(\tilde{r})$  we obtain the (non-differential) equation for it in the interval (0, l)

$$-(\tilde{r}\tilde{\omega} - \beta_1)\tilde{r} - c_0 f'(\tilde{r})\tilde{r} = 0,$$

yielding

$$\beta_1(\tilde{r}) = \tilde{r}\tilde{\omega} + c_0 f'(\tilde{r}). \tag{6.15}$$

Due to the specific linear dependence of energy functional on  $\beta_{1,\tilde{r}}$  leading to the (non-differential) equation for  $\beta_1(\tilde{r})$ ,  $\beta_1(l)$  cannot be varied arbitrarily, so  $\delta\beta_1(l) = 0$ . However, the variation of (6.14) with respect to l and  $\beta_0$  yields two additional conditions

$$\frac{1}{2} \left( \tilde{\omega}l - \beta_1(l) \right)^2 + c_0 f(l) \left( \beta_{1,\tilde{r}} + \frac{\beta_1}{l} \right) - \frac{1}{2} \left( \tilde{\omega}l - \frac{\beta_0}{l} \right)^2 = 0,$$

$$\int_l^1 (\tilde{r}\tilde{\omega} - \frac{\beta_0}{\tilde{r}}) d\tilde{r} = 0.$$
(6.16)

From  $(6.16)_2$  we find that

$$\beta_0 = -\frac{\tilde{\omega}(1 - l^2)}{2\ln l}. (6.17)$$

Because l < 1,  $\beta_0 > 0$  if  $\tilde{\omega} > 0$ . Plugging (6.15) and (6.17) into (6.16)<sub>1</sub>, we obtain the transcendental equation to determine l

$$\frac{1}{2}c_0^2(f'(l))^2 + 2\tilde{\omega}c_0f(l) + c_0^2f(l)\left[f''(l) + \frac{f'(l)}{l}\right] - \frac{1}{2}\tilde{\omega}^2\left(l + \frac{1-l^2}{2l\ln l}\right)^2 = 0. \quad (6.18)$$

We may either solve this equation with respect to l in terms of  $\tilde{\omega}$  or use l as the parameter and find  $\tilde{\omega}$  in terms of l. With respect to  $\tilde{\omega}$ , equation (6.18) can be presented as the quadratic equation

$$a(l)\tilde{\omega}^2 - 2b(l)\tilde{\omega} - c(l) = 0, (6.19)$$

where

$$a(l) = \left(l + \frac{1 - l^2}{2l \ln l}\right)^2, \quad b(l) = 2c_0 f(l),$$
  
$$c(l) = c_0^2 (f'(l))^2 + 2c_0^2 f(l) \left[f''(l) + \frac{f'(l)}{l}\right].$$

Provided the discriminant  $b^2(l) + a(l)c(l)$  is positive, we take the positive root of (6.19) yielding

$$\tilde{\omega}(l) = \frac{b(l) + \sqrt{b^2(l) + a(l)c(l)}}{a(l)}.$$

The smallest  $l = l_m$  that gives a real double root  $\tilde{\omega}_m = b(l_m)/a(l_m)$  is found from the equation

$$b^{2}(l_{m}) + a(l_{m})c(l_{m}) = 0.$$

As will be seen later, this  $l_m$  indicates the onset of dislocation nucleation.

Having  $\beta(\tilde{r})$  according to (6.13), (6.15), (6.17), we find the signed dislocation density from (6.1). For  $\tilde{r} \in (0, l)$  we have

$$\rho = \frac{1}{b}(\beta_{,r} + \frac{\beta}{r}) = \frac{1}{bR}\left(\beta_{,\tilde{r}} + \frac{\beta}{\tilde{r}}\right) = \frac{1}{bR}\left[2\tilde{\omega} + c_0(f''(\tilde{r}) + \frac{f'(\tilde{r})}{\tilde{r}})\right].$$

For  $\tilde{r} \in (l, 1)$  we know that  $\rho = 0$ . With this dislocation density we can also compute the total number of dislocations in a bar

$$N = 2\pi \int_0^R \rho r dr = 2\pi \frac{R}{b} (\tilde{\omega} l^2 - \chi \frac{2l^2}{1 - l^2}).$$

The dimensionless shear stress distribution  $\tau(\tilde{r}) = \sigma_{\theta z}(\tilde{r})/\mu$  is given by

$$\tau(\tilde{r}) = \begin{cases} -c_0 f'(\tilde{r}) & \text{for } \tilde{r} \in (0, l), \\ \tilde{r}\tilde{\omega} + \frac{\tilde{\omega}(1 - l^2)}{2 \ln l \, \tilde{r}} & \text{for } \tilde{r} \in (l, 1). \end{cases}$$

$$(6.20)$$

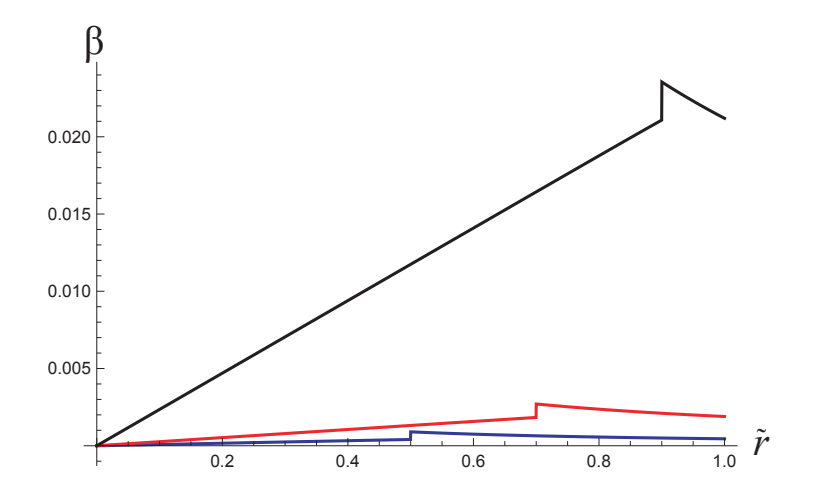


Figure 6.4.: Evolution of the plastic warping  $\beta(\tilde{r})$ : (a) l = 0.5 ( $\tilde{\omega} = 0.00083$ ), (b) l = 0.7 ( $\tilde{\omega} = 0.00265$ ), (c) l = 0.9 ( $\tilde{\omega} = 0.02351$ ).

Note that the jump in shear stress across the cylindrical surface  $\tilde{r} = l$  does not violate the equilibrium condition. The torque is computed as the resultant moment of this shear stress or, alternatively, is obtained by differentiating functional (6.12) with respect to  $\tilde{\omega}$ . This gives

$$\tilde{T}_c = \frac{\partial \tilde{I}}{\partial \tilde{\omega}} = \frac{T_c}{2\pi u R^3} = \int_0^1 (\tilde{r}\tilde{\omega} - \beta)\tilde{r}^2 d\tilde{r}.$$

To compute the dimensionless torque  $\tilde{T}_c$  we substitute  $\beta(\tilde{r})$  from (6.13) into this integral. Using the above solution for  $\beta(\tilde{r})$  we easily find that

$$\tilde{T}_c = -c_0(l^2 + \ln(1 - l^2)) + \frac{\tilde{\omega}}{4}(1 - l^4) + \frac{\tilde{\omega}(1 - l^2)^2}{4\ln l}.$$

For the twist  $\tilde{\omega} < \tilde{\omega}_m$  the plastic warping  $\beta(\tilde{r})$  must be identically zero, so we have the purely elastic solution with  $u_{\theta}(\tilde{r}) = \tilde{r}\tilde{\omega}$  and  $\beta(\tilde{r}) = 0$ . In this case the torque  $\tilde{T}_c$  is proportional to the twist  $\tilde{\omega}$ :

$$\tilde{T}_c = \frac{\tilde{\omega}}{4}.$$

Fig. 6.4 shows the evolution of  $\beta(\tilde{r})$  as  $\tilde{\omega}$  increases. For the simulation we took R=

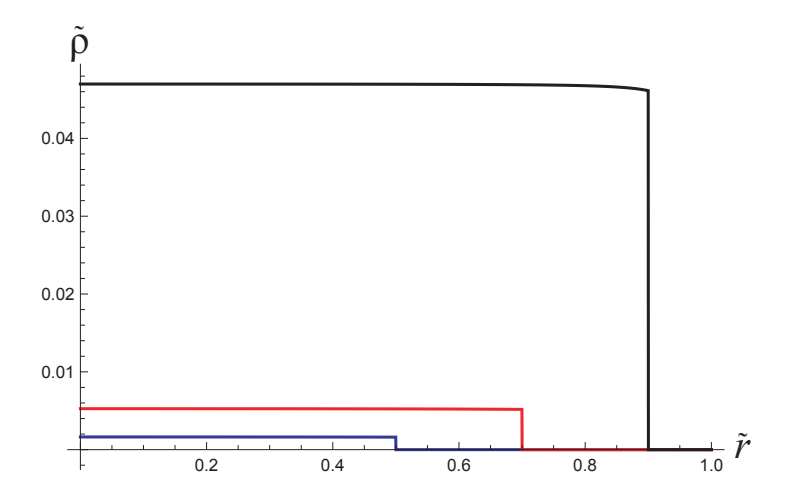


Figure 6.5.: Distribution of normalized dislocation density  $\tilde{\rho}(\tilde{r})$ : (a) l = 0.5 ( $\tilde{\omega} = 0.00083$ ), (b) l = 0.7 ( $\tilde{\omega} = 0.00265$ ), (c) l = 0.9 ( $\tilde{\omega} = 0.02351$ ).

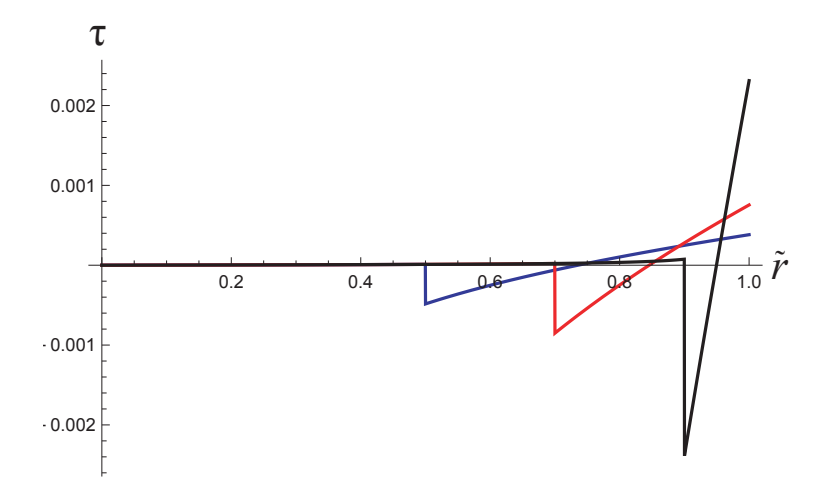


Figure 6.6.: Distribution of dimensionless shear stress  $\tau(\tilde{r})$ : (a) l = 0.5 ( $\tilde{\omega} = 0.00083$ ), (b) l = 0.7 ( $\tilde{\omega} = 0.00265$ ), (c) l = 0.9 ( $\tilde{\omega} = 0.02351$ ).

 $1 \,\mu\mathrm{m}$ ,  $b = r_0 = 1$  Å. We see that  $\beta(\tilde{r})$  increases as  $\tilde{\omega}$  increases. Besides, the plastic warping exhibits a jump at  $\tilde{r} = l$  that also increases as  $\tilde{\omega}$  increases. Since the total strain is continuous, such a jump indicates the misorientation of the lattice across the surface  $\tilde{r} = l$ .

Fig. 6.5 shows the distributions of the normalized dislocation density  $\tilde{\rho}(\tilde{r}) = bR\rho(\tilde{r})$  as  $\tilde{\omega}$  increases. One can see that the dislocation-free zone diminishes as  $\tilde{\omega}$  increases. For small  $\tilde{\omega}$  the dislocation density remains nearly constant. For large  $\tilde{\omega}$ , we see some influence of the free boundary on the distribution of dislocations: the density slightly decreases with  $\tilde{r}$ .

Fig. 6.6 shows the distributions of the dimensionless shear stress given by (6.20) as  $\tilde{\omega}$  increases. We observe that the shear stress is nearly zero in the dislocation zone. This agrees well with the fact that the main contribution to the Peach-Koehler force comes from the shear stress, while the contribution of this force due to the boundary is noticeable only near the free boundary.

Fig. 6.7 presents on the left the normalized torque  $\tilde{T}_c$  as a function of the dimensionless twist  $\tilde{\omega}$ , where on the right the zoom of this curve near the origin is also shown. One can see that at the onset of the dislocation nucleation (at  $\tilde{\omega} = \tilde{\omega}_m \approx 0.000032$  for the above chosen parameters) the torque jumps down. The reason of this "torque-drop"

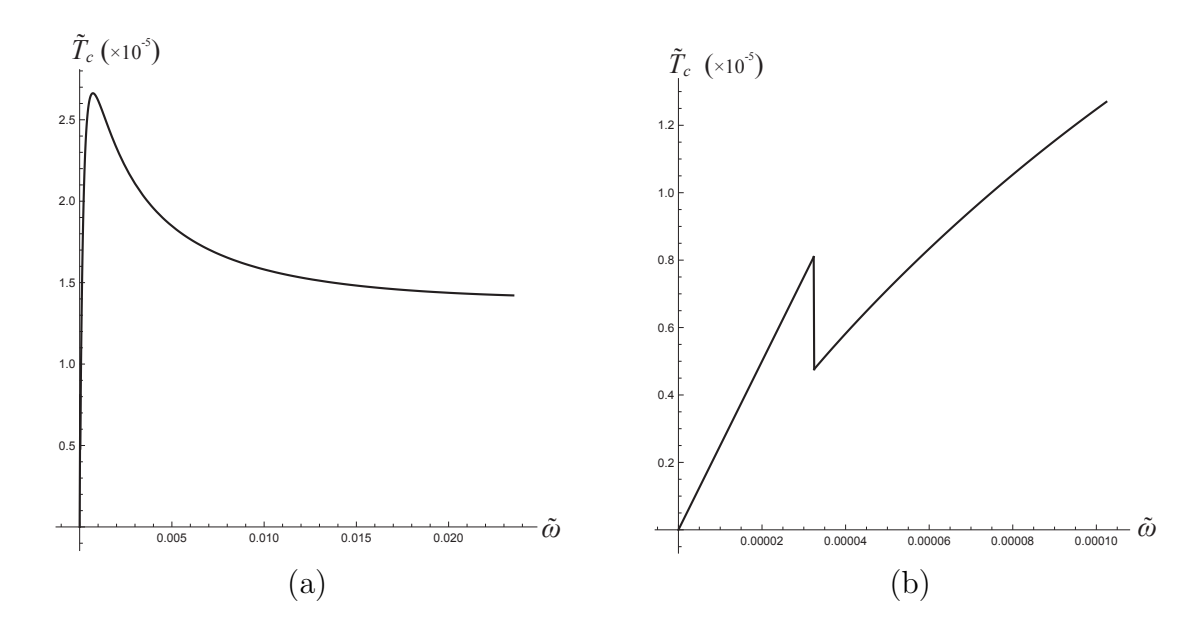


Figure 6.7.: The torque-twist curve: (a) Left: the whole curve, (b) Right: Zoomed near the origin.

is that at  $\tilde{\omega} = \tilde{\omega}_m$  the plastic warping jumps from zero to a small but positive function leading to the reduction of the stress and also the torque. After the torque-drop there is a "work hardening" section followed by the softening behavior as shown on the left of Fig. 6.7.

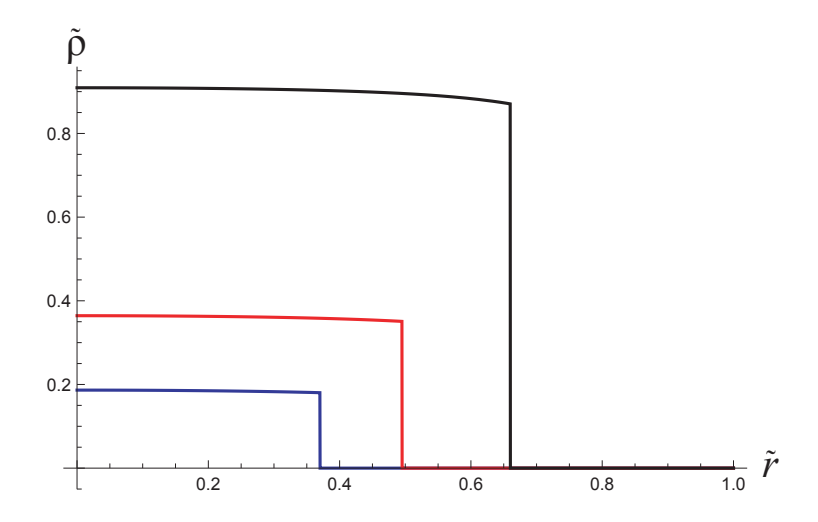


Figure 6.8.: Distribution of normalized dislocation density  $\tilde{\rho}(\tilde{r})$  in nanowire of 5 nm radius: (a) l = 0.37, (b) l = 0.495, (c) l = 0.66.

Weinberger (2011) reported the distribution of screw dislocations in a nanowire under torsion. It is observed that the applied torque leads the uniformly distributed screw dislocations to shrink into a smaller radius circle, and when the torque is beyond a specific value, the configuration of dislocation distribution seems unchanged. For comparison, we took the same paramter values used in Weinberger (2011), R = 5 nm, b = 2.83 Å,  $r_0 = 2.83$  Å, and plotted the normalized dislocation density as a function of  $\tilde{r}$  by present theory for three given values of l in Fig. 6.8, where each l corresponds to a dimensionless twist angle. It is found that the magnitude of  $\tilde{\rho}$  is bigger than that in the wires of micro size (Fig. 6.5), and the density at high twist angle (or high l)

different theories			
Normalized radius at which	(N=10)	(N=20)	(N = 50)
dislocation-free zone starts:	$l_{10}$	$l_{20}$	$l_{50}$
Present theory	0.37	0.495	0.66
Data from Weinberger (2011)	0.375	0.5	0.67

Table 6.1.: Normalized radius l at which dislocation-free zone starts predicted by two different theories

shows gradual decreasing behavior with increasing  $\tilde{r}$  until it reaches dislocation-free zone.

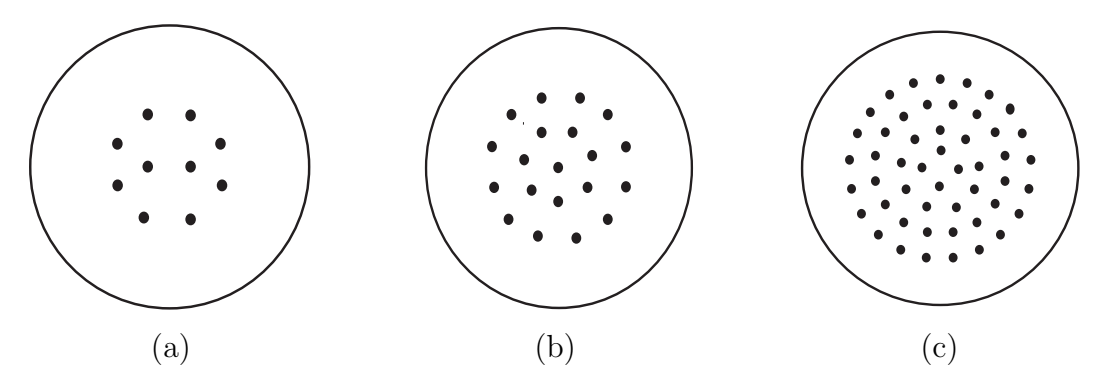


Figure 6.9.: Distribution of screw excess dislocations: (a)  $l_{10}=0.37$ , (b)  $l_{20}=0.495$ , (c)  $l_{50}=0.66$ .

The configurations of distributed screw dislocations in a nanowire with the number of dislocations 10, 20, 50 are shown in Fig. 6.9, where the structures of dislocation net are adopted from Weinberger (2011). Table 6.1 compares the the normalized radius, at which dislocation-free zones start, in a nanowire by two methods. The length of the zone that dislocations occupies for a given number of dislocations can be accurately calculated by continuum dislocation theory with the formula

$$\tilde{\rho}(l) = \frac{b}{\pi R} N. \tag{6.21}$$

For simplicity, we consider here the normalized dislocation density remain constant with respect to  $\tilde{r}$ . Note that the ratio of the occupied area by dislocations to the cross-section for a certain number of dislocations is proportional to square of l. As indicated, the values of l for the number of dislocations 10, 20, 50 are  $l_{10} = 0.37$ ,  $l_{20} = 0.495$ , and  $l_{50} = 0.66$ , respectively.

For the other method, three radii,  $l_{10}$ ,  $l_{20}$ ,  $l_{50}$ , are computed from each state under highest torque from Fig. 12 of Weinberger (2011) (the figure showing the effect of torque on the dislocation distribution) by the formula

$$l = r_w/R_w$$

where  $r_w$  is radius of the circle that dislocations occupied, and  $R_w$  the radius of the cross-section. Both  $r_w$  and  $R_w$  are measured from Fig. 12 of Weinberger (2011). The comparison of the results by two methods shows excellent agreement with each other.

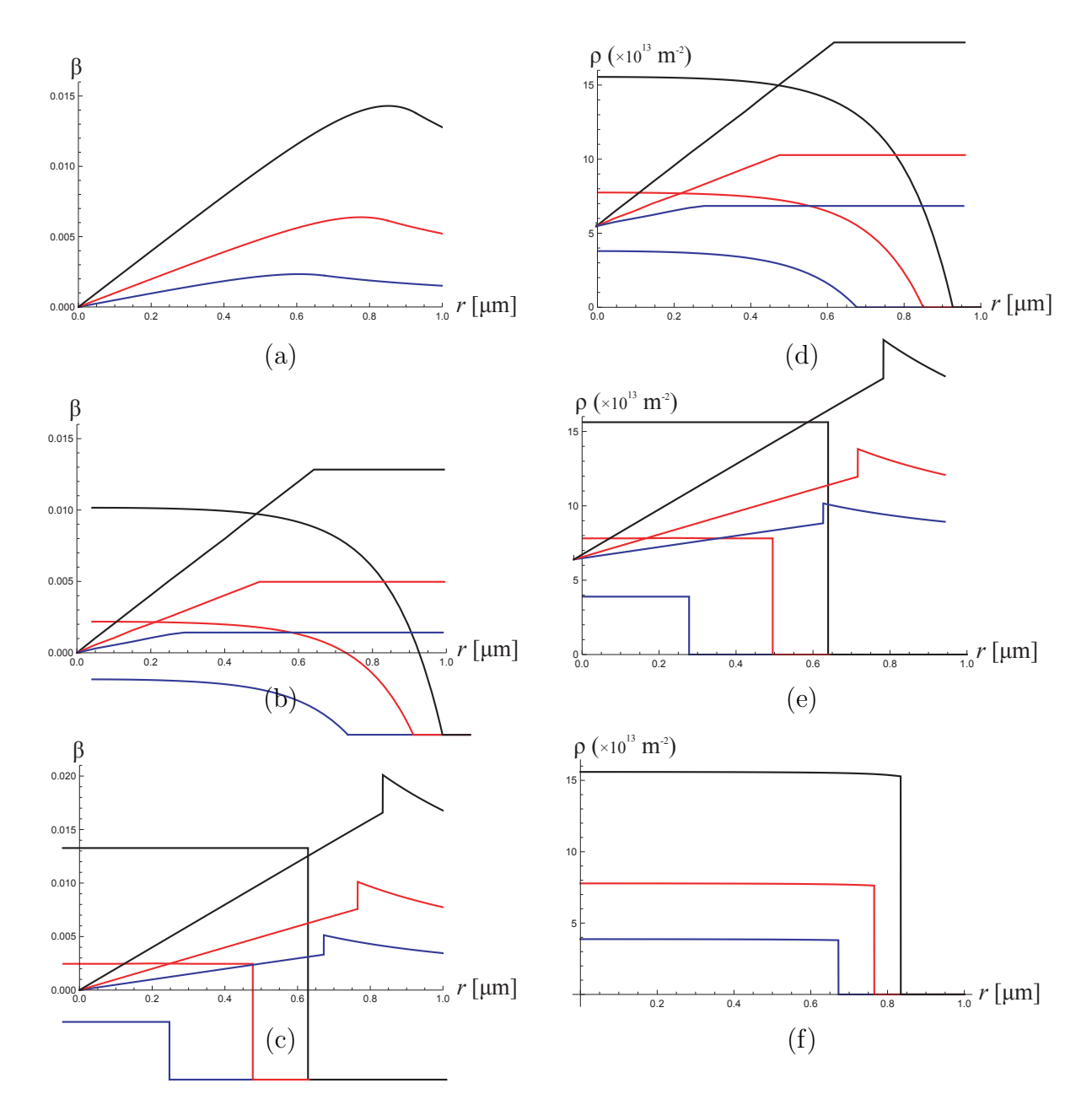


Figure 6.10.: • Left column: The distribution of plastic warping  $\beta$  at different values of surface shear strain,  $R\omega = 0.02$  (black),  $R\omega = 0.01$  (red),  $R\omega = 0.005$  (blue). (a) Prediction by proposed theory with the aid of logarithmic defect energy (see Kaluza & Le (2011)), (b) Prediction by critical thickness theory (see Liu *et al.* (2018)), (c) Prediction by proposed theory with the aid of rank-one defect energy.

• Right column: The distribution of dislocation density of excess screw dislocation at different value of surface strain,  $R\omega = 0.02$  (black),  $R\omega = 0.01$  (red),  $R\omega = 0.005$  (blue). (d) Prediction by proposed theory with the aid of logarithmic defect energy (see Kaluza & Le (2011)), (e) Prediction by critical thickness theory (see Liu *et al.* (2018)), (f) Prediction by proposed theory with the aid of rank-one defect energy.

Kaluza & Le (2011) investigated the same problem with the defect energy in logarithmic formulation proposed by Berdichevsky (2006b), given by

$$\psi_m = \mu k \ln \frac{1}{1 - \frac{\rho}{\rho_s}} \cong \mu k \left[ \frac{\rho}{\rho_s} + \frac{1}{2} \left( \frac{\rho}{\rho_s} \right)^2 \right]$$
 (6.22)

where k is a material constant,  $\rho_s$  the saturated dislocation density. This logarithmic term ensures that the defect energy increases linearly for small dislocation density, which shows the agreement that the energies are devoted by the non-interacting dislocations. When  $\rho$  approaches  $\rho_s$ , the defect energy tends to infinity that behaves as an energy barrier against the over-saturation. For small to moderate  $\rho$ , the defect energy may be approximated by the sum of linear and quadratic terms, as shown in (6.22). The Ansatz function (6.13) is applied and through the same procedure of the energy minimization, and one can obtain the governing equations (6.23) by varying the energy functional with respect to  $\beta_1$ , constant  $\beta_0$ , and l:

$$\beta_{1,rr} + \frac{1}{r}\beta_{1,r} - (1 + \frac{1}{r^2})\beta_1 = -r\omega,$$

$$(\beta_{1,r} + \beta_1/r)|_{r=l} = 0,$$

$$R\omega - \frac{1}{2}\omega(R^2 - l^2) + \beta_0 \ln \frac{R}{l} = 0,$$
(6.23)

where the boundary conditions must satisfy

$$\beta_1(0) = 0, \quad \beta_1(l) = \frac{\beta_0}{l}.$$

Note that, since the differential equation for  $\beta_1$  making  $\beta_1(l)$  vary arbitrarily enables  $(6.23)_2$ , it leads the dislocation density to be continuous. The analytical solution of (6.23) has been given by Kaluza & Le (2011) as

$$\beta_{1}(r) = r\omega - 2\omega \frac{I_{1}(r)}{I'_{1} + I_{1}(l)/l},$$

$$\beta_{0} = \beta_{1}(l)l,$$

$$R\omega - \frac{1}{2}\omega(R^{2} - l^{2}) + \omega \left[l - \frac{2I_{1}(l)}{I'_{1} + I_{1}(l)/l}\right] l \ln \frac{R}{l} = 0,$$
(6.24)

where  $I_1(r)$  denotes the modified Bessel function of the first kind of order one, and the prime represents the derivative with respect to its argument. At the given  $\omega$ , one can compute the corresponding l by solving  $(6.24)_3$ , and  $\beta_1(r)$  and  $\beta_0$  can be explicitly described with the computed l.

Fig. 6.10 shows the comparison of the results by continuum theory with logarithmic defect energy and by critical thickness theory investigated by Liu *et al.* (2018) to those by rank-one defect energy in the continuum theory. The comparison is performed at three different surface strains,  $R\omega = 0.02$  (black),  $R\omega = 0.01$  (red),  $R\omega = 0.005$  (blue), and the sample radius is 1  $\mu$ m.

Fig. 6.10(a), (d) show the evolution of the plastic warping and dislocation density by the continuum theory with logarithmic defect energy. The parameters are given as  $k = 10^{-4}$  and  $\rho_s = 3 \times 10^{14} \,\mathrm{m}^{-2}$ . Fig. 6.10(b), (e) show those by critical thickness theory reported in Liu *et al.* (2018) and Fig. 6.10(c), (f) the results by the continuum theory with rank-one defect energy. One could observe that all magnitudes of plastic warping and dislocation density from figures of three models are in the same order.

Besides, some other common features can be found. The plastic warping are continuous in Fig. 6.10(a) and (b), while in Fig. 6.10(c), there exists a jump at the position that the dislocation-free zone starts. Plastic warping in Fig. 6.10(a) and (c) show a monotonously decreasing behavior at dislocation-free zone, while it is constant in Fig. 6.10(b). Fig. 6.10(b) and (c) show a linear increase of  $\beta$  in dislocation accumulated region, while Fig. 6.10(a) is not. On the other hand, in Fig. 6.10(d), the dislocation density decreases slowly near the origin and fast when it approaches the dislocation-free zone. While the densities in Fig. 6.10(e) and (f) seem constant in the dislocation distributed zone. The predicted positions that dislocation-free zones start by three models are all different.

## 6.4. Dislocation Distribution at Non-zero Dissipation

Berdichevsky (2016) rightly pointed out that the solution found by the continuum theory in the case of zero dissipation contradicts the classical plasticity theory and to the observed behavior of real metals, where a plastic region is formed near the boundary while no plastic deformation develops in the middle of the bar. This contradiction can be resolved if we take into account the resistance to dislocation motion leading to the non-vanishing dissipation. As mentioned in Section 6.2, the plastic warping must then evolve in accordance with the variational equation (6.10) under the constraint  $\beta(t,0) = 0$ . We regard  $\omega$  as a given function of time (the "driving" variable) and try to determine  $\beta(t,r)$ . Provided the sign of  $\dot{\beta}$  does not change during the evolution of  $\beta$ , the variational equation (6.10) reduces to minimizing the following "relaxed energy" functional

$$I(\beta) = 2\pi \int_0^R \left[ \frac{1}{2} \mu (r\omega - \beta)^2 + \frac{\mu b}{4\pi} f(r/R) |\beta_{,r} + \beta/r| + K \operatorname{sign} \dot{\beta} \beta \right] r dr,$$

among all admissible function  $\beta(r)$  satisfying the boundary conditions  $\beta(0) = 0$ . Finally, if  $\dot{\beta} = 0$ , then the plastic warping is frozen, while the stress and the torque should be found with this frozen  $\beta$ . Note that, the dissipation terms for redundant dislocations and effective temperature are not taken into account.

Let us assume that the dislocations have the positive sign:  $\beta_{,r} + \beta/r > 0$ . Besides, we consider the loading process for which sign  $\dot{\beta} = 1$  so that the last term in (6.25) becomes  $K\beta$ . It is convenient to introduce the dimensionless quantities (6.11) and  $\gamma_c = \frac{K}{\mu}$  in terms of which the functional reads

$$\tilde{I}(\beta) = \int_0^1 \left[ \frac{1}{2} (\tilde{r}\tilde{\omega} - \beta)^2 + c_0 f(\tilde{r})(\beta_{,\tilde{r}} + \beta/\tilde{r}) + \gamma_c \beta \right] \tilde{r} d\tilde{r}.$$
(6.25)

Functional (6.25) is similar to functional (6.9). However, the additional term  $\gamma_c\beta$  changes the behavior of the solution radically. Indeed, in the case of non-zero dissipation, dislocations cannot move if the shear stress is less than the critical resolved shear stress K. Since the stress near the middle line of the bar is always small, new dislocations cannot be formed there. Based on this deliberation, we look for the plastic

warping in the form

$$\beta(\tilde{r}) = \begin{cases} 0 & \text{for } \tilde{r} \in (0, l_1), \\ \beta_1(\tilde{r}) & \text{for } \tilde{r} \in (l_1, l_2), \\ \beta_2/\tilde{r} & \text{for } \tilde{r} \in (l_2, 1), \end{cases}$$

$$(6.26)$$

where  $\beta_1(\tilde{r})$ ,  $l_1$ ,  $l_2$ ,  $\beta_2$  are unknowns. The zone  $\tilde{r} \in (0, l_1)$  corresponds to the elastic core. The dislocation zone forms the ring  $\tilde{r} \in (l_1, l_2)$ . We admit that  $\beta(\tilde{r})$  may have jumps at  $\tilde{r} = l_1$  and  $\tilde{r} = l_2$ . Note that this solution Ansatz is consistent with the boundary condition  $\beta(0) = 0$ .

According to (6.26), the functional becomes

$$\tilde{I} = \int_{0}^{l_{1}} \frac{1}{2} (\tilde{r}\tilde{\omega})^{2} \tilde{r} d\tilde{r} + \int_{l_{1}}^{l_{2}} \left[ \frac{1}{2} (\tilde{r}\tilde{\omega} - \beta_{1})^{2} + c_{0} f(\tilde{r}) \left( \beta_{1,\tilde{r}} + \frac{\beta_{1}}{\tilde{r}} \right) + \gamma_{c} \beta_{1} \right] \tilde{r} d\tilde{r} 
+ \int_{l_{2}}^{1} \frac{1}{2} \left[ \left( \tilde{r}\tilde{\omega} - \frac{\beta_{2}}{\tilde{r}} \right)^{2} + \gamma_{c} \beta_{2} / \tilde{r} \right] \tilde{r} d\tilde{r}.$$
(6.27)

Varying energy functional (6.27) with respect to  $\beta_1(\tilde{r})$ , we obtain the (non-differential) equation for it on the interval  $(l_1, l_2)$ 

$$-(\tilde{r}\tilde{\omega} - \beta_1)\tilde{r} - c_0 f'(\tilde{r})\tilde{r} + \gamma_c \tilde{r} = 0,$$

yielding

$$\beta_1(\tilde{r}) = \tilde{r}\tilde{\omega} - \gamma_c + c_0 f'(\tilde{r}). \tag{6.28}$$

Due to the specific linear dependence of energy functional on  $\beta_{1,\tilde{r}}$  leading to the (non-differential) equation for  $\beta_1(\tilde{r})$ ,  $\beta_1(l_1)$  and  $\beta_1(l_2)$  cannot be varied arbitrarily at  $\tilde{r} = l_1$  and  $\tilde{r} = l_2$ , so  $\delta\beta_1(l_1) = \delta\beta_1(l_2) = 0$ . However, the variation of (6.27) with respect to  $l_1$ ,  $l_2$ , and  $l_2$  yields three additional conditions

$$\frac{1}{2}\tilde{\omega}^{2}l_{1}^{2} - \left[\frac{1}{2}(\tilde{\omega}l_{1} - \beta_{1}(l_{1}))^{2} + c_{0}f(l_{1})\left(\beta_{1,\tilde{r}} + \frac{\beta_{1}}{l_{1}}\right) + \gamma_{c}\beta_{1}(l_{1})\right] = 0,$$

$$\left[\frac{1}{2}(\tilde{\omega}l_{2} - \beta_{1}(l_{2}))^{2} + c_{0}f(l_{2})(\beta_{1,\tilde{r}} + \frac{\beta_{1}}{l_{2}}) + \gamma_{c}\beta_{1}(l_{2})\right] - \frac{1}{2}\left(\tilde{\omega}l_{2} - \frac{\beta_{2}}{l_{2}}\right)^{2} - \frac{\gamma_{c}\beta_{2}}{l_{2}} = 0,$$

$$\int_{l_{2}}^{1}\left(-\tilde{r}\tilde{\omega} + \frac{\beta_{2}}{\tilde{r}} + \gamma_{c}\right)d\tilde{r} = 0.$$
(6.29)

From  $(6.29)_3$  we find that

$$\beta_2 = -\frac{\tilde{\omega}(1 - l_2^2) - 2\gamma_c(1 - l_2)}{2\ln l_2}.$$
(6.30)

Because  $l_2 < 1$ ,  $\beta_2 > 0$  if  $\tilde{\omega} > 0$ , plugging (6.28) and (6.30) into (6.29)<sub>2</sub>, we obtain the transcendental equation to determine  $l_2$ , which can be transformed into the quadratic equation

$$a(l_2)\tilde{\omega}^2 - 2b(l_2)\tilde{\omega} - c(l_2) = 0$$
(6.31)

in terms of  $\tilde{\omega}$ , where

$$a(l_2) = \left(l_2 + \frac{1 - l_2^2}{2l_2 \ln l_2}\right)^2, \quad b(l_2) = 2c_0 f(l_2) + \gamma_c \left(l_2 + \frac{1 - l_2^2}{2l_2 \ln l_2}\right) \left(1 + \frac{1 - l_2}{l_2 \ln l_2}\right),$$

$$c(l_2) = c_0^2 (f'(l_2))^2 + 2c_0 f(l_2) \left[-\frac{\gamma_c}{l_2} + c_0 f''(l_2) + c_0 \frac{f'(l_2)}{l_2}\right] - \gamma_c^2 \left(1 + \frac{1 - l_2}{l_2 \ln l_2}\right)^2.$$

We use  $l_2$  as parameter and find the twist  $\tilde{\omega}$  through  $l_2$ . Provided the discriminant  $b^2(l_2) + a(l_2)c(l_2)$  is positive, we take the positive root of (6.31) yielding

$$\tilde{\omega}(l_2) = \frac{b(l_2) + \sqrt{b^2(l_2) + a(l_2)c(l_2)}}{a(l_2)}.$$
(6.32)

The smallest  $l_2 = l_{2m}$  that gives a real double root  $\kappa_m = b(l_{2m})/a(l_{2m})$  is found from the equation

$$b^2(l_{2m}) + a(l_{2m})c(l_{2m}) = 0.$$

As will be seen later, this  $l_{2m}$  indicates the onset of dislocation nucleation. Finally, the length  $l_1$  must be found from equation  $(6.29)_1$  which, after substitution of  $\beta_1(l_1)$  from (6.28) and of  $\tilde{\omega}$  from (6.32), reads

$$\frac{1}{2}\tilde{\omega}^{2}l_{1}^{2} - \frac{1}{2}\left(\gamma_{c} - c_{0}f'(l_{1})\right)^{2} - c_{0}f(l_{1})\left[2\kappa - \frac{\gamma_{c}}{l_{1}} + c_{0}f''(l_{1}) + c_{0}\frac{f'(l_{1})}{l_{1}}\right] - \gamma_{c}\left[\tilde{\omega}l_{1} - \gamma_{c} + c_{0}f'(l_{1})\right] = 0.$$

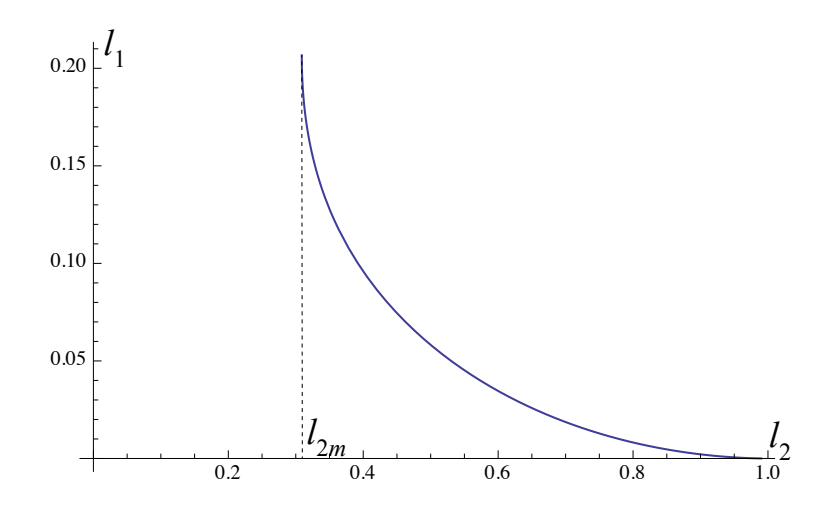


Figure 6.11.: The plot of  $l_1(l_2)$ .

It turns out that this equation for  $l_2 \geq l_{2m}$  has two roots. However, the smaller root corresponds to the minimizer of the relaxed energy functional. The plot of  $l_1$  as a function of  $l_2$  for  $l_2 \in (l_{2m}, 1)$  is shown in Fig. 6.11. We see that  $l_1(l_2)$  is a monotonically decreasing function. At the onset of dislocation nucleation (at  $l_2 = l_{2m}$ )  $l_1$  achieves a maximum which is not much less than  $l_2$ . This means that the dislocation zone at the onset of the dislocation nucleation is a thin ring. As  $l_2$  (and  $\tilde{\omega}$ ) increases,  $l_1$  decreases, so the ring occupied by dislocations expands during the loading process, while the elastic core region diminishes.

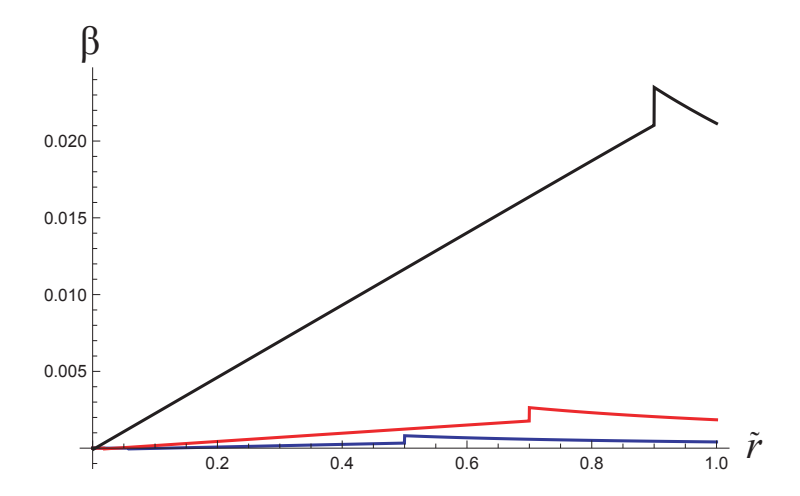


Figure 6.12.: Evolution of the plastic warping  $\beta(\tilde{r})$ : (a) l = 0.5 ( $\tilde{\omega} = 0.00088$ ), (b) l = 0.7 ( $\tilde{\omega} = 0.0027$ ), (c) l = 0.9 ( $\tilde{\omega} = 0.02356$ ).

Having  $\beta(\tilde{r})$  according to (6.26) and (6.28), we find the signed dislocation density from (6.1). For  $\tilde{r} \in (0, l_1)$  and  $\tilde{r} \in (l_2, 1)$  we have  $\rho = 0$ . For  $\tilde{r} \in (l_1, l_2)$ 

$$\rho = \frac{1}{b} \left( \beta_{,r} + \frac{\beta}{r} \right) = \frac{1}{bR} \left( \beta_{,\tilde{r}} + \frac{\beta}{\tilde{r}} \right) = \frac{1}{bR} \left[ 2\tilde{\omega} - \frac{\gamma_c}{\tilde{r}} + c_0 \left( f''(\tilde{r}) + \frac{f'(\tilde{r})}{\tilde{r}} \right) \right].$$

The dimensionless shear stress distribution  $\tau(\tilde{r}) = \sigma_{\theta z}(\tilde{r})/\mu$  is given by

$$\tau(\tilde{r}) = \begin{cases} \tilde{r}\tilde{\omega} & \text{for } \tilde{r} \in (0, l_1), \\ \gamma_c - c_0 f'(\tilde{r}) & \text{for } \tilde{r} \in (l_1, l_2), \\ \tilde{r}\tilde{\omega} + \frac{\tilde{\omega}(1 - l_2^2) - 2\gamma_c(1 - l_2^2)}{2 \ln l_2 \tilde{r}} & \text{for } \tilde{r} \in (l_2, 1). \end{cases}$$

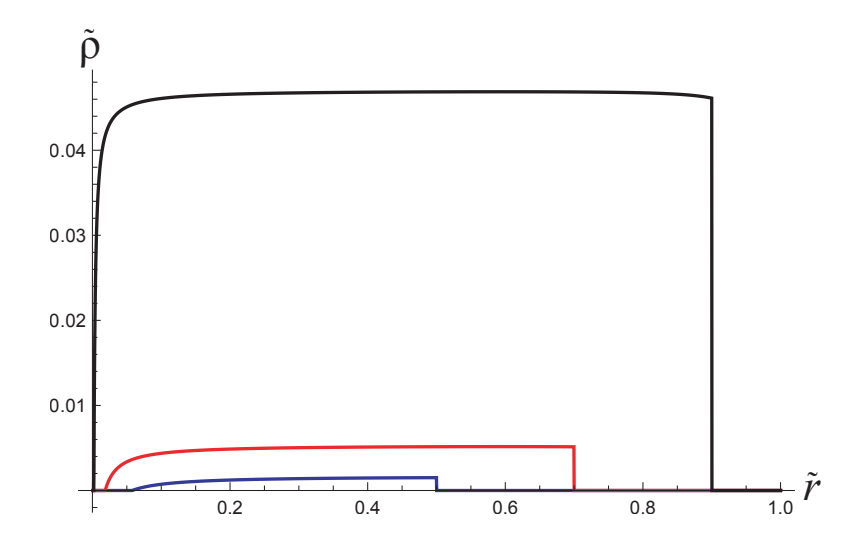


Figure 6.13.: Distribution of normalized dislocation density  $\bar{\rho}(\tilde{r})$ : (a) l=0.5 ( $\tilde{\omega}=0.00088$ ), (b) l=0.7 ( $\tilde{\omega}=0.0027$ ), (c) l=0.9 ( $\tilde{\omega}=0.02356$ ).

In the elastic zone, the stress obeying Hooke's law is a linear function of  $\tilde{r}$ . In the zone occupied by dislocations, due to the smallness of  $c_0$ , the stress is nearly constant and

equals the critical resolved shear stress. The torque is computed as the derivative of the functional (6.25) with respect to  $\tilde{\omega}$  giving

$$\tilde{T}_c = \frac{\partial \tilde{I}}{\partial \tilde{\omega}} = \int_0^1 (\tilde{r}\tilde{\omega} - \beta)\tilde{r}^2 d\tilde{r}.$$

Substituting  $\beta(\tilde{r})$  from (6.26) into this integral, we easily find that

$$\tilde{T}_c = \frac{\tilde{\omega}}{4} l_1^4 + \frac{1}{3} \gamma_c (l_2^3 - l_1^3) - c_0 \left( l_2^2 - l_1^2 + \ln \frac{1 - l_2^2}{1 - l_1^2} \right) + \frac{\tilde{\omega}}{4} (1 - l_2^4) + \frac{\tilde{\omega}(1 - l_2^2) - 2\gamma_c (1 - l_2)}{4 \ln l_2} (1 - l_2^2).$$

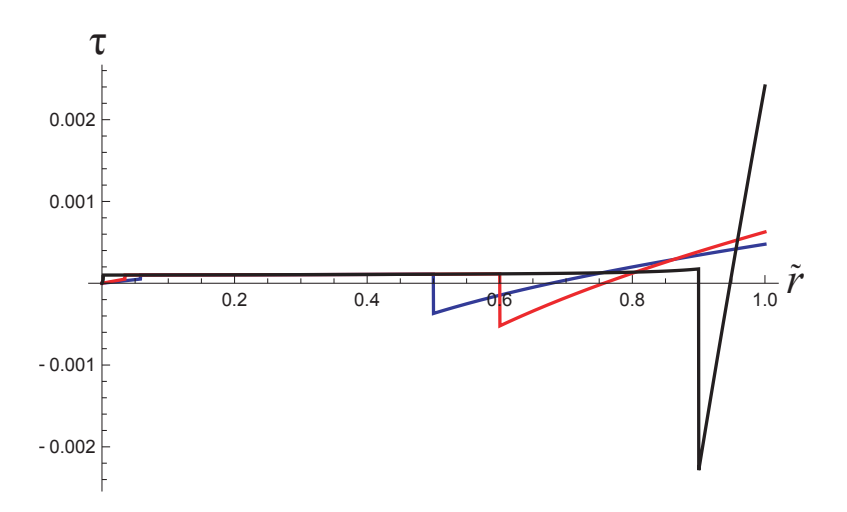


Figure 6.14.: Distribution of dimensionless shear stress  $\tau(\tilde{r})$ : (a) l=0.5 ( $\tilde{\omega}=0.00088$ ), (b) l=0.7 ( $\tilde{\omega}=0.0027$ ), (c) l=0.9 ( $\tilde{\omega}=0.02356$ ).

For the twist  $\tilde{\omega} < \tilde{\omega}_m$ , the plastic warping  $\beta(\tilde{r})$  must be identically zero, so we have the purely elastic solution with  $u_{\theta}(\tilde{r}) = \tilde{r}\tilde{\omega}$  and  $\beta(\tilde{r}) = 0$ . In this case, the torque  $\tilde{T}_c$  is proportional to the twist  $\tilde{\omega}$ :

$$\tilde{T}_c = \frac{\tilde{\omega}}{4}.$$

Fig. 6.12 shows the evolution of  $\beta(\tilde{r})$  as  $\tilde{\omega}$  increases. For the simulation we took  $R=1\,\mu\mathrm{m},\ b=r_0=1$  Å, and  $\gamma_c=10^{-4}$ . For these chosen parameters we found that  $l_{2m}=0.3089$ . As in the previous case,  $\beta(\tilde{r})$  increases with  $\tilde{\omega}$ . Besides, the plastic warping exhibits jumps at  $\tilde{r}=l_1$  and  $\tilde{r}=l_2$ . The difference to the case of zero dissipation is that there is an elastic zone with  $\beta=0$ . The radius of the elastic zone diminishes with the increasing twist.

Fig. 6.13 shows the distributions of the normalized dislocation density  $\tilde{\rho}(\tilde{r}) = bR\rho(\tilde{r})$  as  $\tilde{\omega}$  increases. One sees that the dislocation-free zones at the origin as well as near the free boundary diminish as  $\tilde{\omega}$  increases. For  $\tilde{\omega}$  close to the threshold value at the onset of dislocation nucleation, the dislocation density remains nearly constant except near

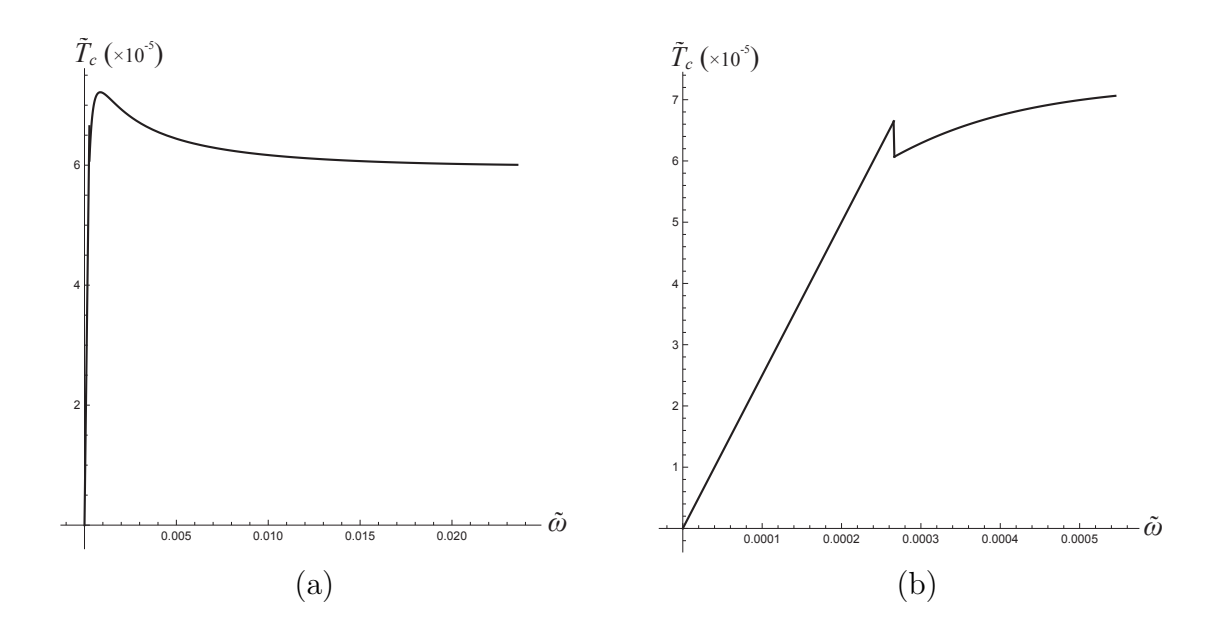


Figure 6.15.: The torque-twist curve: (a) The whole curve, (b) Zoomed near the origin.

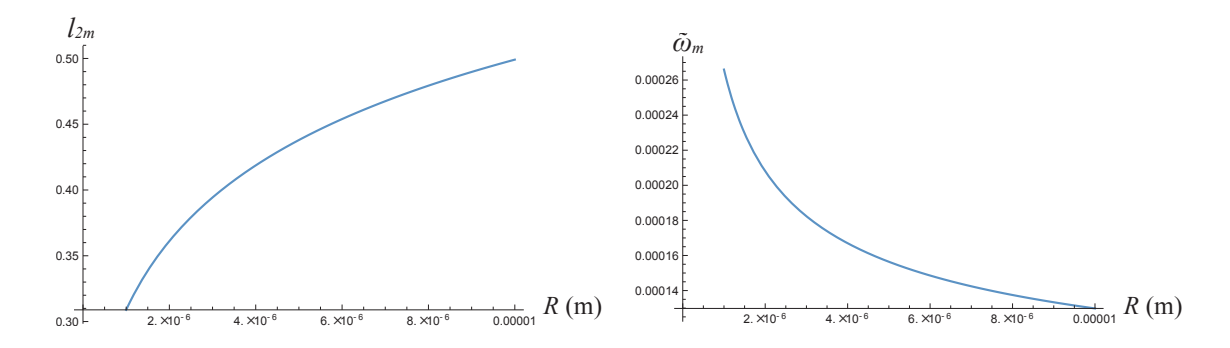


Figure 6.16.: The size effect: (a) Left: function  $l_{2m}(R)$ , (b) Right: function  $\tilde{\omega}_m(R)$ .

the origin. For large  $\tilde{\omega}$ , we see some influence of the free boundary on the distribution of dislocations: the density slightly decreases with  $\tilde{r}$ . Note that the dislocation density is continuous at  $\tilde{r} = l_1$  and discontinuous at  $\tilde{r} = l_2$ .

Fig. 6.14 shows the distributions of the dimensionless shear stress given by (6.20) as  $\tilde{\omega}$  increases. We observe that the shear stress increases first as a linear function in the elastic zone, then remain nearly constant (which is equal to K) in the dislocation zone, and finally jumps down and increases linearly in the outer dislocation-free ring. Fig. 6.15(a) presents the normalized torque  $\tilde{T}_c$  as a function of the dimensionless twist  $\tilde{\omega}$ , while in Fig. 6.15(b), the zoom of the curve near the origin is shown. One can see that at the onset of the collective dislocation nucleation (at  $\tilde{\omega} = \tilde{\omega}_m \approx 0.00027$  for the above chosen parameters), the torque jumps down. The reason for this "torque-drop" is that at  $\tilde{\omega} = \tilde{\omega}_m$ , the plastic warping jumps from zero to a small but positive function, leading to the reduction of the stress and also the torque. After the torque-drop, there is a "work hardening" section followed by the softening behavior, as shown in Fig. 6.15(a). Note that the softening effect is much less pronounced as in the case without dissipation.

We use the analytical solution found above to investigate the dependence of the dislocation-free zones and the threshold twist angle on the radius of the bar's cross-

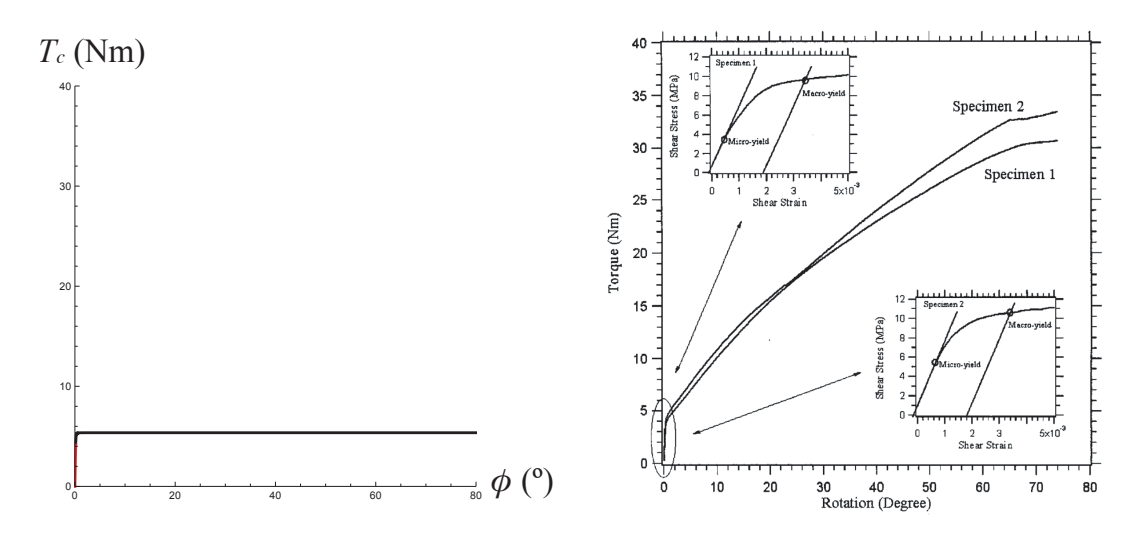


Figure 6.17.: Torque-twist curve: (a) Left: The presented theory, (b) Right: Experiment (taken from Horstemeyer *et al.* (2002))

section. The left of Fig. 6.16 presents the dependence of  $l_{2m}$  on the radius R (measured in meter), while the right figure indicates the function  $\tilde{\omega}_m(R)$  for R in the range  $1 \sim 10 \,\mu\text{m}$ . We see that, as R increases, the outer dislocation-free zone at the onset of dislocation nucleation becomes narrower, while the threshold value of the twist angle  $\tilde{\omega}_m$  decreases. This exhibits clearly the size effect.

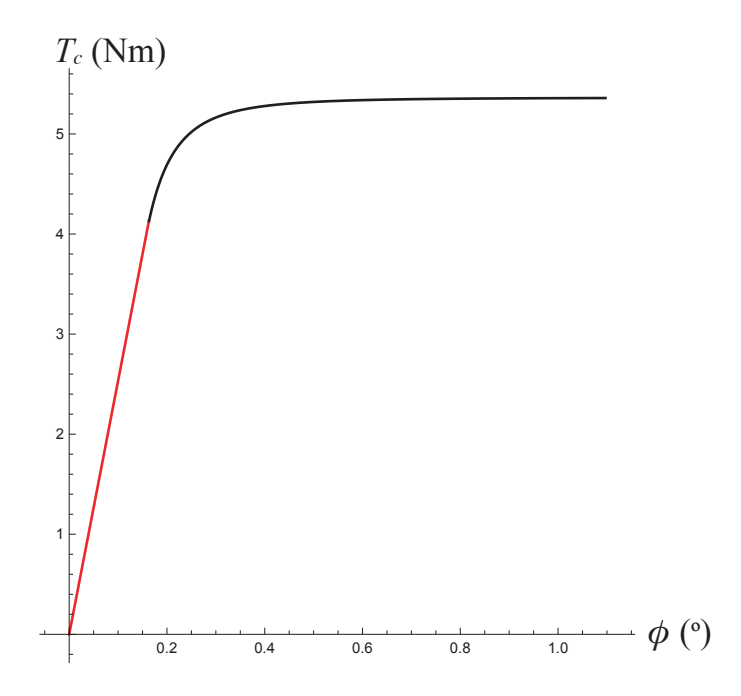


Figure 6.18.: The theoretical torque-twist curve zoomed near the origin.

Fig. 6.17 shows the comparison between the torque-twist curved computed from the presented theory and obtained in experiments conducted by Horstemeyer et al. (2002). For the numerical simulation of the theoretical curve we took  $\mu=10$  GPa, b=2.55 Å, R=6.35 mm, K=10 MPa, and for the comparison with experiments, we present the torque in Nm, while the twist angle in degree. We see that the threshold torque, computed from the presented theory,  $T_c^m=4.06$  Nm, agrees quite well with that observed in the experiment at the onset of the plastic deformation. There exists a tiny torque

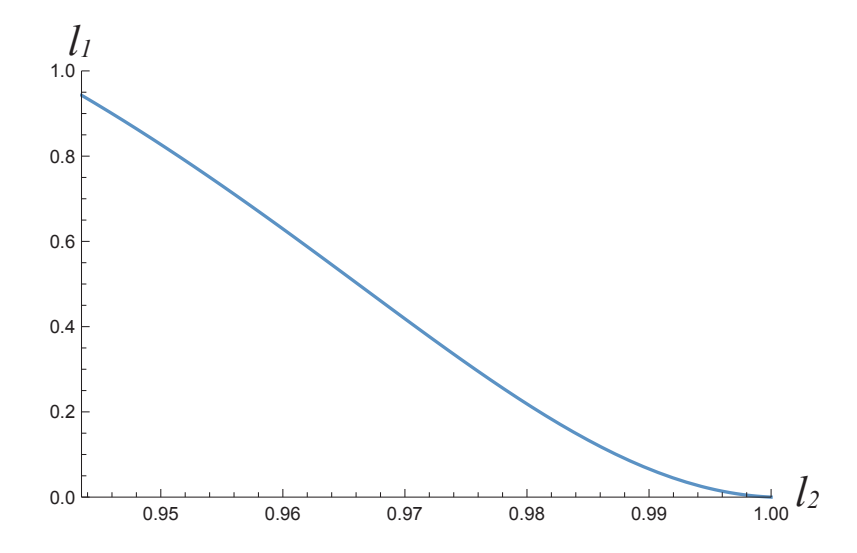


Figure 6.19.: The plot of  $l_1(l_2)$  in a cylindrical bar with 6.35 mm radius.

drop at the onset of dislocation nucleation followed by a short hardening behavior, as shown in Fig. 6.18. However, the theoretical curve at the larger twist angles exhibits no hardening behavior, in contrast to the experimental curve. This discrepancy in the hardening behavior could be explained by the simple dissipation function that does not take into account redundant dislocations and effective temperature.

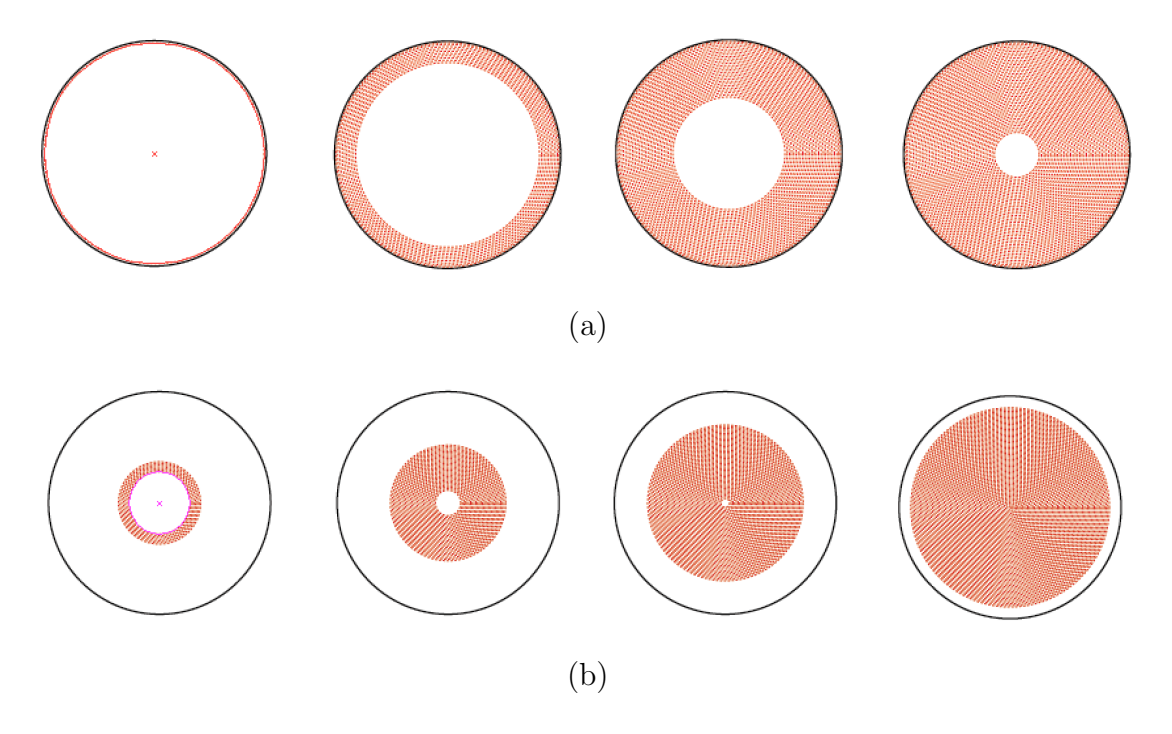


Figure 6.20.: Evolution of the distribution of excess screw dislocations: (a) in a bar of 6.35 mm radius, (b) in a microwire of 6.35  $\mu$ m. The applied twist increases from left to right.

We have analyzed the distribution of screw dislocations in a microwire, Fig. 6.11. It indicates that the dislocations are nucleated in a thin ring,  $(l_1, l_2)$ , at the middle position of the cross-section. This distribution seems contradict to the prediction of

6.5. Conclusion 133

classical plasticity theory that plastic region takes place from the surface. However, it turns out that the size of the wire (or bar) influences the distribution of dislocations. Fig. 6.19 shows the plot of function  $l_1$  in terms of  $l_2$  exhibiting the onset of the nucleation and the distribution of dislocations in a bar of macroscale with 6.35 mm radius. The predicted position at which the dislocations nucleate is  $l_m = l_1 = l_2 = 0.9435$  under the constraint  $0 \le l_1 \le l_2 \le 1$ . With the increasing twist,  $l_2$  increases up to 1 and  $l_1$  decreases toward 0. This process is schematically presented in Fig. 6.20(a), which in agreement with the classical plasticity theory. For comparison, the evolution of dislocation distribution in a microwire with 6.35  $\mu$ m radius is illustrated in Fig. 6.20(b).

## 6.5. Conclusion

In this chapter, we have shown that the torsion of a bar with circular cross-section can be analytically solved within the asymptotically exact continuum dislocation theory. If the resistance to dislocation motion is negligible, then dislocations are concentrated in a circle of radius less than the radius of the cross-section. The outer ring is dislocationfree. The plastic warping suffers a jump across the boundary between dislocation and dislocation-free regions, indicating misorientation of the crystal lattice. There is a threshold torque for dislocation nucleation. The torque drop takes place at the onsets of dislocation nucleation followed by the short hardening and subsequent softening. The normalized radius, at which the dislocation-free zone starts, predicted by continuum dislocation theory is compared with the result of Weinberger (2011). The evolutions of plastic warping, as well as the dislocation density, are compared with those investigated by Kaluza & Le (2011) and Liu et al. (2018). The configurations of the plastic warping and the density of dislocation by three models show several common features. If the resistance to dislocation motion is taken into account, then there exists the elastic zone in the middle of the cross-section. Dislocations are concentrated in a ring, whose size increases as the twist increases. The torque drop is also observed at the onsets of dislocation nucleation, but the hardening and softening effects are much less pronounced compared to the case without dissipation. The threshold value of the torque decreases with the increasing radius of the bar's cross-section exhibiting the size effect. No hardening behavior is observed at large twist angles, which is due to the absence of redundant dislocations and effective temperature in the dissipation potential. Last but not least, it would be quite convincing if this theoretical result for the dislocation distribution could be compared with the experimental observations and measurements. It is hoped that this chapter would serve as motivation for experimentalists using EBSD-technique (see, e.g., Kysar et al. (2010)) or, alternatively, the etch pits method to observe the dislocation zone in twisted bars and to measure the dislocation density.

## 7. Summary and Outlook

Microstructures of the crystalline materials characterize the properties on engineering scales. There are various sorts of macroscopic methods based on the phenomenological modeling that reproduce the properties of materials. However, the insights of the microstructure remain unclear. On the other hand, the microscopic methods possess the ability to attain the detailed information on the microstructures and the dynamics of discrete dislocations, but they are weak in acquiring the evolution of collective microstructures and in predicting the corresponding properties in the engineering application. Another challenge of them is the high cost of computation. This dissertation is concerned with the thermodynamic dislocation theory that first proposed by Langer et al. (2010) and further developed by Le (2018). The presented work attempts to bring together the advantages of microscopic and macroscopic methods so that it not only is utilized in the engineering scale but also describe the microstructures of the solid.

One main difference of the thermodynamic dislocation theory from the others is that it involves the entropy of dislocations, which has been ignored from the thermodynamic principle due to the fact that the entropy of dislocation is extremely small. However, in this theory, it is supposed that the entropy of total dislocations is an essential ingredient of the dislocation-mediated plasticity theory. The entropy of dislocations leads the thermodynamic system to have a well-defined temperature (the effective temperature), which is much higher than the ordinary temperature. Therefore, the system is characterized by two weakly interacted subsystems, the kinetic-vibrational subsystem and the configurational subsystem, and a set of physics-based parameters are introduced. We showed the development of this theory and explored the applications in various types of problem, such as problems on different scales and in different deformations. A feature of the thermodynamic dislocation theory on the mesoscopic scale is that it deals with the different types of boundary conditions and relates them to the physical property of the surfaces and interfaces. For example, the fixed boundaries behave as the obstacles such that the plastic warping possesses a homogeneous Dirichlet boundary condition, while at the free boundary, the plastic warping is subjected to the Neumann boundary condition. The results that are based on the solution of the boundary-value problem of the equilibrium of crystals containing dislocations allow one to find out the explicit outcomes. This dissertation discussed mainly three categories of the problem. One category is when the effect of excess dislocations on microforce equilibrium is ignored. It happens when the sample undergoes a uniform deformation that no excess dislocations are created or when the length of samples is on the macroscopic scale. The second category is crystal sample on microscale undergoes non-uniform deformation, such that the excess dislocations must be taken into account. In this case, the boundary value problem of the microforce equilibrium is added to the governing equations. The last one is a special case for the continuum dislocation theory using rank-one defect energy.

The main accomplishments of this dissertation comprised the following:

- We demonstrated a variational formulation for the thermodynamic dislocation theory. An equilibrium of microforces containing the flow stress, back stress, and the resolved shear stress is derived from the variational formulation. This approach allows one to investigate the isotropic and kinematic work hardening. The isotropic work hardening is caused by the redundant dislocations, and the kinematic hardening is caused by the pile-up of excess dislocations against the grain boundaries. On the engineering scale, the isotropic hardening is dominant, while when the length scale decreases down, the kinetic hardening becomes non-negligible.
- Dipole energy with respect to the distance between two dislocations is studied. The result showed that there exists an energy barrier that prevents the dipole from being dissolved into freely moving dislocations. When an external force is applied, the barrier is decreased, such that the thermal fluctuation helps dislocations to overcome the barrier.
- The asymptotically exact energy density of screw dislocations is found by the averaging procedure, where it is a product of linear and logarithmic functions. Its extrapolation in the extremely small and large region of dislocation density allows it to be used in the continuum approach.
- Size effect describing the phenomenon that "the smaller, the stronger," attributed to excess dislocations due to non-uniform deformation is studied. A modified Read-Shockley energy is involved in the energy functional, and it leads to a new type of boundary (the natural boundary) condition. The torque-twist simulation on microwires based on thermodynamic dislocation theory exhibiting size effect is compared to the corresponding experiment. The contributions of the flow stress and back stress are explicitly computed.
- Hardening and thermal softening behaviors, on single crystal copper bars and polycrystal aluminum bars, have been studied by thermodynamic dislocation theory, and the simulations are also compared to the experiments. It turns out that the hardening is due to the entanglement of the dislocations, and the thermal softening is caused by temperature rise inside the material body. The satisfactory simulation owes to the sensitivity of the theory to temperature and strain rates.
- In the continuum dislocation theory, the rank-one defect energy leads to a jump on the plastic warping and the torque in twisted wire. The evolutions of the plastic warping and dislocation density by continuum dislocation theory with the logarithmic defect energy and by critical thickness theory showed comparable results and exhibited several features in common. The distribution of dislocations in the circular cross-section of nanowires achieved an excellent agreement with numerical results by the microscopic methods. The analytical solution for the problem enabled one to predict the onset of the plastic deformation.

Despite the preliminary success of the theory and its satisfactory agreements to experiments, there are still spaces to improve. One could be the proof of the newly introduced parameters, such as the activation temperature  $T_P$ , the input power conversion factor  $K_\rho$ , the dimensionless factor  $K_\chi$ , and others (not listed all here). Since there is rare experimental evidence, although they are mostly physics-based, it is criticized for the curve fitting suspicion. Another one is introducing other defects into the theory in order to cover extensive problems.

Several topics are interesting to investigate in the future:

• It is found that the aspect ratio of the rectangular cross-section influences the en-

ergy of the crystal containing a dislocation dipole. When the ratio is beyond specific value, the energy of the crystal does not show big differences. However, when the ratio decreases from that critical value, the energy of the crystal increases distinctly. This phenomenon might be related to the size effect reported by Chen & Ngan. (2010); Keller *et al.* (2011) that there exists a strengthening effect depending on the shape and size of the sample.

- Torsion of bars at the same temperature, but at different strain rates have been solved well within the thermodynamic dislocation theory. However, the cases in twisted bars at the same strain rate, but different temperatures does not give acceptable results. The reason is probably the grain growth, and grain boundaries (or entropy of the grain boundary) are not taken into account.
- The experiments of cyclic loading (loading, unloading, and reloading) have been performed on the copper microwires and exhibited the Bauschinger effect. The investigation using thermodynamic dislocation theory is on the list.

#### A. Green's function

The solution of the boundary-value problem (3.12) is found as follows

$$\check{\Psi}(\mathbf{x}) = -\int_{\mathcal{A}} N(\mathbf{x}, \boldsymbol{\xi}) \mu \alpha_r(\boldsymbol{\xi}) d\xi,$$

where  $N(\mathbf{x}, \boldsymbol{\xi})$  is the Neumann function satisfying the equation

$$\begin{cases} -\nabla^2 N = \delta(\mathbf{x} - \boldsymbol{\xi}) - 1/|\mathcal{A}| & \text{in } \mathcal{A}, \\ N_{,n} = 0 & \text{on } \partial \mathcal{A}. \end{cases}$$

Substituting this solution into formula (3.13) for the energy of the crystal containing a dislocation dipole, we obtain

$$\underline{I} = \frac{1}{2}\mu\gamma^2|\mathcal{A}| - \mu\gamma lb + \frac{1}{2}\mu\int_{\mathcal{A}}\int_{\mathcal{A}}\alpha_r(\mathbf{x})N(\mathbf{x},\boldsymbol{\xi})\alpha_r(\boldsymbol{\xi})\mathrm{d}\boldsymbol{\xi}\mathrm{d}x. \tag{A.1}$$

The first two terms in (A.1) can be interpreted as the energy caused by the external field, while the last term is the energy of the dislocation dipole. Plugging  $\alpha_r = b[\delta_{r_0}(\mathbf{x} - \mathbf{x}^+) - \delta_{r_0}(\mathbf{x} - \mathbf{x}^-)]$  into (A.1) to get

$$\begin{split} \underline{I} &= \frac{1}{2} \mu \gamma^2 |\mathcal{A}| - \mu \gamma l b + \frac{1}{2} \mu b^2 \left[ \int_{C_+} \int_{C_+} \frac{1}{\pi r_0^2} \frac{1}{\pi r_0^2} N(\mathbf{x}, \boldsymbol{\xi}) \mathrm{d} \boldsymbol{\xi} \mathrm{d} x \right. \\ &+ \int_{C_-} \int_{C_-} \frac{1}{\pi r_0^2} \frac{1}{\pi r_0^2} N(\mathbf{x}, \boldsymbol{\xi}) \mathrm{d} \boldsymbol{\xi} \mathrm{d} x - 2 \int_{C_+} \int_{C_-} \frac{1}{\pi r_0^2} \frac{1}{\pi r_0^2} N(\mathbf{x}, \boldsymbol{\xi}) \mathrm{d} \boldsymbol{\xi} \mathrm{d} x \right]. \end{split}$$

Here  $C_+$  and  $C_-$  are the circles of radius  $r_0$  centered at  $\mathbf{x}^+$  and  $\mathbf{x}^-$ , respectively. The first two double integrals in the square brackets correspond to the self-energies of positive and negative dislocations, the last double integral being the interaction energy between them. To accelerate the numerical integration we use the Neumann function for the rectangle in the form of rapidly converging logarithmic series found by Marshall (1999)

$$N(\mathbf{x}, \boldsymbol{\xi}) = \frac{1}{c} n_y(x_2, \xi_2) + \frac{1}{2\pi} [G(\frac{\pi}{h}(x_2 + \xi_2)) + G(\frac{\pi}{h}|x_2 - \xi_2|)],$$

where  $\mathbf{x} = (x_1, x_2), \, \boldsymbol{\xi} = (\xi_1, \xi_2),$ 

$$n_y(x_2, \xi_2) = \begin{cases} \frac{1}{3}h - \xi_2 + \frac{x_2^2 + \xi_2^2}{2h}, & 0 \le x_2 < \xi_2, \\ \frac{1}{3}h - x_2 + \frac{x_2^2 + \xi_2^2}{2h}, & \text{otherwise,} \end{cases}$$

A. Green's function

and

$$G(y) = -\frac{1}{4} \ln \left[ 1 - 2e^{-hy/c} \cos \frac{\pi}{c} (x_1 - \xi_1) + e^{-2hy/c} \right]$$

$$-\frac{1}{4} \ln \left[ 1 - 2e^{-hy/c} \cos \frac{\pi}{c} (x_1 + \xi_1) + e^{-2hy/c} \right]$$

$$-\frac{1}{4} \sum_{m=1}^{\infty} \left\{ \ln \left[ 1 - 2e^{-(h/c)(2m\pi + y)} \frac{\pi}{c} (x_1 - \xi_1) + e^{-(2h/c)(2m\pi + y)} \right] + \ln \left[ 1 - 2e^{-(h/c)(2m\pi + y)} \frac{\pi}{c} (x_1 + \xi_1) + e^{-(2h/c)(2m\pi + y)} \right]$$

$$-\frac{1}{4} \sum_{m=1}^{\infty} \left\{ \ln \left[ 1 - 2e^{-(h/c)(2m\pi - y)} \frac{\pi}{c} (x_1 - \xi_1) + e^{-(2h/c)(2m\pi - y)} \right] + \ln \left[ 1 - 2e^{-(h/c)(2m\pi - y)} \frac{\pi}{c} (x_1 + \xi_1) + e^{-(2h/c)(2m\pi - y)} \right] \right\}.$$

The result of numerical integration with Mathematica is shown in Fig. 3.4. Marshall (1999) also constructed an alternative representation

$$N(\mathbf{x}, \boldsymbol{\xi}) = \frac{1}{c} n_y(x_2, \xi_2) + \frac{2}{\pi} \sum_{k=1}^{\infty} [Q_k(x_2, \eta_2) \cos(\frac{k\pi x_1}{c}) \cos(\frac{k\pi \xi_1}{c})], \tag{A.2}$$

where

$$Q_k(x_2, \xi_2) = \begin{cases} \frac{\cosh\frac{k\pi}{c}(h - \xi_2)\cosh\frac{k\pi x_2}{c}}{k\sinh\frac{k\pi h}{c}}, & 0 \le x_2 < \xi_2, \\ \frac{k\sinh\frac{k\pi h}{c}}{c}, & \cosh\frac{k\pi \xi_2}{c}, \\ \frac{\cosh\frac{k\pi}{c}(h - x_2)\cosh\frac{k\pi \xi_2}{c}}{k\sinh\frac{k\pi h}{c}}, & \text{otherwise.} \end{cases}$$

1.1.	TEM of cryogenic deformation microstructures of austenitic steels:(a) Dislocation networks, (b) Planar dislocation array, (c) Interaction between dislocation slip band and stacking fault (Fu et al., 2005). Images reprinted by permission	1
	- v -	
2.1. 2.2.	(a) Elastic and (b) Plastic deformation on atomic scale Four slip systems in unit cell of lattice and in the corresponding cylindrical sample: S.P-1 (red lines); S.P-2 (blue lines); S.P-3 (orange lines);	7
2.3.	S.P-4 (green lines)	8
	in tension (Wrobel & Piela, 2010). Images reprinted by permission	9
2.4.	Slips in compression: (a) Schematics of slips in a single crystal under compression, (b) Compressed cylindrical microsample of Ni with $10$ - $\mu$ m diameter (Uchic <i>et al.</i> , 2004), (c) Severely compressed nanopillar of the	
2.5.	single-crystal Nb (Kim et al., 2009). All images reprinted by permission Dislocation observation: (a) Two schematic illustrations of perspective and top view showing the arrangement of grain boundary and the edge dislocations, (b) Dark-field TEM image of the initial low-angle tilt grain boundary consisting of an array of edge dislocations (Kondo et	10
	al., 2016). Image reprinted by permission	11
2.6. 2.7.	<ul><li>(a) Edge dislocation,</li><li>(b) Closed circuit drawn in perfect crystal</li><li>(a) Screw Dislocation,</li><li>(b) Crystal with screw dislocation located at the</li></ul>	12
	origin with the dislocation line oriented towards $x_3$ -axis	13
2.8.	Dislocation Motion leading to plastic slip	13
2.9.	Schematic illustration of the mechanism of the bending and indenta-	
	tion: (a) A crystal containing dislocations, (b) Dissolved dislocations	
	from edge dislocation dipoles under applied moment, (c) Bent beam by having additional half planes, (d) A crystal before indentation, (e) One	
	atomic plastic deformation formed by storing a pair of edge dislocations,	
	(f) The crystal indented further	17
2.10.	Three types of work hardening: (a) Isotropic hardening, (b) Kinematic	
	hardening, (c) The combination of isotropic and kinematic hardening .	18
2.11.	Vertically shaded area: the strain energy $\mathcal{F}(\varepsilon_0)$ , and the horizontally shaded area: the complementary energy $\mathcal{F}^c(\sigma_0)$ in one dimensional elas-	
	ticity theory	25
	Additive decomposition of the total strain	31
2.13.	Decomposition of thermodynamic system into kinetic-vibrational and configurational subsystems	41
3.1.	Anti-plane constrained shear	47
3.2.	A cut creating a pair of dislocations.	48

3.3.	Dimensionless energy of dislocation dipole as function of $l/c$ : a) $\gamma = 0$ (yellow), b) $\gamma = 0.001$ (red), c) $\gamma = 0.01$ (black), d) Zoom in for the case $\gamma = 0$ , e) Zoom in for the case $\gamma = 0.001$ , f) Zoom in for the case	
	$\gamma = 0.01. \dots \dots$	53
3.4.	Combination of three cases of Fig. 3.3	54
3.5.	Energy of the crystal containing a dislocation dipole for different aspect ratio $h/c$ of the rectangular cross section: (a) $h/c = 1$ (black), $h/c = 5$ and $h/c = 10$ (blue, two curves overlapped), (b) $h/c = 1$ (black), $h/c = 1$	- 1
3.6.	0.5 and $h/c = 0.1$ (red)	54 56
3.7.	Dimensionless energy density $f = \psi_m/\mu$ versus dimensionless dislocation density $y = b^2 \rho^g$	57
3.8.	The dimensionless energy density $\psi_m/\mu$ versus the density of excess dislocations $\rho^g$ : (i) (3.19) (dashed line), (ii) (3.21) (bold line)	58
3.9.	Functions $g(\gamma) = \tau_Y(\gamma)/\mu$ : (i) $\tilde{q}_0 = 10^{-12}$ (black), (ii) $\tilde{q}_0 = 10^{-14}$ (red), (i) $\tilde{q}_0 = 10^{-16}$ (yellow)	63
3.10.	Normalized total density of dislocations $\tilde{\rho}(\gamma) = a^2 \rho$ : (i) $\tilde{q}_0 = 10^{-12}$ (black), (ii) $\tilde{q}_0 = 10^{-14}$ (red), (i) $\tilde{q}_0 = 10^{-16}$ (yellow)	64
3.11.	Relative thickness of the boundary layers $l(\gamma)$	64
3.12.	The plastic slip $\beta(x)$ : (i) $\gamma=0.002$ (black), (ii) $\gamma=0.005$ (red), (iii) $\gamma=0.01$ (yellow)	65
3.13.	Comparison of the plastic slip at $\gamma = 0.002$ , $\gamma = 0.005$ and $\gamma = 0.01$ by two methods: (i) Results by present method (solid line), (ii) Results by solving (3.28) (Le <i>et al.</i> , 2018) (dots)	65
3.14.	The normalized density of excess dislocations $b^2 \rho^g = \beta'$ : (i) $\gamma = 0.002$ (black), (ii) $\gamma = 0.005$ (red), (iii) $\gamma = 0.01$ (yellow)	66
3.15.	Dimensionless average shear stress versus shear strain curve: (i) present theory: $c=5.1$ micron (black), $c=51$ micron (red) (ii) LBL-theory	
3.16.	(yellow)	67
3.17.	boundary condition in the interval $x_1 \in (0, c/2)$ (blue) Stress-strain curves at the strain rate $\tilde{q}_0 = 10^{-13}$ , for room temperature: (a) with Dirichlet-Dirichlet boundary conditions (blue), Eq. (3.41), (b) with Dirichlet-Neumann boundary conditions (red), Eq. (3.42), (c) flow stress $\tau_Y/\mu$ versus strain $\gamma$ (dashed black)	68 69
4.1.	Configurations of excess screw dislocation in torsion loaded wire: (a)	0.5
	stress components in the cylindrical polar coordinate, (b) Stress acting on planes parallel and perpendicular to wire axis, (c) Screw dislocations parallel to wire axis on $\theta$ -face (Weertman, 2002), (d) Screw dislocations	
4.2.	perpendicular to wire axis on z-face (Weertman, 2002) Dislocation microstructure in the sample of micro-scale $(1 \times 1 \times 3 \mu m^3)$ : (a) wire axis oriented in the $\langle 234 \rangle$ which almost parallel to glide plane, (b) wire axis oriented in the $\langle 100 \rangle$ (Songer et al. 2011). Images	74
	(b) wire axis oriented in the $\langle 100 \rangle$ . (Senger <i>et al.</i> , 2011). Images reprinted by permission	75

4.3.	Comparison of torque-twist curves by two different configuration of screw dislocations, red for $\langle 234 \rangle$ (screw dislocations parallel to wire axis) orientation and blue for $\langle 100 \rangle$ (screw dislocations perpendicular to wire exist; (a) with the gross slip activated (b) without the gross	
	to wire axis): (a) with the cross slip activated, (b) without the cross slip activated. The data are taken from (Senger <i>et al.</i> , 2011)	76
4.4.	Torsion of a wire	76
4.5.	Solution of Eq. (4.27) with (i) original Read-Shockley's $f_2(\beta) = \frac{1}{4\pi} \ln(\beta_*/\beta)$	
	for $\beta < \beta_*$ and 0 otherwise: red, (ii) modified $\tilde{f}_2(\beta)$ from (4.30): black.	82
4.6.	Torque-twist curves with twist rate $L\dot{\omega} = \frac{\pi}{30}/s$ and for room temper-	
	ature, for four different radii $R=9$ micron (black), $R=15$ micron	
	(blue), $R = 21$ micron (green) and $R = 52.5$ micron (red): (i) TDT	0.0
1 7	(bold lines), (ii) experimental points taken from Liu et al. (2012) (circles).	83
4.7.	Torque-twist curves with twist rate $L\dot{\omega} = \frac{\pi}{30}/\text{s}$ and for room temperature, for four different radii $R = 9$ micron (black), $R = 15$ micron	
	(blue), $R = 21$ micron (green) and $R = 52.5$ micron (red): (i) TDT	
	(bold lines), (ii) LBL-theory (dashed lines)	84
4.8.	Stress distributions $\tau(\tilde{r})$ at twist rate $L\dot{\omega} = \frac{\pi}{30}/s$ and for room temper-	01
	ature, at $\tilde{\omega} = 0.198$ and for four different radii $R = 9$ micron (black),	
	R=15 micron (blue), $R=21$ micron (green), and $R=52.5$ micron	
	$(\mathrm{red}). \ldots \ldots$	84
4.9.	Plastic distortion $\beta(\tilde{r})$ at twist rate $L\dot{\omega} = \frac{\pi}{30}/s$ and for room temper-	
	ature, at $\tilde{\omega} = 0.198$ and for four different radii $R = 9$ micron (black),	
	R = 15 micron (blue), $R = 21$ micron (green), and $R = 52.5$ micron	٥٣
1 10	(red)	85
4.10.	Total density of dislocations $\rho(\tilde{r})$ at twist rate $L\dot{\omega} = \frac{\pi}{30}/s$ and for room temperature, at $\tilde{\omega} = 0.198$ and for four different radii $R = 9$ micron	
	(black), $R = 15$ micron (blue), $R = 21$ micron (green), and $R = 52.5$	
	micron (red)	85
4.11.	Density of excess dislocations $\rho^g(\tilde{r})$ at twist rate $L\dot{\omega} = \frac{\pi}{30}/s$ and for	
	room temperature, at $\tilde{\omega}=0.198$ and for four different radii $R=9$	
	micron (black), $R=15$ micron (blue), $R=21$ micron (green), and	
	$R = 52.5 \text{ micron (red)}. \dots \dots$	86
4.12.	Distributions of flow stress $\tau_Y(\tilde{r})$ at twist rate $L\dot{\omega} = \frac{\pi}{30}/\text{s}$ and for room	
	temperature, at $\tilde{\omega} = 0.198$ and for four different radii $R = 9$ micron (block) $R = 15$ micron (block) $R = 21$ micron (recon) and $R = 52.5$	
	(black), $R = 15$ micron (blue), $R = 21$ micron (green), and $R = 52.5$ micron (red)	88
4.13.	Distributions of $\alpha_{zz} = \omega_r + \omega/r$ , where $\omega$ is the average misalignment	00
1.10.	taken from Figure 7b of (Ziemann et al., 2015) for $\gamma_{pl}(R) = 0.01$	88
4.14.	Distributions of back stress $\tau_B(\tilde{r})$ at twist rate $L\dot{\omega} = \frac{\pi}{30}/\text{s}$ and for room	
	temperature, at $\tilde{\omega} = 0.198$ and for four different radii $R = 9$ micron	
	(black), $R=15$ micron (blue), $R=21$ micron (green), and $R=52.5$	
	micron (red)	90
4.15.	Contribution of flow stress $\tau_Y(\tilde{r})$ to the torque versus twist angle at	
	twist rate $L\dot{\omega} = \frac{\pi}{30}/\text{s}$ and for room temperature, at four different radii	
	R = 9  micron (black), R = 15  micron (blue), R = 21  micron (green),	Ω1
1 16	and $R = 52.5$ micron (red)	91
4.10.	twist rate $L\dot{\omega} = \frac{\pi}{30}/\text{s}$ and for room temperature, at four different radii	
	R=9 micron (black), $R=15$ micron (blue), $R=21$ micron (green),	
	and $R = 52.5$ micron (red)	91

5.1.	The geometry of a solid bar	94
5.2.	Gauge section of crystal sample	94
5.3.	The torque-twist curves at the twist rate $\dot{\phi} = 0.25^{\circ}/\text{s}$ and for room temperature: (i) sample 1: TDT-theory: black curve, experiment (Horstemeyer <i>et al.</i> , 2002): black circles (ii) sample 2: TDT-theory: red/dark	07
E 1	gray curve, experiment (Horstemeyer <i>et al.</i> , 2002): red/dark gray circles	97
5.4.	Stress distribution $\tau(r)$ at the twist rate $\dot{\phi}=0.25^{\circ}/\mathrm{s}$ and for room temperature: (i) $\phi=10^{\circ}$ (black), (ii) $\phi=30^{\circ}$ (red/dark gray), (iii) $\phi=50^{\circ}$ (yellow/light gray)	98
5.5.	Stress-twist curves at particular position of $r$ at the twist rate $\dot{\phi} = 0.25^{\circ}/\text{s}$ and for room temperature: (i) $r = 3.18\text{mm}$ (black), (ii) $r = 4.76\text{mm}$ (red/dark gray), (iii) $r = 6.35\text{mm}$ (yellow/light gray)	99
5.6.	Total density of dislocations $\rho(r)$ at the twist rate $\dot{\phi} = 0.25^{\circ}/\text{s}$ and for room temperature: (i) $\phi = 10^{\circ}$ (black), (ii) $\phi = 30^{\circ}$ (red/dark gray), (iii) $\phi = 50^{\circ}$ (yellow/light gray)	100
5.7.	The torque-twist curves for the bars twisted at different twist rates and for room temperature: (i) $\dot{\phi} = 0.25^{\circ}/\text{s}$ (black), (ii) $\dot{\phi} = 2.5^{\circ}/\text{s}$ (red/dark	
	gray), (iii) $\phi = 25^{\circ}/\text{s}$ (yellow/light gray)	101
5.8.	The torque-twist curves for the bars twisted at the same twist rate $\dot{\phi} = 0.25^{\circ}$ /s and for three different ambient temperatures: (i) $T = 25^{\circ}$ C	
	(black), (ii) $T = 250^{\circ}$ C (red/dark gray), (iii) $T = 500^{\circ}$ C (yellow/light gray)	102
5.9.	Torque-twist curves for ambient temperature $T_0 = 773 \mathrm{K}$ , and for five different twist rates $R\dot{\omega} = 19.7/\mathrm{s}$ (black), $R\dot{\omega} = 6.44/\mathrm{s}$ (blue), $R\dot{\omega} = 1.84/\mathrm{s}$ (red), $R\dot{\omega} = 0.21/\mathrm{s}$ (green) and $R\dot{\omega} = 0.02/\mathrm{s}$ (cyan): (i) TDT (bold lines), (ii) experimental points taken from Zhou & Clode (1998)	
		104
5.10.	Stress-twist curves at $r = 5$ mm for ambient temperature $T_0 = 773 \mathrm{K}$ , and for five different twist rates $R\dot{\omega} = 19.7/\mathrm{s}$ (black), $R\dot{\omega} = 6.44/\mathrm{s}$ (blue), $R\dot{\omega} = 1.84/\mathrm{s}$ (red), $R\dot{\omega} = 0.21/\mathrm{s}$ (green) and $R\dot{\omega} = 0.02/\mathrm{s}$ (gyan)	104
5.11.	(blue), $R\dot{\omega} = 1.84/\text{s}$ (red), $R\dot{\omega} = 0.21/\text{s}$ (green) and $R\dot{\omega} = 0.02/\text{s}$ (cyan). Stress-twist curve for four different position in $r$ axis at ambient temperature $T_0 = 773 \text{ K}$ and twist rate $R\dot{\omega} = 19.7/\text{s}$ : $r = 5 \text{mm}$ (black),	104
		105
5.12.	Stress distributions $\tau(r)$ at $\bar{\omega}_* = 1.5$ for ambient temperature $T_0 = 773 \mathrm{K}$ , and for five different twist rates $R\dot{\omega} = 19.7/\mathrm{s}$ (black), $R\dot{\omega} = 6.44/\mathrm{s}$ (blue), $R\dot{\omega} = 1.84/\mathrm{s}$ (red), $R\dot{\omega} = 0.21/\mathrm{s}$ (green) and $R\dot{\omega} = 0.02/\mathrm{s}$	
		106
5.13.	Density of dislocations $\rho(r)$ at $\bar{\omega}_* = 1.5$ for ambient temperature $T_0 = 773 \mathrm{K}$ , and for five different twist rates $R\dot{\omega} = 19.7/\mathrm{s}$ (black), $R\dot{\omega} = 6.44/\mathrm{s}$ (blue), $R\dot{\omega} = 1.84/\mathrm{s}$ (red), $R\dot{\omega} = 0.21/\mathrm{s}$ (green) and $R\dot{\omega} = 0.02/\mathrm{s}$	
		107
5.14.	Temperature rise $\Delta T(r)$ at $\bar{\omega}_* = 1.5$ for ambient temperature $T_0 = 773 \mathrm{K}$ , and for five different twist rates $R\dot{\omega} = 19.7/\mathrm{s}$ (black), $R\dot{\omega} = 6.44/\mathrm{s}$ (blue), $R\dot{\omega} = 1.84/\mathrm{s}$ (red), $R\dot{\omega} = 0.21/\mathrm{s}$ (green) and $R\dot{\omega} = 0.02/\mathrm{s}$	40-
	(cyan)	108
	0 0	112
6.2.	Function $f(x)$ for $R/r_0 = 10^4$	114

6.3.	The normalized energy and normalized twist per unit length as functions	
	of the number of dislocations: (i) bold line: The proposed continuum	110
	3/ ( <i>)</i> 1	116
6.4.	Evolution of the plastic warping $\beta(\tilde{r})$ : (a) $l = 0.5$ ( $\tilde{\omega} = 0.00083$ ), (b)	
	$l = 0.7 \ (\tilde{\omega} = 0.00265), \ (c) \ l = 0.9 \ (\tilde{\omega} = 0.02351). \dots \dots \dots$	119
6.5.	Distribution of normalized dislocation density $\tilde{\rho}(\tilde{r})$ : (a) $l=0.5$ ( $\tilde{\omega}=$	
	0.00083), (b) $l = 0.7$ ( $\tilde{\omega} = 0.00265$ ), (c) $l = 0.9$ ( $\tilde{\omega} = 0.02351$ )	120
6.6.	Distribution of dimensionless shear stress $\tau(\tilde{r})$ : (a) $l = 0.5$ ( $\tilde{\omega} = 0.00083$ ),	
	(b) $l = 0.7$ ( $\tilde{\omega} = 0.00265$ ), (c) $l = 0.9$ ( $\tilde{\omega} = 0.02351$ )	120
6.7.	The torque-twist curve: (a) Left: the whole curve, (b) Right: Zoomed	101
0.0	near the origin.	121
6.8.	Distribution of normalized dislocation density $\tilde{\rho}(\tilde{r})$ in nanowire of 5 nm	101
		121
6.9.	Distribution of screw excess dislocations: (a) $l_{10} = 0.37$ , (b) $l_{20} = 0.495$	
	$l_{50} = 0.66. \dots \dots$	122
6.10.	• Left column: The distribution of plastic warping $\beta$ at different values	
	of surface shear strain, $R\omega = 0.02$ (black), $R\omega = 0.01$ (red), $R\omega = 0.005$	
	(blue). (a) Prediction by proposed theory with the aid of logarithmic	
	defect energy (see Kaluza & Le (2011)), (b) Prediction by critical thick-	
	ness theory (see Liu et al. (2018)), (c) Prediction by proposed theory	
	with the aid of rank-one defect energy.	
	• Right column: The distribution of dislocation density of excess screw	
	dislocation at different value of surface strain, $R\omega = 0.02$ (black),	
	$R\omega = 0.01$ (red), $R\omega = 0.005$ (blue). (d) Prediction by proposed the-	
	ory with the aid of logarithmic defect energy (see Kaluza & Le (2011)),	
	(e) Prediction by critical thickness theory (see Liu et al. (2018)), (f)	
	Prediction by proposed theory with the aid of rank-one defect energy.	123
6.11.	The plot of $l_1(l_2)$	127
6.12.	Evolution of the plastic warping $\beta(\tilde{r})$ : (a) $l = 0.5$ ( $\tilde{\omega} = 0.00088$ ), (b)	
	$l = 0.7 \ (\tilde{\omega} = 0.0027), \ (c) \ l = 0.9 \ (\tilde{\omega} = 0.02356)$	128
6.13.	Distribution of normalized dislocation density $\bar{\rho}(\tilde{r})$ : (a) $l=0.5$ ( $\tilde{\omega}=$	
	0.00088), (b) $l = 0.7$ ( $\tilde{\omega} = 0.0027$ ), (c) $l = 0.9$ ( $\tilde{\omega} = 0.02356$ )	128
6.14.	Distribution of dimensionless shear stress $\tau(\tilde{r})$ : (a) $l = 0.5$ ( $\tilde{\omega} = 0.00088$ ),	
	(b) $l = 0.7$ ( $\tilde{\omega} = 0.0027$ ), (c) $l = 0.9$ ( $\tilde{\omega} = 0.02356$ )	129
6.15.	The torque-twist curve: (a) The whole curve, (b) Zoomed near the origin.	130
	The size effect: (a) Left: function $l_{2m}(R)$ , (b) Right: function $\tilde{\omega}_m(R)$ .	
		131
6.18.		
		132
6.17. 6.18. 6.19.	The size effect: (a) Left: function $l_{2m}(R)$ , (b) Right: function $\omega_m(R)$ . Torque-twist curve: (a) Left: The presented theory, (b) Right: Experiment (taken from Horstemeyer $et~al.~(2002))$	131 131 132

## **List of Tables**

2.1.	Slip systems in face-centered cubic crystal with S.P denotes slip plane and S.D indicates slip direction. In each slip system there are three slip	
	directions	8
4.1.	The initial values of $\tilde{\rho}_i$ and $\tilde{\chi}_i$	86
	The initial values of $\tilde{\rho}_i$ and $\tilde{\chi}_i$	
6.1.	Normalized radius $l$ at which dislocation-free zone starts predicted by two different theories	122

### **Nomenclature**

#### **Greek Symbols**

- $\alpha$  Nye's dislocation tensor
- β Plastic distortion tensor
- $\boldsymbol{\beta}^t,~\boldsymbol{\beta}^e$  Total and elastic distortion tensor
- $\Omega$  Rotation tensor
- $\Omega^e$ ,  $\Omega^p$  Elastic and plastic rotation tensor
- $\sigma$  Stress tensor
- $\varepsilon$  Strain tensor
- $\boldsymbol{\varepsilon}^{e}$  Elastic strain tensor
- $\chi$  Effective temperature
- $\chi_0$  Steady-state configurational temperature
- $\mu$  Shear modulus
- $\rho^g$  Excess dislocation density
- $\rho^r$  Redundant dislocation density
- $\rho^{ss}$  Steady-state dislocation density
- $\rho_0$  Material's density
- au Shear stress
- $\tau_B$  Back stress

Nomenclature Nomenclature

$ au_T$	Taylor stress
$ au_Y$	Flow stress
Θ	Ordinary temperature
Math	nematical functions
( )′	Derivative w.r.t its argument
(´)	Fluctuation of the variable
( )	Prescribed variable
$(\check{\ })$	Average of the variable
$\check{(}$	Minimizing/Maximizing element
( )	Time derivative
$\nabla$	Nabla operator
div	Divergence operator
$\mathrm{tr}(\ )$	Trace operature
$\tilde{(\ )}$	Rescaled variable
Roma	an Symbols
$\mathrm{d}a$	Area element
$\mathrm{d}s$	Line element
$\mathbb{C}$	Fourth order elastic stiffness tensor
В	Resultant Burgers vector
b	Burgers vector
$\mathbf{F}$	Deformation gradient
f	Surface force

Nomenclature 151

$\mathbf{F}^e,~\mathbf{F}^p$ Elastic deformation gradient and plastic deformation gradient		
$\mathbf{f}_B$	Body force	
h	Heat flux	
v	Velocity vector	
${\cal E}$	Total energy	
$\mathcal{K}$	Kinetic energy	
$\mathcal{P}$	Input power	
$\mathcal{R}$	Rate of heat supply	
$\mathcal{U}$	Internal energy	
$\partial \mathcal{A}$	Boundary of cross section	
$\partial \mathcal{V}$	Surface of the region in 3-dimensional space	
$\partial \mathcal{V}_t$	Surface with prescribed force	
$\partial \mathcal{V}_u$	Surface with prescribed displacement	
$\partial_k$	Boundary of cross-section with prescribed displacement	
$\partial_s$	Boundary of cross-section with prescribed force	
D	Dissipation potential	
$e_D$	Energy per dislocation	
$k_B$	Boltzmann factor	
$S_C$	Entropy of configurational subsystem	
$S_R$	Entropy of kinetic-bivrational subsystem	
T	Kinetic-vibrational temperature	
$T_P$	Activation temperature	

Nomenclature Nomenclature

 $U_C$  — Internal energy of configurational subsystem

 $U_P$  Potential well in the pinning site

 $U_R$  Internal energy of kinetic-bivrational subsystem

- Abbod, M.F., Sellars, C.M., Cizek, P., Linkens, D.A., Mahfouf, M. (2007). Modeling the flow behavior, recrystallization, and crystallographic texture in hot-deformed Fe-30 Wt Pct Ni Austenite. Metallurgical and Materials Transactions A 38:2400-2409.
- Aifantis, E.C. (1999). Strain gradient interpretation of size effects. International Journal of Fracture 95, 299–314.
- Aifantis, E.C. (2009). Non-singular dislocation fields. In: IOP Conference Series: Materials Science and Engineering (Vol. 3, No. 1, p. 012026). IOP Publishing.
- Aifantis, E.C. (2009b). On scale invariance in anisotropic plasticity, gradient plasticity and gradient elasticity. International Journal of Engineering Science 47, 1089–1099.
- Akarapu, S., Zbib, H.M., Bahr, D.F. (2010). Analysis of heterogeneous deformation and dislocation dynamics in single crystal micropillars under compression. International Journal of Plasticity 26, 239-257.
- Al-Rub, R.K.A., Voyiadjis, G.Z. (2004). Analytical and experimental determination of the material intrinsic length scale of strain gradient plasticity theory from micro-and nano-indentation experiments. International Journal of Plasticity 20, 1139-1182.
- Al-Rub, R.K.A., Voyiadjis, G.Z. (2006). A physically based gradient plasticity theory. International Journal of Plasticity 22, 654–684
- Arsenlis, A., Parks, D.M. (1999). Crystallographic aspects of geometrically-necessary and statistically-stored dislocation density. Acta Materialia 47, 1597–1611.
- Ashby, M.F. (1970). The deformation of plastically non-homogeneous materials. Philosophical Magazine 21, 399-424.
- Baitsch, M., Le, K.C., Tran, T.M. (2015). Dislocation structure during microindentation. International Journal of Engineering Science 94, 195–211.
- Bakhvalov, N.S. (1974). Homogenized properties of periodically heterogeneous solids. Doklady Akademii Nauk SSSR 218:1046-1048.
- Bardella, L., Panteghini, A. (2015). Modelling the torsion of thin metal wires by distortion gradient plasticity. Journal of the Mechanics and Physics of Solid 78, 467–492.
- Bensoussan, A., Lions, J.L., Papanicolaou, G. (1978). Asymptotic analysis for periodic structures. North-Holland Publishing Company, Amsterdam.
- Berdichevsky, V.L. (2006a). Continuum theory of dislocations revisited. Continuum Mechanics and Thermodynamics 18, 195–222.

Berdichevsky, V.L. (2006b). On thermodynamics of crystal plasticity. Scripta Materialia 54, 711–716.

- Berdichevsky, V.L. (2008). Entropy of microstructure. Journal of the Mechanics and Physics of Solid 56, 742–771.
- Berdichevsky, V.L. (2009). Variational principles of continuum mechanics: I. Fundamentals. Springer Science and Business Media, Berlin.
- Berdichevsky, V.L. (2016). On a continuum theory of dislocation equilibrium. International Journal of Engineering Science 106:10–28.
- Berdichevsky, V.L. (2017). A continuum theory of screw dislocation equilibrium. International Journal of Engineering Science 116:74–87.
- Berdichevsky, V.L. (2018). Entropy and temperature of microstructure in crystal plasticity. International Journal of Engineering Science 118:24–30.
- Berdichevsky, V.L. (2019). Beyond classical thermodynamics: Dislocation-mediated plasticity. Journal of the Mechanics and Physics of Solid 129, 83–118.
- Berdichevsky, V.L., Le, K.C. (2002). Theory of charge nucleation in two dimensions. Physical Review E 66:026129.
- Berdichevsky, V.L., Le, K.C. (2007). Dislocation nucleation and work hardening in anti-planed constrained shear. Continuum Mechanics and Thermodynamics 18, 455–467.
- Berdichevskii, V.L., Sedov, L.I. (1967). Dynamic theory of continuously distributed dislocations. its relation to plasticity theory. Journal of Applied Mathematics and Mechanics 31, 989–1006.
- Berthier, L., Barrat, J., Kurchan, J. (2000). A two-time-scale, two-temperature scenario for nonlinear rheology. Physical Review E 61, 5464–5472.
- Bilby, B. (1955). Types of dislocation source, in: Report of Bristol Conference on Defects in Crystalline Solids (The Physical Soc. Bristol, London), pp. 124–133.
- Bilby, B.A., Bullough, R., Smith, E. (1955). Continuous distributions of dislocations: a new application of the methods of non-Riemannian geometry. Proceedings of the Royal Society (London) A 231, 263–273.
- Bilby, B.A. (1960). Continuous distribution of dislocations. Progress in Solid Mechanics 1, 329–398.
- Bouchbinder, E., Langer, J.S., 2009a. Nonequilibrium thermodynamics of driven amorphous materials. I. Internal degrees of freedom and volume deformation. Physical Review 80, 031131
- Bouchbinder, E., Langer, J.S. (2009). Nonequilibrium thermodynamics of driven amorphous materials. II. Effective-temperature theory. Physical Review E 80, 031132.
- Bouchbinder, E., Langer, J.S., (2009c). Nonequilibrium thermodynamics of driven amorphous materials. III. Shear-transformation-zone plasticity. Physical Review E 80, 031133

Brinckmann, S., Siegmund, T., Huang, Y. (2006). A dislocation density based strain gradient model. International Journal of Plasticity 22, 1784–1797

- Callister, W.D., Rethwisch, D.G. (2007). Fundamentals of materials science and engineering: An integrated approach. John Wiley & Sons, 4th edition, New York.
- Cai, W., Arsenlis, A., Weinberger, C.R., Bulatov, V.V. (2006). A non-singular continuum theory of dislocations. Journal of the Mechanics and Physics of Solids 54, 561-587.
- Chen, S.R., Stout, M.G., Kocks, U.F., MacEwen, S.R., Beaudoin, A.J. (1998). Constitutive modeling of a 5182 aluminum as a function of strain rate and temperature. Technical report, Los Alamos National Lab., NM (United States).
- Chen, X.X., Ngan, A.H.W. (2010). Specimen size and grain size effects on tensile strength of Ag microwires. Scripta Materialia 64, 717–720.
- Chokshi, A.H., Rosen, A., Karch, J., Gleiter, H.(1989). On the Validity of the Hall-Petch Relationship in Nanocrystalline Materials. Scripta Metallurgica, 23, 1679-1683.
- Chowdhury, S.R., Roy, D., Reddy, J.N., Srinivasa, A. (2016). Fluctuation relation based continuum model for thermoviscoplasticity in metals. Journal of the Mechanics and Physics of Solids 96, 353–368.
- Chowdhury, S.R., Kar, Gurudas, Roy, D., Reddy, J.N. (2018). Metal viscoplasticity with two-temperature thermodynamics and two dislocation densities. Continuum Mechanics and Thermodynamics 30: 397–420.
- Coleman, B.D., Noll, W. (1963). The thermodynamics of elastic materials with heat conduction and viscosity. Archive for rational mechanics and analysis 13 (1), 167–178.
- Cottrell, A.H. (1953). Dislocations and Plastic Flow in Crystals. Clarendon Press, Oxford.
- Cugliandolo, L., Kurchan, J., Peliti, L. (1997). Energy flow, partial equilibration, and effective temperatures in systems with slow dynamics. Physical Review E 55, 3898–3914
- Das, S., Hofmann, F., Tarleton, E. (2018). Consistent determination of geometrically necessary dislocation density from simulations and experiments. International Journal of Plasticity 109, 18–42.
- Demir, E., Raabe, D., Zaafarani, N., Zaefferer, S. (2009). Investigation of the indentation size effect through the measurement of the geometrically necessary dislocations beneath small indents of different depths using EBSD tomography. Acta Materialia 57, 559-569.
- Demir, E., Raabe, D., Roters, F. (2010). The mechanical size effect as a mean-field breakdown phenomenon: Example of microscale single crystal beam bending. Acta Materialia 58, 1876-1886.

Demir, E., Raabe, D. (2010a). Mechanical and microstructural single-crystal Bauschinger effects: Observation of reversible plasticity in copper during bending. Acta Materialia 58, 6055-6053.

- Duffy, Dean G. (2001). Green's Functions with Applications. Chapman & Hall/CRC.
- Dunstan, D.J., Bushby, A.J. (2004). Theory of deformation in small volumes of material. Proceedings of the Royal Society London A.460, 2781–2796.
- Dunstan, D.J., Ehrler, B., Bossis, R., Joly, S., P'NG, K.M.Y., Bushby, A.J. (2009). Elastic limit and strain hardening of thin wires in torsion. Physical Review Letters 103, 155501.
- Dunstan, D.J., 2012. Critical thickness theory applied to micromechanical testing. Advanced Engineering Materials 14, 942–947
- Dunstan, D.J. (2016). Validation of a phenomenological strain-gradient plasticity theory. Philosophical Magazine Letters 96, 305–312
- Edwards, S.F. (1990). The rheology of powders. Pheologica Acta 29, 493–499.
- Edwards, S. F. (1994). The role of entropy in specifications of powder. Granular matter: An interdisciplinary approach 121–140. New York: Springer-Verlag
- Eshelby, J.D. (1953). Screw dislocations in thin rods. Journal of Applied Physics 24, 176–179.
- Engels, P., Ma, A., Hartmaier, A. (2012). Continuum simulation of the evolution of dislocation densities during nanoindentation. International Journal of Plasticity 38, 159–169.
- Espinosa, H.D., Panico, M., Berbenni, S., Schwarz, K.W. (2006). Discrete dislocation dynamics simulations to interpret plasticity size and surface effects in freestanding FCC thin films. International Journal of Plasticity 22, 2091–2117.
- Fu, R., Qiu, L., Wang, T., Wang, C., Zheng, Y. (2005). Cryogenic deformation microstructures of 32Mn-7Cr-1Mo-0.3N austenitic steels. Materials Characterization 55, 355–361.
- Fleck, N.A., Muller, G.M., Ashby, M.F., Hutchinson, J.W. (1994). Strain gradient plasticity: Theory and experiment. Acta Metallurgica et Materialia 42, 475–487.
- Fleck, N.A., Hutchinson, J.W. (2001). A reformulation of strain gradient plasticity. Journal of the Mechanics and Physics of Solids 49, 2245-2271.
- Follansbee, P.S., Kocks, U.F. (1988). A constitutive description of the deformation of copper based on the use of the mechanical threshold stress as an internal state variable. Acta Metallurgica 36:81-93.
- Gan, Z., He, Y., Liu, D., Zhang, B., Shen, L. (2014). Hall-Petch effect and strain gradient effect in the torsion of thin gold wires. Scripta Materialia 87, 41–44
- Gao, H., Huang, Y., Nix, W.D. (1999). Modeling plasticity at the micrometer scale. Naturwissenschaften 86, 507–515.

Gao, H., Huang, Y. (2003). Geometrically necessary dislocation and size-dependent plasticity. Scripta Materialia 48, 113–118.

- Gelfand, I.M., Shilov, G.E. (1964). Generalized functions. Vol. 1. Properties and operations. Academic Press, New York.
- Greer, J.R., Oliver, W.C., Nix, W.D. (2005). Size dependence of mechanical properties of gold at the micron scale in the absence of strain gradients. Acta Materialia 53, 1821–1830.
- Groma, I., Csikor, F., and Zaiser, M. (2003). Spatial correlations and higher-order gradient terms in a continuum description of dislocation dynamics. Acta Materialia 51:1271–1281
- Gurtin, M.E. (2002). A gradient theory of single-crystal viscoplasticity that accounts for geometrically necessary dislocations. Journal of the Mechanics and Physics of Solids 50, 5-32.
- Gurtin, M.E., Anand, L. (2005). A gradient theory of strain-gradient plasticity for isotropic, plastically irrotational materials. Part I: small deformations. Journal of the Mechanics and Physics of Solids 53, 1624–1649.
- Haasen, P. (1958). Plastic deformation of nickel single crystals at low temperatures. Philosophical Magazine 3, 384–418.
- Hackl, K., Fischer, F.D.(2008). On the relation between the principle of maximum dissipation and inelastic evolution given by dissipation potentials. Proceedings of the Royal Society A 464, 117–132.
- Hackl, K., Fischer, F.D., Svoboda, J.(2011). A study on the principle of maximum dissipation for coupled and non-coupled non-isothermal processes in materials. Proceedings of the Royal Society A 467, 1186–1196.
- Hansen, N., Kuhlmann-Wilsdorf, D. (1986). Low energy dislocation structures due to unidirectional deformation at low temperatures. Materials Science and Engineering 81, 141–161.
- Hall, E.O.(1951). The Deformation and Ageing of Mild Steel: III Discussion of Results. Proceedings of the Physical Society B, 64, 747–753.
- Haxton, T.K., Liu, A.J. (2007). Activated dynamics and effective temperature in a steady state sheared glass. Physical Review Letters 99, 195701.
- Hayashi, I., Sato, M., Kuroda, M. (2011). Strain hardening in bent copper foils. Journal of the Mechanics and Physics of Solids 59, 1731–1751.
- Hughes, D.A., Hansen, N., 1997. High angle boundaries formed by grain subdivision mechanisms. Acta Materialia 45, 3871–3886.
- Hull, D., Bacon, D.J. (2011). Introduction to dislocations. Butterworth-Heinemann, Amsterdam.
- Hochrainer, T., Zaiser, M., Gumbsch, P. (2007). A three-dimensional continuum theory of dislocation systems: kinematics and mean-field formulation. Philosophical Magazine 87, 1261–1282.

Hochrainer, T., Sandfeld, S., Zaiser, M., Gumbsch, P. (2014). Continuum dislocation dynamics: towards a physical theory of crystal plasticity. Journal of Mechanics and Physics of Solids 63, 167–178.

- Horstemeyer M.F., Lim J., Lu W.Y., Mosher D.A., Baskes M.I., Prantil V.C., Plimpton S.J. (2002). Torsion/simple shear of single crystal copper. Journal of Engineering Materials and Technology 124, 322–328.
- Huang, G., Svendsen, B. (2010). Effect of surface energy on the plastic behavior of crystalline thin films under plane strain constrained shear. International Journal of Fracture 166, 173-178.
- Huang, Y., Qu, S., Hwang, K.C., Li, M., Gao, H. (2004). A conventional theory of mechanism-based strain gradient plasticity. International Journal of Plasticity 20, 753-782.
- Kametani, R., Kodera, K., Okumura, D., Ohno, N.(2012). Implicit iterative finite element scheme for a strain gradient crystal plasticity model based on self-energy of geometrically necessary dislocations. Computational Materials Science 53, 53–59.
- Kamrin, K., Bounchbinder, E. (2014). Two-temperature continuum thermomechanics of deforming amorphous solids. Journal of Mechanics and Physics of Solids 73, 269–288.
- Kaluza, M., Le, K.C. (2011). On torsion of a single crystal rod. International Journal of Plasticity 27, 460–469.
- Keller, C., Hug, E., Feaugas, X. (2011). Microstructural size effects on mechanical properties of high purity nickel. International Journal of Plasticity 27, 635–654.
- Kim, J., Jang, D., Greer, J. (2009). Insight into the deformation behavior of niobium single crystals under uniaxial compression and tension at the nanoscale. Scripta Materialia 61, 300–303.
- Klusemann, B., Svendsen, B., Bargmann, S.(2013). Analysis and comparison of two finite element algorithms for dislocation density based crystal plasticity. GAMM-Mitteilungen 36, 219–238.
- Kochmann, D.M., Le, K.C. (2008). Dislocation pile-ups in bicrystals within continuum dislocation theory. International Journal of Plasticity 24, 2125–2147.
- Kochmann, D.M., Le, K.C. (2009a). Plastic deformation of bicrystals within continuum dislocation theory. Mathematics and Mechanics of Solids 14, 540–563.
- Kochmann, D.M., Le, K.C. (2009b). A continuum model for initiation and evolution of deformation twinning. Mathematics and Mechanics of Solids 14, 540–563.
- Kocks, U.F., Mecking, H. (2003). Physics and phenomenology of strain hardening: the FCC case. Progress in Materials Science, 48, 171-273.
- Kondo, S., Mitsuma, T., Shibata, N., Ikuhara, Y. (2016). Direct observation of individual dislocation interaction processes with grain boundaries. Science Advances 2016;2:e1501926.

Koster, M., Le, K.C., Nguyen, B.D. (2015). Formation of grain boundaries in ductile single crystals at finite plastic deformations. International Journal of Plasticity 69, 134-151.

- Kröner, E. (1955). Der fundamentale Zusammenhang zwischen Versetzungsdichte und Spannungsfunktionen. Zeitschrift für Physik A Hadrons and Nuclei 142, 463–475.
- Kröner, E. (1958). Kontinuumstheorie der Versetzungen und Eigenspannungen. Springer, Berlin.
- Kröner, E. (1962). Dislocations and continuum mechanics. Appl. Mech. Rev. 15, 599–606.
- Kröner, E. (1992). Mikrostrukturmechanik. GAMM-Mitteilungen 15, 104–119.
- Kuroda, M., Tvergaard, V. (2008). A finite deformation theory of higher-order gradient crystal plasticity. Journal of the Mechanics and Physics of Solids 56, 2573–2584.
- Kysar, J.W., Saito, Y., Oztop, M. S., Lee, D., Huh, W.T. (2010). Experimental lower bounds on geometrically necessary dislocation density. International Journal of Plasticity 26, 1097–1123.
- Laird, C., Charsley, P., Mughrabi, H., 1986. Low energy dislocation structures produced by cyclic deformation. Materials Science and Engineering 81, 433–450.
- Langer, J.S. (2008). Shear-transformation-zone theory of plastic deformation near the glass transition. Physics Review E 77, 021502
- Langer, J.S., Bouchbinder, E., Lookman, T. (2010). Thermodynamic theory of dislocation-mediated plasticity. Acta Materialia 58:3718-3732.
- Langer, J.S.(2015). Statistical thermodynamics of strain hardening in polycrystalline solids. Physical Review E 92:032125.
- Langer, J.S. (2016). Thermal effects in dislocation theory. Physical Review E 94:063004.
- Langer, J.S. (2017a). Thermal effects in dislocation theory. II. Shear banding. Physical Review E 95:013004.
- Langer, J.S. (2017b). Yielding transitions and grain-size effects in dislocation theory. Physical Review E 95:033004.
- Langer, J.S. (2017c). Thermodynamic theory of dislocation-enabled plasticity. Physical Review E 96:053005.
- Langer, J.S. (2018). Thermodynamic analysis of the Livermore molecular-dynamics simulations of dislocation-mediated plasticity. Physical Review E 98: 023006.
- Le, K.C. (1999). Vibrations of shells and rods. Springer, Berlin.
- Le, K.C. (2010). Introduction to Micromechanics. Nova Science, New York.
- Le, K.C. (2016a). Three-dimensional continuum dislocation theory. International Journal of Plasticity 76, 213–230.

Le, K.C. (2016b). Self-energy of dislocations and dislocation pileups. International Journal of Engineering Science 100, 1–7.

- Le, K.C. (2018). Thermodynamic dislocation theory for non-uniform plastic deformations. Journal of the Mechanics and Physics of Solids 111:157-169.
- Le, K.C. (2019). Thermodynamic dislocation theory: Finite deformations. International Journal of Engineering Science 139, 1–10.
- Le, K.C., Günther, C. (2014). Nonlinear continuum dislocation theory revisited. International Journal of Plasticity 53, 164–178.
- Le, K.C., Günther, C. (2015). Martensitic phase transition involving dislocations. Journal of the Mechanics and Physics of Solids 79, 67–79.
- Le, K.C., Nguyen, B.D. (2012). Polygonization: Theory and comparison with experiments. International Journal of Engineering Science 59:211-218.
- Le, K.C., Nguyen, B.D. (2013). On bending of single crystal beam with continuously distributed dislocations. International Journal of Plasticity 48, 152–167.
- Le, K.C., Piao, Y. (2016). Distribution of dislocations in twisted bars. International Journal of Plasticity 83, 110-125.
- Le, K.C., Piao, Y., (2018). Non-uniform plastic deformations of crystals undergoing anti-plane constrained shear. Arch. Appl. Mech. 88, https://doi.org/10.1007/s00419-018-1425-3.
- Le, K.C., Piao, Y., (2019a). Thermodynamic dislocation theory: Size effect in torsion. International Journal of Plasticity 115, 56-70.
- Le, K.C., Piao, Y., (2019b). Thermal softening during high-temperature torsional deformation of aluminum bars. International Journal of Engineering Science 137, 1–7.
- Le, K.C., Sembiring, P. (2008a). Analytical solution of the plane constrained shear problem for single crystals within continuum dislocation theory. Archive of Applied Mechanics 78, 587–597.
- Le, K.C., Sembiring, P. (2008b). Plane constrained shear of single crystal strip with two active slip systems. Journal of the Mechanics and Physics of Solids 56, 2541–2554.
- Le, K.C., Sembiring, P. (2009). Plane constrained uniaxial extension of a single crystal strip. International Journal of Plasticity 25, 1950–1969.
- Le, K.C., Stumpf, H., (1996). A model of elastoplastic bodies with continuously distributed dislocations. International Journal of Plasticity 12, 611-627.
- Le, K.C., Tran, T.M., (2017). Dislocation mediated plastic flow in aluminum: comparison between theory and experiment. International Journal of Engineering Science 119, 50-54.
- Le, K.C., Tran, T.M. (2018). Thermodynamic dislocation theory: Bauschinger effect. Physical Review E 97:043002.

Le, K.C., Piao, Y., Tran, T.M., (2018). Thermodynamic dislocation theory: Torsion of bars. Physical Review E 98: 063006.

- Le, K.C., Sembiring, P., Tran, T.N. (2016). Continuum dislocation theory accounting for redundant dislocations and Taylor hardening. International Journal of Engineering Science 106:155-167.
- Le, K.C., Tran, T.M., Langer, J.S. (2017). Thermodynamic dislocation theory of high-temperature deformation in aluminum and steel. Physical Review E 96:013004.
- Le, K.C., Tran, T.M., Langer, J.S. (2018). Thermodynamic dislocation theory of adiabatic shear banding in steel. Scripta Materialia 149:62-65.
- Leung, H.S., Leung, P.S.S., Cheng, B., Ngan, A.H.W., (2015). A new dislocation-density-function dynamics scheme for computational crystal plasticity by explicit consideration of dislocation elastic interactions. International Journal of Plasticity 67, 1-25.
- Li, D., Zbib, H., Sun, X., Khaleel, M. (2014). Predicting plastic flow and irradiation hardening of iron single crystal with mechanism-based continuum dislocation dynamics. International Journal of Plasticity 52, 3-17.
- Liu, D., He, Y., Tang, X., Ding, H., Hu, P., Cao, P., (2012). Size effects in the torsion of microscale copper wires: experiment and analysis. Scripta Materialia 66, 406-409.
- Liu, D., He, Y., Dunstan, D.J., Zhang, B., Gan, Z., Hu, P., Ding, H., (2013). Anomalous plasticity in the cyclic torsion of micron scale metallic wires. Physical Review Letters 110, 244301.
- Liu, D., He, Y., Dunstan, D. J., Zhang, B., Gan, Z., Hu, P., Ding, H., (2013a). Toward a further understanding of size effects in the torsion of thin metal wires: an experimental and theoretical assessment. International Journal of Plasticity 41, 30-52.
- Liu, D., Dunstan, D.J., (2017). Material length scale of strain gradient plasticity: A physical interpretation. International Journal of Plasticity 98, 156-174.
- Liu, D., Zhang, X., Li, Y., Dunstan, D.J., (2018). Critical thickness phenomenon in single-crystalline wires under torsion. Acta Materialia 150, 213-223.
- Ma, A., Roters, F., Raabe, D. (2006). A dislocation density based constitutive model for crystal plasticity FEM including geometrically necessary dislocations. Acta Materialia 54, 2169 2179.
- Ma, Q., Clarke, D.R. (1995). Size dependent hardness of silver single crystals. Journal of Materials Research 10, 853–863.
- Marchand, A., Duffy, J. (1988). An experimental study of the formation process of adiabatic shear bands in a structural steel. Journal of the Mechanics and Physics of Solids 36, 251-283.
- Marshall, S.L. (1999). A rapidly convergent modified Green's function for Laplace's equation in a rectangular region. Proc Roy Soc London A 455:1739-1766.

Matthews, J.W., Blakeslee, A.E. (1974). Defects in epitaxial multilayers: I. Misfit dislocations. Journal of Crystal Growth 27, 118–125.

- Mayeur, J.R., McDowell, D.L. (2014). A comparison of Gurtin type and micropolar theories of generalized single crystal plasticity. International Journal of Plasticity 57, 29-51.
- Mehta, A., Edwards, S.F. (1989). Statistical mechanics of powder mixtures. Physica A 157, 1091–1100.
- Meyers, M.A., Andrade, U.R., Chokshi, A.H. (1995). The effect of grain size on the high-strain, high-strain-rate behavior of copper. Metallurgical and Materials Transactions A, 26:2881–2893.
- Mianroodi, J.R., Hunter, A., Beyerlein, I.J., Svendsen, B. (2016). Theoretical and computational comparison of models for dislocation dissociation and stacking fault/core formation in fcc crystals. Journal of the Mechanics and Physics of Solids, 95:719–741.
- Moser, B., Kuebler, J., Meinhard, H., Muster, W., Michler, J. (2005) Observation of instabilities during plastic deformation by in-situ SEM indentation experiments. Advanced Engineering Materials 7, 388–392
- Motz, C., Schöberl, T., Pippan, R. (2005). Mechanical properties of micro-sized copper bending beams machined by the focused ion beam technique. Acta Materialia 53, 4269–4279.
- Motz, C., Dunstan, D.J. (2012). Observation of the critical thickness phenomenon in dislocation dynamics simulation of microbeam bending. Acta Materialia 60, 1603–1609.
- Nix, W.D., Gao, H. (1997). Indentation size effects in crystalline materials: A law for strain gradient plasticity. Journal of the Mechanics and Physics of Solids 46, 411–425.
- Nye, J.F. (1953). Some geometrical relations in dislocated crystals. Acta Metallurgica 1, 153–162.
- Ono, I.K., O'Hern, C.S., Durian, D.J., Langer, S.A., Liu, A.J., Nagel, S.R. (2002). Effective temperatures of a driven system near jamming. Physical Review Letters, 89 (9), 095703
- Oztop, M.S., Niordson, C.F., Kysar, J.W. (2013). Length-scale effect due to periodic variation of geometrically necessary dislocation densities. International Journal of Plasticity 41, 189–201.
- Read, W.T., Shockley, W. (1950). Dislocation models of crystal grain boundaries. Physical Review 78, 275-289.
- Rittel, D., Zhang, L.H., Osovsky, S. (2017). The dependence of the Taylor-Quinney coefficient on the dynamic loading mode. Journal of the Mechanics and Physics of Solids 107, 96–114.
- Rycroft, C.H., Bouchbinder, E., 2012. Fracture toughness of metallic glasses: annealing-induced embrittlement. Physical Review Letter 109, 194301

Petch, N.J.(1953). The Cleavage Strength of Polycrystals. The journal of the iron and steel institute 174, 25–28.

- Po, G., Lazar, M., Seif, D., Ghoniem, N. (2014). Singularity-free dislocation dynamics with strain gradient elasticity. Journal of the Mechanics and Physics of Solids 68:161-178.
- Puglisi, G., Truskinovsky, L. (2005). Thermodynamics of rate-independent plasticity. Journal of the Mechanics and Physics of Solids 53:655-679.
- Sandfeld, S., Hochrainer, T., Zaiser, M., Gumbsch, P. (2011). Continuum modeling of dislocation plasticity: Theory, numerical implementation, and validation by discrete dislocation simulations. Journal of Material Research 26, 623-632.
- Sandfeld, S. and Zaiser, M. (2015). Pattern formation in a minimal model of continuum dislocation plasticity. Modelling Simul. Mater. Sci. Eng., 23:065005
- Sandfeld, S., Thawinan, E., Wieners, C. (2015). A link between microstructure evolution and macroscopic response in elasto-plasticity: formulation and numerical approximation of the higher-dimensional continuum dislocation dynamics theory. International Journal of Plasticity 72, 1–20.
- Sedov, L.I. (1965). Mathematical methods of constructing models of continuum media. Russian Mathematical Surveys 20, 123–182.
- Senger, J., Weygand, D., Kraft, O., Gumbsch, P. (2011). Dislocation microstructure evolution in cyclically twisted microsamples: a discrete dislocation dynamics simulation. Modelling and Simulation in Materials Science and Engineering 19, 074004.
- Shi, H., McLaren, A.J., Sellars, C.M., Shahani, R., Bolingbroke, R. (1997). Constitutive equations for high temperature flow stress of aluminum alloys. Journal of Materials Science and Technology 13, 210-216.
- Sollich, P., Cates, M.E. (2012). Thermodynamic interpretation of soft glassy rheology models. Physical Review E 85, 031127.
- Stölken, J.S, Evans, A.G. (1998). A microbend test method for measuring the plasticity length scale. Acta Materialia 46, 5109-5115.
- Sun, S., Adams, B.L., Shet, C., Saigal, S., King, W. (1998). Mesoscale investigation of the deformation field of an aluminum bicrystal. Scripta Mater. 39, 501–508.
- Svendsen, B., Bargmann, S. (2010). On the continuum thermodynamic rate variational formulation of models for extended crystal plasticity at large deformation. Journal of the Mechanics and Physics of Solids 58:1253-1271.
- Uchic, M., Dimiduk, D., Florando, J., Nix, W. (2004). Sample dimensions influence strength and crystal plasticity. Science 305, 986–989.
- Vitek, V., (1987). On the difference between the misorientation dependences of the energies of tilt and twist boundaries. Scripta Metallurgica 21, 711-714.
- Varshni, Y.P., (1970). Temperature dependence of the elastic constants. Physical Review B 2, 3952.

Wang, W., Huang, Y., Hsia, K. J., Hu, K. X., Chandra, A., (2003). A study of microbend test by strain gradient plasticity. International Journal of Plasticity 19, 365-382.

- Weertman, J. (2002) Anomalous work hardening, non-redundant screw dislocations in a circular bar deformed in torsion, and non-redundant edge dislocations in a bent foil. Acta Materialia 50, 673–689.
- Weinberger, C.R., Cai, W. (2010). Plasticity of metal wires in torsion: Molecular dynamics and dislocation dynamics simulations. Journal of the Mechanics and Physics of Solids 58, 1011–1025.
- Weinberger, C.R. (2011). The structure and energetics of, and the plasticity caused by, Eshelby dislocations. International Journal of Plasticity 27, 1391–1408.
- Wrobel, M., Piela, K. (2010). Basal slip localization in zinc single crystals. Philosophical magazine 90, 1873–1891.
- Wulfinghoff, S., Bayerschen, E., Böhlke, T. (2013). A gradient plasticity grain boundary yield theory. International Journal of Plasticity 51, 33–46.
- Wulfinghoff, S., Forest, S., Böhlke, T. (2014). Strain gradient plasticity modelling of the cyclic behaviour of laminate microstructures. Journal of the Mechanics and Physics of Solids 79, 1–20.
- Wulfinghoff, S., Böhlke, T. (2015). Gradient crystal plasticity including dislocation-based work-hardening and dislocation transport. International Journal of Plasticity 69, 152–169.
- Zaiser, M. (2015). Local density approximation for the energy functional of three-dimensional dislocation systems. Physical Review B 92(17), 174120.
- Zhou, M., Clode, M. (1998). A finite element analysis for the least tem- perature rise in a hot torsion test specimen. Finite Elements in Analysis and Design 31, 1–14.
- Zhu, Y., Wang, H., Zhu, X., Xiang, Y. (2014). A continuum model for dislocation dynamics incorporating Frank-Read sources and Hall-Petch relation in two dimensions. International Journal of Plasticity 60, 19–39.
- Zhu, Y., Xiang, Y. (2015). A continuum model for dislocation dynamics in three dimensions using the dislocation density potential functions and its application to micro-pillars. Journal of the Mechanics and Physics of Solids 84, 230–253.
- Ziemann, M., Chen, Y., Kraft, O., Bayerschen, E., Wulfinghoff, S., Kirchlechner, C., Tamura, N., Bölke, T., Walter, M., Gruber, P.A., (2015). Deformation patterns in cross-sections of twisted bamboo-structured Au microwires. Acta Materialia 97, 216-222.

Curriculum Vitae 165

#### Curriculum Vitae

#### Personal Data

Name Yinguang Piao

Date of Birth April 20, 1989

Place of Birth Yanji, Jilin, China

Nationality China

Marital Status Married

#### **School Education**

09/2001–07/2004 Yanji Experimental Middle School

09/2004–07/2007 Yanbian Number One high School

### University Education

09/2007-07/2011 Mechanical Engineering,

Yanbian University, China, Bachelor of Science (B.Sc.)

02/2009-02/2010 Mechanical Engineering,

Korea Advanced Institute of Science and Technology (KAIST),

South Korea,

Bachelor of Science (B.Sc.)

10/2011-03/2014 Computational Engineering,

Ruhr-Universität Bochum (RUB), Germany,

Master of Science (M.Sc.)

Mitteilungen aus dem Institut für Mechanik RUHR-UNIVERSITÄT BOCHUM Nr. 183

ISBN 978-3-935892-61-2